MIXED CONVECTION AND HYDRODYNAMIC MODELING OF FLOWS IN ROD BUNDLES

Vol 1

by

APOSTOLOS EFTHIMIADIS

Mech.-Elec. Engr. Dipl., National Technical University of Athens
(1978)

M.S., Purdue University
(1980)

Submitted to the Department of
Nuclear Engineering
in Partial Fulfillment of the
Requirements of the Degree of

DOCTOR OF PHILOSOPHY

at the

June 1984

Signature redacted

Signature of Author _____
Department of Nuclear Engineering
April 30, 1984

Signature redacted

Certified by _____
Professor Neil E. Todreas
Thesis Supervisor

Signature redacted

Accepted by _____
Allen F. Henry
Chairman, Department Graduate Committee

Vol. 1

MIXED CONVECTION AND HYDRODYNAMIC MODELING OF FLOWS IN ROD BUNDLES

by

Apostolos Efthimiadis

Submitted to the Department of Nuclear Engineering on April 30, 1984 in partial fulfillment of the requirements for the degree of Doctor of Philosophy in Nuclear Reactor Engineering.

Abstract

A 19-pin wire-wrapped vertical rod bundle was designed and built in order to perform pressure drop, heat transfer, velocity and temperature measurement experiments under low Reynolds mixed convection flow conditions. The mixed-to-forced friction factor ratio data was significantly lower than the corresponding circular tube or the 91-pin wire-wrapped rod bundle data found in the literature. An instrumented rod (IR) was designed and built to allow detailed wall temperature measurements at any axial or peripheral location of the IR wall. Based on the IR data, the Nusselt number as a function of the ratio of Grashof to Reynolds number was estimated.

Three-dimensional flow hydrodynamic resistance models for rod bundles were developed. These models specifically account for the presence of the wire-wrap spacer and may be used for any lumped parameter thermo-hydraulic analysis numerical program. Attribute functions were developed to incorporate these models in the ASFRE subchannel analysis code for the particular case of Δz (axial size of the numerical mesh) equal to H/12 (H is the wire-wrap lead length).

Subchannel velocity and temperature data were obtained at the exit region of the 19-pin bundle. These data may directly be used for validation studies of lumped parameter numerical programs. It was found that the subchannel temperature profiles tend to become flatter with increasing buoyancy forces. It was also found that for isothermal laminar flows in the 19-pin wire-wrapped bundle, the edge flow split parameter was approximately equal to 1.12.

Validation studies for the hydrodynamic resistance models were also performed. The models were tested against our subchannel velocity and temperature data plus other data available in the literature. Overall the models performed satisfactorily predicting the most important qualitative trends for flows in wire-wrapped bundles. It was found that the s/ℓ subchannel analysis parameter plays an important role in correctly modeling the transverse velocity field.

Thesis Supervisor: Professor Neil E. Todreas
Title: Head, Department of Nuclear Engineering

Thesis Reader: Professor Warren M. Rohsenow
Title: Chairman of the Graduate Committee, Department of Mechanical Engineering

to my wife Maria
to our son Yiannis
to all children of the world
to Peace

στην γυναίκα μου Μαρία
στον γυιο μας Γιάννη
σε όλα τα παιδια του κόσμου
στην Ειρήνη

Acknowledgements

I wish to express my deep graditude and respect to my thesis advisor, Professor Neil Todreas for his numerous and decisive discussions, directions and suggestions during the course of this work. His emphasis on the essentials and organization, his emphasis on both the fundamentals and the applications, his respect to his students, both as scientists and as people and his long standing work on the peaceful use of nuclear energy, has left a permanent impression on me and taught me how academia can perform at its best.

I also want to thank Professor Warren Rohsenow, my thesis reader for the inspiring discussions and suggestions. Thanks are also extended to Professors Andrei Schor, John Meyer, and Mujid Kazimi for their discussions and academic support.

Dr. Hisashi Ninokata is gratefully acknowledged for his detailed explanation of the intricancies of the ASFRE numerical program. The experimental expertise of Mr. Toshio Okada drastically improved the quality of our pressure drop mixed convection data.

This project could not have been accomplished without the machining work of Bob Bara and the machining, assembling and electrical work of Fred Johnson. Both these men as well as Don Wassmouth, Bill Finley, Tinny Caloggero and John Williams who also helped in the laboratory work, are gratefully acknowledged.

Elenore Kehoe with her excellent typing and organization as well as her friendly and warm presence created a first-rate office environment and substantially facilitated my adjustment at MIT particularly at the

early period of my life here. I also enjoyed working with Sarah Finigan who typed most of my thesis always in a cheerful mood. Judy Bolger was always ready to help when a small but urgent piece of work had to be done.

Long associations and discussions with my colleagues and friends: Shih-Kuei Cheng, Paul Symolon, Derek Ebeling-Koning, Shih-Ping Kao and Sang-Nyang Kim as well as Kune Suh, Tsing Huang, Tae-Sun Ro and Ildo Sauer were particularly helpful in promoting an academic environment full of scientific ideas and personal understanding.

I also want to thank my Greek and Greek-American friends who made life in Cambridge and Boston look like home and who also helped create an environment for social participation and integration.

Special thanks are due to my mother-in-law, Ioanna Gini who for almost one year took care of our first child, Yiannis, and to my wife, Maria Gini who successfully managed to combine the enormous responsibilities of maternity with the hardships of graduate work at MIT.

The financial and academic support of Power Reactor and Nuclear Fuel Development Corporation (Japan) is greatfully acknowledged.

Tolis Efthimiadis

Cambridge, April 1984

TABLE OF CONTENTS

TABLE OF CONTENTS (cont')

TABLE OF CONTENTS (cont'd)

TABLE OF CONTENTS (cont'd)

TABLE OF CONTENTS (cont'd)

TABLE OF CONTENTS (cont'd)

LIST OF FIGURES

LIST OF FIGURES (cont'd)

LIST OF FIGURES (cont'd)

Page

LIST OF FIGURES (cont'd)

Page

LIST OF FIGURES (cont'd)

LIST OF FIGURES (cont'd)

LIST OF TABLES

CHAPTER 1

INTRODUCTION AND MATHEMATICAL FORMULATION OF THE MIXED CONVECTION PROBLEM

1.1 Introduction

Understanding of the buoyancy driven or buoyancy dominated flows in energy exchanging industrial components (nuclear reactors, heat exchangers, passive solar systems) is becoming increasingly important. Such conditions arise when at a given component the heat input-to-flow rate ratio increases to a point where local buoyancy effects drastically alter the structure of the flow field, rendering forced convection heat transfer and pressure drop correlations inaccurate. Safety considerations associated with buoyancy driven low flow transients in both thermal and Fast Breeder reactors as well as design considerations for industrial and power generating equipment have triggered a number of analytical, computational and experimental studies of mixed convection flows in vertical ducts. Most of these studies are concentrated in circular tube geometry whereas the rod bundle geometry has receive considerable less attention.

In this work we are primarily interested in geometrical and flow characteristics which arise in Liquid Metal Fast Breeder Reactor cores under natural circulation transients. The Reynolds number in the core is expected to range between 1,000 and 5,000 and the heat input is considered to be equal to the residual heat (~ 6% of nominal reactor power). Such transients are expected to occur during loss of pump power or pump seizure accidents. Natural circulation is expected to occur due to temperature

differences between the heat exchangers (heat sink) and the reactor core (heat source).

The scope of the present work includes the following:

(a) Study the fundamental characteristics of mixed convection low Reynolds flows in rod bundles.

(b) Develop a numerical program to be used as a design tool for wire-wrapped rod bundle thermohydraulic analysis under the above conditions.

(c) Experimentally obtain a set of data to be used for calibration and testing of the above program.

(d) Initiate validation/calibration studies for the numerical program developed in this work.

Next some of the most fundamental mixed convection phenomena and the relevant terminology are presented.

1.2. Terminology Definition and Mixed Convection Fundamental Characteristics

The terms forced, mixed, and natural (or free) are commonly used in the literature together with the nouns circulation or convection. However, in most cases no distinction is made about the scale of the experiment i.e. global or local. To explain these terms refer to Figure 1.1. In Figure 1.1. (a), the pool of liquid is initially at rest. If the tube is heated, the average density of the liquid in the tube decreases. This reduced density causes an increase in the buoyant force and the fluid tends to rise and pass out the top of the tube where it mixes with the large mass of the unheated surrounding fluid. This type of flow will be called natural circulation (also called free convection).

If the surrounding fluid is replaced by the cooler piping

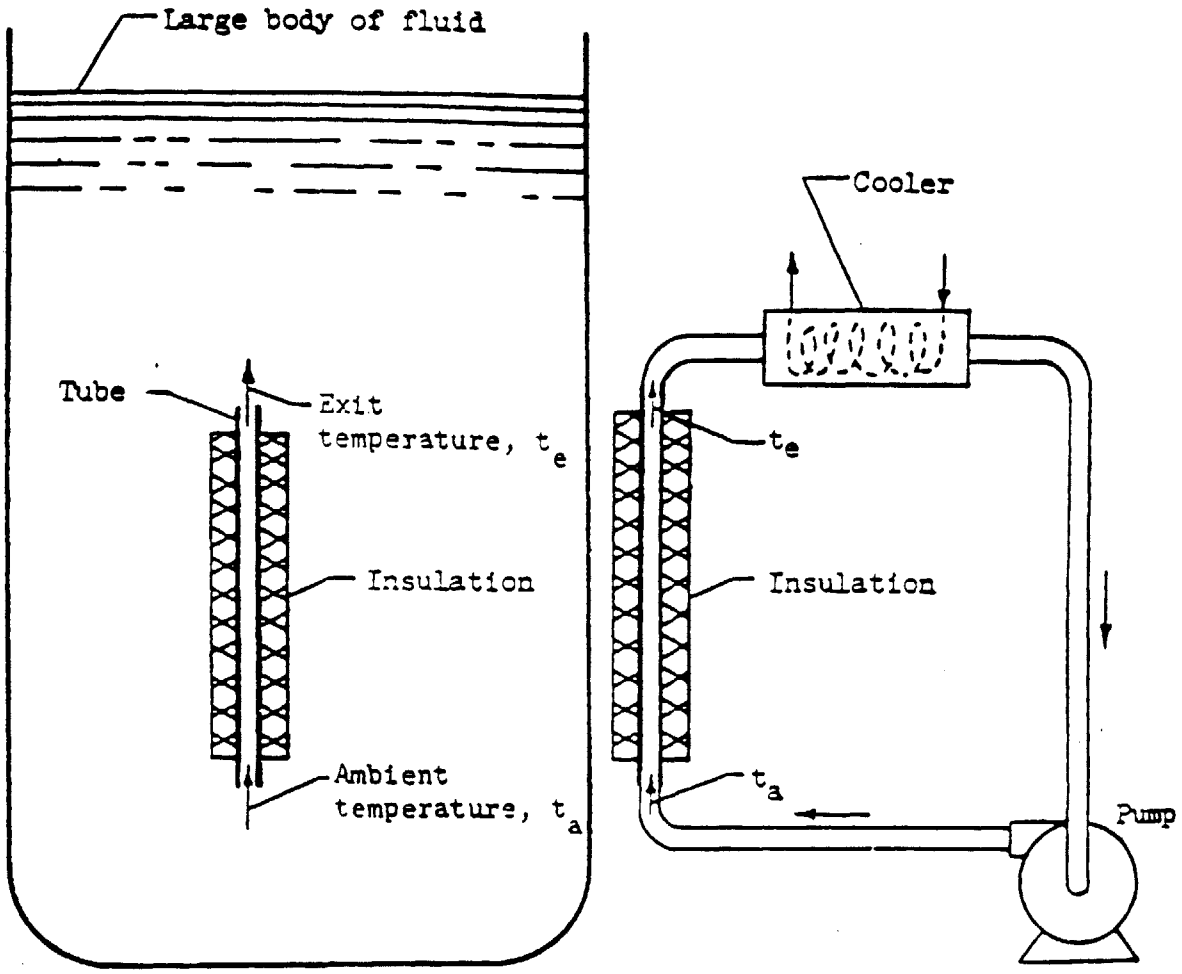

(a) NATURAL CIRCULATION (b) MIXED CIRCULATION

FIGURE 1.1. ILLUSTRATION OF NATURAL CIRCULATION AND MIXED CONVECTION CONDITIONS

system and pump shown in Figure 1.1 (b) and the cooling and pumping rates are controlled to maintain the temperatures t_a and t_e, conditions are unchanged inside the pipe. This situation will be called mixed circulation.

In a global sense, there is an important distinction between these two conditions. In natural circulation, for a given heating rate in the tube, there is a unique flow rate established, which is such that the pressure drop through the tube is exactly balanced by the net buoyant force. In mixed circulation, there is freedom to adjust the pump flow rate to any desired value. Of course, when the flow rate is changed, the heat transfer rate must be changed in order to keep t_a and t_e unchanged. The buoyant forces still exist, regardless of the flow rate, but only one flow rate corresponds to the natural circulation situation.

In a local (subchannel) sense though, at a certain axial level the flow is not dependent upon the global mechanism of circulation. Local balance of the buoyancy, viscous and inertia foces will determine whether the buoyant effects are important (mixed convection) or not (forced convection).

The situation in which the buoyancy effects are not important in a global or local sense will be called forced circulation or forced convection respectively.

Note that in recirculating flow systems, like those of Figure 1.1 (a) and 1.1 (b), there is always some flow going through the core, as long as some external cooling takes place. However, in some exotic scenarios the recirculation in the loop of Figure 1.1 (b) could be completely inhibited. In that case the flow will recirculate within the heated tube or rod

bundle. This case is commonly called natural circulation (or convection) in enclosure.

Next the most important effects of mixed convection flows on both pressure drop and heat transfer characteristics are briefly examined.

The term aiding flow indicates the fact that the buoyant flow is concurrent with the pumped flow (i.e., upward flow in heated channel, downward flow in cooled channel). Exactly the opposite is meant by the term opposing flow.

Figure 1.2 shows qualitatively the velocity profile in vertical parallel plates under both foced convection (FC) and mixed convection (MC) conditions. Aiding (AF) and opposing (OF) flows are shown in Figures 1.2(a) and 1.2(b) respectively. Assuming that the mass flux remains constant and for increasing the heat flux, a smooth transition occurs from the FC to MC situations.

For AF, the velocity profile becomes steeper at the wall region, and depending on the magnitude of the ratio $\dot{q}''_w/\dot{m}$, a second velocity peak toward the heated walls might occur. Due to the increase of $\partial u/\partial z\,|_{wall}$, the friction factor f will increase too. The laminar heat transfer (Nu number) will be also augmented. This is due to the fact that the heat transfer coefficient is in general determined by two factors: the velocity and heat diffusivity distributions in the fluid. For laminar flow, the diffusivity remains constant but the velocity increases at the wall region. The higher the velocity close to the wall, the higher the resulting heat transfer coefficient (see Chapter 4 for Nu number behavior in turbulent mixed convection flows).

Exactly the opposite phenomena occur for laminar OF. Note that the

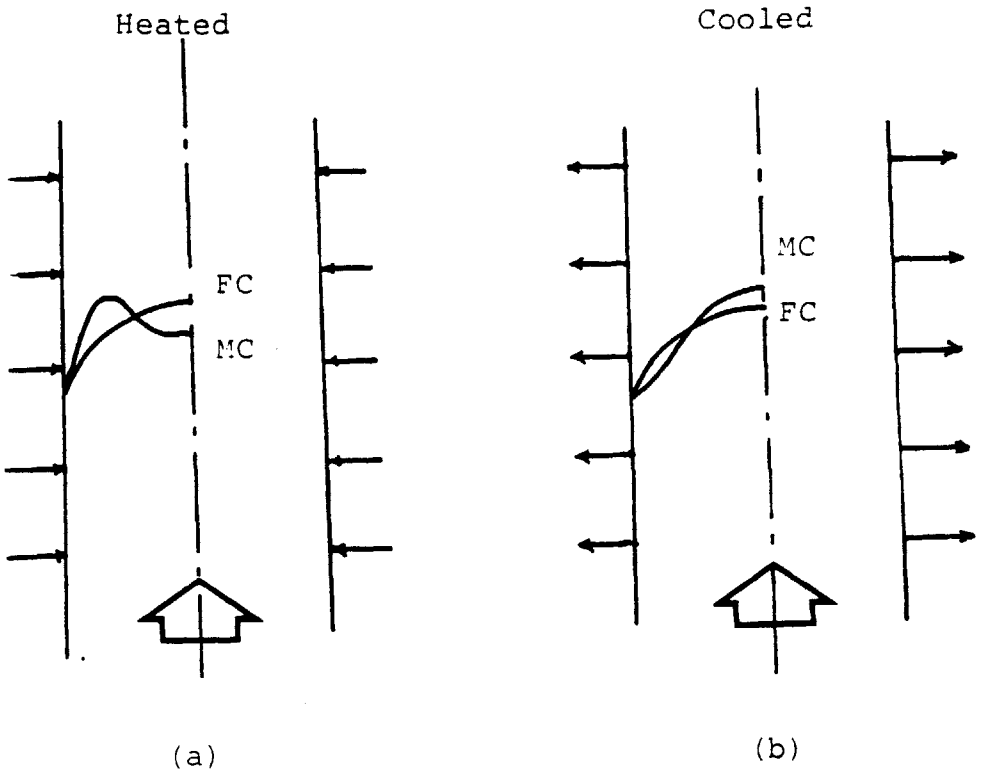

FIGURE 1.2. : Velocity Profiles in Vertical Channels for Forced Convection (FC) and Mixed Convection (MC)
(a) Aiding Flows
(b) Opposing Flows

steeper the velocity profiles become, due to buoyancy effects, the more imminent is the onset of instability and transition to turbulence. Onset of instability maps are therefore needed to establish the region of validity of the laminar MC analyses.

1.3 Statement of the Problem

In this work the following Tasks were set forth and accomplished.

Task I Fundamentals of Low Flow Mixed Convection in Rod Bundles

(a)The non-dimensional differential conservation equations and the boundary conditions are formulated and the dominant dimensionless parameters for developing and fully developed flows are identified. Also generalized expressions for friction factors and heat transfer coefficients are developed (Chapter 1).

(b) A 19-pin wire-wrapped rod bundle is designed and constructed such that it allows detailed measurements of subchannel velocities and temperatures (Chapter 2).

(c) Isothermal and mixed convection pressure drop data are obtained for low Reynold's flows in both bare and wire-wrapped rod bundles. For these data, a systematic measurement procedure is developed in order to minimize uncertainties due to uncontrollable temperature variations (Chapter 3).

(d) An Instrumented Rod is designed and constructed in order to perform detailed temperature measurements at the wall of a heated rod. Mixed convection Nusselt number data are also obtained (Chapter 4).

Task II Subchannel Analysis for Wire-Wrapped Rod Bundles

(a) The applicability of the subchannel analysis approach for thermo-hydraulic analysis of wire-wrapped rod bundles is qualitatively and quantitatively considered. The advantages and limitations of the subchannel analysis versus the porous body approach are also examined (Chapter 6).

(b) Flow resistance models for flows of arbitrary direction in wire-wrapped rod bundles are developed (Chapter 7).

(c) The above resistance models are incorporated in a subchannel analysis numerical program (ASFRE). Special geometrical pattern identification attribute functions are developed for this purpose (Chapter 8).

Task III Data Base for Code Validation

(a) A Hot-film Anemometry technique is developed to perform subchannel axial velocity measurements in the wire-wrapped bundle. Velocity profile and flow split data are obtained (Chapter 5).

(b)Subchannel temperature data are obtained under low Reynolds mixed conveciton flows and power skew conditions in the 19-pin wire-wrapped bundle (Chapter 5).

Task IV Preliminary Code Validation Studies

(a) The flow resistance models in the code are tuned and tested against velocity data of Task III (laminar flows) and other data available in the literature (Chapter 8).

(b) The code is also tested against the mixed convection temperature data presented in Task III (Chapter 8).

1.4 Mathematical Formulation of the Mixed Convection Problem

1.4.1 The Governing Equations

In this section the dominant non-dimensional parameters of the problem are derived, based on the governing differential conservation equations for mass, momentum and energy: (incompressible form)

Continuity: $$\vec{\nabla} \cdot \vec{V} = 0 \tag{1.1}$$

Momentum: $$\rho \frac{D\vec{V}}{Dt} = - \vec{\nabla} p + \mu \nabla^2 \vec{V} + \vec{F} \tag{1.2}$$

Energy: $$\rho c_p \frac{DT}{Dt} = k \nabla^2 T + \mu\Phi + W \tag{1.3}$$

where $\vec{F}$ = body force per unit volume

$\mu\Phi$ = rate of energy increase per unit volume by viscous dissipation.

W = rate of energy generation per unit volume.

When the gravitational force is the only form acting on the system the body force term $\vec{F}$ can be represented as:

$$\vec{F} = \vec{F}_z = \mp g_o \vec{k} \tag{1.4}$$

where the minus and plus correspond to aiding and opposing flows respectively and $\vec{k}$ is the unit vector along the vertical direction. Using the Boussinesq approximation, all physical properties may be considered to be constant except ρ which satisfies the following relationship:

$$\rho = \rho_o (1 - \beta(T - T_o)) \tag{1.5}$$

where T_o is some reference temperature.

Let ρ_o, μ_o, k_o, C_{p_o} represent the characteristic reference magnitude of the corresponding property. Let the average velocity V_o, the hydraulic diameter De and $(T_1 - T_o)$ represent some characteristic scales of the system.

The temperature T_o is usually taken approximately equal to the film temperature $(\overline{T}_w + T_m)/2$, where $\overline{T}_w$ is the average wall temperature and T_m is the mean temperature of the fluid. In practice the film temperature is not "a priori" available and therefore T_o can be only approximately estimated. Alternatively the inlet temperature may be used as T_o. The following dimensionles variables are defined:

dimensionless distance: $$z^* = \frac{z}{De} \tag{1.6}$$

dimensionless velocity: $$\vec{V}^* \equiv \frac{\vec{V}}{V_o} = (u^*, v^*, w^*) \tag{1.7}$$

dimensionless pressure: $$p^* \equiv \frac{p}{\rho_o V_o^2} \tag{1.8}$$

dimensionless time: $$t^* \equiv \frac{t\ V_o}{De} \tag{1.9}$$

dimensionless temperature: $$T^* \equiv \frac{T - T_o}{T_1 - T_o} \tag{1.10}$$

dimensionless density: $$\rho^* \equiv \frac{\rho}{\rho_o} \tag{1.11}$$

dimensionless viscosity: $$\mu^* \equiv \frac{\mu}{\mu_o} \tag{1.12}$$

dimensionless specific heat: $c_p^* = \frac{c_p}{c_{p_o}}$ (1.13)

Writing equations 1.1, 1.2 and 1.3 in dimensionless form and using the Boussinesq approximation yields:

$$\vec{\nabla}^* \cdot \vec{V}^* = 0 \tag{1.14}$$

$$\frac{D^* \vec{V}^*}{Dt^*} = - \vec{\nabla}^* p^* + \frac{1}{Re} \nabla^{*2} V^* \mp \left(\frac{Gr_{\Delta T}}{Re^2} T^* - \frac{1}{Fr}\right) \tag{1.15}$$

$$\frac{D^* T^*}{Dt^*} = \frac{1}{Re\ Pr} \nabla^{*2} T^* + \frac{De}{(T_1 - T_o)\ \rho_o\ c_{p_o}\ V_o} W + \frac{Ec}{Re} \Phi^* \tag{1.16}$$

where again the minus and plus in the momentum equation correspond to aiding and opposing flows respectively.

In the above dimensionless equations five dimensionless numbers arise:

Reynolds number: $Re = \frac{\rho_o\ De\ V_0}{\mu_o}$ (1.17)

Grashof number: $Gr_{\Delta T} = \frac{g\ \beta \rho_o^2\ (T_1 - T_o)\ De^3}{\mu_o^2}$ (1.18)

Prandtl number: $Pr = \frac{c_{p_o}\ \mu_o}{k_o}$ (1.19)

Froude number: $Fr = \frac{V_o^2}{g\ De}$ (1.20)

Neglecting the heat source and viscous dissipation, the energy equation 1.16 becomes:

$$\frac{D^* T^*}{Dt^*} = \frac{1}{Re\ Pr} \nabla^{*2}\ T^* \tag{1.21}$$

and therefore the dominant dimensionless groups are the following:

$$Re,\ \frac{Gr_{\Delta T}}{Re^2},\ Fr,\ Re\ Pr$$

We now turn our attention to fully developed laminar mixed convection flows in vertical direction. Then the momentum and energy equations are written as follows:

$$-\frac{dp^*}{dz^*} + \frac{1}{Re} \nabla^{*2}\ w^* \mp \left(\frac{Gr_{\Delta T}}{Re^2}\ T^* - \frac{1}{Fr}\right) = 0 \tag{1.22}$$

$$w^* \frac{\partial T^*}{\partial z^*} = \frac{1}{Re\ Pr} \nabla^{*2}\ T^* \tag{1.23}$$

1.4.2 The Axially Constant Heat Flux Boundary Condition Case

Let A_c be a two-dimensional domain on a horizontal plane enclosed by the boundary S. The domain A_c represents the cross-section of the duct, on which equations 1.22 and 1.23 will be integrated. The boundary surface S is composed from two parts; S_w and S_f which represent the wall-fluid and the fluid-fluid interfaces respectively.

The constant heat flux boundary condition can be written as follows:

$$\frac{\partial \dot{q}''_w}{\partial z}\ \Big|_{S_w} = 0 \tag{1.24a}$$

$$\text{thus} \quad \bar{\dot{q}}''_w = \frac{1}{P_w} \int_{S_w} \dot{q}''_w \Big|_{S_w} dS = \text{constant} \tag{1.24b}$$

where $P_w = \int_S dS$: The wetted perimeter,

and $\dot{q}''_w$ is the local heat flux at a point of S_w. For the constant heat flux case from a heat balance obtain:

$$\frac{\partial T^*}{\partial z^*} = \frac{4}{PrRe} \frac{\bar{\dot{q}}''_w \, De}{k(T_1 - T_o)} = \text{const.} \tag{1.25}$$

In order to further simplify equation 1.23 introduce a new dimensionless temperature θ^*:

$$\theta^* = \frac{T^*}{Re \; Pr \; \frac{\partial T^*}{\partial z^*}} \tag{1.26}$$

Using equation 1.25, θ^* can be written as follows:

$$\theta^* = \frac{(T - T_o)}{4 \; \bar{\dot{q}}''_w \; De/k} \tag{1.27}$$

Equation 1.23 is then written as:

$$\nabla^{*2} \; \theta^* - w^* = 0 \tag{1.28}$$

The momentum equation can also be written as:

$$\nabla^{*2} \; w^* \mp 4 \frac{Gr_q}{Re} \theta^* = - Re \; (\frac{dp^*}{dz^*} \mp \frac{1}{Fr}) \tag{1.29}$$

A new form of the Grashof number arises in equation 1.29

$$Gr_q = \frac{g \; \beta \; \rho_o^2 \; \bar{\dot{q}}''_w \; D_e^4}{\mu^2 \; k} = \frac{Re \; Pr}{4} \frac{\partial T^*}{\partial z^*} \; Gr_{\Delta T} \tag{1.30}$$

where $\bar{\dot{q}}''_w$ is the wall heat flux (for aiding flows).

The right hand side equation 1.29 can be further analyzed as follows. From a force balance in the axial direction obtain:

$$\frac{4}{De}\ \bar{\tau}_w = -\left[\frac{dp}{dz} \mp \rho g\right] \tag{1.31}$$

where $\bar{\tau}_w$ is the average wall shear stress and - and + signify the upward or downward flow directions respectively.

Since

$$\bar{\tau}_w = -\frac{\mu_o}{P_w} \int_{S_w} \frac{\partial w}{\partial \hat{n}} \Big|_{wall} dS \tag{1.32}$$

where $\hat{n}$ is a horizontal unit vector normal to the duct wall, and P_w is the wetted perimeter,

$$\text{then} \qquad \frac{4\ \mu_o}{De\ P_w} \int_{S_w} \frac{\partial w}{\partial \hat{n}} \Big|_{wall} dS = \left[\frac{dp}{dz} \mp \rho g\right] \tag{1.33}$$

Expressing 1.33 in dimensionless form:

$$\frac{4}{Re} \int_{S_w} \frac{\partial w}{\partial \hat{n}} \Big|_{wall} \frac{dS}{P_w} = \left[\frac{dp^*}{dz^*} \mp \frac{1}{Fr}\right] \tag{1.34}$$

Substituting equation 1.34 into 1.29 obtain:

$$\nabla^{*2} w^* \mp 4 \frac{Gr_q}{Re} \theta^* = 4 \int_{S_w} \frac{\partial w^*}{\partial \hat{n}^*} \Big|_{wall} \frac{dS}{P_w} \tag{1.35}$$

From equations 1.35 and 1.28 we observe that the only dimensionless number left is the Gr_q/Re parameter, arising in the momentum equation 1.35. Note that the energy equation does not depend on any dimensionless number. The Gr_q/Re parameter physically represents:

$$\frac{Gr_q}{Re} \sim \frac{\text{(Buoyancy Forces)}}{\text{(Viscous Forces)}} \tag{1.36}$$

We turn now our attention to the specific velocity and temperature boun-

dary conditions to be applied. For the dimensionless velocity w* two kinds of B.C.s on S_f and S_w may exist:

$$w^* \Big|_{S_w} = 0 \qquad \text{(Dirichlet)} \tag{1.37}$$

or

$$\frac{\partial w^*}{\partial \hat{n}^*} \Big|_{S_f} = 0 \qquad \text{(Neumann)} \tag{1.38}$$

The boundary conditions for the dimensionless temperature θ^* are of the Neumann type:

$$\frac{\partial \theta^*}{\partial \hat{n}} \Big|_{S_f} = 0 \tag{1.39}$$

$$\frac{\partial T^*}{\partial \hat{n}^*} \Big|_{S_w} = \frac{\dot{q}_w'' \, De}{k(\bar{T}_1 - \bar{T}_o)} = \frac{\bar{\dot{q}}_w'' \, De}{k(\bar{T}_1 - \bar{T}_o)} \frac{\dot{q}_w''}{\bar{\dot{q}}_w''}$$

or

$$\frac{\partial \theta^*}{\partial \hat{n}^*} \Big|_{S_w} = \frac{1}{4} \frac{\dot{q}_w''}{\bar{\dot{q}}_w''} \qquad \text{(Neumann)} \tag{1.40}$$

From equations 1.37, 1.38, 1.39 and 1.40 it is observed that the boundary conditions for velocity and temperature depend only on the geometrical characteristics of the duct and the shape function $\dot{q}_w''/\bar{\dot{q}}_w''$. It can be concluded therefore that the only dimensionless parameter arising in the conservation equations and their boundary conditions is Gr_q/Re.

1.4.3 The Axially Constant Temperature Boundary Condition Case

The constant temperature B.C. is defined as follows:

let

$$\bar{T}_w = \frac{1}{P_w} \int_{S_w} T \Big|_{S_w} \, dS_w \tag{1.41a}$$

then $$\frac{\partial \overline{T}_w}{\partial z} = \frac{\partial T}{\partial z}\Big|_{S_w} = 0 \qquad (1.41b)$$

For fully developed temperature conditions it is well know that: [R-7]

$$\hat{T} = \frac{\overline{T}_w - T}{\overline{T}_w - T_m} = f(\vec{r}^*) \qquad (1.42)$$

where $$T_m = \frac{\int_{A_c} w\, T\, dA_c}{\int_{A_c} w\, dA_c} \qquad (1.43)$$

and $\vec{r}^*$ is a dimensionless location vector. For the constant temperature boundary condition, differentiating 1.42 take:

$$\frac{\partial T}{\partial z} = f(\vec{r}^*)\, \frac{\partial T_m}{\partial z} \qquad (1.44)$$

or $$\frac{\partial T^*}{\partial z^*} = f(\vec{r}^*)\, \frac{\partial T^*_m}{\partial z^*} \qquad (1.45)$$

Substituting 1.45 into the energy equation 1.23 obtain:

$$w^* f(\vec{r}^*)\, \frac{\partial T^*_m}{\partial z^*} = \frac{1}{Re\ Pr}\, \nabla^{*2}\, T^* \qquad (1.46)$$

In addition:

$$\frac{\partial T_m}{\partial z} = \frac{\overline{\dot{q}}''_w\, P_w}{\dot{m}\, C_p} = \frac{k\, \frac{\overline{\partial T}}{\partial \hat{n}}\Big|_{S_w} P_w}{\dot{m}\, C_p} = \frac{k(\overline{T}_w - T_o)}{\dot{m}\, C_p\, De} \int_{S_w} \frac{\partial T^*}{\partial \hat{n}^*}\Big|_{S_w} dS_w$$

or $$\frac{\partial T^*_m}{\partial z^*} = \frac{4}{Re\ Pr} \int_{S_w} \frac{\partial T^*}{\partial \hat{n}^*}\Big|_{S_w} \frac{dS_w}{P_w} \qquad (1.47)$$

Substituting equation 1.47 into 1.46 obtain:

$$\nabla^{*2} T^* = 4f(\vec{r}^*)\, w^* \oint_{S_w} \frac{\partial T^*}{\partial \hat{n}^*}\Big|_{S_w} \frac{dS_w}{P_w} \tag{1.48}$$

Again the energy equation is independent of any dimensionless parameter. From equations 1.22 and 1.34 the momentum equation becomes:

$$\nabla^{*2} w^* \mp \frac{Gr_{\Delta T}}{Re} T^* = 4 \oint_{S_w} \frac{\partial w^*}{\partial \hat{n}^*}\Big|_{S_w} \frac{dS_w}{P_w} \tag{1.49}$$

The temperature B.C.s are:

$$T^*\big|_{S_w} = \frac{T_w - T_o}{\overline{T}_w - T_o} \qquad \text{(Dirichlet)} \tag{1.50}$$

or

$$\frac{\partial T^*}{\partial \hat{n}^*}\Big|_{S_w} = 0 \qquad \text{(Neumann)} \tag{1.51}$$

In summary, the only dimensionless parameter in the constant temperature B.C. case is $Gr_{\Delta T}/Re$. The temperature and the velocity solutions depend also on the duct geometry and the shape function $(T_w-T_o)/(\overline{T}_w-T_o)\big|_{S_w}$.

1.4.4 Friction Factors and Nusselt Numbers

The friction factor is given from:

$$f = \frac{dp_f}{dz} \frac{2}{\rho_o \overline{w}^2} = \left(\frac{dp^*}{dz^*} \mp \frac{1}{Fr}\right) \Big/ \left(\int_{A_c} w^* \frac{dA_c}{A_c}\right)^2 \tag{1.52}$$

or using equation 1.34:

$$f = \frac{K}{Re} \tag{1.53}$$

where $$K = 4 \int_{S_w} \frac{\partial w^*}{\partial \hat{n}^*}\Big|_{S_w} \frac{dS_w}{P_w} \Big/ \left(\int_{A_c} w^* \frac{dA_c}{A_c} \right)^2 \tag{1.54}$$

For isothermal flows the momentum equation term that includes the Gr_q/Re (or $Gr_{\Delta T}/Re$) parameter drops out. In that case the velocity w* and consequently the parameter K are functions of the duct geometry only.

then $$f_o = \frac{K_o}{Re} \tag{1.55}$$

where f_o is the isothermal flow friction factor. From equations 1.53 and 1.55 take:

$$f/f_o = \frac{K}{K_o} \tag{1.56}$$

where K is given from equation 1.54. As discussed in the previous paragraph the velocity field w* depends on the Gr_q/Re (or $Gr_{\Delta T}/Re$) parameter, the duct geometry and the B.C.'s for heat flux (or temperature). Consequently the parameter K and the f/f_o ratio are functions of the same parameters only. Note that in forced convection, $K \equiv K_o$ and therefore $f \equiv f_o$.

The Nusselt number can be written as follows:

$$\frac{1}{Nu} = \frac{k(\bar{T}_w - T_m)}{\bar{q}''_w \, De} \tag{1.57}$$

For the constant heat flux case:

$$\frac{1}{Nu} = 4 \int_{S_w} (\theta_w^* - \theta_m^*) \frac{dS_w}{P_w} \tag{1.58}$$

For the constant temperature case:

$$\frac{1}{Nu} = \frac{1 - T_m^*}{4 \int_{S_w} \frac{\partial T^*}{\partial \hat{\eta}^*} \frac{dS_w}{P_w}} \tag{1.59}$$

where $$T_m^* = \frac{\int_{A_c} w^* T^* \, dA_c^*}{\int_{A_c} w^* \, dA_c^*} \tag{1.60}$$

In summary observe that for fully developed mixed convection flows the parameters f/f_o and Nu depend on the following parameters:

constant heat flux B.C.	constant temperature B.C.
Gr_q/Re	$Gr_{\Delta T}/Re$
Duct Geometry	Duct Geometry
$\dot{q}_w'' / \bar{\dot{q}}_w \mid_{S_w}$	$(T_w - T_o) / (\bar{T}_w - T_o) \mid_{S_w}$

In the case of forced convection fully developed flows the Gr_q/Re (or $Gr_{\Delta T}/Re$) dependency drops out. In the case of developing mixed convection flows or turbulent mixed convection flows, the Reynolds number Re as well as the Prandtl number Pr become of importance too.

CHAPTER 2

THE EXPERIMENTAL APPARATUS

2.1 Introduction

As stated in Chapter 1, the test section should provide two kinds of data namely (a) low Reynolds pressure drop and heat transfer coefficient data and (b) subchannel velocity and termperature field data to be used for calibration/validation studies of thermo-hydraulic numerical programs. The following design goals were set:

(a) Design a versatile/multi-purpose test section which could be used to obtain the above data as well as other kinds of data (swirl flow, onset of flow recirculation).

(b) In particular, for the required subchannel velocity and temperature data, it was decided to perform such measurements at the exit region of the test section. This was made possible by designing a waterproof support system of the heated rods such that the power wire end of these rods was placed at the bottom of the test section. In addition it was also decided that the scale of the experiment should be large enough to allow detailed measurements at the subchannel level.

(c) Finally as a third design goal it was required that maximum use should be made of equipment and facilities available at the Thermohydraulics Laboratory. The following equipment/facilities were used:

- A hexagonal housing, lower plenum and upper plenum. (see Figure 2.1). The flat-to-flat distance of the hexagonal test section is 4.336" and the total length 64".

- Twelve sets of autotransformer variacs, Amper-meters and Volt-meters, capable of driving 2KW of power per variac.

- A water loop providing filtered degassified water at ambient temperature. Maximum volumetric flow rate of the loop is 4.34×10^{-4} m^3/sec.

Based on the above design goals the following decisions were made at a very early stage.

(a) Build a 19-pin wire-wrapped bundle (as opposed to a 37-pin bundle). The rod diameter D was selected equal to 0.745" and since the flat-to-flat distance D_F equals 4.336", the pitch-to-diameter ratio P/D was determined equal to:

$$P/D = 1.248 \text{ (Fuel Bundle Geometry)} \tag{2.1}$$

The result given in (2.1) is based on the following easily derived formula:

$$D_F = 2\sqrt{3}\,P + D + 2D_W \tag{2.2}$$

where D_W is the diameter of the wire-spacer. Here D_W was taken equal to P-D. Since the diameter of the actual fuel rod is 0.23", the scale of our test section is of order of 3.2:1.

Based on this geometry and the maximum flow rating of our loop, the Reynolds number Re could reach as high as 1000 depending on inlet tem-

perature conditions.

(b) It was decided to keep the maximum rod power level at 2KW per rod. This would allow us to fully use the previous power supply system. Seven additional sets of variacs, A-meters and Volt-meters were also purchased. Based on this maximum power rating, it was calculated that Gr_q/Re numbers could reach 2.0×10^4 for Re around 700 to 800. As discussed in chapter 3, these numbers for the Gr_q/Re parameter lie well within the mixed convection regime.

Figure 2.1 is a schematic description of the test section including the lower plenum, the hex housing and the upper plenum. The test section is situated on two I-beams to allow the power wires of the heated rods to enter the bottom of the lower plenum. Figure 2.2 is a cross-section of the hex housing with the wire-spacer illustrated at a random position (angle).

Next the design, construction and assembly procedures of the various components of the test section and the loop are presented.

A brief discussion is also presented on the 16-pin square array bare rod bundle that it is also used for mixed convection pressure drop measurements (see Chapter 3).

2.2 Component Design and Construction

2.2.1 The Hexagonal Housing

The housing consists of a cold-formed hexagonal tube with welded flanges at each end. The overall length is 64" (162.56 cm) and the inner flat-to-flat distance is 4.335" ± 0.002" (11.013 ± 0.005 cm). The housing was available from a previous 37-pin experiment. An observation window is

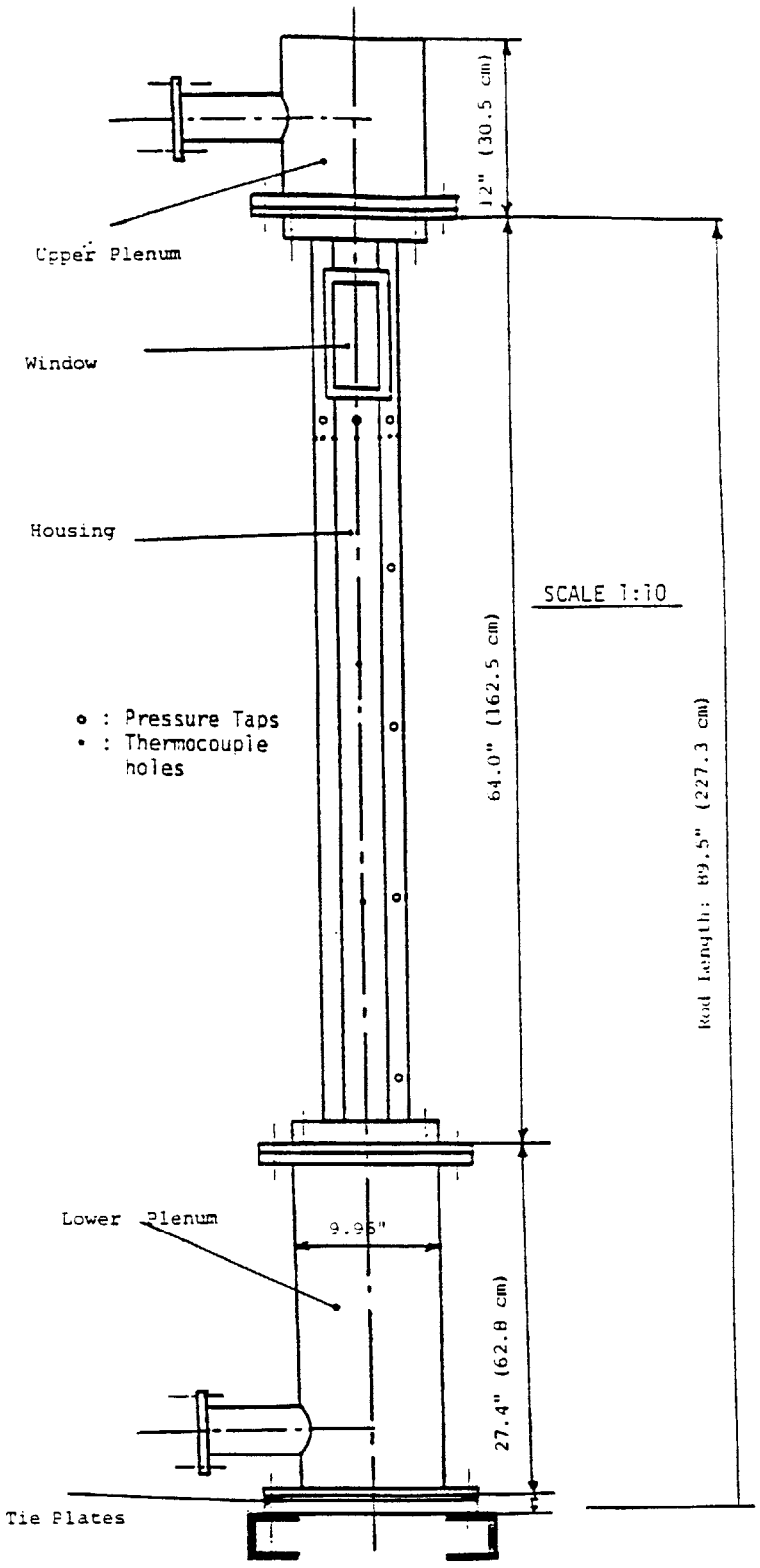

FIGURE 2.1: A SCHEMATIC REPRESENTATION OF THE TEST SECTION.

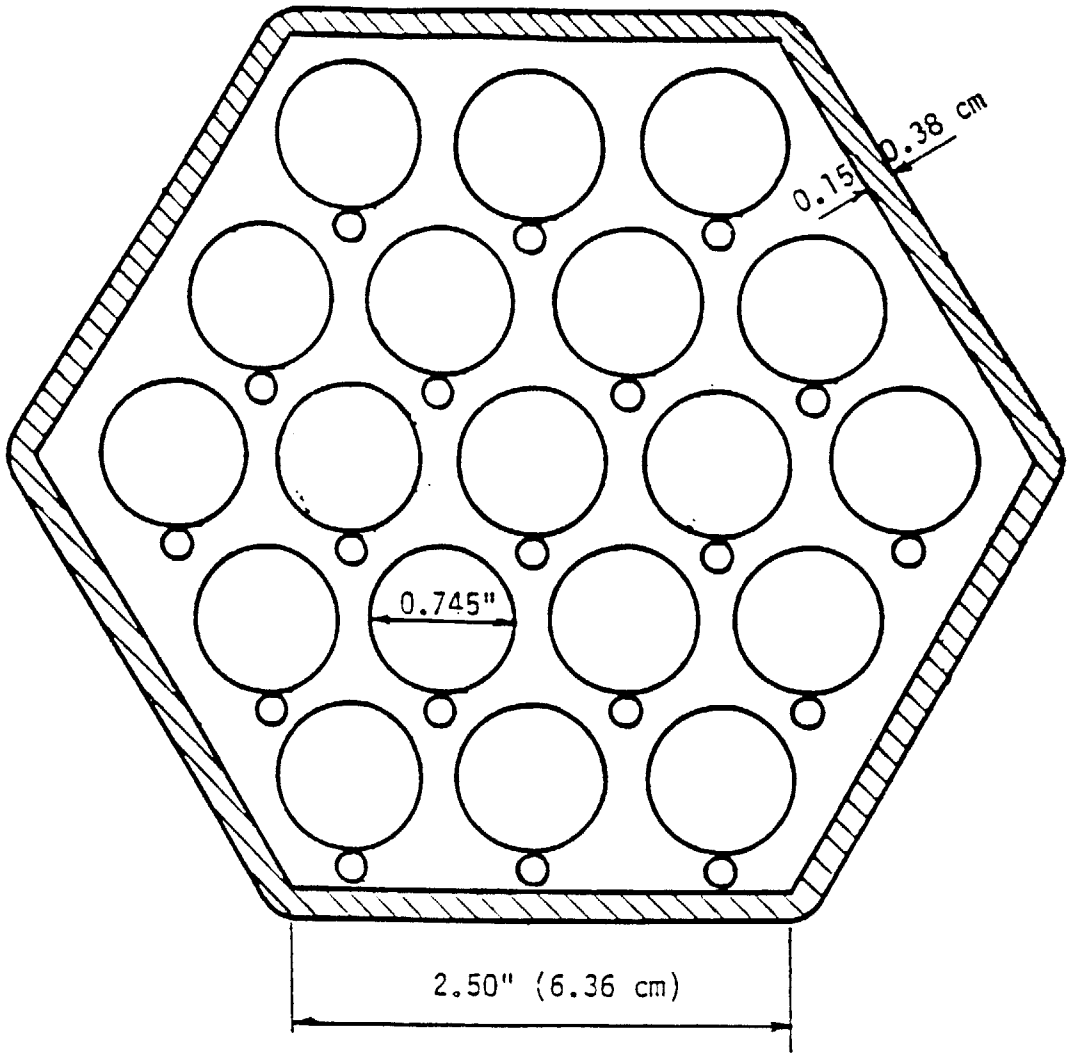

FIGURE 2.2 TEST SECTION CROSS-SECTION.

installed in the housing to be used for flow visualization. The location of this window is shown in Figure 2.1. It may be used for two purposes:

- Swirl flow velocity measurements using the hydrogen bubble technique (HBT)
- Onset of flow recirculation measurements using dye techniques

A window schematic, including the location of the HBT wire, is given in Figure 2.8. Note that due to the limited thickness of the housing walls, and for better observability, an extra stainless steel plate was welded on the test section. A plexiglass piece is made to exactly fit the window opening. A rubber O-ring is used for water sealing. In the present work the above capabilities for swirl flow velocity measurements and onset of flow recirculation measurements are not explored.

2.2.2 The Heater Rods

Nineteen heated rods were ordered from Ramarod, Inc. The technical specifications for these rods are:

Nominal Diameter: 3/4" (1.905 cm)

Actual Diameter D_r: 0.745" ± 0.003"

Total Length L_R: 89.5" (227.33 cm) ± 2.5%

Heated Length L_H: 64" (162.5 cm) starting from the top end

Material: stainless steel type 304

Figure 2.3 is a vendor's schematic of a typical rod. Note that MgO has been used for filling the rod. This material has very low thermal conductivity, as is the case with the actual fuel oxide in a LMFBR rod. Note also that the power wires <u>are not</u> immersible in water, and con-

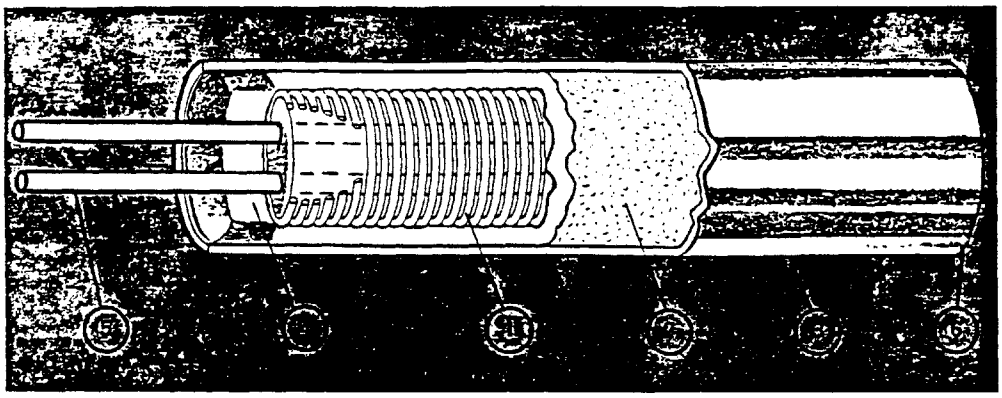

1 The highest quality resistance wire, is evenly coiled and uniformly centered in close proximity to the heater sheath.

2 Magnesium Oxide, compacted to a very high density by proper filling and swaging, forms the heat conducting electrical insulation between the resistance wire and the sheath. The ability of high density MgO to act as a heat conductor and an electrical insulator at high temperatures allows the resistance wire to be in close proximity to the heater sheath. Because of the low temperature drop from resistance wire to sheath, the sheath can be allowed to run hotter without overheating the resistance wire.

3 Incoloy sheath material provides high temperature corrosion resistance and a high emissivity factor. Other materials are available upon request.

4 A moisture and contaminant resistant lava seal is provided as standard. Other seal materials are available.

5 Solid nickel terminal pins are attached to the resistance wire by our patented high temperature connection which makes the RAMAROD superior to other so called high temperature cartridge heaters.

6 All RAMARODS are sealed at the end with a welded metal disc allowing immersion in liquids when required.

FIGURE 2.3: THE HEATER ROD (Taken from RAMAROD CORPORATION)

sequently the lower end of the rods has to be rigorously sealed. In addition, due to high hydroscopic properties of the MgO, the rods cannot be pierced through for support purposes. Instead, external support has to be provided as shown later.

All rods were tested for possible heat flux profile deviations along the axial or the circumferential direction. For that purpose, surface temperatures of the heated rod walls were measured while the rods were cooled by natural circulation of the ambient air. Thermocouple wires were used for this measurement. Figure 2.4 gives some typical temperature profile results along the axial direction of a given rod. As Figure 2.4 indicates, the heat flux profile can be considered as uniform except for 1-2 cm at the vicinity of both ends of the heated zone.

Finally it should be mentioned that due to manufacturing problems the tolerances of the total length of the heater rods could not be accurately controlled and consequently the total length exhibited a ± 2.5% deviation from the nominal dimension.

2.2.3 The Wire-Spacer and the Wrapping Procedure

A wire-wrap type of spacer is used for all 19 rods. A schematic representation of a heater rod with a wire-wrapped spacer is given in Figure 2.5. The wire diameter D_W was selected equal to 0.183" (0.465 cm). Based on Equation 2.2 the flat-to-flat distance D_F' needed for this D_W is calculated equal to 4.3346". Therefore the clearance is estimated as follows:

$$\text{Clearance} = D_F^{\text{NOMINAL}} - D_F' = 0.00140"$$

This clearance was established to assure smooth fit of the housing over

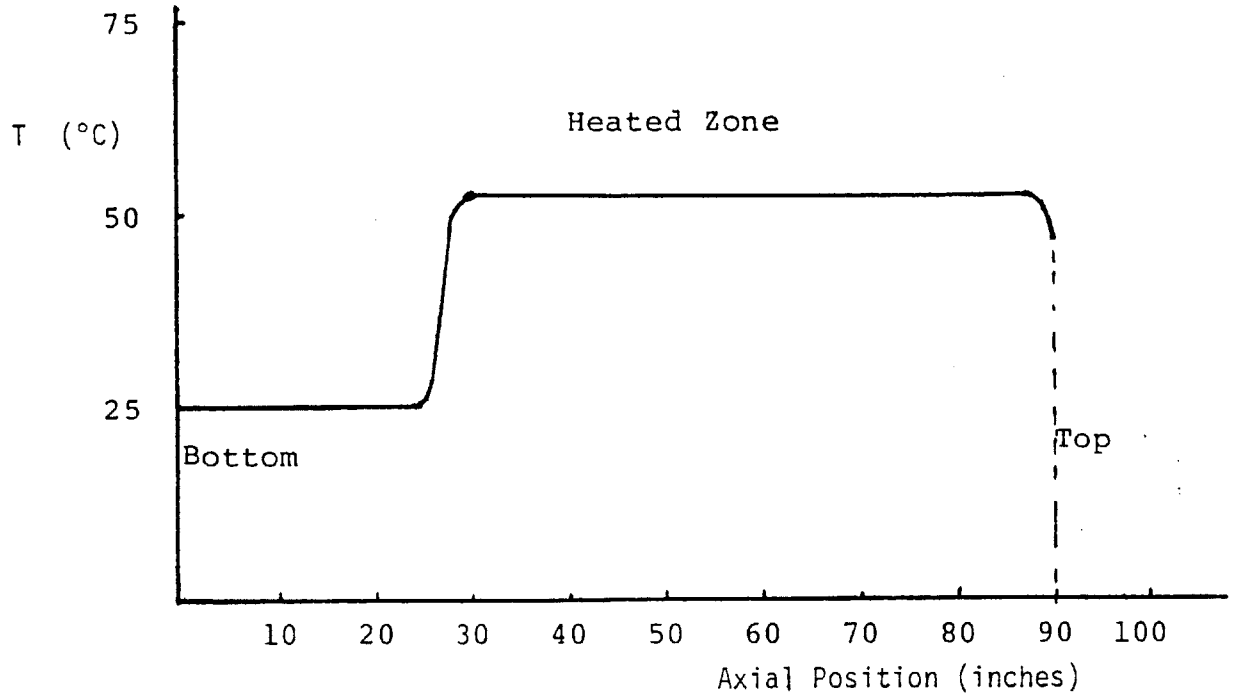

FIGURE 2.4: TYPICAL TEMPERATURE PROFILE FOR A HEATED ROD AS MEASURED BY THERMOCOUPLES ATTACHED ON THE ROD'S SURFACE.

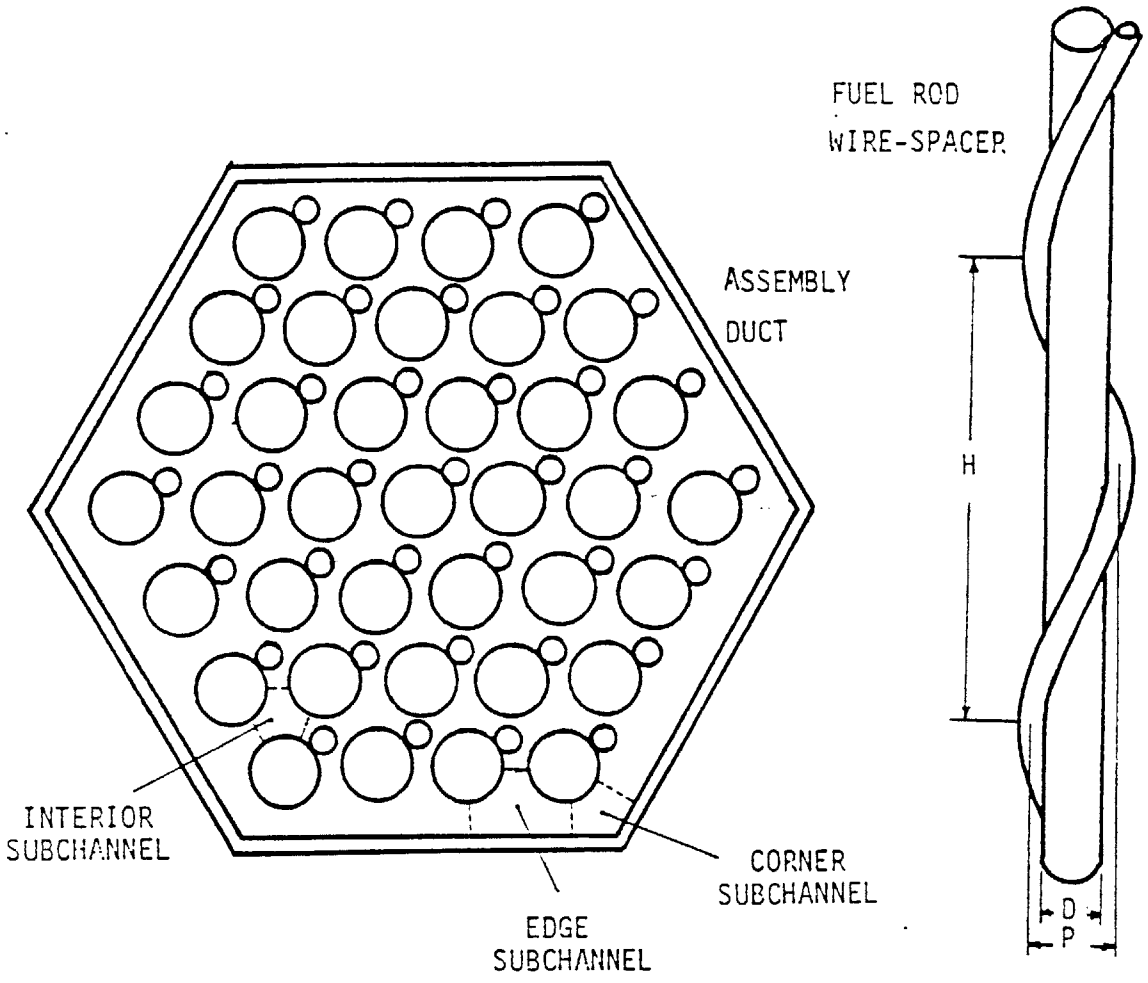

FIGURE 2.5: TYPICAL WIRE-WRAPPED BUNDLE.

the wire-wrapped rod bundle.

The wire-spacer lead length H was selected to be equal to 35.2 D. This choice was made on the basis of rough estimates for the hydrodynamic entry length (see W-6). It was required that entrance effects should die out in the first half on the bundle. It was also required that the total housing length L_H should be equal or larger than two lead lengths. For H/D = 35.2 the L_H/H ratio was equal to 2.44.

All of the stainless-steel wires were silver-soldered on the heater rods at the two end positions (top and bottom). The welding at the top position is performed first, the wrapping of the wire-spacer follows and the welding at the bottom position completes the wrapping procedure. One major problem that arises here is the accurate alignment of the wire-spacer with respect to the rod at the top position before performing the first silver-soldering. This problem was solved with the use of the aligner design of Figure 2.7 The cylindrical piece (aligner) has a wall thickness less than the spacer-wire diameter. A cylindrical slot has been made on its surface at an angle φ equal to 6.4°. Note that

$$\tan \varphi = \frac{\pi \ P/D}{H/D}$$

At the beginning of the wrapping procedure the wire spacer is placed within the slot and it is mechanically attached on the rod surface with the use of a clamp. Subsequently the spacer is wrapped for an approximately $\frac{H}{12}$ axial distance before the top sliver-soldering is performed.

Due to the fact that (a) the heater rods have different lengths, (b) all wire-spacers start from the top of the heated rods and (c) all heater rods are supported by the tie plates with their bottom ends lieing at the

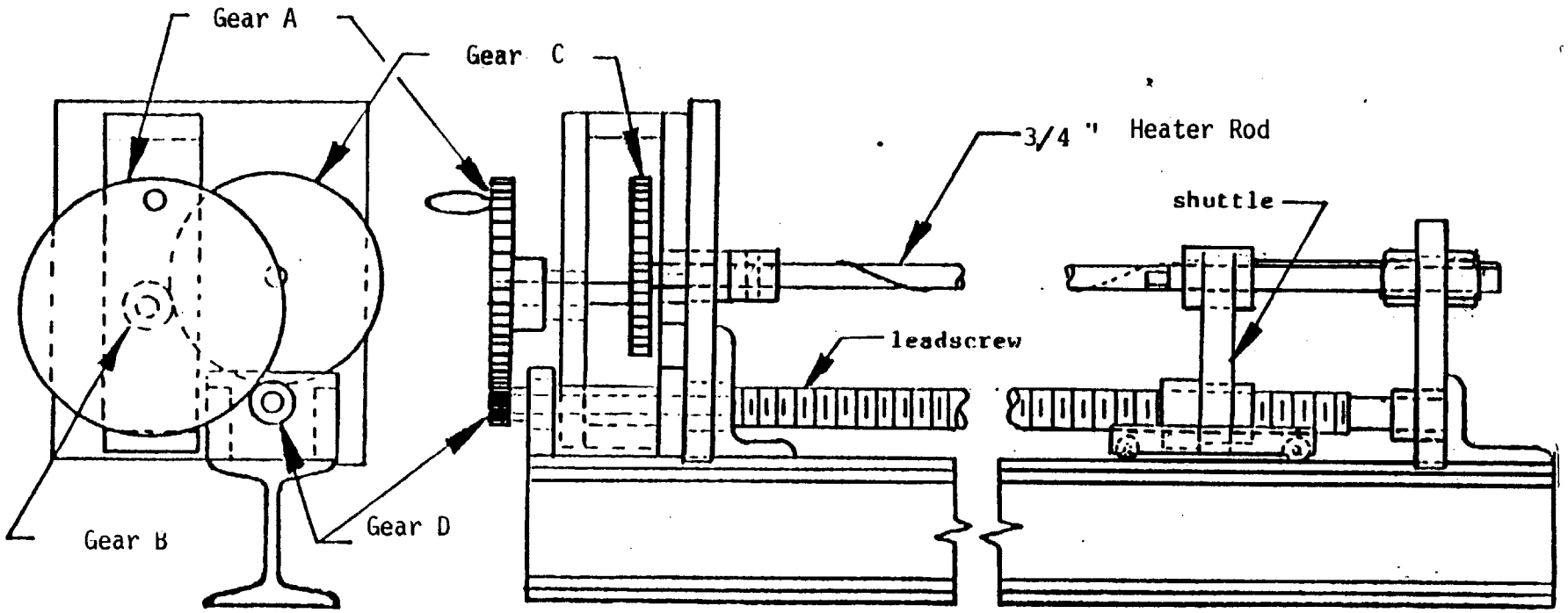

FIGURE 2.6: SCHEMATIC REPRESENTATION OF THE WRAPPING APPARATUS.
(Taken from reference B-7)

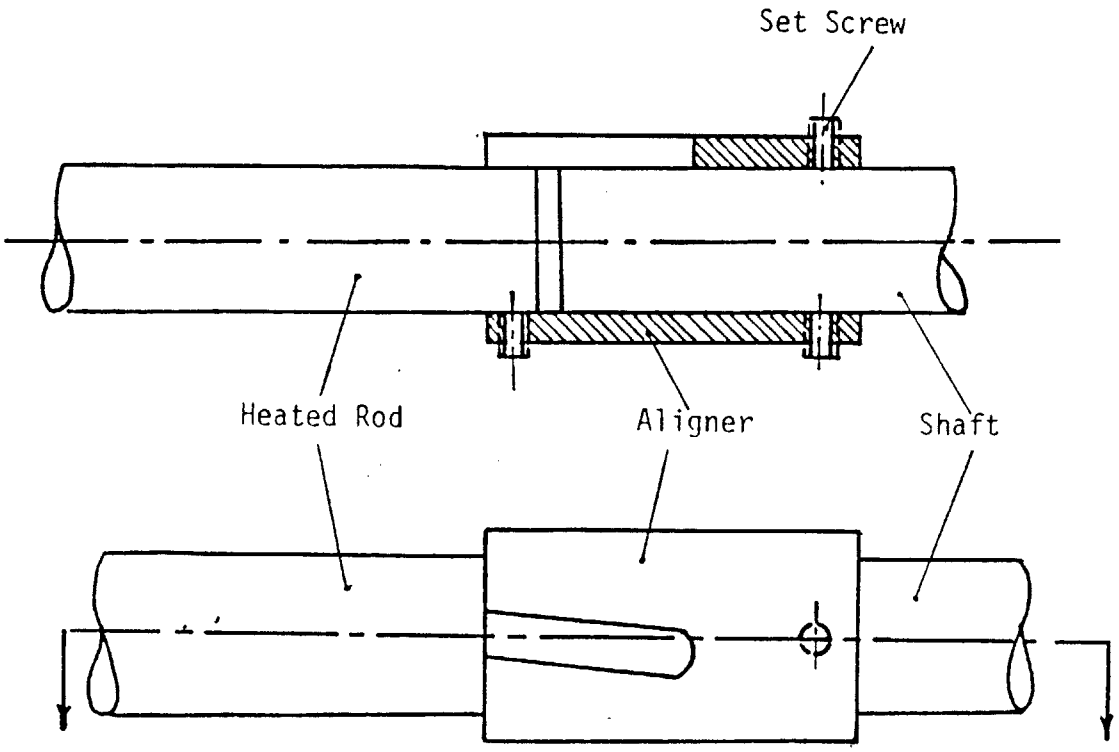

FIGURE 2.7: HEATER ROD AND ALIGNER SET-UP.

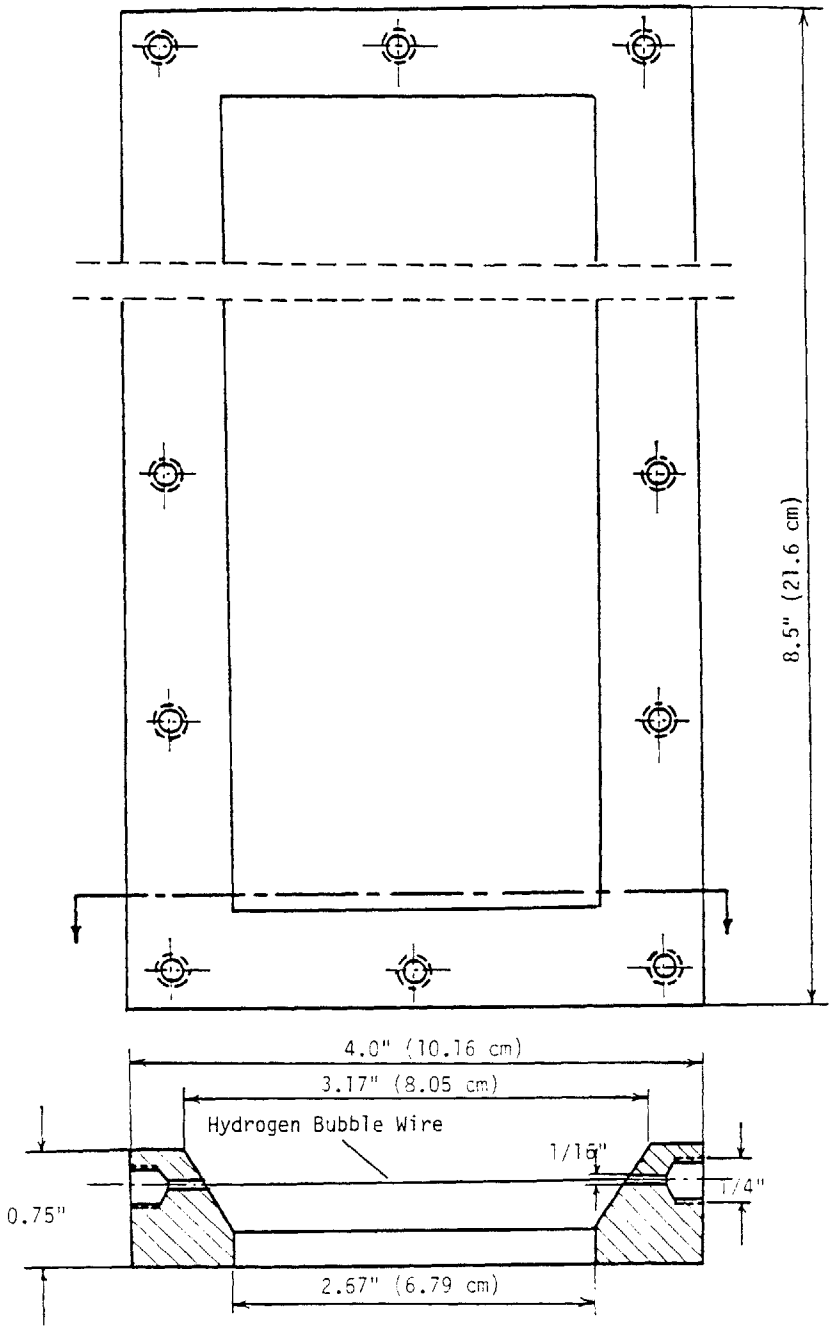

FIGURE 2.8: SCHEMATIC REPRESENTATION OF THE OBSERVATION WINDOW.

same horizontal plane, then the top end of the heater rods and the wire-spacers could not be lying at the same plane. In order to facilitate the velocity and temperature measurements at the exit (top) region of the bundle, the top end of the wire-spacer wrapped on a longer rod was cut so that the new top end would lie at the same horizontal plane with the top end of the wire-spacer wrapped on the shortest heater rod.

2.2.4 The Lower Plenum and the Tie Plates

The lower plenum is shown schematically in Figure 2.1. It is made of aluminum and its total height is 27.4" (62.8 cm). The top flange of the lower plenum is connected with the bottom flange of the housing. Sealing is achieved through the use of an 11.5" diameter rubber O-ring.

The lower plenum was cleaned and electrochemical plated to avoid corrosion of the copper material, in particular at the copper-stainless steel interface where the electrochemical potential is high.

At the lower flange of the lower plenum the design considerations are much more complex and are shown schematically in Figure 2.9. We distinguish the two tie plates, namely the sealing plate and the support plate which is thicker. The sealing plate seals the 19 piercing rods with the use of 19 0.738" inner diameter rubber O-rings. The purpose of the support plate is two-fold: (a) to keep the 19 O-rings of the sealing plate in place, and (b) to support the weight of these rods and transfer this load to the I-beams, as shown in Figure 2.1. Note that the weight of the upper plenum, test section and lower plenum is passed to the I-beams through the bottom flange of the lower plenum. Note also that the 19 O-rings of the sealing plate are used to inhibit any rotational motion of the rods around their axis.

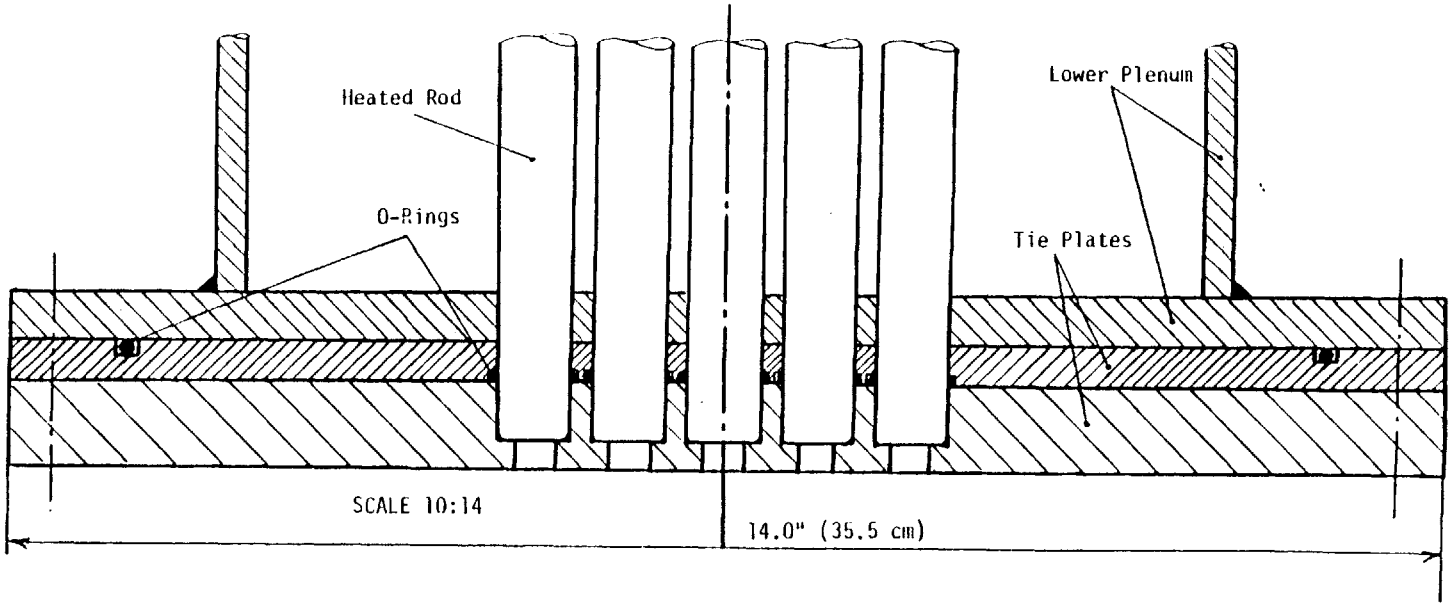

FIGURE 2.9: THE LOWER PLENUM AND THE TIE PLATES.

2.2.5 The Upper Plenum

The upper plenum is shown schematically in Figure 2.1. It is also aluminum and it is connected to the test section through its lower flange. Note that its upper part is open to the atmosphere, so that it provides a constant pressure boundary condition at the outlet of the rod bundle. In addition this open upper plenum design allows easy access to the exit region of the rod bundle in order to perform subchannel velocity and temperature measurements (see chapter 5).

2.2.6 Test Section Assembly Procedure

In order to assemble this rather complex test section (tie plates, lower plenum, housing, upper plenum, heater rods) the following steps are performed:

(a) Tie plates preparation

The tie-plates are thoroughly cleaned using some methanol solution. The 19 O-rings are covered with vacuum grease and are put in place.

(b) Tie plates-lower plenum attachment

The tie-plates are attached at the bottom flange of the lower plenum. The tie bolts are then slightly tied. At this point the lower plenum rests at a horizontal position.

(c) Heater Rod Insertion

Subsequently the heater rods are inserted in the tie plates from the top of the lower plenum, one-at-a-time. To facilitate insertion the rods are lubricated with a low viscosity lubricant. At this stage care must be taken so that all wire spacers are completely aligned with each other. After the insertion and the alignment is completed, the tie plate bolts are thoroughly tied.

(d) Housing Slip-over

At this point, the upper plenum and the heater rods remain in a horizontal position. The rods are supported in a hexagonal shape with the use support plates and wires. The housing is located in a horizontal position at the same level with the rods with the help of a portable crane. Consequently it is slipped over the rods in small discrete steps. Each pushing step is performed with the minimum possible pushing force, after realignment of the housing and the rods is established. After the housing has reached the lower plenum, the bolts are put on and thoroughly tied.

(e) This tie plates-lower plenum-rods-housing assembly is carried with the use of a portable crane over I-beams. Here the test section is tilted to a vertical position and it is placed, aligned and bolted on the I-beams.

(f) Finally the upper plenum is bolted on the top of the housing. The test section is subsequently connected to the loop and a leak test is performed. Particular attention is directed to the tie-plates where any leak could force the repetition of the whole assembly procedure. When all leaks are sealed, the test section (including upper and lower plena) is thoroughly insulated using successive layers of fiberglass material up to a 4 cm total thickness.

2.3 Loop, Instrumentation and Operations

2.3.1 The Loop

The objective of the loop is to provide purified, degassed water at a desired constant inlet temperature and flow rate at the intake of the lower plenum. A schematic description of the loop used in the work is

given in Figure 2.10. Most of the components of this loop were already build in conjunction with the 4 x 4 square array bare rod bundle (see W-7 for details). In this work the following improvements were made:

(a) A heat exchanger (S-303 HY Single Pass Model, Peeco Corp.) was added at the intake part of the loop in order to control the inlet temperature in the lower plenum at a desired and constant temperature level.

(b) A loop was added for gravity feed of water from the upper plenum back to the water supply tank.

As Figure 2.10 indicates the intake part of the loop consists of the supply tank, pumps, heat exchanger, filter, and flow meters FM1 and FM2. The heat exchanger was placed after the pumps in order to increase the absolute pressure in the suction region of the loop (region before the pumps) and thus minimize air sucking or cavitation problems. However, in this arrangement the pumps operate in higher temperature particularly when the loop is used for cooling purposes as explained below.

The loop is used for two purposes:

(a) To degasify the water in the supply tank. This is accomplished by first heating the supply tank water to the boiling temperature and boiling for five to ten minutes. Then use the heat exchanger and the by-pass line to cool this water down to ambient temperatures (20 to 25°C). It is through this later operation that the pumps experience temperatures higher than 80°C for approximately 1/2 hour.

(b) To provide steady, constant temperature water flow at the lower plenum inlet nozzle.

2.3.2 The Flow Meters

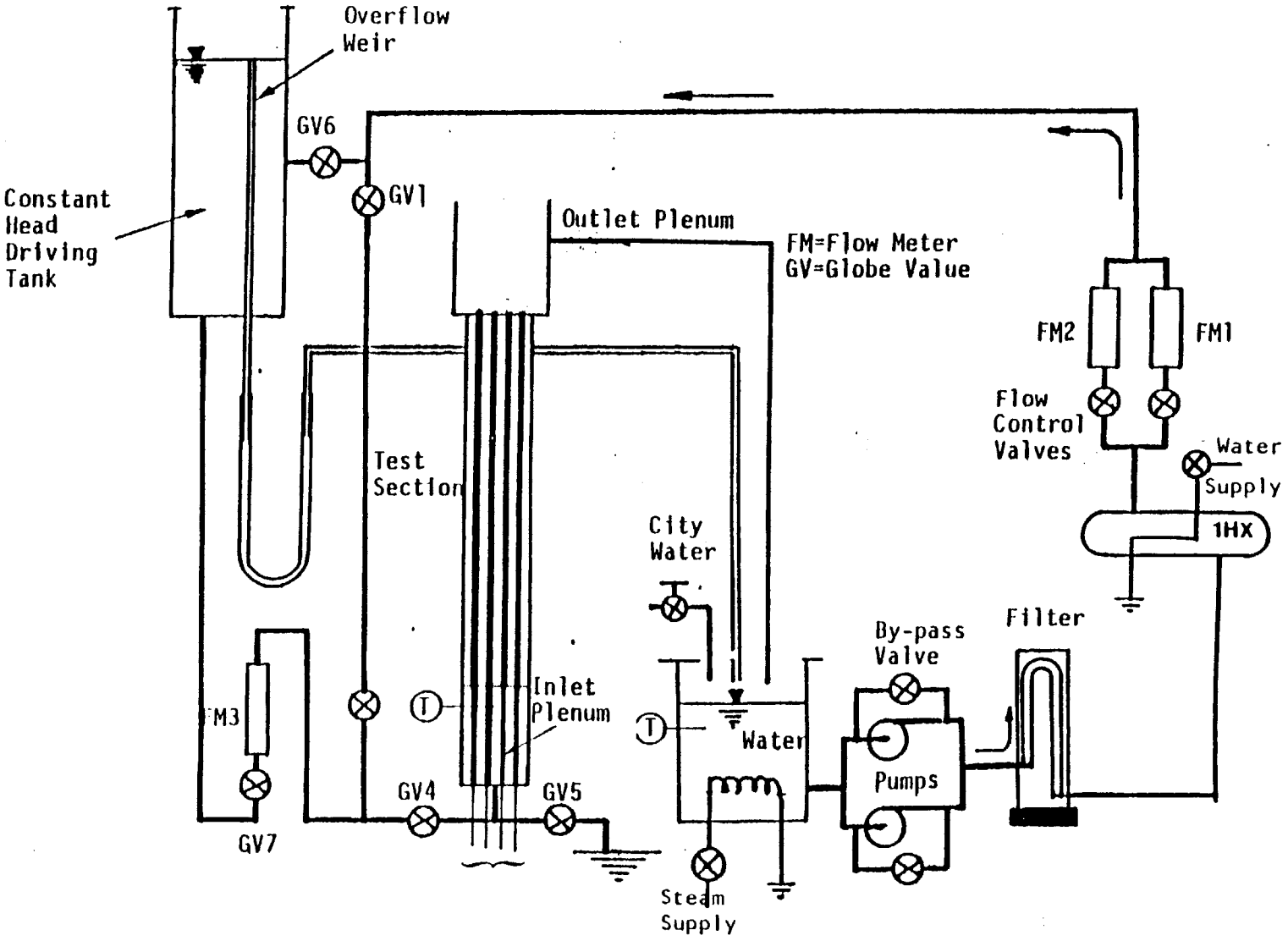

FIGURE 2.10: THE TEST SECTION AND THE LOOP.

Two rotameter flow meters FM1 and FM2 are used to measure the volumetric flow rate in the test section. These flow meters were calibrated individually using the classical bucket/stop watch method. In both cases the error of this calibration procedure for the maximum flow rate was less than 1.5%. Both flow meters exhibited linear behavior with the flow rate. The maximum flow rates measured by these flow meters were as follows:

$$\text{FM1: } Q_{max} = 1.24 \times 10^{-4}\ m^3/sec \pm 0.75\%$$

$$\text{FM2: } Q_{max} = 3.10 \times 10^{-4} m^3/sec \pm 0.75\%$$

This calibration procedure was repeated for two different temperature levels, namely 22°C and 33°C. It was found that the calibration curves were practically the same for the two temperature levels.

2.3.3 The Power Supply

Each heater rod was heated electrically using a dual-coil variac autotransformer made by Techni-power. Each rod was placed in a series circuit on the secondary side of the variac as shown in Figure 2.11. Power was drawn from the 208 volt A.C. source through the primary side. When the variac was turned to position B, a maximum of approximately 200 volts and 10 amperes were obtained at the secondary side.

On line with each variac, a volt-meter and a A.C. ammeter were placed to monitor the total power and current per heater rod. Each pair of these meters was calibrated with a pre-calibrated digital multimeter (Model 262, United Systems Corp.).

During operations the power in each rod was set individually through the corresponding variac and estimated through the Volt-meter and A-meter

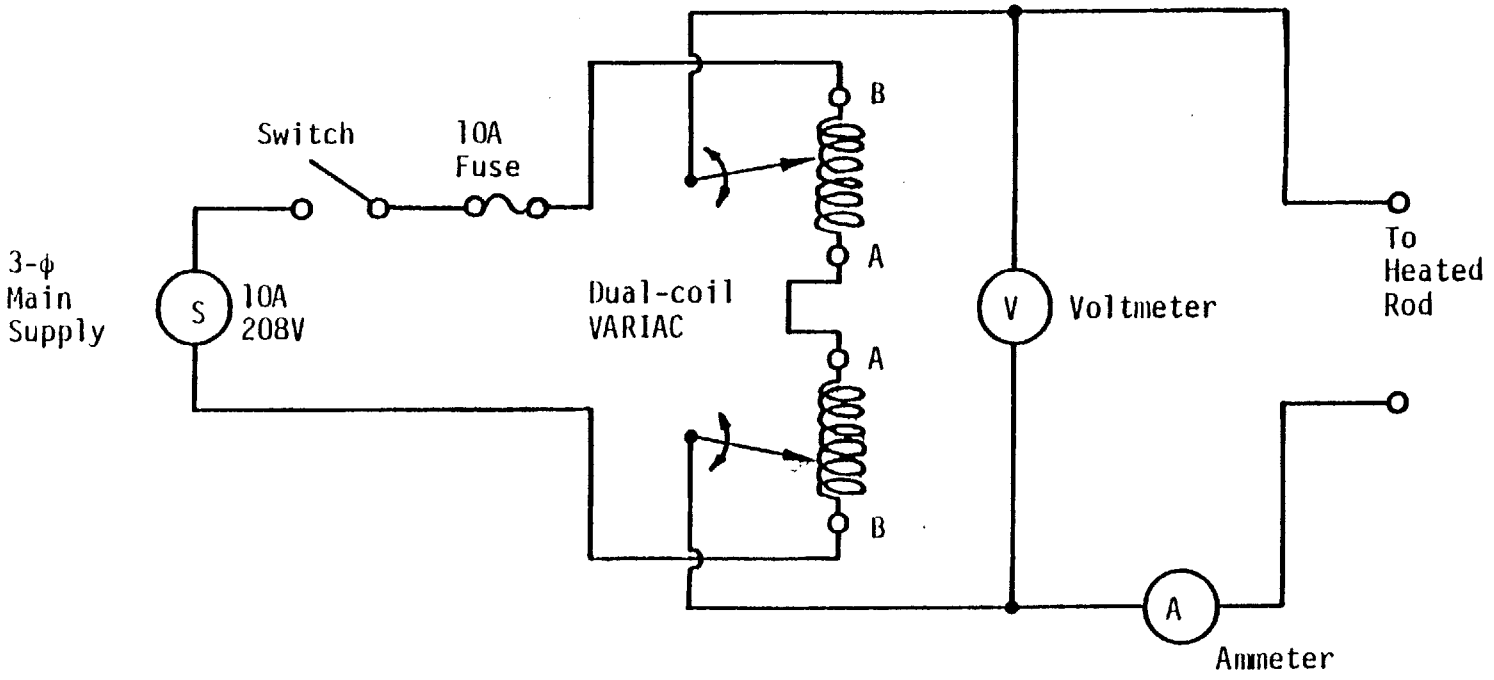

FIGURE 2.11: POWER SUPPLY CIRCUIT.

readings. Due to limited resolution of the read-out panel for both meters the power level was estimated within ± 2.0% error.

2.3.4 Temperature Measurements and Heat Losses

The inlet and outlet temperatures T_{in} and T_{out} of the test section flows were constantly monitored with high resolution mercury thermometers of accuracy ± 0.1°C. The ambient temperature T_a was also monitored with mercury thermometers at three different axial levels:

$$\bar{T}_a = (T_{a,in} + T_{a,m} + T_{a,out})/3$$

where subscripts in, m and out stand for inlet nozzle, middle and outlet nozzle level respectively.

The above temperatures are used to estimate the heat losses in mixed convection for the particular case of the insulation used in our test section. It consists of two layers of fiberglass insulation with total thickness approximately equal to 4.5 cm. In order to experimentally determine the heat losses, several runs were made with zero heater power. The heat losses $\dot{Q}_{loss}$ were estimated as follows:

$$\dot{Q}_{loss} = - \overline{\rho C_p}\, \dot{V}\, (T_{out} - T_{in}) \qquad (2.1)$$

where $\dot{V}$ is the volumetric flow rate given by the flow meter, and $\overline{\rho C_p}$ is estimated at $\bar{T}_f$ where

$$\bar{T}_f = (T_{in} + T_{out})/2 \qquad (2.2)$$

In some runs $\bar{T}_a$ was larger than $\bar{T}_f$ and therefore the coolant in the test section gained heat from the environment.

In all cases the heat exchange between the flow and the environment can be also approximated as follows:

$$\dot{Q}_{loss} \simeq h_{tot} \cdot A_{hex} (\bar{T}_f - \bar{T}_a) \tag{2.3}$$

where $$\frac{1}{h_{tot}} \sim \frac{1}{h_f} + \frac{\delta_w}{K_w} + \frac{\delta_{insul.}}{K_{insul.}} \sim \frac{\delta_{insul.}}{K_{insul.}} \tag{2.4}$$

since $$\frac{\delta_{insul.}}{K_{insul.}} \gg \frac{\delta_w}{K_w} \text{ and } \frac{1}{h_f} .$$

Therefore h_{tot} can be considered as constant. Consequently equation (2.3) suggests that $\dot{Q}_{loss}$ should be plotted against $(\bar{T}_f-\bar{T}_a)$. Figure 2.12 gives the $\dot{Q}_{loss}$ estimated from (2.1) versus $(\bar{T}_f-\bar{T}_a)$ for several zero power runs. It is observed that a linear relationship between these two parameters is established. Figure 2.12 can be used to estimate the heat losses in any mixed convection run. In a typical case of well established mixed convection flow, $\bar{T}_a \sim 25°C$, $\bar{T}_f \sim 55°$ and power per rod ~ 1600W. From Figure 2.12 we estimate that $\dot{Q}_{loss} \sim 900W$ or in terms of percentage.

$$\frac{\dot{Q}_{loss}}{\dot{Q}_{TOT}} \sim \frac{900}{19 \times 1600} \simeq 3.0\%$$

Figure 2.12 results were used to give an "a priori" estimate of the heat losses for given environmental conditions and Reynold's number. It was found that for Re < 200 the heat losses became significant. In any mixed convection run the heat losses could be estimated as follows:

$$\dot{Q}_{loss} = \dot{Q}_{Nominal} - \dot{Q}_{Real} \tag{2.5}$$

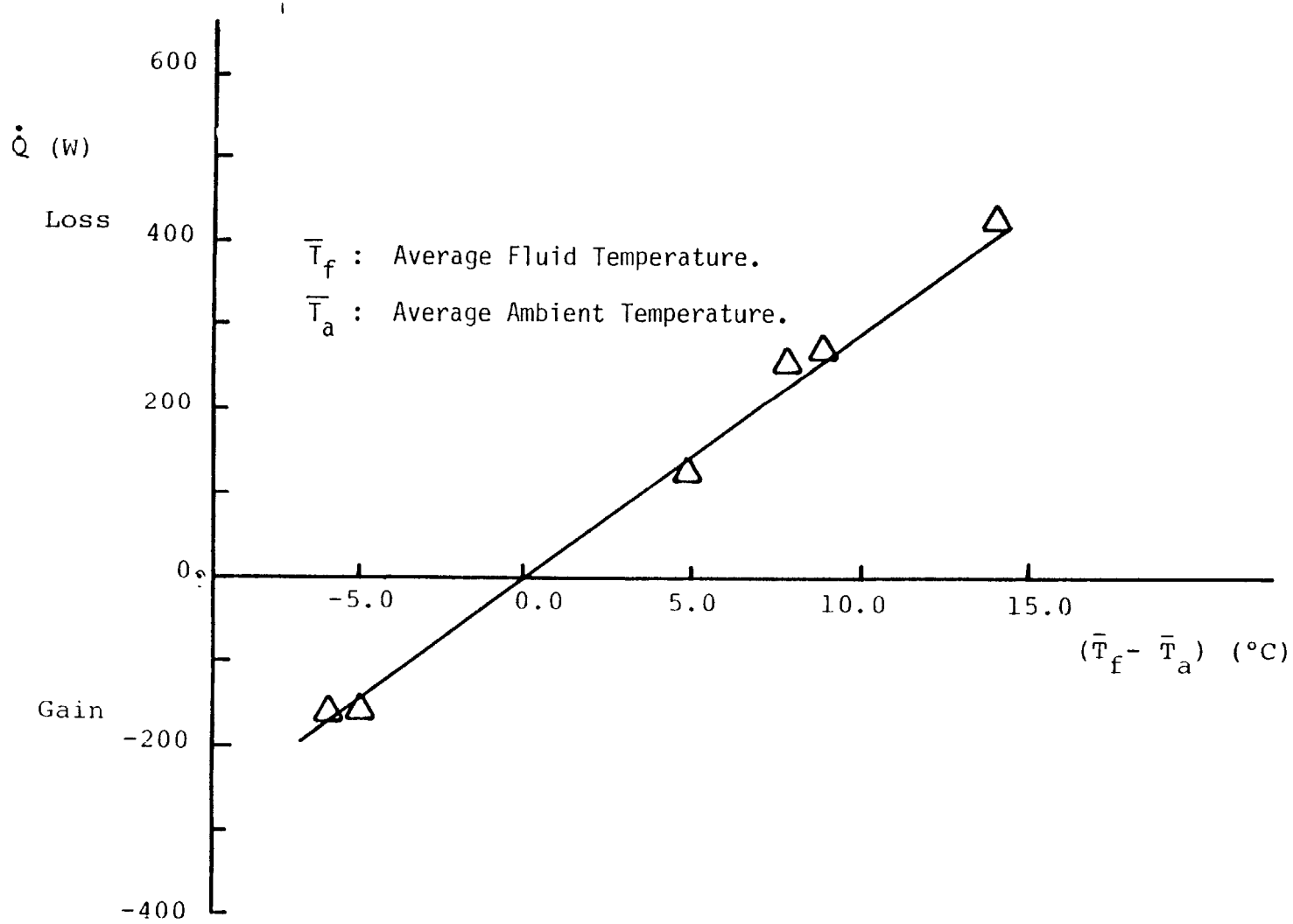

FIGURE 2.12: BUNDLE HEAT LOSS (OR GAIN)

where:

$$\dot{Q}_{Real} = \overline{\rho Cp}\ \dot{V}\ (T_{out} - T_{in}) \qquad (2.6)$$

and $\dot{Q}_{Nominal}$ is the nominal power supplied to the rods, determined by the power meters. It was also found that in mixed convection flows the ratio $(\dot{Q}_{Nominal} - \dot{Q}_{Real})/\ \dot{Q}_{Nominal}$ was always less than 6.0% for Re > 250. In any case for Nusselt and Grashof number calculations, the heat flux was always estimated using $\dot{Q}_{real}$ rather than $\dot{Q}_{Nominal}$.

2.3.5 Experimental apparatus operation.

In a typical mixed convection run, the following steps are followed:

(a) Degassify the supply tank water. This is a time consuming operation and it includes two steps.

- Water Boiling
- Water Cooling

The cooling process can be accomplished either by letting the boiled water cool overnight, or by using the heat exchanger and the by-pass line. This latter process is faster (~ 2 hrs) but it usually causes some water gasification due to cavitation phenemena.

(b) Start the loop and establish the desired flow rate level. Initiate the flow at the cooling side of the heat exchanger also. Constantly monitor the test section inlet temperature and wait until it reaches steady state. Depending on the initial conditions this may take ten minutes to half hour. When steady state is reached perform any zero power measurements, if needed.

(c) If only zero power data are needed, make sure that T_{in} and T_{out} remain constant during the course of the measurement session. In case a new flow rate is established, repeat step (b) above.

(d) For a mixed convection run, prepare the power supply. Turn on all switches. Make sure that all safety fuses are intact before dialing the power in each variac. Also post HIGH VOLTAGE warning signs to avoid any accident.

(e) Set power of each variac at the desired level. This procedure is performed in two steps. First, do a gross adjustment of the power level in all variacs and second, follow up with fine adjustment. Depending on the complexity of the power level pattern, this process may take from five to fifteen minutes.

(f) Keep track of inlet and outlet temperature transients. T_{out} is used to determine when the transient is over and a new steady state condition has been established. Then perform all required measurements.

2.4 The 16-pin Square Array Rod Bundle.

A 4x4 pin square array rod bundle was also employed in this work for pressure drop measurements in mixed convection. This bundle was built by Wang (W-7) and it consists of 16 bare rods of 0.496" diameter supported by home-made grid spacers. A side view of this test section is given in Figure 2.13. The locations of instrumentation taps which can be used for velocity, temperature and pressure measurements (V,T,P,) are shown. Three plexiglass windows (not shown) are located at the level of the instrumentation taps to allow flow visualization. A cross-section of the test section is given in Figure 2.14. Note that at one side of the test section a cooling channel has been installed to allow external cooling of the corresponding side of the test section. The pitch-to-diameter for this bare rod bundle is again 1.248 (same with the wire wrapped bundle).

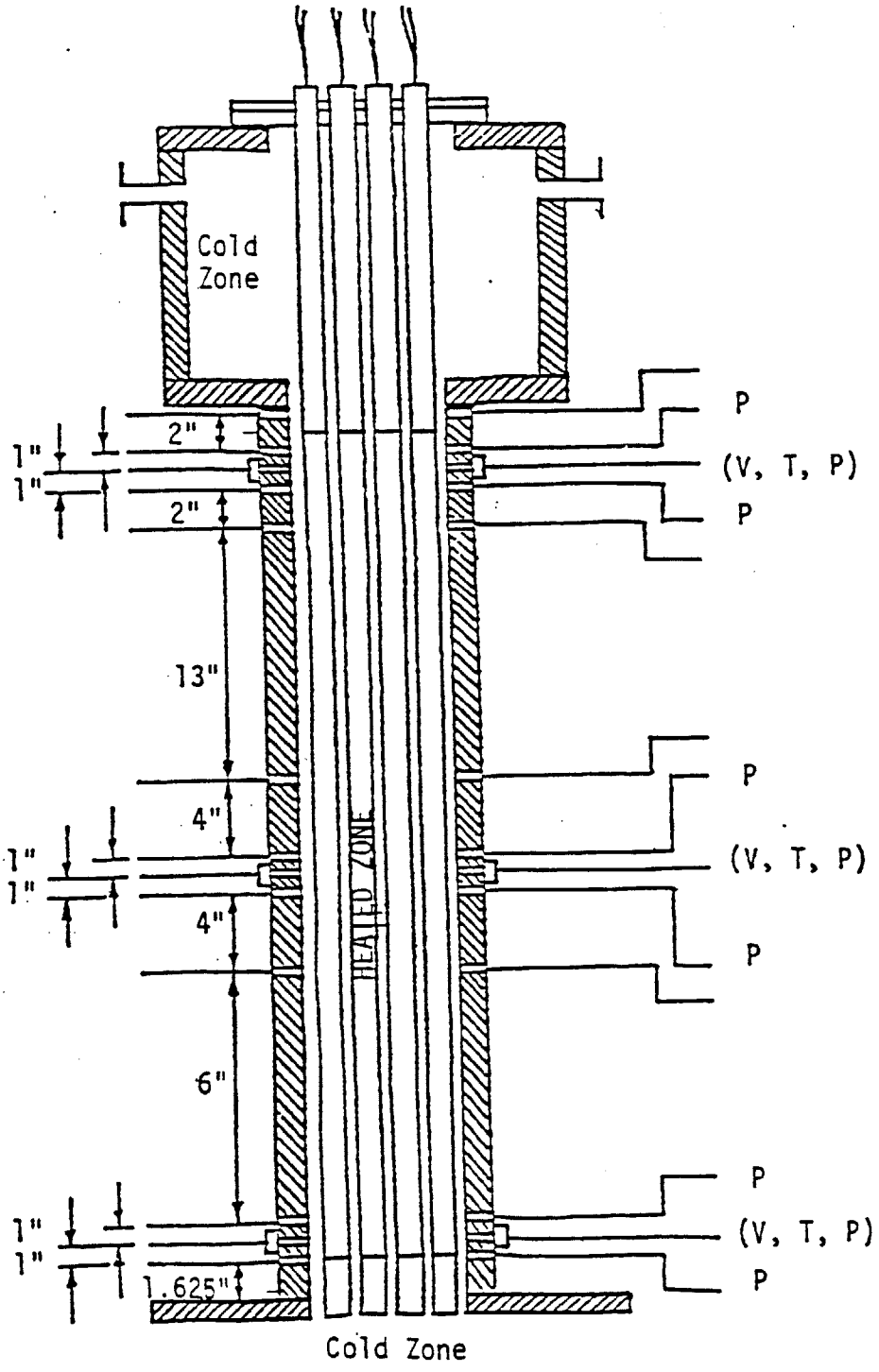

FIGURE 2.13: SIDE VIEW OF THE MIT 4x4 BARE ROD BUNDLE.
(Taken from reference W-7)

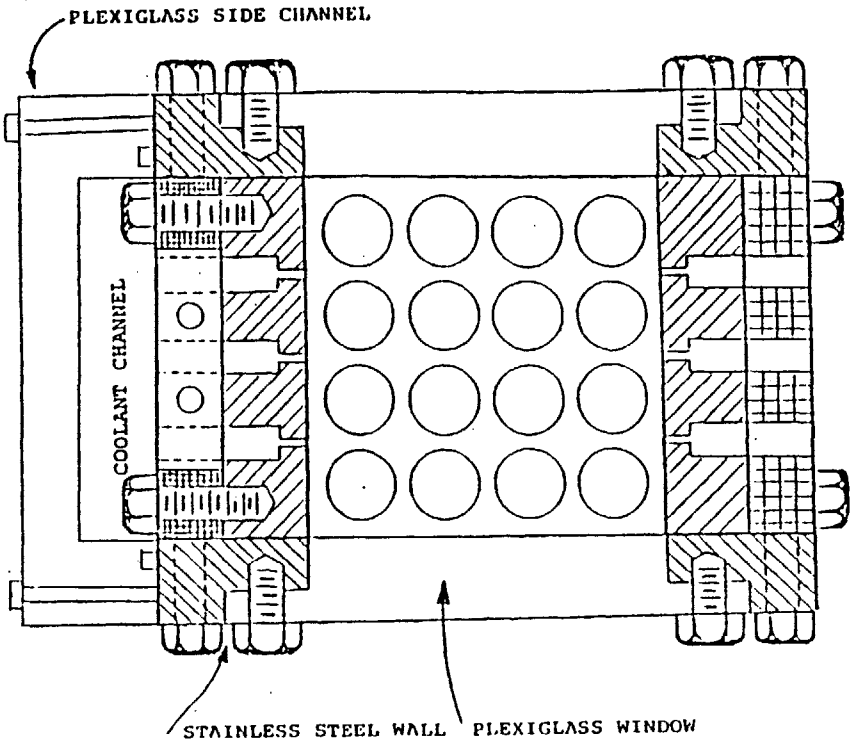

FIGURE 2.14: CROSS-SECTION OF THE MIT 4x4 BARE ROD BUNDLE.
(Taken from reference W-7)

CHAPTER 3

MIXED CONVECTION PRESSURE DROP IN VERTICAL ROD BUNDLES

3.1. Introduction

The knowledge of the pressure drop characteristics of flows in energy components (nuclear reactors, heat exchangers, solar loops) is vital to the design of the particular energy system. In most cases the pressure drop characteristics are deduced from experimental and/or analytical work under isothermal flow conditions. Here the claim is made that the forced convection heat transfer regime is prevailing and the hydrodynamic characteristics of the flow field are independent of the thermal phenomena. However this claim is not true in cases where the heat flux - to - flow rate ratio is high enough so that a local buoyancy effects drastically alter the velocity profiles. Here the forced convection correlations may prove to be inadequate and a need arises to study the thermal and hydraulic characteristics of the flow in a coupled sense. Such thermosyphon effects and other various applications are reviewed in J-1. Examples of such applications include industrial and power generating equipment, cooling systems of nuclear reactors, passive solar energy collection systems and geothermal and geophysical processes.

In this chapter, we study the pressure drop characteristics of aiding, low Reynolds, fully developed, mixed convection flows in vertical wire-wrapped and bare rod bundles. The focus of the work is to provied mixed convection preessure drop data under laminar/transition flow conditions. Turbulent flow conditions are not treated in this work.

The governing equations and the dominant dimensionless parameters

were presented in chapter 1. A literature review of all relevant experimental and analytic work in circular tubes and rod bundles follows. The instrumentation and its associated error in measuring low magnitude pressure drops is also presented together with a method to measure pressure drops under mixed convection conditions. Finally the data are presented and discussed.

3.2 Literature Review

In this section, most of the experimental and theoretical work on low Reynolds pressure drop in mixed convection is reviewed. Since only limited work exists for rod bundle geometries, tube geometry results are also considered. All data discussed here was taken with a constant heat flux boundary condition.

Kemeny and Somers (K-5) obtained extensive pressure drop data for laminar mixed convection flows in vertical circular tubes using oil and water. It was found that the ration f/f_o was as high 20 for Gr_q/Re around 4×10^4. Here f is the mixed convection friction factor and fo is the isothermal (or forced convection) flow friction factor under the same Reynolds number. It was also found that the Pr effect on the data was minor. Some of these data are shown in Figure 3.1. As reported in K-5 transition to turbulence had occurred in at least half of their data presented in Figure 3.1. However the authors (K-5) could not differentiate between laminar and non-laminar data with respect to parameters of Figure 3.1. Some pressure drop data, also displayed in Figure 3.1, were taken by Greene and Scheele (G-2).

Bishop, Willis and Markley (B-9) theoretically studied the effects of

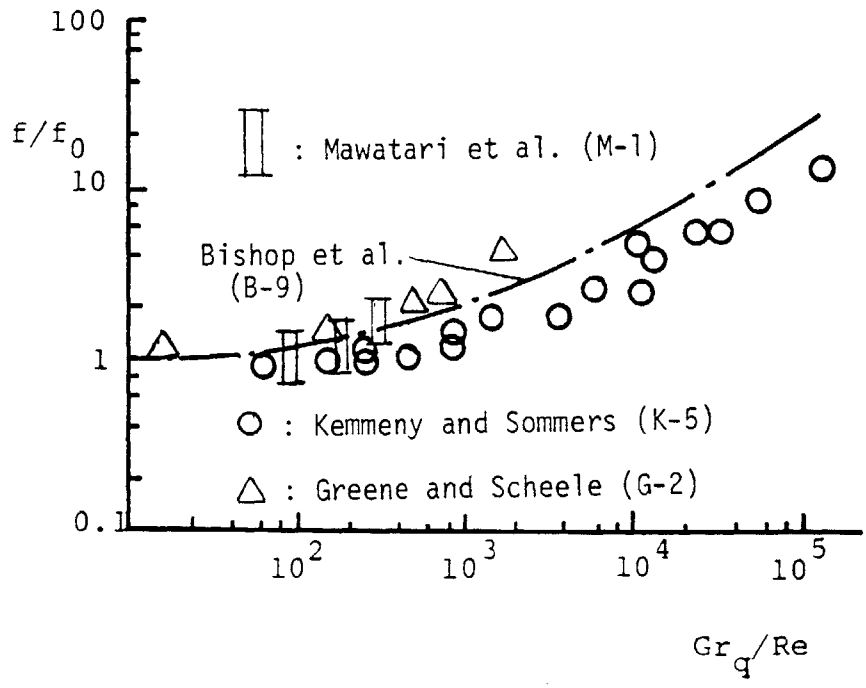

FIGURE 3.1: MIXED CONVECTION PRESSURE DROP DATA FOR FLOWS IN CIRCULAR TUBES AND WIRE-WRAPPED ROD BUNDLES.

buoyancy on laminar upflow friction factors in circular tubes. Using infinite series solution, they solved the following equation:

$$\nabla^4 w^* + 4(Gr_q/Re)\, w^* = 0 \tag{3.1}$$

Equation 3.1 can be directly derived from equations 1.28 and 1.29, by differentiating equation 1.29 twice and subtracting out equation 1.28. The velocity field was expressed in terms of B_{er} and B_{ei} functions and the parameter Gr_q/Re. From the velocity field the friction factor was derived. An algebraic fit to the analytic solution was found to be:

$$\frac{f}{f_o} = \left(1 + 2.97 \times 10^{-3} \frac{Gr_q}{Re}\right)^{0.655} \equiv F \tag{3.2}$$

where f and fo are the friction factors in mixed and forced convection respectively under the same Reynolds number. For tubes f_o is equal to:

$$f_o = \frac{64}{Re} \tag{3.3}$$

Bishop et al. (B-9) even attempted to extend their model to include developing flow effects. They used the water velocity profiles in G-2, in order to deduce the friction factors in developing flows for $Gr_q/Re = 465$. A best fit correlation was found to be:

$$\frac{f}{f_o} = 1 + \frac{F-1}{1 + 0.36\, Z^{-3}} \tag{3.4}$$

where $Z = 50\ (\frac{L}{D})$.

Equation 3.4 is not generally valid for any Gr_q/Re value. It is not also valid for any Pr number since it was based on water data. As discussed in

section 1.4. Pr number effects are important for developing mixed convection flows.

Comparison of equation 3.2 with data is shown in Figure 3.1 for the data of Kemeny and Somers.

Mawatari et al. (M-1) presented water friction factor data for mixed convection flows in a 91-pin wire-wrapped rod bundle with P/D = 1.21 and H/D = 47.2. Their results are shown in Figure 3.1 and 3.2. The Gr number they defined is equal to 380 Gr_q/Re. (see Appendix A.3.1) The data have been plotted in Figure 3.1 in the form of vertical bars. The upper part of these bars correspond to the lower Reynolds data of Figure 3.2. The opposite is true for the lower part of the bars. Observe that laminar data for f/f_o by Mawatari et al. (corresponding to the upper bar part) are higher than all of the circular tube data reported yet.
The following remarks can be made, based on this data:

(a) For $Gr_q/Re \sim 420$ and $Re < 600$, f/f_o is approximately equal to 1.5.

(b) For $Re < 700$, the f/fo ratio increases with Gr_q/Re.

(c) When Re approaches 1000 and up the f/f_o ratio approaches 1.

The authors are not aware of any other pressure drop mixed convection data in rod bundles. In contrast there are several mixed convection analyses of laminar fully developed flows in bare rod bundles (R-5, Y-2, W-8, W-7). S-F Wang, Rohsenow and Todreas (W-8) solved equations 1.28 and 1.29, for interior and edge subchannels of bare rods situated in both square and triagular arrays. Both aiding and opposing mixed convection flows where considered. Friction factors and heat transfer coefficients were calculated and plotted against the Gr_q/Re parameter. The

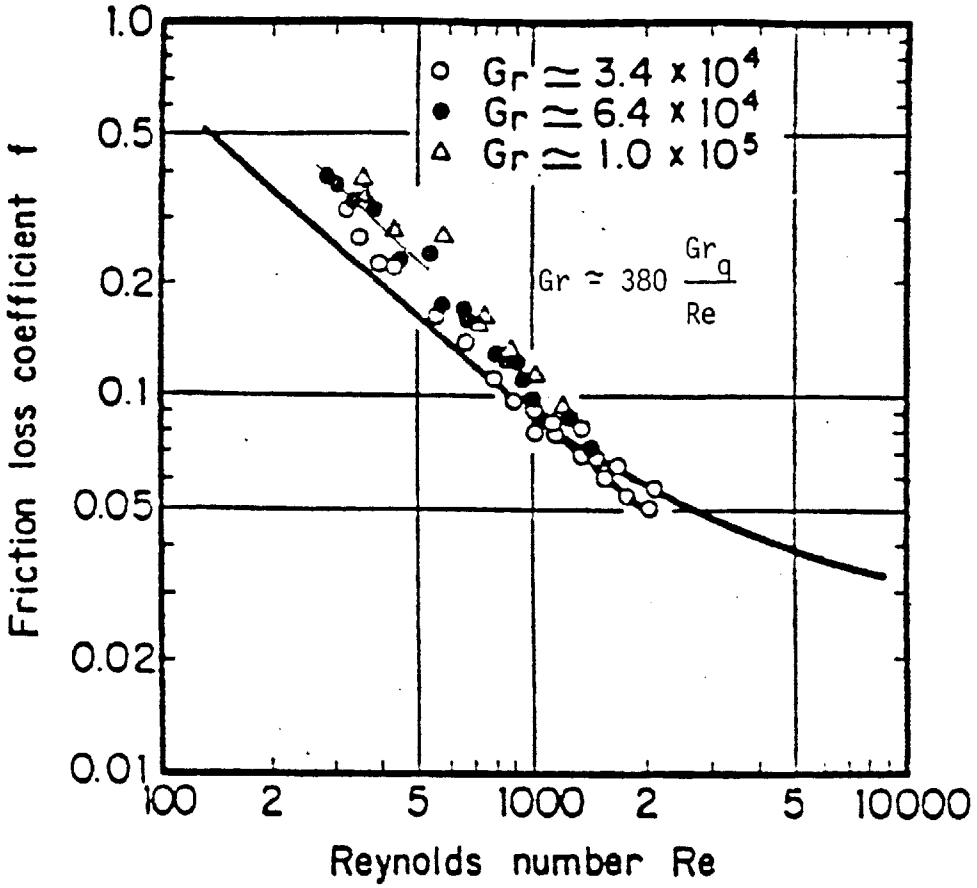

FIGURE 3.2: FRICTION FACTOR CHARACTERISTICS IN MIXED CONVECTION FOR A 91-PIN WIRE-WRAPPED ROD BUNDLE (Taken from reference M-1)

effect of the parameter P/D was also considered. In Figure 3.3 we recast their aiding flow friction factor data for convenient form: f/f_o versus Gr_q/Re, in order to facilitate comparisons with our data. Based on Figure 3.5, the following remarks can be made:

(a) There is a strong P/D effect. For P/D approaching unity, mixed convection effects are mainfested earlier for the same Gr_q/Re.

(b) The circular tube analytic solution exhibits less steeper gradients than all subchannel solutions.

(c) The circular tube solution envelops from below all subchannel solutions.

One should keep in mind that all these solutions assume complete laminar flow conditions where as the data in K-5 indicate, transition to turbulence has occured at most of the data.

3.3 Instrumentation and Measurement Procedures

3.3.1 Instrumentation

Both the 16-pin bare rod bundle and the 19-pin wrapped rod bundle were used for mixed convection pressure drop studies. These bundles were described in Chapter 2. In this section the pressure drop measurement set-up, the relevant instrumentation and the associated error of the measurement are discussed.

Figure 3.4 gives a schematic of the pressure measurement set-up for both bundles. The static pressure measurements were made between points 1 and 2 and the pressure signal was transmitted by 1/4 inch tygon tubes to the electric manometer. 1/8 inch wall pressure taps were used at points 1 and 2.

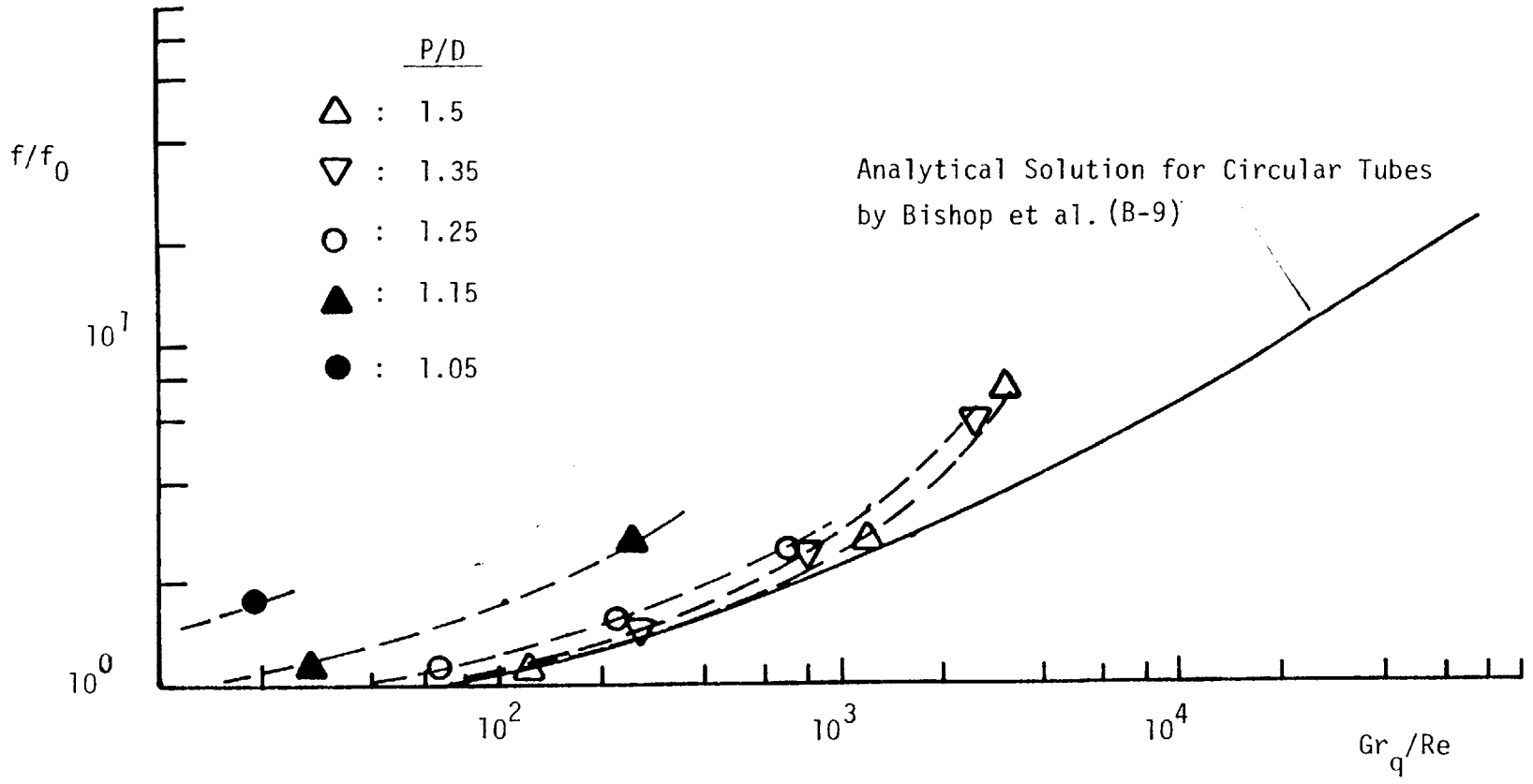

FIGURE 3.3: ANALYTICAL SOLUTION FOR FULLY DEVELOPED LAMINAR MIXED CONVECTION FLOWS IN INTERIOR SUBCHANNELS OF BARE ROD BUNDLES BY WANG et al.(W-8)

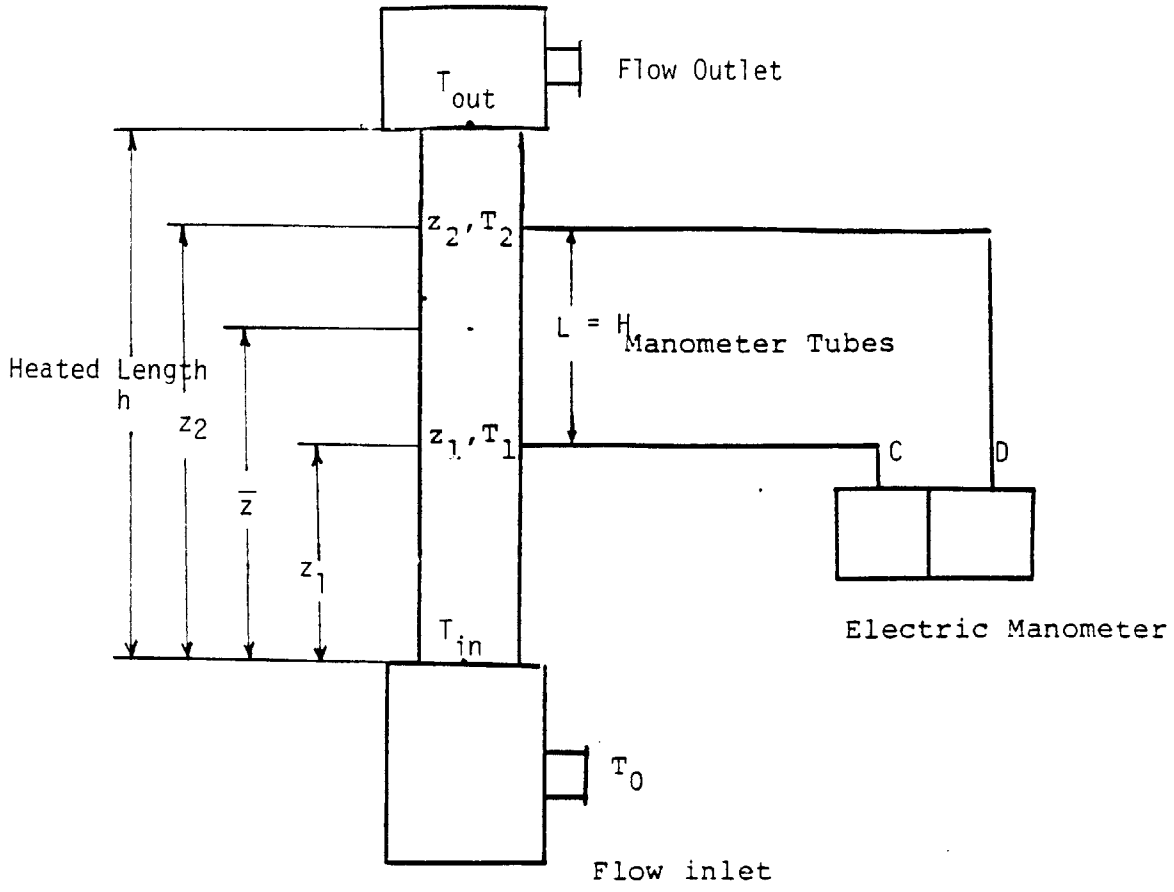

FIGURE 3.4: SCHEMATIC REPRESENTATION OF THE TEST SECTION WITH THE MANOMETER TUBES AND THE ELECTRIC MANOMETER.

The differential pressure at C and D was measured with an electric manometer and a time-averaging voltmeter. The electric manometer was made by Datametric and it contains a multi-range differential pressure transducer which measures 0.002 to 20 psi (0.1 to 1000 Torr) (For details see E-3). This particular manometer is very sensitive to ambient temperature changes. Such changes cause significant drifts that render the low scale measurements practically impossible. In order to minimize this problems, the whole electric manometer was thermally isolated using a 5 cm layer of fiberglass.

3.3.2 Pressure Drop Measurements

Two kinds of pressure drop measurements were performed namely: (a) isothermal flow measurements, (b) heated flow measurements. In the case of isothermal flows the frictional pressure drop Δp_f^{iso} between points A and B was directly measured in the voltmeter since the static heads in the test section and tygon tubes cancel out: (see Appendix A.3.2)

$$\Delta p_f^{iso} = \Delta p_M \tag{3.5}$$

In the case of mixed convection frictional pressure drop measurements, the following formula is used: (see Appendix A.3.2)

$$\Delta p_f^{MC} = \Delta p_M + Hg\ (\bar{\rho}_M - \bar{\rho}_{1,2}) \tag{3.6}$$

where H is the distance between positions 1 and 2 in the test section, $\bar{\rho}_M$ is the average manometer density and $\bar{\rho}_{1,2}$ is the average water density in the test section between points 1 and 2.

In order to evaluate $\bar{\rho}_M$ the following procedure is adopted. At the beginning of each measurement, both power and flow rate are set to zero,

and isothermal flow conditions are established in both the test section (at T_o) and the manometer tubes (T_M). At this point the manometer will not read zero if $T_o \neq T_M$. Subsequently we set the manometer reading to zero in order to artificially make the manometer read as if $T_M = T_o$. Under such conditions:

$$\overline{\rho}_M = \rho_{water}\ (T_o) \tag{3.7}$$

Subsequently the flow and then the power are turned on. The $\overline{\rho}_{1,2}$ is estimate as:

$$\overline{\rho}_{1,2} \simeq \rho_{water}\ (\overline{T}) \tag{3.8}$$

where $$\overline{T} \simeq \frac{T_1 + T_2}{2} \tag{3.9}$$

and T_1 and T_2 can be estimated by assuming a linear temperature profile along the heated zone. Refering to Figure 3.4 take:

$$T_1 = T_{in} + (T_{out} - T_{in}) \frac{Z_1}{L} \tag{3.10}$$

$$T_2 = T_{in} + (T_{out} - T_{in}) \frac{Z_2}{L}$$

3.3.3. Error Estimation

The error of each individual term in equation 3.6 is now estimated. The manometer reading Δp_M has the same accuracy for both isothermal and mixed convection measurements. The following factors affect the accurancy of this term:

(a) Some permanent deformation of the sensing diaphragm.

(b) Any air bubbles present in the manometer tubes.

(c) Any oil leak from the electric manometer.

The manometer was calibrated for static pressure measurements using a water column in a marked tube. Within the accurancy of the water column length measurement (the water level in the tube is curved due to capilary phenomena), the electric manometer measured "exactly" the weight of the water column for column lengths down to 3 mm. For the lowest scale the Δp_M error was statistically estimated to be of order of ±3.0%. This was done by repeating isothermal pressure drop measurements under the same flow rate conditions and by recording the scattering of the data. Note that this error includes also the error imposed by the resolution of the flow meter. Therefore:

$$\Delta p_M = \Delta p_{M,meas} \pm 3.0\% \tag{3.11}$$

The accurancy of the manometer drastically deteriorates when Δp_M is less than 0.0002 psi. In this case it was estimated that the error is ±16.0% because of suspected non-linear behavior of the manometer diaphragm. The term $gH\ (\overline{\rho}_M - \overline{\rho}_{1,2})$ in equation 3.6 introduces more serious errors than that in Δp_M. This error is caused by temperature drifts (T_{in}, T_M) during the course of the measurement and the drift in temperature $\overline{T}$ which follows any drift in the inlet termperature.

The drift in temperature T_M is caused by two reasons:

(a) Ambient Temperature T_a changes

(b) T_M is much different (usually colder) than T_a and therefore a

transient occurs to nullify this difference.

As discussed in Appendix A.3.1, note that it is T_M changes at the vertical part of the manometer tubes in Figure 3.4 that affect the measurement of Δp_M.

If during the course of a mixed convection measurement (typically from 30 to 40 minutes) T_M changes by $\pm \Delta T_M$ and then the error introduced in the term $g H (\bar{\rho}_M - \bar{\rho}_{1,2})$ can be calculated as follows:

$$e = \frac{g H (\Delta\bar{\rho}_M + \Delta\bar{\rho}_{1,2})}{g H (\bar{\rho}_M - \bar{\rho}_{1,2})} \tag{3.12}$$

where $\Delta\bar{\rho}_M$ and $\Delta\bar{\rho}_{1,2}$ are the uncertainties in the $\bar{\rho}_M$ and $\bar{\rho}_{1,2}$ estimations respectively. Using the relation

$$\Delta\rho \sim \rho\, \beta \Delta T$$

equation 3.12 is written as:

or
$$e \simeq \frac{\bar{\rho}_M \Delta T_M \beta(T_M) + \rho_{1,2} \Delta\bar{T} \beta(\bar{T})}{\bar{\rho}_M (\bar{T} - T_M) \bar{\beta}} \tag{3.13}$$

where $\bar{\beta}$ is evaluated at temperature $(\bar{T} + T_M)/2$.

In a typical mixed convection run with $Re \sim 450$ and $Gr_q/Re \sim 2200$, approximately have:

$$\begin{aligned} T_{in} &\sim 25°C \\ T_M &\sim 20°C, \beta_M \sim 1.82\times10^{-4}\ °K^{-1},\ \bar{\rho}_M \sim 998\ kg/m^3 \\ \bar{T} &\sim 43°C, \beta_{1,2} \sim 4.0\times10^{-4}\ °K^{-1},\ \bar{\rho}_{1,2} \sim 990\ kg/m^3 \\ \Delta T_{in} &\sim \Delta\bar{T} \sim 1°C \end{aligned} \tag{3.14}$$

$$\Delta T_M \sim 1°C$$

Using equation 3.13 and property tables get:

$$e \sim 10.0\% \tag{3.15}$$

In order to calculate the total error let

$$X = g\ H\ (\bar{\rho}_M - \bar{\rho}_{1,2})$$

$$Y = -\Delta p_M \text{ (Note: } \Delta p_M < 0) \tag{3.16}$$

$$F = \Delta\ p_f^{MC}$$

Then $$e_{\Delta p_f}^{MC} = \frac{\Delta F}{F} = \frac{\Delta X + \Delta Y}{X - Y} \tag{3.17}$$

Based on data reduction experience, the following is true:

$$X \sim Y \text{ and } X - Y \sim 0.1\ X \tag{3.18}$$

Substituting in 3.17 take:

$$e_{\Delta p_f}^{MC} \sim 10\ (e_X + e_Y) \tag{3.19}$$

and since $e_X \sim 0.1$ and $e_Y \sim 0.03$ we get that:

$$e_{\Delta p_f}^{MC} \sim 130.0\% \tag{3.20}$$

This error estimate for a typical mixed convection pressure drop measurement clearly indicates the difficulties of the measurement even when assumint $\Delta\bar{T} \sim \pm\Delta T_M \sim 1°C$. Typically in our experiments ΔT_{in} was around 0.5°C and ΔT_M around 0.4°C. For these temperature uncertainties the total error $e_{\Delta p_f}^{MC}$ is around 65%. (This error is indicated with an error bar in our data of Figure 3.8). Obviously a new experimental approach is

required to drastically reduce this temperature drift particularly the drift of T_M. One easy but time consuming way consists of two basic steps:

(a) Operate the loop in an open-loop mode and discard the hot water to the drain. In this way $\Delta\bar{T}$ can be controlled within ± 0.1°C.

(b) Fill manometer tubes and test section with water and let them stay overnight, in order to equate T_M with the ambient temperature. Here again ΔT_M is expected to be ~ 0.1°C.

For $\Delta T_M \sim \Delta\bar{T} \sim 0.1°C$ the total error $e^{MC}_{\Delta p_f}$ is similarly estimated approximately equal to ~ 25%. Such approach was followed recently by Okada (T-9), the results of whom are presented in this work (see Figure 3.8).

3.4 Results and Discussion

3.4.1 Isothermal flows

The isothermal friction factor coefficients f_o are experimentally obtained first. These coefficients are needed to calculate the f/f_o ratio (mixed-to-forced convection friction factor coefficient ratio). Experiments are conducted in both the bare and the wire-wrapped bundle. All data are plotted as f_o versus Re.

The friction factor is estimated as follows:

$$f_o = \frac{\Delta p}{\frac{1}{2}\rho\bar{w}^2}\,\frac{De}{H} = \frac{P_w^2\, De^3}{8\, H}\,\frac{1}{\rho}\,\frac{\Delta p}{\dot{V}^2} \qquad (3.21)$$

where Δp is the pressure drop between positions 1 and 2 in Figure 3.4, De is the equivalent (hydraulic) diameter, H is the distance between the pressure taps, P_w is the wetted perimeter and $\dot{V}$ is the volumetric flow rate. Δp and $\dot{V}$ are measured by the manometer and rotameter with ±3.0

(maximum) and ±0.5% error respectively. The Reynolds number is estimated as:

$$Re = \frac{4\,\dot{V}}{P_w\,\nu} \tag{3.22}$$

where ν is the kinematic viscosity. The values of the geometrical parameters can be found in Table 3.1. Using equations 3.21 and 3.22 our laminar friction factor data for the bare and wire-wrapped bundles are plotted in Figures 3.5 and 3.6. We begin our analysis and discussion with the bare rod bundle results.

The flow is assured to be fully developed for Re < 700. This can be justified by using the approximate formula to estimate the hydrodynamic entry length in pipes developed by Schmidt and Zeldin (see W-6):

$$\frac{L_e}{De} \simeq 0.08\ Re \tag{3.23}$$

Taking L_e equal to $(z_1 + z_2)/2$ (see Figure 3.4) L_e = 60 cm, De = 1.05 cm, then from equation 3.23, observe that the flow in the middle plane is fully developed for Re < 700.

The data in Figure 3.5 display a remarkable linear behavior. An analytical expression predicting this data can be found using Rehme's approach (R-3, S-7). Each subchannel of the square array, is considered to form an isolated channel. Using the friction factor constants C = f Re, the bundle friction factor can be estimated as follows: The pressure drop in each subchannel is constant:

$$\Delta p = f_i \frac{L}{De_i} \rho \frac{u_i^2}{2} = f_b \frac{L}{De_b} \rho\, u_b^2 /2 \tag{3.24}$$

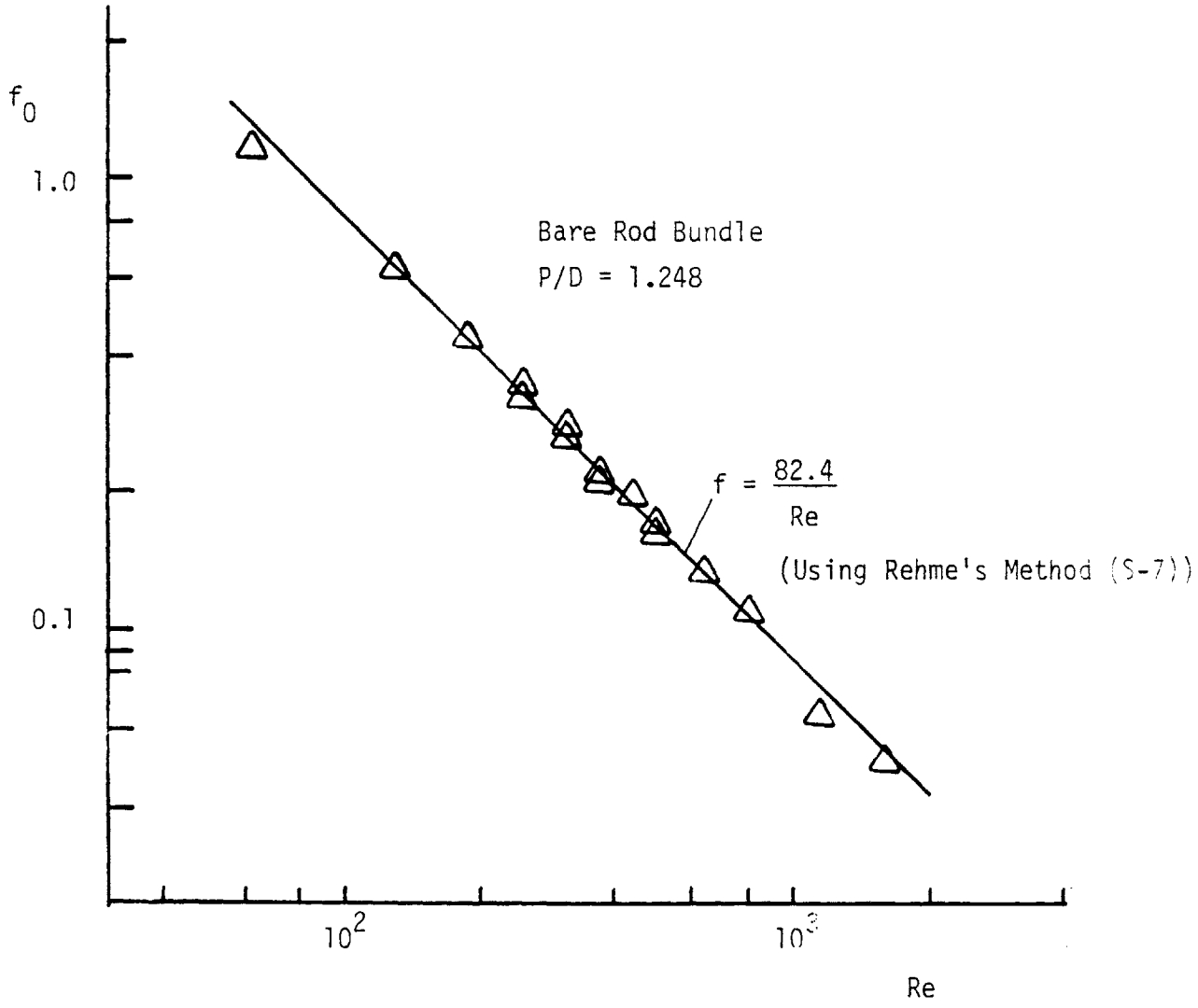

FIGURE 3.5: ISOTHERMAL FLOW FRICTION FACTOR COEFFICIENT FOR THE MIT 4x4 BARE ROD BUNDLE.

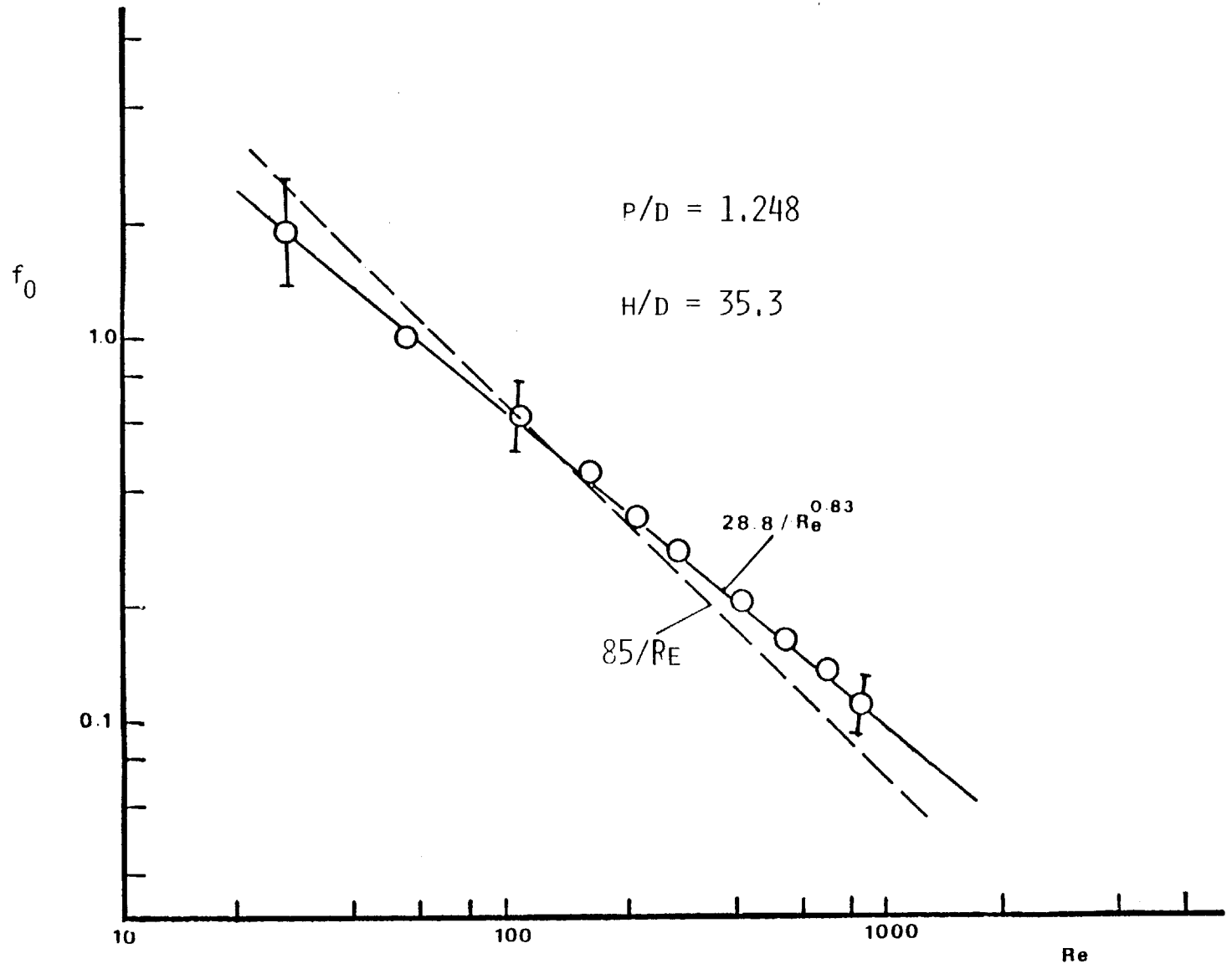

FIGURE 3.6 FRICTION FACTOR FOR THE 19-PIN WIRE-WRAPPED ROD BUNDLE

where $$f_i = \frac{C_i}{Re_i} = \frac{C_1 \nu}{De_i u_i} \tag{3.25}$$

subscript i stands for interior, edge or corner subchannel and subscript b indicates bundle averaged quantities. Substituting 3.25 into 3.24 get:

$$\frac{u_i}{u_b} = \frac{C_b}{C_i} \cdot \frac{De_i^2}{De_b^2} \tag{3.26}$$

Also from continuity equation take:

$$\sum_i \frac{u_i A_i}{u_b A_b} = 1 \tag{3.27}$$

where A_i is the subchannel cross section and $\sum_i A_i = A_b$. From equations 3.26 and 3.27 finally obtain:

$$\frac{1}{C_b} = \sum \left\{ \frac{1}{C_i} \left(\frac{De_i}{De_b}\right)^2 \frac{A_i}{A_b} \right\} \tag{3.28}$$

The C_i's are obtained from literature numerical calculations and for P/D = 1.25.

$$\left.\begin{aligned} C_{interior} &= 89.4 \\ C_{edge} &= 86.2 \end{aligned}\right\} \quad \text{(W-7)}$$

$$C_{corner} = 85.7 \qquad \text{(S-7)}$$

Based on these numbers C_b is calculated to be 82.4. As it can be seen in Figure 3.5 the correlation f = 82.4/Re predicts our data with less than 3% error (except some extreme data points).

We turn now our attention to the wire-wrapped bundle data displayed in Figure 3.6. The position of the lower tap is at 83.6 cm and De = 1.086 cm. Using equation 3.23 it is roughly estimated that the flow will be

fully developed there for Re < 962.

As it is shown in Figure 3.6 an empirical correlation was fitted through the data:

$$f_o = \frac{28.8}{Re^{0.83}} \quad ; \text{ Re} < 1000 \tag{3.29}$$

This result is in good agreement with data of Mawatari et al. (M-1) for a wire-wrapped rod bundle with P/D = 1.21 and H/D = 47.2. Spencer and Markley (S-5) conducted similar experiments in a rod bundle with P/D = 1.24 and H/D = 40. Based on their data it was suggested that:

$$f_o = \frac{85}{Re} \tag{3.30}$$

This correlation is also shown in Figure 3.6. Apparently the slope of Spencer's and Markley's data is different than the slope of our data. Further experimental work may be required to clarify the deviations between these two correlations.

3.4.2 Mixed Convection Pressure Drop Data

Both bundles were run under mixed convection conditions with uniform radial nominal power distribution. The friction factor coefficient is estimated as follows:

$$f = \frac{P_w^2 \, De^3}{8 \, L} \frac{\rho}{\rho_o^2} \frac{(\Delta p)^{MC}}{\dot{V}_o^2} \tag{3.31}$$

where ρ_o is evaluated at inlet temperature and ρ at temperature $\bar{T} = (T_1 + T_2)/2$, where $\bar{T}$ is the average water temperature between the pressure taps. The procedures to measure Δp have been outlined in section 3.4. The Gr_q and Re numbers are evaluated from:

$$Gr_q = \frac{\beta\, g\, \dot{q}''\, De^4}{\nu^2\, k} = \frac{\beta\, g}{k\, \nu^2}\, \frac{De^4}{\pi\, D\, h}\, \dot{P} \tag{3.32}$$

$$Re = \frac{4\, \rho_o\, \dot{V}_o}{P_w\, \mu} \tag{3.33}$$

where $\dot{q}''$ is the heat flux per rod, $\dot{P}$ is the total power per rod, h is the rod heated length, D is the rod diameter, β is the water thermal expansion coefficient and k is the conductivity of the water. All physical properties are evaluated at $\bar{T} = (T_1 + T_2)/2$. As extensively discussed in section 3.3, the major source of error is introduced through the $(\Delta p)^{MC}$ term. The power per rod $\dot{P}$ is estimated using the flow rate and temperature rise measurements as discussed in Chapter 2. Due to test section heat losses the rod power estimated as above was found to be 3 to 5.0% lower than the nominal rod power.

Figure 3.7 gives the mixed-to-forced friction factor ratio f/f_o as a function of the Gr_q/Re parameter for the bare rod bundle. The error bars plotted for each data point are of order ± 40%. This significant error is caused by manometer tube temperature variations during the course of each measurement. All data have Re less than 750. The corrlation $f_o = 82.4/Re$ was used for f_o estimation. The following remarks can be made:

(a) The f/f_o ratio ranges from 1.0 to 2.0 with no clear-cut behavior as a function of Gr_q/Re. This later remark is due to the large error associated with the measurement.

(b) Bishop et al. circular tube correlation lies well above the data. The same is true for the circular tube data presented in Figure 3.1.

At this point it should be mentioned that transition to turbulence had occurred in some of our mixed convection data in the 16-pin bare rod

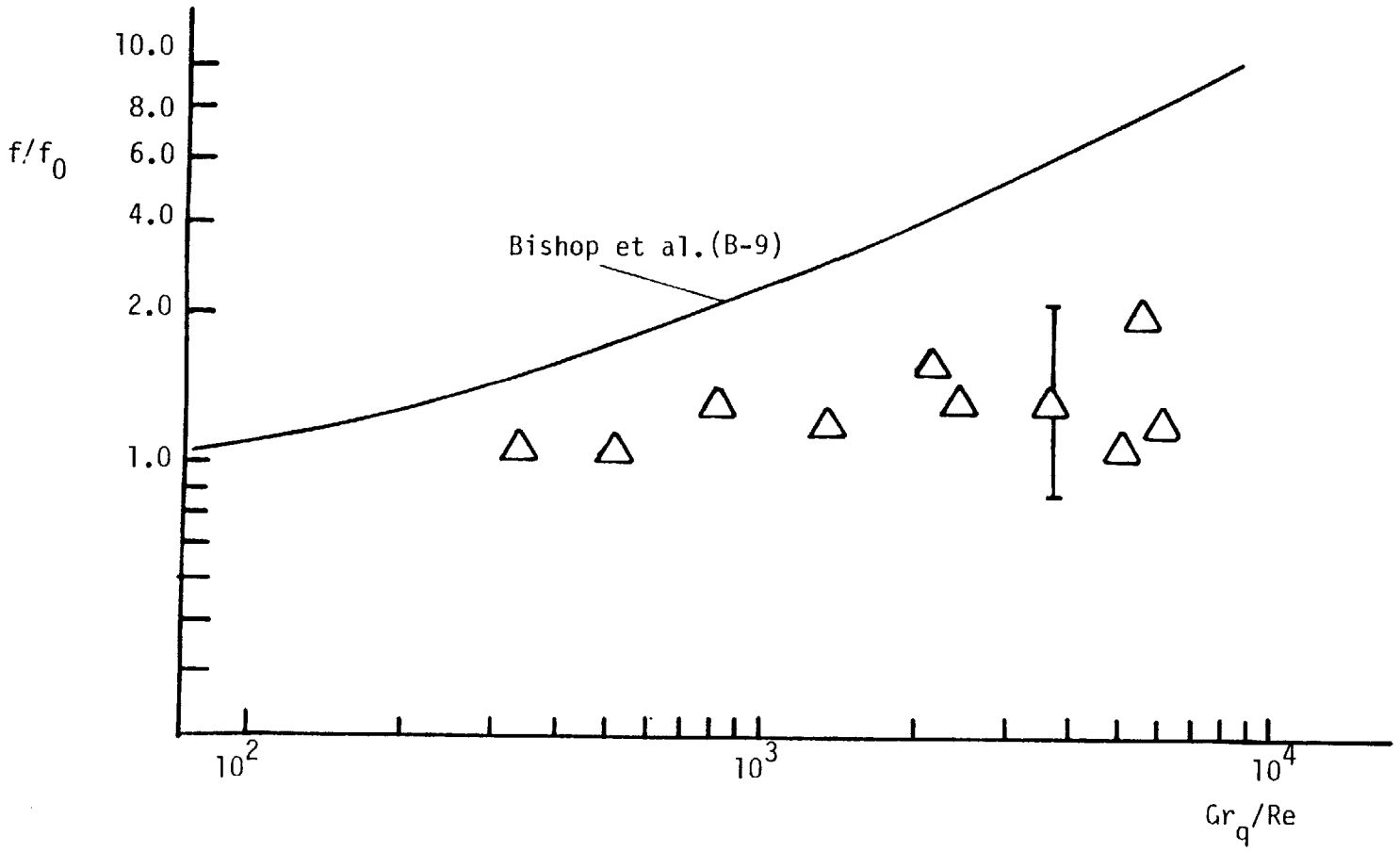

FIGURE 3.7: MIXED-TO-FORCED CONVECTION FRICTION FACTOR COEFFICIENT RATIO FOR THE MIT 4x4 BARE ROD BUNDLE.

bundle. This was experimentally found by observing the signature of a thermocouple inserted within an interior subchannel of the bundle. The flow was not laminar for Re ranging from 300 to 500 and $Gr_q/Re \sim 3.0 \times 10^3$ or higher. A systemic study of the onset of flow instability for a 2 x 2 square array bare rod bundle was presented in E-1.

Figure 3.8 presents the f/f_o ratio versus the Gr_q/Re parameter for the case of the 19-pin wire-wrapped rod bundle. For completeness, recent data by Okada (O-2) are also presented. These data were taken after our first series of data was accomplished and with the improved temperature control procedures mentioned earlier in order to minimize the systematic error. The following remarks can be made:

(a) Both Okada's and our data are significantly lower the circular the circular tube analytic prediction as well as Mawatari's 91-pin wire-wrapped bundle data.

(b) A Reynold's number effect seems to exist in our data, similar to that in Mawatari's et al. data. The f/f_o ratio is higher for lower Reynold's number. No such behavior can be clearly observed in Okada's data. Note that the systematic error (see error bar in Figure 3.8) in our data is ~ 65% rendering the Reynold's effect exhibited by our data questionable. Further work is required to clarify this point.

We now speculate about why all our f/f_o data exhibit relatively lower values than those of the circular tube experiments (Figure 3.1) as well as the circular tube analytic solution. In both our bundles the heat-to-flow ratio is higher for the interior than the peripheral subchannels. Due to the fact that housing walls are not heated it is expected therefore that buoyancy effects will render the velocities at the interior subchannels

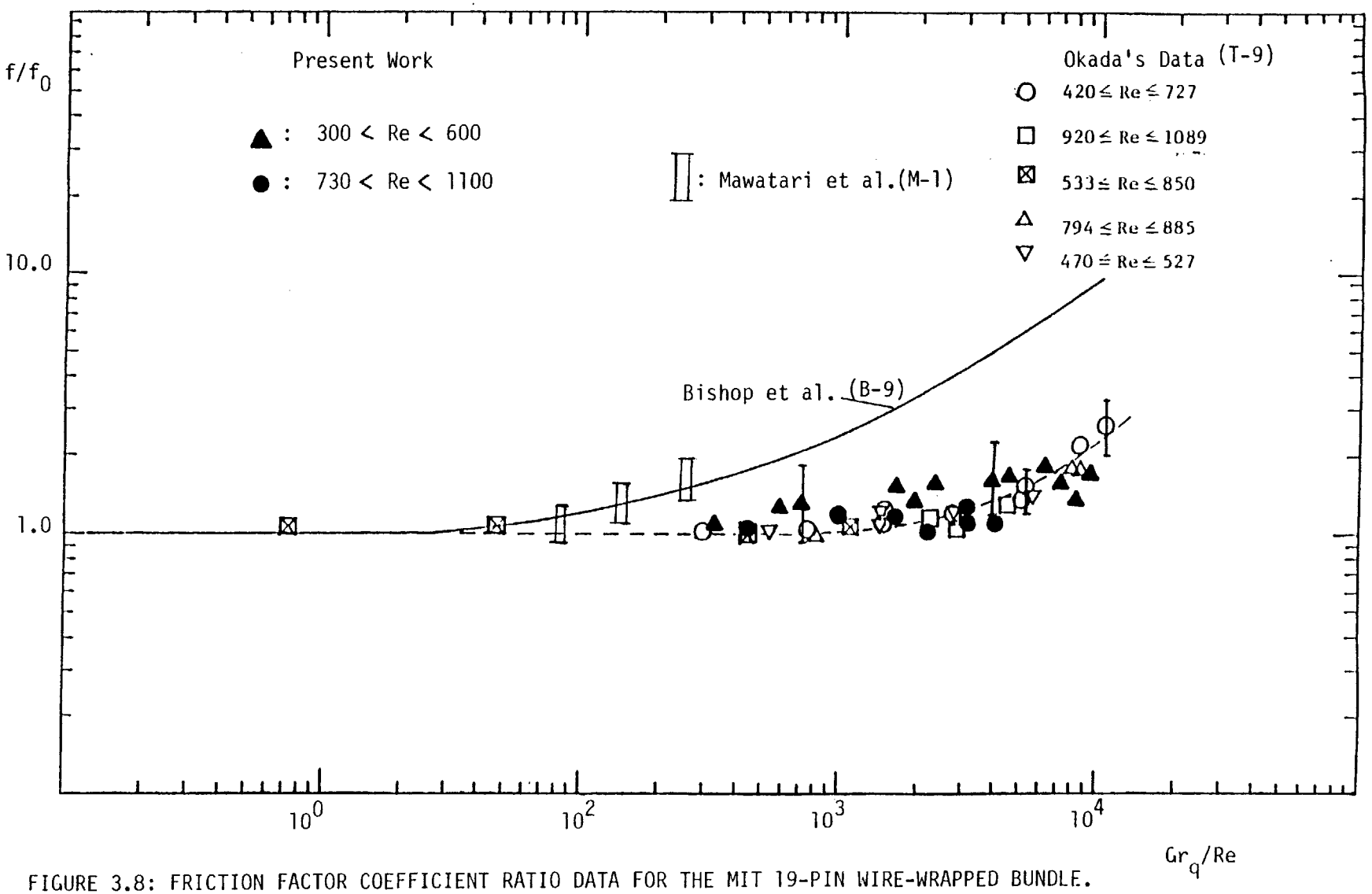

FIGURE 3.8: FRICTION FACTOR COEFFICIENT RATIO DATA FOR THE MIT 19-PIN WIRE-WRAPPED BUNDLE.

higher than the velocities in the peripheral ones. The frictional forces while increasing in the core region will decrease or even reverse direction at the housing walls. Such phenomena are not present in the case of circular tubes, where buoyancy effects always increase friction in aiding flows. We postulate that these "unheated wetted perimeter" effects slow down the pace of $(f/f_o)_{bundle}$ increase with buoyancy forces increasing. The higher the ratio "unheated wetted perimeter"/"heated wetted perimeter", the more pronounced this slow down effects are expected to be.

The above postulate has to be validated analytically and checked with new experimental results. For the later, it is important to improve the accuracy by minimizing the ΔT_M uncertainty down to 0.1°C by the technique already employed by Okada. In addition new rod power distributions should be established, i.e., higher power at the peripheral rods and vice-versa. Such data will allow the development of a subchannel based f/f_o ratio using a 2-channel model similar to that employed in S-4 by Symolon.

CHAPTER 4

MIXED CONVECTION HEAT TRANSFER IN WIRE-WRAPPED ROD BUNDLES

4.1 Introduction

In this chapter, mixed convection effects on temperature distributions at heated rod walls and heat transfer coefficients are studied. As discussed in Section 1.2, in aiding flows buoyancy effects increase the velocity magnitude and consequently the convective forces in the vicinity of the heated walls. Therefore in laminar aiding mixed convection flows, heat transfer is expected to improve as buoyancy forces increase. The opposite is true for laminar opposing mixed convection flows.

In turbulent flows opposite phenomena may happen. In certain cases, buoyancy effects reduce turbulence production at the wall region. In this case the turbulent diffusion heat transfer mechanism is impaired, rendering lower heat transfer coefficients. A thorough discussion of the buoyancy effects on turbulent mixed convection flows can be found in S-4. In this work we concentrate our experimental work on low Reynolds mixed convection aiding flows where the flows are either laminar or low intensity turbulent.

A special designed instrumented rod is used in this work to obtain detailed clad temperature measurements at any axial position. This instrumented rod is placed in the center of the 19-pin wire wrapped bundle. Temperature data are obtained for low flow mixed convection aiding flows. Based on this data, an empirical formula for the average heat transfer coefficient is proposed.

4.2 Literature Review

All experimental and analytical work reviewed in this section was performed under constant heat flux boundary conditions. Halman (H-1) performed temperature and heat transfer coefficient measurements for mixed convection aiding laminar water flows in circular tubes. He suggested the following correlation for accurate approximation of his data:

$$Nu = 1.40 \left(\frac{1}{4}\frac{Gr_q}{Re}\right)^{0.28} = 0.95 \left(\frac{Gr_q}{Re}\right)^{0.28} \qquad (4.1)$$

for $\quad 4 \times 10^2 < \frac{Gr_q}{Re} < 4 \times 10^4$

where Nu is the Nusselt number. The physical properties in the above dimensionless numbers were evaluated at the average fluid temperature between the pressure taps that were used for pressure drop measurements. The pressure taps were placed at an appropriate distance from the entrance, in order to assure fully developed flow conditions. Halman also performed analytic calculations for fully developed laminar mixed convection flows in circular tubes. The analytic predictions were in excellent agreement with the experimental results. (see H-1 and also Figure 4.8)

The same type of data but using sodium as the working fluid were obtained by Wendling et al (W-9). They suggested the following empirical correlation:

$$Nu = 2 + 0.21\left(\frac{Gr_q}{Re}\right)^{0.28} \qquad (4.2)$$

These data are in agreement with similar data obtained by Volchcov et al. (as reported in W-9). However, they are significantly lower than Halman's data and the circular tube analysis.

Recently, Gruszczynski and Viskanta (G-4) performed heat transfer studies in a 7-pin bare tube bundle, arranged in a triangular array with P/D = 1.25. The flow in the bundle is driven through a natural circulation loop. Mixed convection flow conditions were established in the 7-pin bundle since:

$$10^3 < \frac{\overline{Gr}_q}{\overline{Re}} < 3.6 \times 10^3 \tag{4.3}$$

where the bars indicate average values for the whole tube length, including the hydrodynamic and thermal entrance region where the flow is still developing. After some algebraic manipulation we recast their heat transfer data as a function of $\overline{Gr}_q/\overline{Re}$ (See Appendix A.4.1):

$$\overline{Nu} = 2.8 \times 10^{-3} \left(\frac{\overline{Gr}_q}{\overline{Re}}\right)^{0.87} \overline{Pr}^{0.49} \tag{4.4}$$

Note that $\overline{Nu}$ given by equation 4.4 represents an average value over the whole heated length. In addition the authors do not report the exact angular positions of the thermocouples employed for temperature measurements. It cannot be concluded therefore, whether the Nusselt number is also averaged along the peripheral direction.

Yang (Y-2, Y-3) performed numerical studies for fully developed mixed convection flows in infinite arrays of bare rods in both square and triangular arrangements. He found that for a given P/D both Nu number and friction factor coefficient increase with Gr_q/Re.

Recently Wang (W-7, W-8) performed a similar type of numerical analysis for fully developed mixed convection flows in isolated cells. Nusselt numbers versus Gr_q/Re were presented for both aiding and opposing

flows and for interior, edge and corner subchannels. Different P/D values were also studied. After reducing their data, we found that for the same Gr_q/Re number, the Nusselt number decreased with P/D. It is interesting to note that Wang used a different dimensionless parameter to plot his Nu number results, namely the Ra_D which was defined as follows:

$$Ra_D = Pr\ Gr_D\ \frac{\partial T^*/\partial z^*}{T^*}\ \frac{D}{De} \tag{4.5}$$

where $$Gr_D = \frac{\beta\ g\ (T - T_o)\ D^3}{\nu^2} \tag{4.6}$$

D is the rod diameter and T*, z* are dimensionless quantities defined in Section 1.4. The parameter Ra_D can be expressed in terms of the Gr_q/Re parameter as follows: (See Appendix A.4.2)

$$Ra_D = 4\ \frac{Gr_q}{Re}\ \left(\frac{D}{De}\right)^4 \tag{4.7}$$

Plotting his Nusselt numbers as a function of Ra_D Wang found that for the same Ra_D, Nu increases with P/D. As stated above, exactly the opposite happens when the Gr_q/Re parameter is employed. This "paradox" can be explained using the following relations:

$$\frac{Gr_q}{Re} \sim \frac{\dot{q}''}{\dot{m}}\ De^4\ P_w \sim \frac{\dot{q}''}{\dot{m}}\ De^4\ D \tag{4.8}$$

$$Ra_D = 4\ \frac{Gr_q}{Re}\ \left(\frac{D}{De}\right)^4 \sim \frac{\dot{q}''}{\dot{m}}\ D^5 \tag{4.9}$$

For interior subchannels:

$$\frac{De}{D} = \frac{2\sqrt{3}}{\pi}\ \left(\frac{P}{D}\right)^2 - \frac{1}{4} \tag{4.10}$$

Therefore

$$\frac{Gr_q}{Re} \sim \frac{\dot{q}''}{\dot{m}} D^5 \left(\frac{2\sqrt{3}}{\pi} (P/D)^2 - \frac{1}{4}\right)^4 \tag{4.11}$$

or

$$\frac{Gr_q}{Re} \sim Ra_D \left(\frac{2\sqrt{3}}{\pi} (P/D)^2 - \frac{1}{4}\right)^4 \tag{4.12}$$

From equation 4.12 observe that for constant Gr_q/Re the Ra_D number decreases with increasing P/D. In addition Wang's results indicate that:

Nu increases with Ra_D (P/D = const.)

Therefore the fact that for Gr_q/Re = constant, the Nu number decreases with increasing P/D, can be attributed to the corresponding decrease of the Ra_D number, and this explains the paradox.

Currently there is no published experimental study of mixed convection heat transfer in wire-wrapped rod bundles. In this work we perform temperature measurements under the above conditions for the instrumented center rod of our 19-pin wire-wrapped rod bundle. The instrumented center rod is described in the next section. In all measurements the power distribution was uniform.

4.3 The Instrumented Rod and Wall Temperature Measurements

4.3.1 The Instrumented Rod.

The concept of the instrument rod we adopted was developed by Stephens et al. (S-9) and modified by Symolon (S-4). A similar experimental technique was also presented by Rehme (R-6). The instrumented rod design employed in this work closely parallels that in S-4. Figure 4.1 presents a detailed schematic of our instrumented rod. It consists of

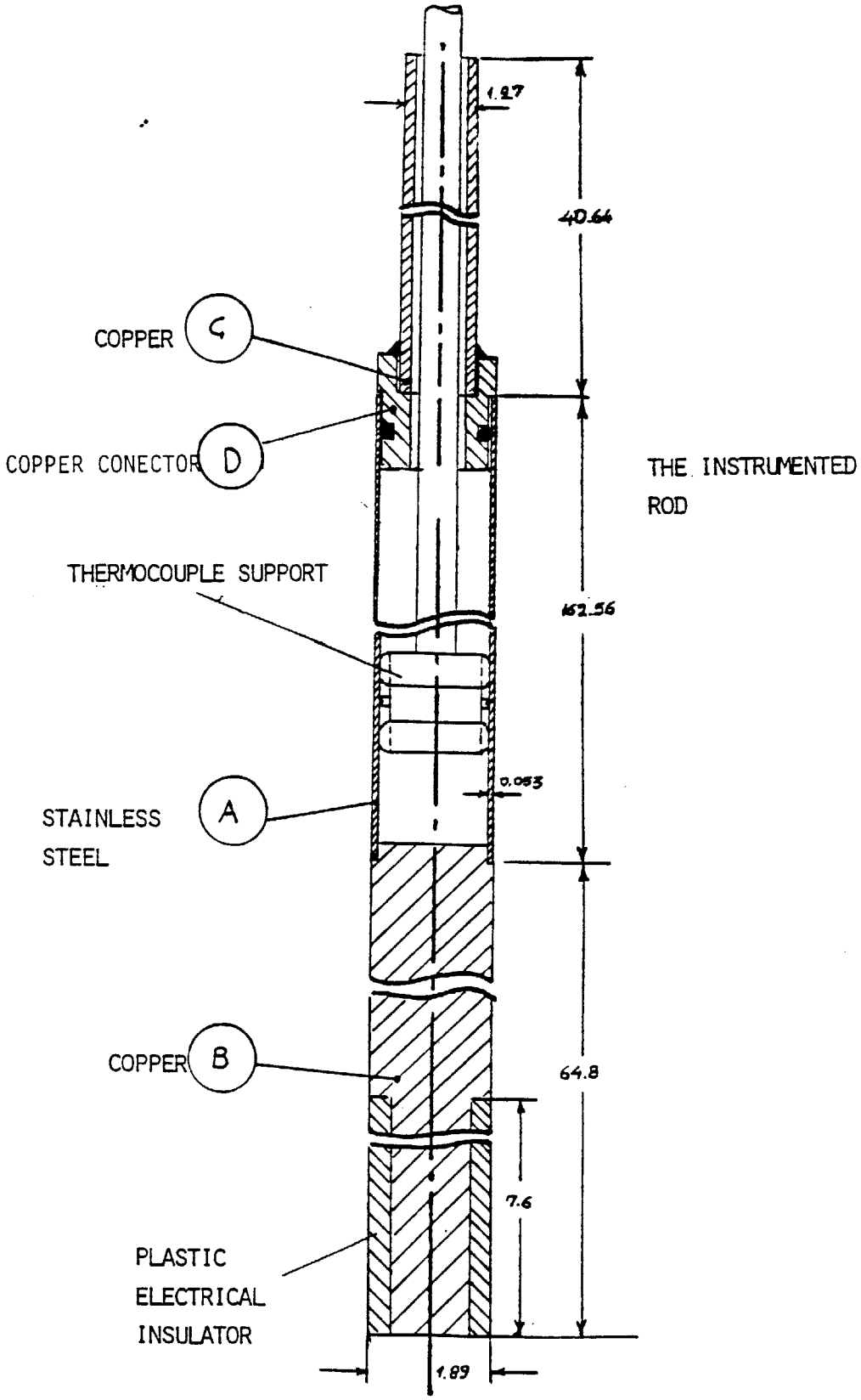

FIGURE 4.1: THE INSTRUMENTED ROD (IR)
(All numbers in cm)

mainly three pieces, a copper tube C, a stainless steel tube A and a copper rod B (see Figure 4.1). Pieces A-B and A-C are silver soldered together in order to assure both durability and good electrical contact. (Note that pieces A and C are not directly connected. Another copper piece D is silver-soldered between pieces A and C.) The stainless steel tube A has a 3/4" diameter and total length of 64" (162.56 mm) which corresponds to the heated length of the rest of the rods. This tube A is heated by high voltage alternating current going through all pieces B-A-C. Since the electric resistance of copper is much lower than that of stainless steel, practically all ohmic heat is generated in part A.

Wall temperature measurements are performed at the interior wall of stainless steel tube A using thermocouples. Figure 4.2 gives a more detailed schematic of the thermocouple support mechanism. As both Figures 4.1 and 4.2 indicate two thermocouples are placed at the top ends of two copper pins. These copper pins are pressed on the tube walls by a small spring. The thermocouples are in good thermal contact with the copper pins. The copper pins in turn are in thermal contact with the tube walls. Extensive work with the instrumented rod revealed that steady state temperature conditions on the copper pins (and therefore at the thermocouples) are established within 5 to 10 seconds. Details about the accuracy of the temperature measurement will be given in the next paragraph.

As discussed earlier, the instrumented rod is heated by an alternating current produced by a transformer with maximum power rating of 18 KVA. This transformer is directly connected to the instrumented rod using heavy duty power cables. These cables are soldered at the top of

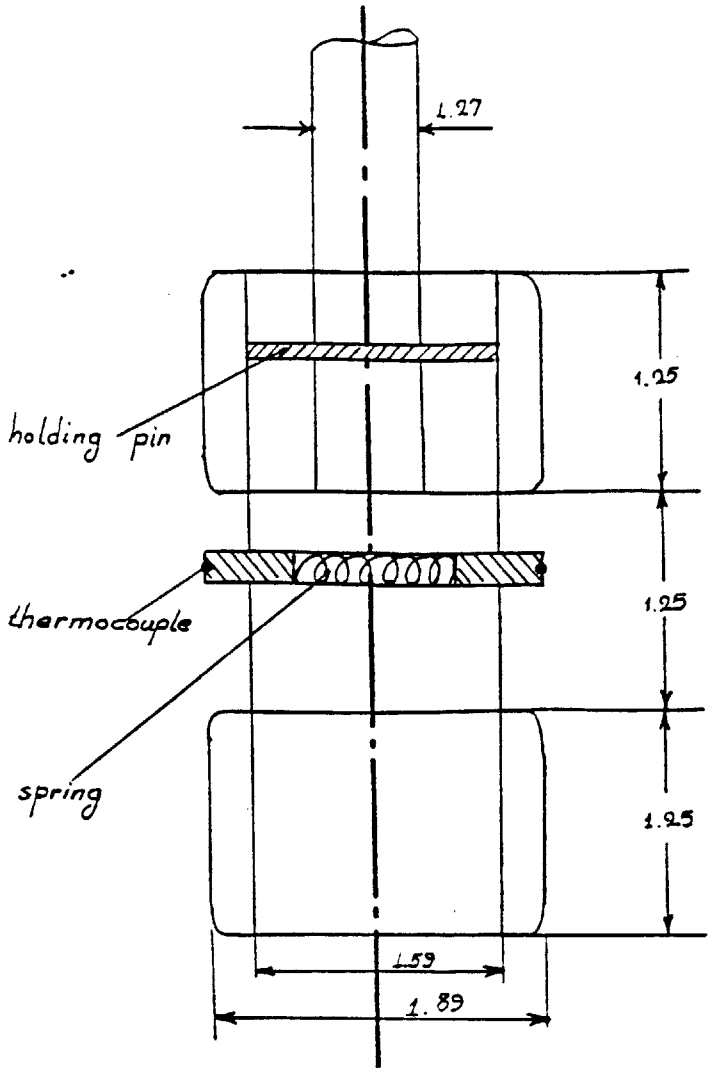

All numbers in cm.

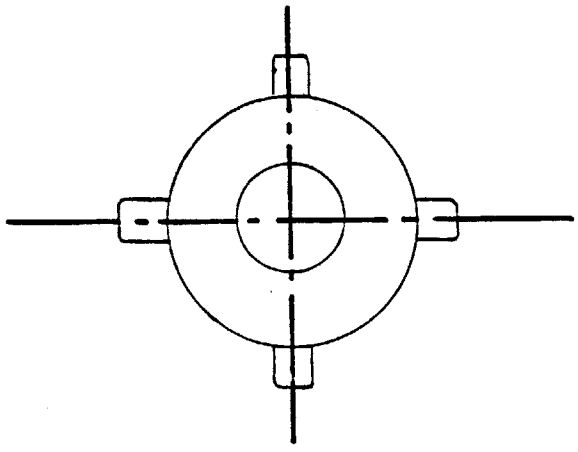

FIGURE 4.2: THE THERMOCOUPLE DRIVING MECHANISM OF THE IR.

tube C and bottom of rod B respectively.

One major problem for the introduction of the instrumented rod was the electrical insulation of the rod from all other conductors that happen to be in contact with it. Such conductors were the stainless steel wire spacers of the instrumented rod itself as well as of the neighbor rods. This problem was solved by replacing all stainless steel wire spacers of the instrumented rod and the six neighbor heater rods with non-conducting plastic wire spacers made from teflon. The teflon material was selected based on its relatively good hardness characteristics and its high temperature melting point. It is also flexible enough to allow wrapping around the rods.

In order to glue the teflon wire-spacer on the stainless steel rods a two part special epoxy adhesive made by CHEMGRIP was used. This epoxy adhesive requires that the teflon material is chemically etched before application. The etching procedure consisted of dipping the teflon into a 50% solution of napthalene flakes in a THF solvent to which metallic sodium has been added. The resulting epoxy bond can withstand temperatures well above 150 degrees C.

During the course of the heat transfer experiments some epoxy bonds failed and some dislocation of the teflon wire at the visible exit region of the bundle occured. It was necessary therefore to check if any dislocation had occurred in the middle and upper middle section of the bundle were most of the instrumented rod temperature measurements were performed.

After disassembling the bundle, it was found that despite the fact that 30 to 40 percent of the epoxy bonds in this region had failed, the teflon wire spacers remained in place due to sufficient mechanical

support provided from the tight rod bundle.

4.3.2. Wall Temperature Measurements and Error.

Before the instrumented rod (IR) was assembled into the rod bundle, it was tested in a hot bath of water at 80°C. Both thermocouples gave a reading of 80°C. The test was repeated for a hot bath of 40°C with similar results. In both cases the IR was not heated and therefore the exterior wall temperature T_{w_e} of the IR is expected to be equal to the interior wall temperature T_{w_i}. The accuracy of our thermocouple reader is ± 0.5°F.

Since the IR measures T_{w_i} only while T_{w_e} is needed for Nusselt number calculations, a simplified analysis is performed in order to estimate a conservative value for the parameter $I \equiv (T_{w_i}-T_{w_e})/(T_{w_e}-T_b)$. T_b is the bulk temperature of the surrounding fluid. Note that the temperature difference $T_{w_e}-T_b$ is used for Nusselt number calculations. In order to simplify the analysis we assume that the IR is indirectly heated from some internal heat source rather directly heated by the passing electrical current, as Figure 4.3 indicates. Then

$$(T_{w_i} - T_{w_e})_{\text{indirect}} \geq (T_{w_i} - T_{w_e})_{\text{direct}} \tag{4.13}$$

Assuming that the heat flux $\dot{q}''$ is constant through the IR wall take:

$$\dot{q}'' \simeq k_w \frac{(T_{w_i} - T_{w_e})}{\delta} = h_f (T_{w_e} - T_b) \tag{4.14}$$

where $k_w \simeq 46.0$ W/m°K (steel conductivity at 50°C)

$k_f = 0.63$ W/m°K (water conductivity at 40°C)

$\delta = 0.53$ mm (IR wall thickness)

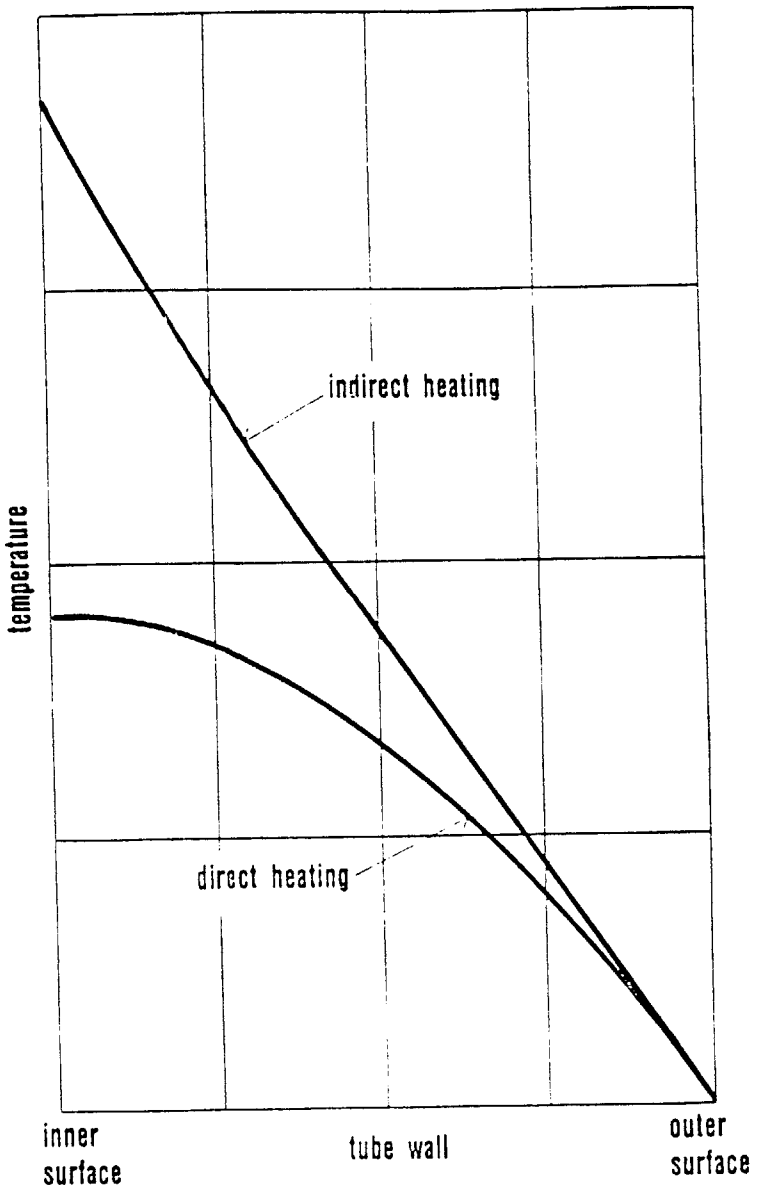

FIGURE 4.3: TEMPERATURE DISTRIBUTION IN THE HEATED ROD WALL.
(Taken from reference R-6)

and h_f is the convective heat transfer coefficient.

From equation (4.14) obtain I as:

$$I \equiv \frac{T_{w_i} - T_{w_e}}{T_{w_e} - T_b} \simeq \frac{h_f\ De}{k_f} \frac{k_f}{k_w} \frac{\delta}{De}$$

or
$$I \simeq Nu \frac{k_f}{k_w} \frac{\delta}{De} \qquad (4.15)$$

where De(= 0.01085 m) is the hydraulic diameter. As our experimental results indicate the maximum value of the Nusselt number Nu for the range considered was around 19. For Nu_{max} equal to 20, equation 4.15 gives I equal to 0.014. In other words:

$$(T_{w_i} - T_b) \simeq 1.014\ (T_{w_e} - T_b) \qquad (4.16)$$

From equation 4.16 it is concluded that the IR can be used to estimate $(T_{w_e}-T_b)$ with less than 1.5% error.

4.4 Results and Discussion

4.4.1. Instrumented Rod Temperature Measurements.

Using the instrumented rod (IR), wall temperature profiles were measured along the axial and peripheral directions. Measurements were performed at the middle and upper part of the heated zone. As discussed in Chapter 3, the flow is expected to be "fully developed" at this region (For wire wrapped rod bundles the term "fully developed" is used here to indicate periodically similar flow conditions.)

Figure 4.4 gives some typical temperature profiles along the periphery of the IR at a given axial level. The Gr_q/Re parameter is equal to 1.3×10^3. The position of the wire-spacer for the given axial

level is indicated by the black circles. The temperature profile, plotted in a polar diagram, includes data from both IR thermcouples indicated by circles and triangles respectively. Note that the temperature peaks at the periphery region where the wire-spacer is located. Another secondary peak is recorded exactly at the opposite wall region where the wire-spacer that belongs to the neighbor rod is located. Figure 4.5 gives some typical temperature distribution data along the axial direction by both IR thermocouples. The thermocouples are kept in a constant angular position while they are moving along the axial direction. The positions 1 through 7 in Figure 4.5 mark various axial levels which correspond to the wire-spacer positions at the right hand side of Figure 4.5. The same qualitative conclusions can be drawn here as in the case of Figure 4.4. The temperature profiles peak at the vicinity of the wire-spacer location.

For data reduction purposes, the temperature data of all runs were plotted in the form of Figure 4.6a. The vertical bars in this Figure indicate the thermocouple reader resolution capability which was 1°F. Figure 4.6b presents similar data for a high Gr_q/Re case. In all cases the temperature profile peaked at the wire-spacer region.

From our data in the form of Figures 4.6 (a) and (b) the following information was extracted:

(a) The average wall temperature $\overline{T}_w$

(b) The maximum temperature variation along the circumference of the Instrumented Rod: $\Delta T_w^{max} = T_w^{max} - T_w^{min}$.

This information was subsequently used for quantitative analysis as discussed next.

4.4.2. Nusselt Number Estimation and Error

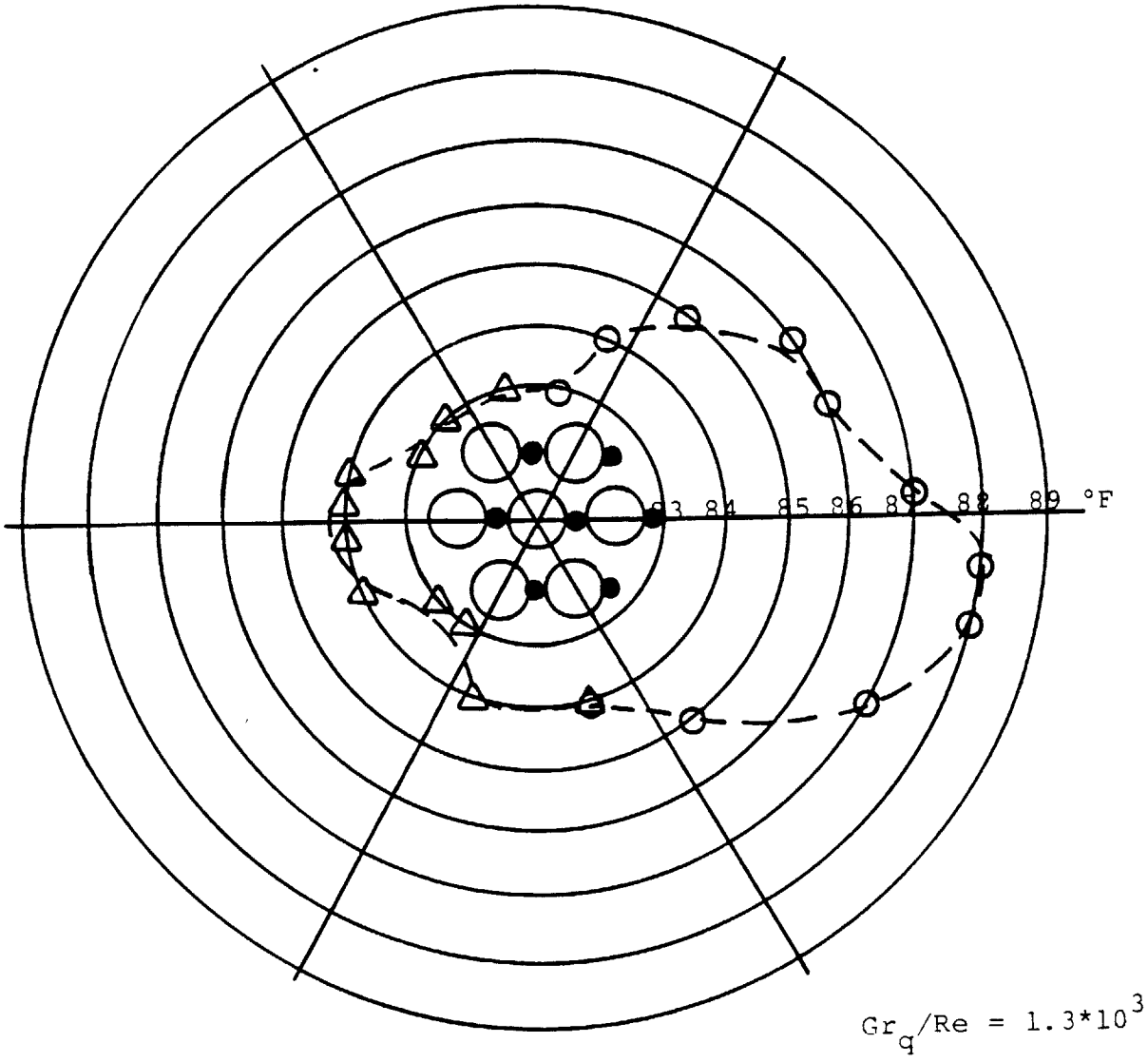

FIGURE 4.4: POLAR DIAGRAM OF TEMPERATURE DISTRIBUTION ALONG THE CIRCUMFERENCE OF THE INSTRUMENTED ROD WALL.

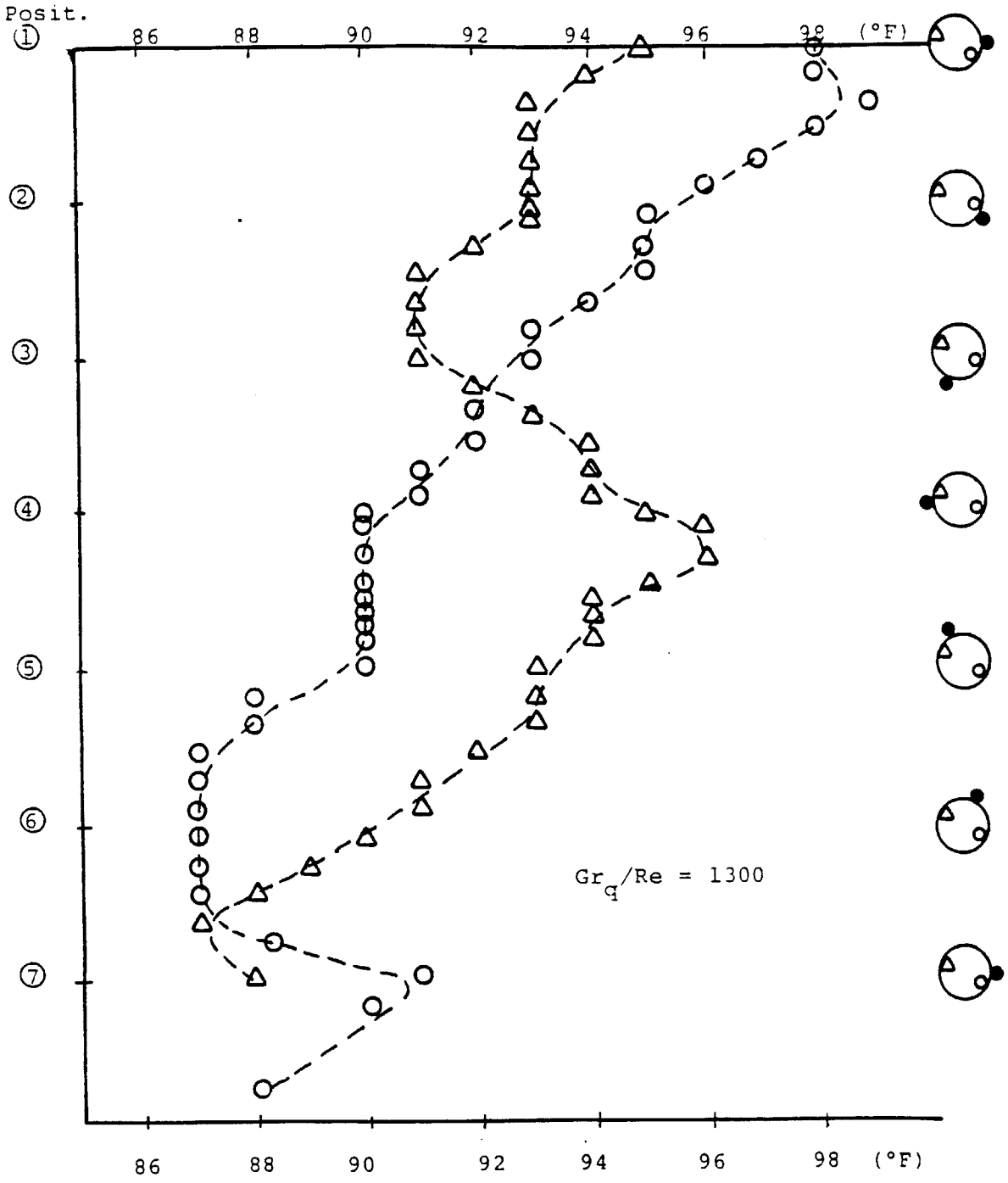

FIGURE 4.5: AXIAL TEMPERATURE DISTRIBUTION GIVEN BY THE INSTRUMENTED ROD AT TWO DISTINCT ANGULAR POSITIONS.

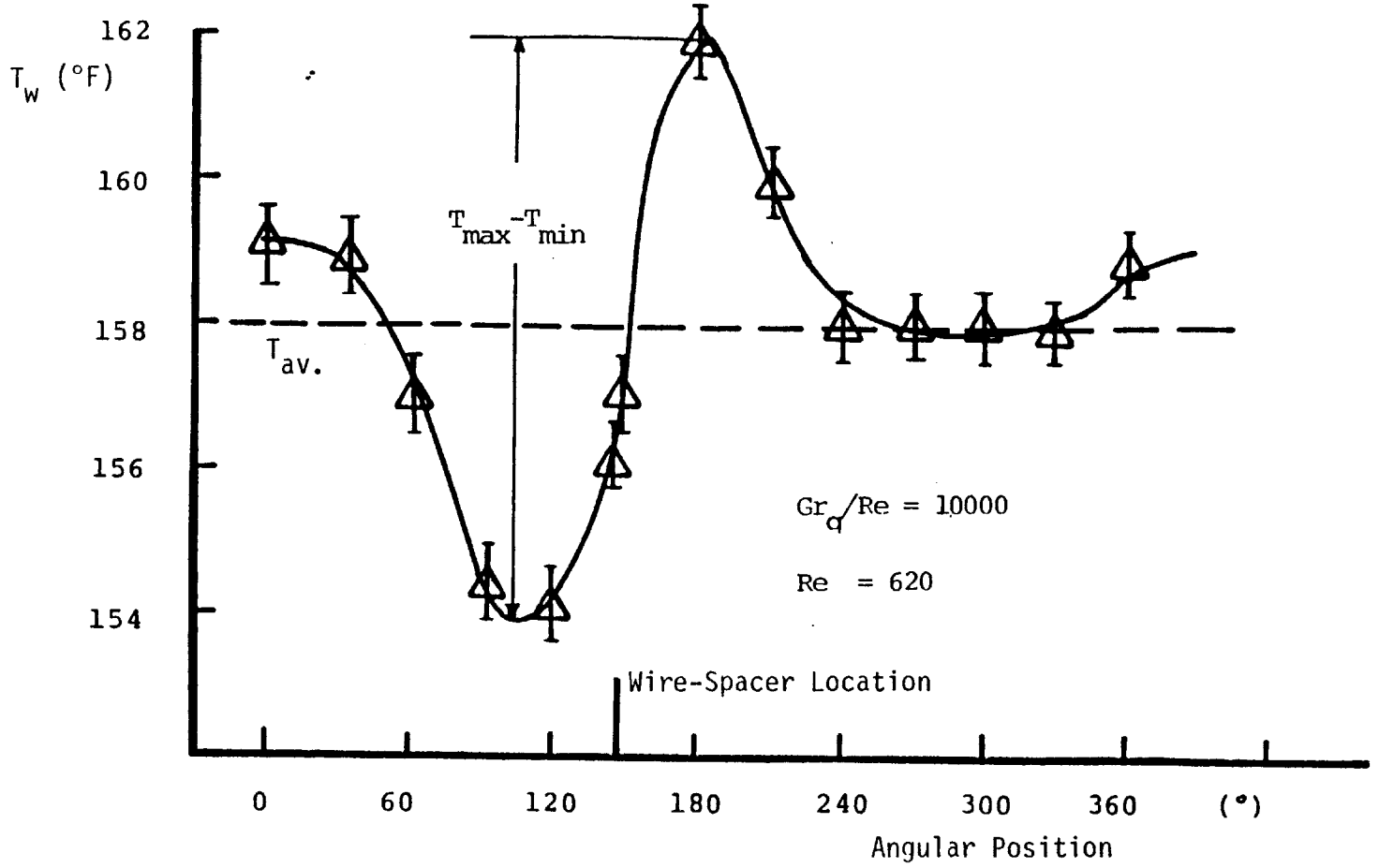

FIGURE 4.6(a) : TEMPERATURE DISTRIBUTION ALONG THE CIRCUMFERENCE OF THE INSTRUMENTED ROD.

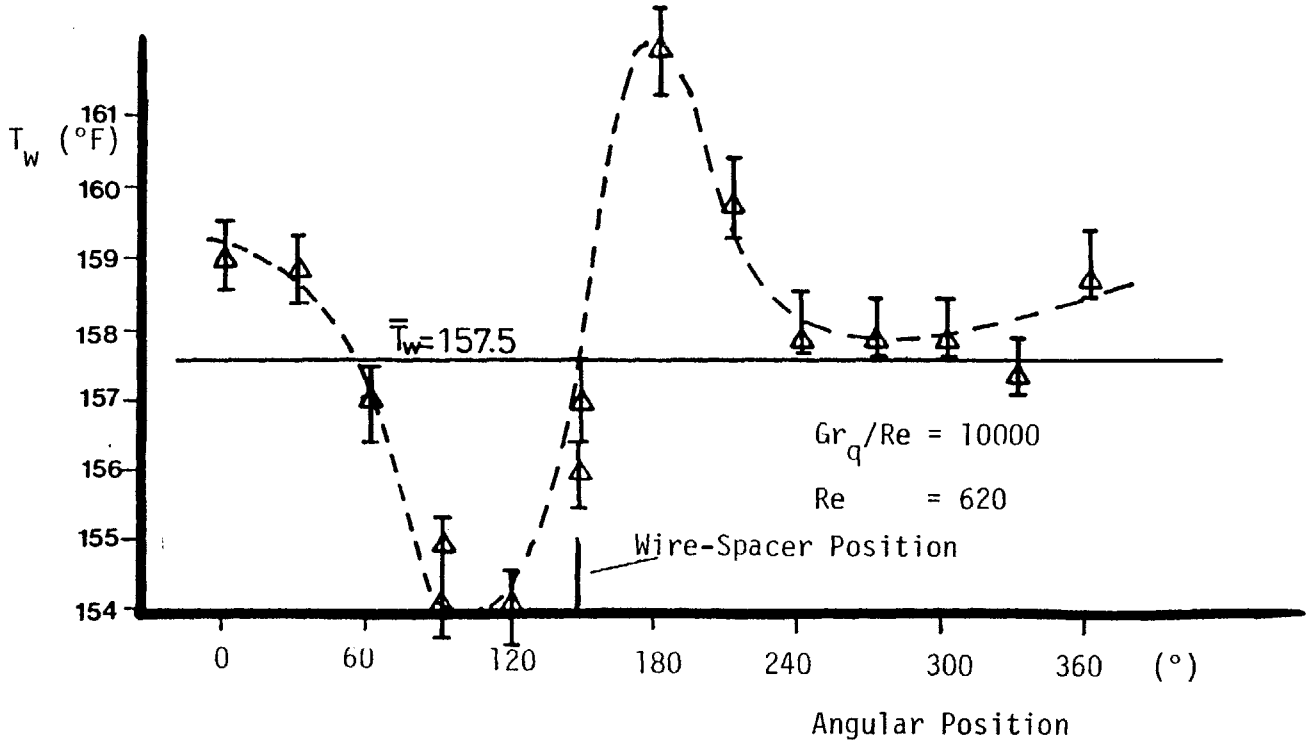

FGURE 4.6(b) : TEMPERATURE DISTRIBUTION ALONG THE CIRCUMFERENCE OF THE INSTRUMENTED ROD.

Based on the above temperature data the circumferentially averaged Nusselt number was estimated as follows:

$$Nu = \frac{\dot{q}''_{IR}\ De}{k_f\ \Delta T} \tag{4.17}$$

where $\dot{q}''_{IR}$: Instrumented Rod Heat Flux

De : hydraulic diameter of the bundle

$\Delta T = \overline{T}_w(z) - \overline{T}_b(z)$

and k_f : fluid thermal conductivity evaluated at $\overline{T}_b(z)$.

From equation 4.17 we express the Nusselt number estimation error $e_{Nu} \equiv \Delta Nu/Nu$ (where ΔNu is the uncertainty) which can be estimated as follows:

$$e_{Nu} \simeq e_{\dot{q}''_{IR}} + e_{\Delta T} \tag{4.18}$$

The IR heat flux was estimated as follows:

$$\dot{q}''_{IR} = \frac{c\ \dot{P}_N}{\pi\ DL} = \frac{\dot{P}_c}{\pi\ DL} \tag{4.19}$$

where D is the IR diameter and L is the heated length. $\dot{P}_N$ is the nominal power supplied to the IR. This quantity was measured using a voltmeter and an amperometer. However due to power losses at the power cables connected with the IR, a loss coefficient c was introduced in order to account for these losses. The loss coefficient was experimentally estimated by measuring total temperature rise due to IR heating only. The rest of the rods were kept at zero power. The c coefficient was estimated as follows:

$$c = \frac{\dot{P}_c}{\dot{P}_N} \tag{4.20}$$

where P_c was calculated from thermal balance considerations. The parameter c is plotted in Figure 4.7 as a function of $\dot{P}_N$. The estimation error for $\dot{P}_c$ is obtained as:

$$e_{\dot{P}_c} = e_{\dot{P}_N} + e_c \tag{4.21}$$

where $e_{\dot{P}_N} \simeq 10\%$: Readout error.

$e_c \simeq 2.0\%$: Data scatter error in Figure 4.7

Note that the e_c is not independant of $e_{\dot{P}_N}$. Therefore we conclude that $e_{\dot{P}_c} \simeq 10 - 12\% \sim e_{\dot{q}''_{IR}}$

Next estimate $e_{\Delta T}$ which, based on the definition of ΔT equals

$$e_{\Delta T} \equiv \frac{\Delta T}{\overline{T}} = \frac{\Delta \overline{T}_w + \Delta \overline{T}_b}{\overline{T}_w - \overline{T}_b}$$

In our work $\overline{T}_b(z)$ is the average bulk fluid temperature at elevation z, estimated by linear interpolation:

$$\overline{T}_b(z) = T_{in} + (T_{out} - T_{in}) \frac{z}{L} \tag{4.22}$$

The $\overline{T}_b$ temperature estimation error is of the order of 0.2°C. The average temperature $\overline{T}_w(z)$ is calculated based on the IR data, as explained in the previous paragraph:

$$\overline{T}_w = \sum_{i=1}^{12} T_{w,i} \tag{4.23}$$

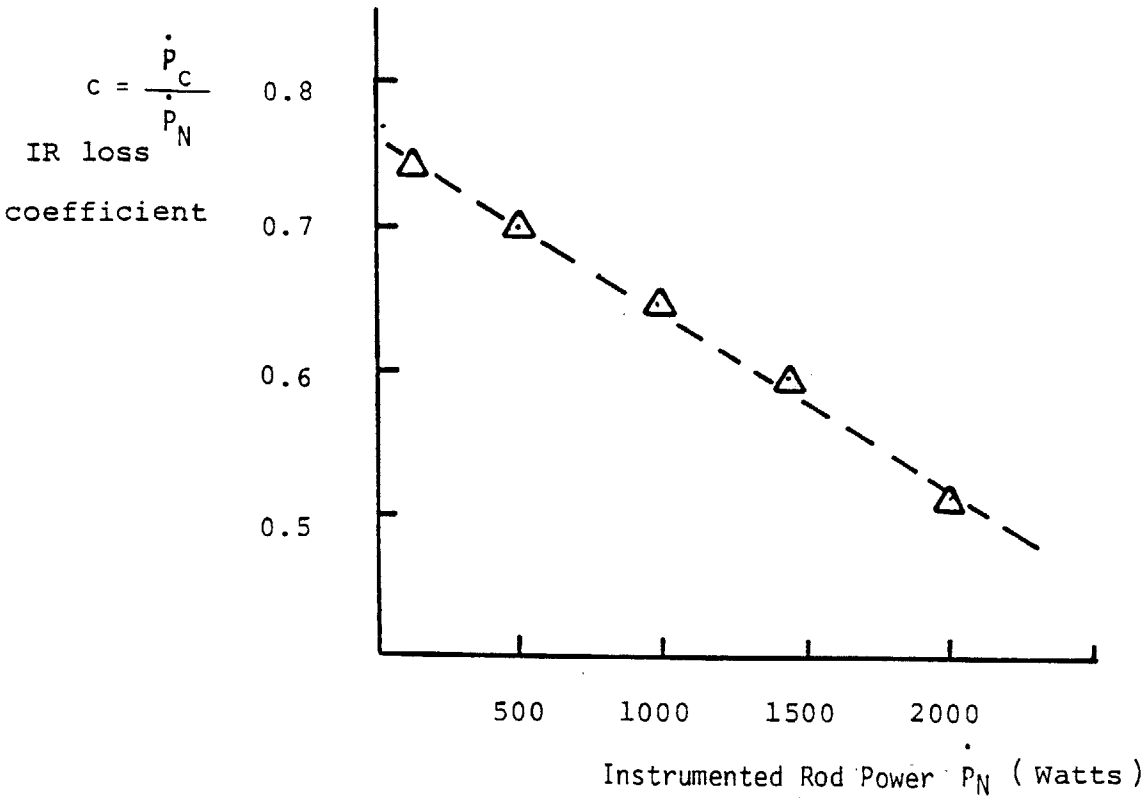

FIGURE 4.7: INSTRUMENTED ROD POWER LOSS COEFFICIENT AT VARIOUS IR POWER LEVELS.

Since $T_{w,i} \sim \overline{T}_w$ and the resolution error for each IR measurement $E_{T_{w,i}} \simeq$ 1°F then $\Delta\overline{T}_w \leq 0.1°F$. One additional source of uncertainty here is the fact that all interior subchannels do not experience the same heat input due to uncertainties in dialing the heat input per heater rod. This "additional nonuniformity" in the subchannel temperatures will directly affect $\overline{T}_w$. However due to the averaging process the total error $\Delta\overline{T}_w$ is small, less than 0.4°F. Finally the total error for ΔT estimation is expected to be less than 0.4°C. For a typical mixed convection run, $\overline{T}_w - \overline{T}_b$ was around 5.5°C or higher. Therefore

$$e_{\Delta T} \leq 7.5\% \ .$$

In summary, refering to equation 4.18, the maximum error for the Nusselt number estimation e_{Nu} is less than 12.0 + 7.5 = 19.5%. This error increases for the laminar forced convection case because ΔT is smaller approximately 1.5 to 3.0°C.

Figure 4.8 presents our Nusselt number data (open triangles), as estimated from equation 4.17, together with Halman's analytic solution for fully developed flows in circular tubes (H-1) and Wang's et al. solution for bare rod bundles with P/D = 1.25. (W-8). The Gr_q/Re parameter is estimated in the same way as in Chapter 3. Based on our data we suggest the following empirical correlation;

$$Nu = 3.11 \ (Gr_q/Re)^{0.178} \qquad (4.24)$$

for $10^3 \leq \frac{1}{4} Gr_q/Re < 2.0 \times 10^4$ and $330 < Re < 670$

Using the Figure 4.8 the equivalent Nusselt number under forced convection Nu_o $(Gr_q \to 0)$ is estimated equal to 8.0. Then equation 4.24 can be written

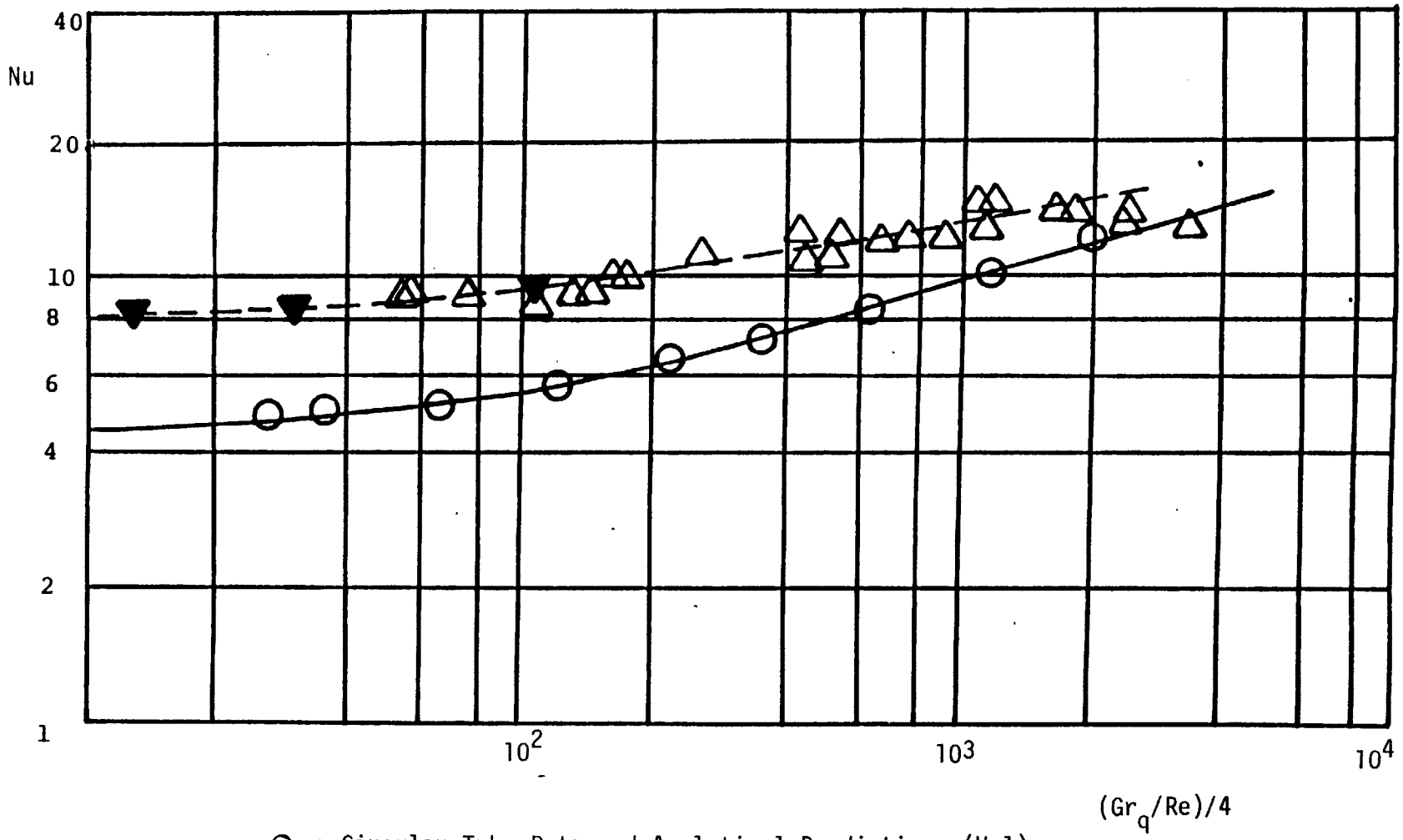

FIGURE 4.8: MIXED CONVECTION NUSSELT NUMBERS FOR THE MIT 19-PIN WIRE-WRAPPED ROD BUNDLE.

as follows:

$$Nu/Nu_o = 0.39\ (Gr_q/Re)^{0.178} \tag{4.25}$$

The corresponding Nusselt number for the circular tube results is given by the empirical formula of Halman:

$$Nu = 1.40\ (Gr_q/Re)^{0.28} \tag{4.26}$$

where $Gr_q/Re > 100$

Refering to Figure 4.8 our wire-wrapped rod bundle data are in good agreement with the bare rod analytic solution for the Gr_q/Re region that overlap. However when compared with the circular tube results, the wire-wrapped bundle data exhibit the following differences:

(a) The magnitude of the Nu number is higher for the wire-wrap data and the bare rod analytic prediction.

(b) The slope of the Nu versus Gr_q/Re curve for the wire-wrap curve is smaller than the slope of the circular tube data curve.

(c) The wire-wrap Nu data level off or even decrease for $Gr_q/Re > 10^3$. Note that the corresponding Re number for this case ranged between 550 and 630. No such behavior is observed in the cirucular tube data.

Observation (a) above is due to the geometrical differences of the duct cross-section. For the slope differences however (observation (b) above) it is not clear whether they are due to rod bundle geometry in general or due to the presence of the wire-spacer in particular. In order to clarify this point, the bare rod analytic solution should be extended to higher Gr_q/Re numbers. Finally the "leveling off" phenomenon, discussed in observation (c) above can be attributed to turbulence effects as

explained below.

Extensive work in turbulent aiding flow mixed convection revealed that the heat transfer coefficient may decrease with Gr_q number increasing, due to flow relaminarization phenomena. (For an extensive literature review see S-4). Here the turbulence generation at the wall region is drastically reduced due to development of inflection (zero gradient) points of the velocity profile at this region. This renders the Nu number smaller since the turbulent heat transport mechanism is decreased. Most of our data were taken under turbulent flow conditions for $\frac{1}{4} Gr_q/Re > 10^3$ and $550 < Re < 630$. In contrast, most of Halman's circular tube data were in laminar flow for the same Gr_q/Re range (H-1). It is appropriate therefore to assume that there is a geometrical effect on the flow stability and on the onset of transition to turbulence which in turn directly affects the heat transfer characteristics. It is recommended that stability maps be constructed for both bare and wire-wrapped bundles to define the range of the Gr_q and Re parameters under which different heat transfer characteristics are to be expected. Such a stability map was constructed for a 2 x 2 square array of rods under aiding mixed convection flow conditions (E-1).

4.4.3. Nusselt Number Bulk Temperature Correction

In the Nu number definition, equation 4.17, the temperature difference $\Delta T = \overline{T}_w - \overline{T}_b$ was based on the bundle averaged fluid bulk temperature $\overline{T}_b$. In some practical applications of Nu number correlations (subchannel analysis and porous body code development) another ΔT definition is required namely:

$$\Delta T_{\ell} = \overline{T}_{w}(z) - \overline{T}_{\ell}(z) \tag{4.27}$$

where $\overline{T}_{\ell}$ indicates the average local fluid temperature at the region around the heated rod on hand. In the case of our experiment, $\overline{T}_{\ell}$ is the average temperature of the water at the six interior subchannels surrounding the instrumented rod. Note that:

$$\overline{T}_{\ell}(z) \geq \overline{T}_{b}(z) \tag{4.28}$$

since for uniform power conditions the power-to-flow ratio is higher for the central region of the rod-bundle. Therefore:

$$Nu_{\ell} \geq Nu \tag{4.29}$$

where Nu_{ℓ} is based on ΔT equal to $(\overline{T}_{w} - \overline{T}_{\ell})$.

The measurement of $\overline{T}_{\ell}$ is a tedious experimental process, requiring the use of many thermocouples for different axial levels. In order to avoid these experimental complications, we did not measure $\overline{T}_{\ell}$ in this this work. In what follows we propose an indirect way to measure $\overline{T}_{\ell}$ and therefore to estimate Nu_{ℓ}. We assume that the ratio:

$$R = \frac{\overline{T}_{\ell} - \overline{T}_{b}}{\overline{T}_{w} - \overline{T}_{b}} \tag{4.30}$$

remains constant for all axial positions in the "fully developed" region. This assumption is a direct extension of the definition of "thermally fully developed flows" in ducts to the wire-wrap bundle case. This assumption, while adequate for practial purposes, is not theoretically true

since $\overline{T}_\ell$ should exhibit a weak periodicity with period of 30° angular rotation of the wire-spacer. The ratio R can be experimentally determined by measuring at the exit plane of the rod bundle the temperatures $\overline{T}_\ell$ and $\overline{T}_b$ ($\equiv T_{out}$) and by estimating $\overline{T}_w - \overline{T}_b$ using equation 4.17:

$$R = \frac{\overline{T}_\ell - \overline{T}_b}{\dot{q}''_{IR}\ De/k_f}\ Nu \tag{4.31}$$

Using equation 4.31, Nu_ℓ can be estimated as:

$$Nu_\ell = Nu \cdot \frac{\overline{T}_w - \overline{T}_b}{\overline{T}_w - \overline{T}_\ell} = Nu\ \left(\frac{1}{1 - R}\right) \tag{4.32}$$

Additional experimental work is needed to estimate the ratio R as a function of Gr_q/Re. It requires a consistent experimental approach to measure $\overline{T}_\ell$ and $\overline{T}_b$ by measuring all exit subchannel temperatures and calculating $\overline{T}_\ell$ and $\overline{T}_b$ as arithmetic averages of the corresponding subchanels.

4.4.4. Maximum Rod Wall Temperature Variations

From the instrumented rod temperature data along the periphery of its surface the maxium wall temperature difference $\Delta T_{w,max}$ can be estimated. As explained for Figure 4.5, the maximum wall temperature occurs at the vicinity of the wire spacer whereas the minimum occurs at ± 90° degrees from the location of the maximum temperature.

In Figure 4.9 the dimensionless temperature difference:

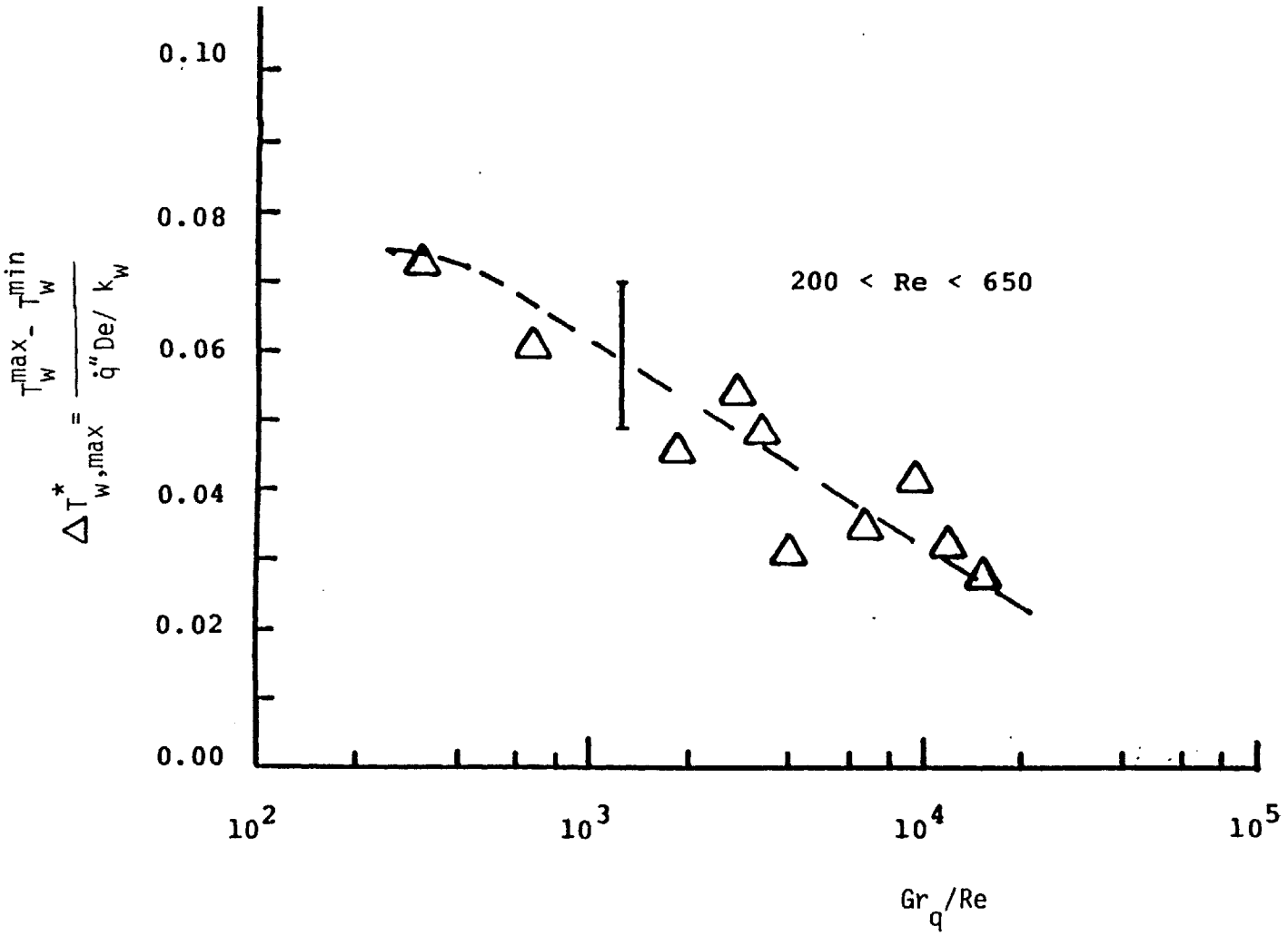

FIGURE 4.9: MAXIMUM CIRCUMFERENTIAL WALL TEMPERATURE VARIATION FOR LOW REYNOLDS MIXED CONVECTION FLOWS IN THE MIT 19-PIN WIRE-WRAPPED ROD BUNDLE.

$$\Delta T^*_{w,max} = \frac{T_w^{max} - T_w^{min}}{\dot{q}'' \, De/k_f} \tag{4.33}$$

is plotted against the Gr_q/Re parameter. The large scatter of the data is due to the fact that in the difference operation in equation 4.33, the uncertainties for each temperature measurement are summed up resulting in a relatively large error of 2.0°F. Note that the corresponding error for $\bar{T}_w$ estimation was less than 0.4°F.

As expected the $\Delta T^*_{w,max}$ parameter decreases when the Gr_q/Re parameter is increased. As it will be discussed in the next chapter the subchannel fluid temperature profile tends to get smoother as the buoyancy effects become more pronounced. Consequently the temperature gradients in the solid surfaces decrease accordingly. This observation is important for the materials analyst since it states that in the wire-wrapped rod bundles the dimensionless temperature difference $\Delta T^*_{w,max}$ attains its maximum value under forced convection conditons.

Based on the data of Figure 4.9, a conservative estimate for the forced convection limit of $\Delta T^*_{w,max}$ is 0.1. Note that IR temperature measurements under in water laminar forced convection conditions are extremely challenging to due to

(a) small temperature gradients (to be measured) and relatively large resolution error (± 0.5°F)

(b) thermal stability problems. Even 0.5°F change in the inlet temperature may cause severe error.

Recall that all data were taken under uniform power distribution. It is expected that power skew conditions will increase the values of $\Delta T^*_{w,max}$.

It is recommended therefore that experiments be repeated under power skew conditions and with improved temperature instrumentation (with resolution less than 0.2°F).

CHAPTER 5

SUBCHANNEL VELOCITY AND TEMPERATURE DATA

5.1 Introduction

Subchannel velocity and temperature data are needed for validation/calibration studies of numerical programs that perform thermal and hydraulic analysis of wire-wrapped rod bundles. In the mixed convection regime, subchannel temperature data for sodium flow in a 61-pin, blanket geometry, rod bundle under power skew conditions were presented in E-5 and M-2. In this work we obtain detailed, subchannel temperature data for water flows at the exit region of our 19-pin wire-wrapped bundle under mixed convection and power skew conditions. In all our runs, the Reynold's number was kept below 1250.

The use of subchannel velocity data for code validation allows calibration and testing of the hydrodynamic constitutive models built into the code. Currently there are no subchannel velocity data for flows in rod bundles under mixed convection conditions. Additionally, there is only one study for laminar, isothermal flows in wire-wrapped bundles (C-4). In C-4 a Laser Doppler Anemometer was used to measure detailed axial and transverse velocity profiles in the edge subchannels of a wire-wrapped LMFBR fuel assembly. No interior subchannel velocity profiles were measured. In this work we perform subchannel axial velocity measurements, in all subchannels at the exit region of our wire-wrapped rod bundle, using a Hot-Film Anemometry technique. (HFA). All flows were isothermal and the Reynold's number was less than 350. For reasons that

will be discussed later, no mixed convection velocity data were obtained in this work. However, a calibration methodology is outlined in order to allow such measurements.

Our velocity and temperature data are used to validate ASFREMIT: a new version of ASFRE numerical program which performs thermal and hydraulic analysis of wire-wrapped rod bundles. The new hydrodynamic models of ASFREMIT are given in Chapter 7 and the code itself and the validation studies are presented in Chapter 8. Next we outline the calibration procedures for the Hot-Film Anemometry system used in this work. The velocity and temperature data are then presented and the most important characteristics of these data are discussed.

5.2 Instrumentation and Measurements

5.2.1 The Hot-Film Probe Anemometry System.

The Hot-Film Anemometry Technique was selected for axial velocity measurements of water flow in all interior, edge and corner subchannels. This technique made full advantage of the fact that the upper plenum was made free of piecing rods and open, in order to allow instrumentation to be inserted from its top and access the exit region of rod bundle. Several other options were considered and rejected. Laser Doppler Velocimetry cannot be used for velocity measurements in triangular rod arrays unless the whole bundle (including the wrapper tube and the heated rods) is optically transparent. This of course cannot be accomplished in the case of heated rod bundle experiments. Furthermore, flow visualization techniques were also excluded due to the fact that they allow velocity measurements at the peripheral subchannels only.

A custom built TSI Hot-Film Anemometry probe was employed. A schematic representation of this probe is given in Figure 5.1 This probe is a slight modification of the TSI 1264W miniature cone probe with quartz coated Hot-Film. The reason for selecting a miniature size conical probe was that the small diameter of the probe support cylindrical tube (1.5 mm diameter, as shown in Figure 5.1) has a minimum impact of the velocity field. Note that even at the narrow gap region, the average gap width of 4.7 mm is three times larger in size than the miniature probe diameter.

A TSI Model 1050 general purpose Anemometer, a TSI Model 1051-2 Monitor and Power Supply module and a TSI Model 1040 Temperature and switching module completed our HFA system. The 1050 model bridge was used in a constant temperature mode for velocity measurements whereas the model 1040 bridge was operated in a constant current mode for temperature measurements. The Model 1040 provided also a mechanical switch to select one of the two bridges. In summary, model 1040 allows simultaneous velocity and temperature measurements using the same probe. The knowledge of temperature is required to calibrate the velocity measurement since the later is a strong function of temperature also (see paragraph 5.2.3). However one major obstacle in using Model 1040 is the fact that the resistance of the electrical contact of its switch may change substantially each time a new bridge is selected. In practice the error in velocity estimation due to this variability of the electrical contact was as high as ± 50%. As will be discussed later, that was the main reason that prohibited us from extending our velocity measurements from isothermal to mixed convection flows.

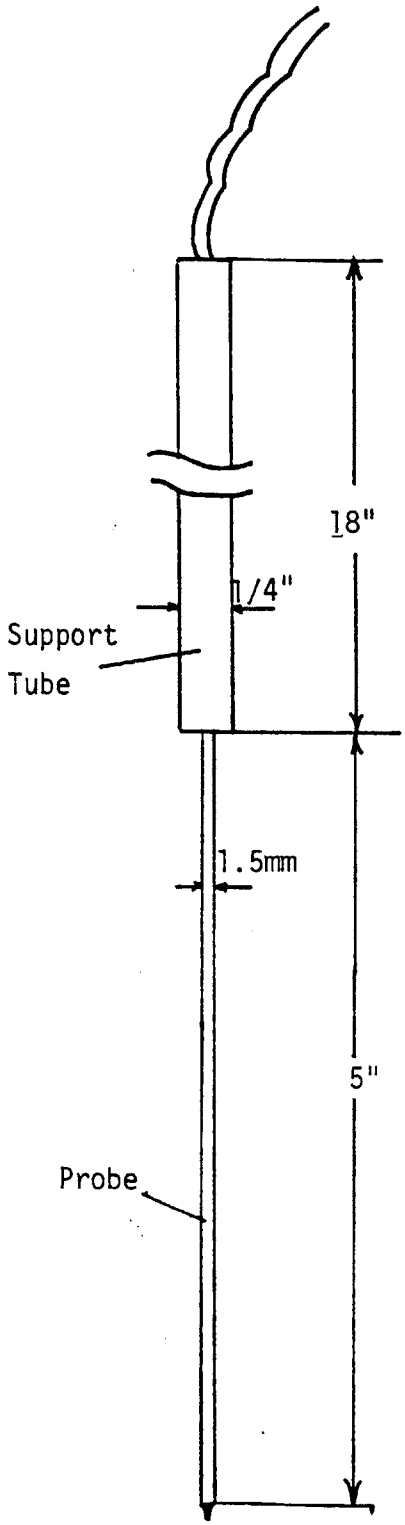

FIGURE 5.1: THE HOT-FILM ANEMOMETER CONICAL PROBE AND ITS SUPPORT TUBE.

5.2.2 Probe Driving Mechanism and Geometrical Considerations

Both velocity and temperature measurements were performed at the exit plane of the 19-pin wire-wrapped bundle. Figure 5.2 gives a schematic top view of the exit region of the rod bundle. The location of the wire-spacer at the exit plane was approximately at -10° to -15° from the reference position. Note that the geometrical conditions portrayed by Figure 5.2 are ideally symmetric. The real gap dimensions at the exit plane are indicated in Figure 5.3. The number given at each gap in Figure 5.3, multiplied by 1/64" gives the gap size in inches, as measured at the exit plane. Note that the gap sizes varied substantially, with an average size of 12/64" and maximum deviation of ± 20%.

Figure 5.3 also indicates the locations within each subchannel at which velocity and temperature measurements were performed. The final subchannel velocity or temperature was calculated as an arithmetic average of these measurements. Approximately 9 to 10 locations for each interior subchannel were sampled. For edge subchannels, 13 to 15 locations were sampled, depending on whether the wire-spacer was present or not.

The HFA probe was operated in a vertical position with the tip of the probe in a downward position at the bundle exit plane. In order to move the probe from location to location within each subchannel and in all 48 subchannels in a quick, reliable and accurate way, a probe driving mechanism was designed and built. A schematic representation a top view of this mechanism is given in Figure 5.4. The driving mechanism consists of the following parts: (see Figure 5.4) (a) Support Cube (b) Driving Rods (c) Rotating Disk, and (d) Driving Disk. All pieces were made from aluminum except the Driver Rods that were made from stainless steel. The

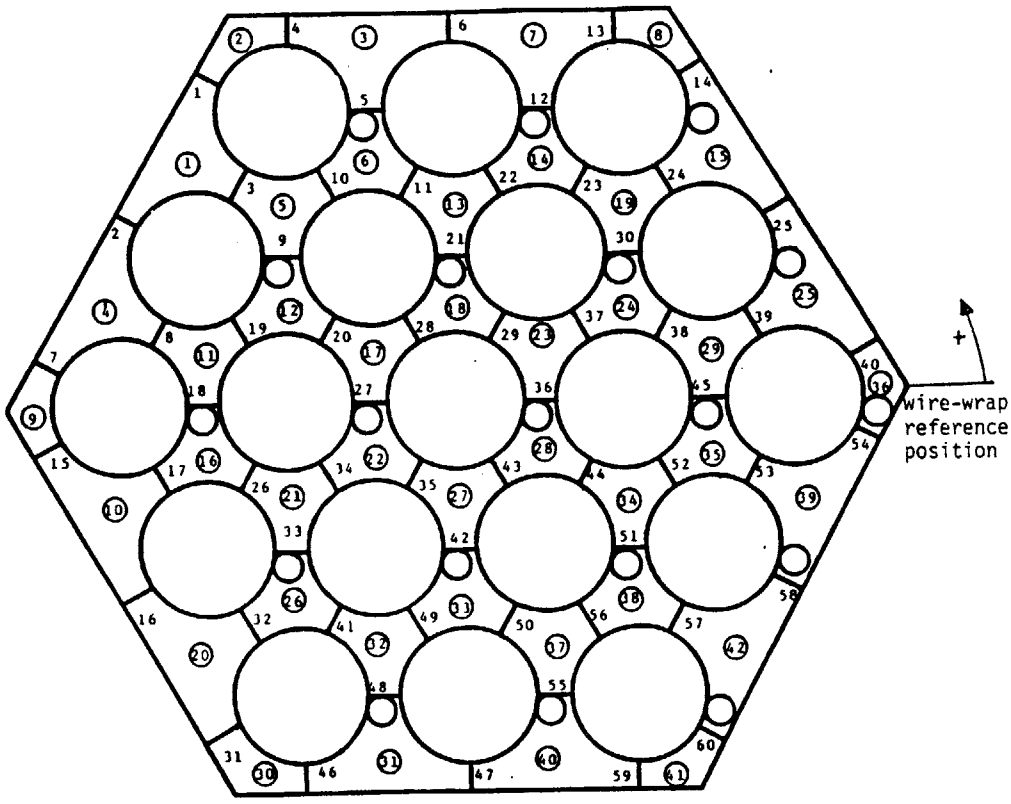

FIGURE 5.2: TOP VIEW OF THE MIT WIRE-WRAPPED BUNDLE. NUMBERS IN CIRCLES INDICATE SUBCHANNEL NUMBER AND THE REST INDICATE GAP NUMBER.

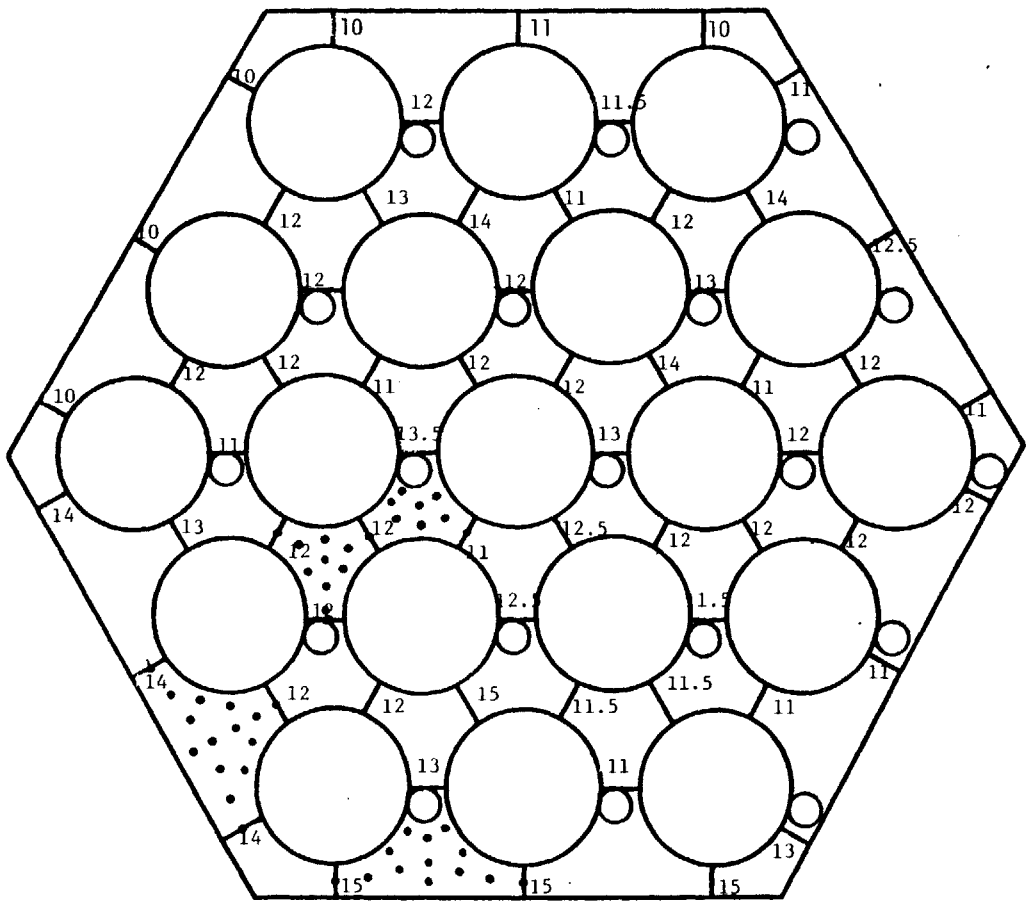

FIGURE 5.3: GAP SIZE (IN MULTIPLES OF 1/64") AT THE EXIT PLANE OF THE MIT WIRE-WRAPPED BUNDLE. THE BLACK DOTS INDICATE TYPICAL LOCATIONS WHERE VELOCITY OR TEMPERATURE MEASUREMENTS WERE PERFORMED.

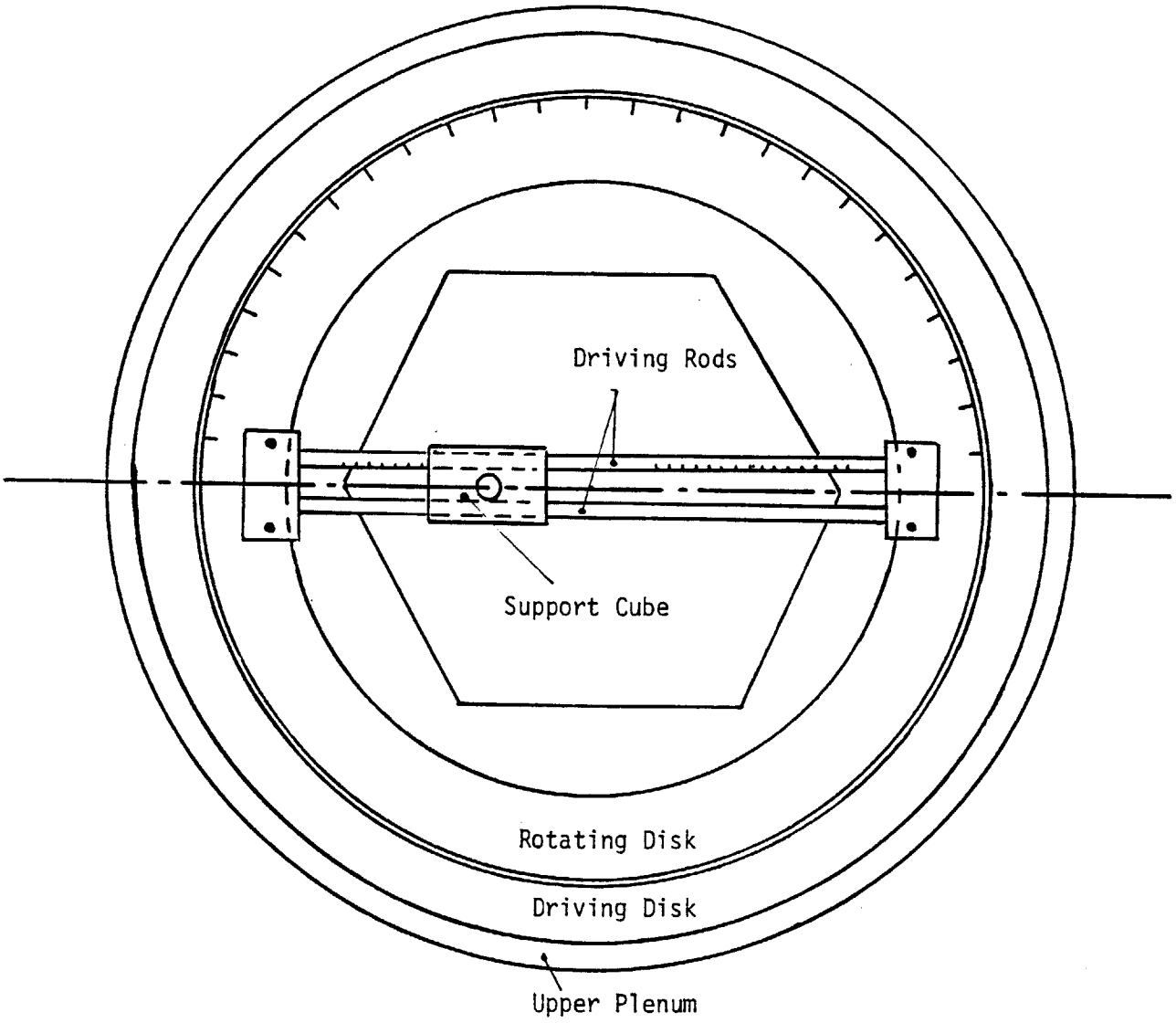

FIGURE 5.4: THE HOT-FILM ANEMOMETRY PROBE DRIVING MECHANISM.

Support Cube holds the HFA probe which fits in its central hole through the use of set screws. The probe may move up and down in order to adjust the final vertical position of the tip of the probe along the z-axis. The Cube may also slide along the two Driving Rods. These rods are marked so that any Cube position along the Rods (radial direction) can be easily reproduced. The Driving Rods are fixed on the Rotating Disk of Figure 5.4. This disk in turn may assume any angular position (θ-direction) by simply rotating it within the Driving Disk. The Driving Disk is firmly supported on the upper plenum walls and it is connected with the Rotating Disk through a male-female type of connection. The Rotating Disk is also marked so that any angular position θ may be easily reproduced.

5.2.3 Hot-Film Anemometry Calibration

In order to calibrate the HFA probe for velocities ranging from 0 to 5.0 cm/see in water flows, a special calibration apparatus was designed and built, as shown in Figure 5.5. Following Dring and Gebhard (D-3), the probe was fixed in space using the probe holder whereas the cylindrical water tank made from PVC could move up and down with the help of a DC electric motor and a counter weight. The speed of the motor was controlled by a DC Motor Speed Controller, made by Bodine Electric Company. Therefore the speed of the transversing cylindrical tank was accurately controlled through the DC Motor controller. In Figure 5.6, the calibration curve for the tank velocity versus the motor dial is presented. The tank velocity was accurately estimated (with less than 1.0% error) using reference marks and a stop-watch.

Next, the output voltage of the HFA bridge was calibrated against the fluid (tank) velocity V, with the bridge operating in the constant tem-

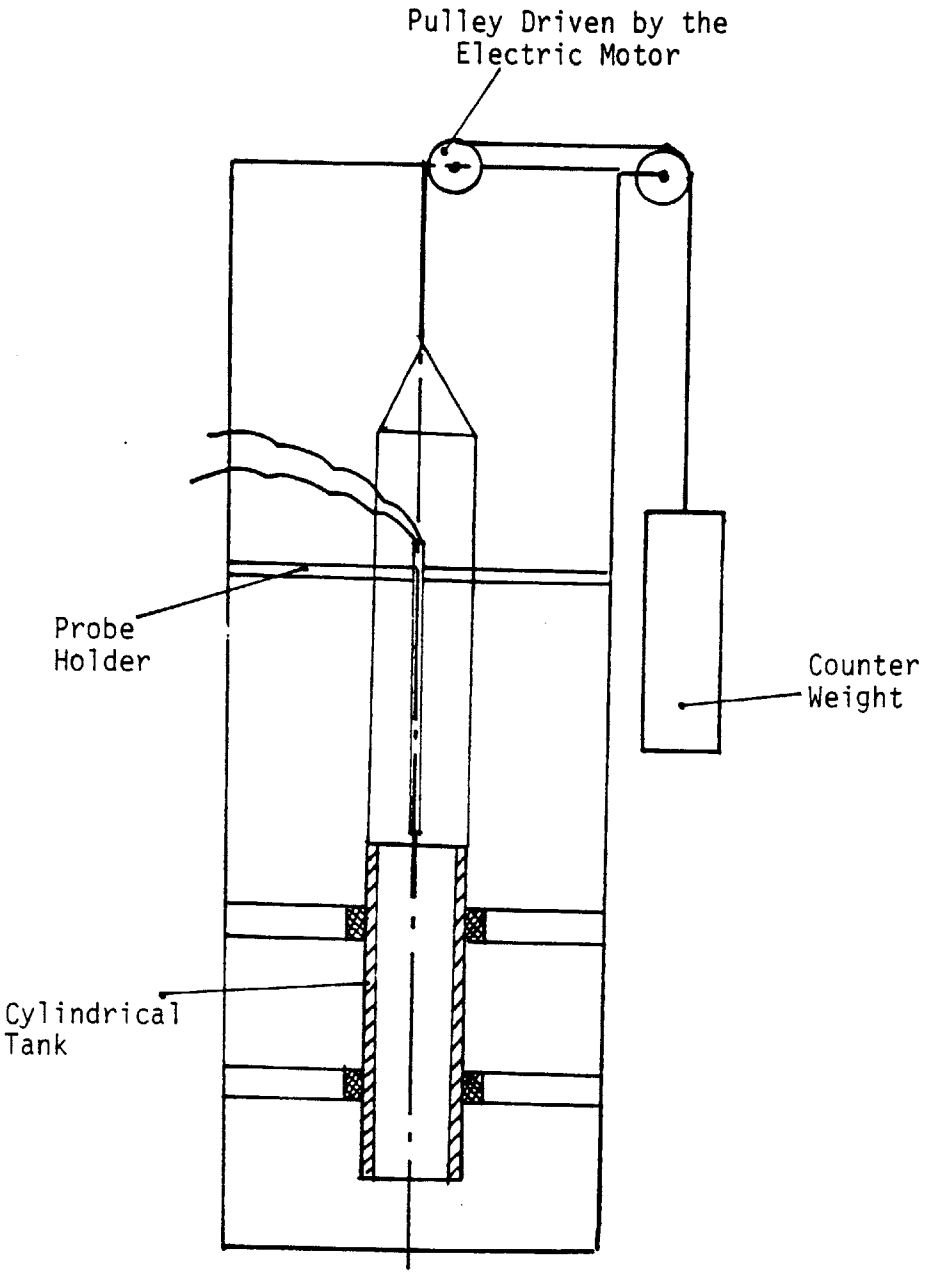

FIGURE 5.5: A SCHEMATIC REPRESENTATION OF THE HOT-FILM ANEMOMETRY CALIBRATION APPARATUS.

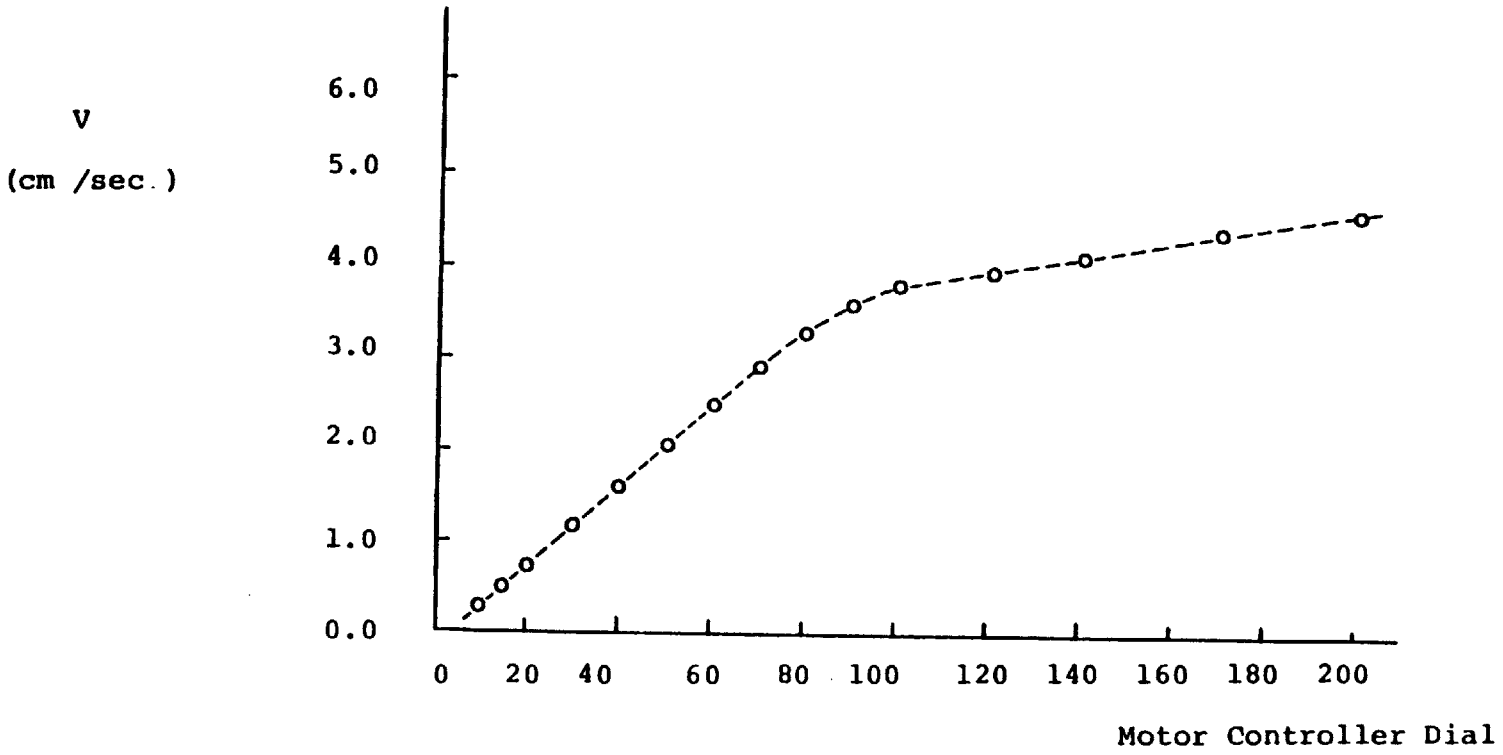

FIGURE 5.6: Calibration curve for the velocity of the transversing cylindrical tank versus the controller dial of the diving motor.

perature mode. It has been theoretically proven and experimentally verified that $\sqrt{V} \sim E^2$ (H-3). Following H-3, we correlate our data in the following form:

$$\frac{E^2}{E_o^2} = a + b\sqrt{V} \tag{5.1}$$

where E_o is the bridge output corresponding to zero velocity and the same fluid temperature.

The presence of the E_o in equation 5.1 accounts for the temperature effect since both E and E_o are strong functions of temperature. In Figure 5.7 our calibration data are plotted as $\sqrt{V}$ versus $(E/E_o)^2$ for two different water temperatures (22°C and 28°C). Within the experimental error, the following curve satisfactorily correlates our data:

$$\sqrt{V} = 2.90\ (E/E_o)^2 - 2.47 \tag{5.2}$$

where V is the fluid velocity in cm/sec.

The zero velocity voltage E_o is a strong function of temperature. It was experimentally found that for a 1°C temperature increase, E_o experienced a 0.065 to 0.075 Volt change. E_o typically ranged from 5.4 to 5.8 Volts. In a typical measurement E_o equals 5.6 Volts, E ~ 6.6 Volts and the corresponding velocity (calculated from equation 5.2) is 2.428 cm/sec. For a ΔE_o uncertainty equal to 0.01 Volts, the velocity uncertainty ΔV is calculated from equation 5.2 equal to 0.33 cm/sec. Therefore the velocity estimation error $e_V = \Delta V/V$ is equal to 13.6%. Similarly we

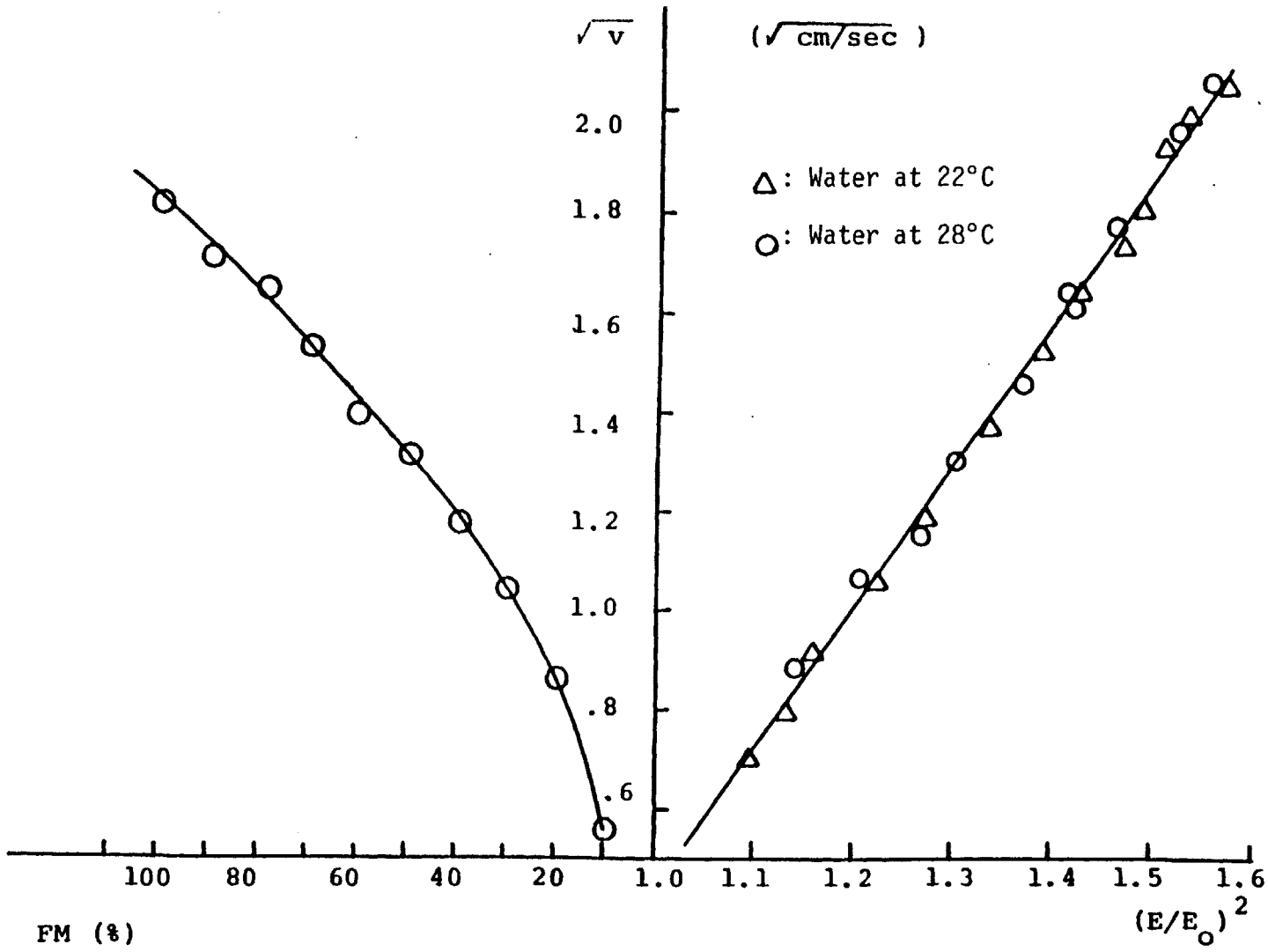

FIGURE 5.8: Reference Point Calibration curve. Velocity versus flow meter setting.

FIGURE 5.7: HFA calibration curve velocity versus bridge voltage.

find that for lower velocity conditions, with E = 6.0 Volts, E_o = 5.6 Volts and ΔE_o = 0.01 Volts then e_V = 21.0%.

For laminar mixed convection flows with water as the working fluid the temperature is expected to vary 5°C to 10°C at the exit plane of our bundle. Simultaneous E and E_o measurements are needed therefore in order to accurately estimate the velocity V. In heated flows, E_o cannot be measured directly. Instead, the fluid temperature T_f can be measured and E_o is estimated using a E_o versus T_f calibration curve. This latter calibration curve can be constructed using a stagnant pool of liquid at a known temperature and measuring the HFA bridge voltage E_o.

For simultaneous measurements of E and T_f, an additional bridge was purchased (Model 1040) in order to allow the HFA probe to be used as a resistance thermometer. After calibration of the probe, operated as a resistance thermometer, the temperature resolution achieved was 0.2°C. Unfortunately, as discussed earlier the electrical resistance of the velocity-to-temperature mode switch was not reproducible, causing two major problems: (a) When switching to Model 1040 bridge (constant current mode for temperature measurements) the probe readout could drift as high as 1.5°C (b) When switching to Model 1050 bridge (constant temperature mode for E measurements), E_o could drift more than 0.1 volts. The combined effect of these uncertainties yielded $e_V \sim$ 80 to 100% rendering the use of model 1040 bridge for temperature measurements impossible. Since the resolution of thermocouple systems is only 1.0°F, it was decided to perform isothermal velocity measurements only until some more sophisticated model 1040 switch or a high resolution thermocouple (attached close to the tip of the HFA probe) is introduced.

5.3 Exit Subchannel Velocity Measurements

5.3.1 "In-Situ" Calibration and Measurement Procedures

In this section the exit subchannel velocity data for isothermal flows in our 19-pin wire-wrapped bundle are presented. All 48 channels were scanned with our HFA probe for three different Reynolds numbers, namely 316, 158 and 80. In all cases, laminar flow conditions are expected to prevail. Nine to fifteen locations per subchannel were sampled as discussed in 5.2.2.

In case of a bare interior subchannel (see Figure 5.3) 10 locations were sampled: one at the subchannel center, three at the center of the neighboring gaps, three at the half distance between the center and the center of the gaps and three at approximately 1.0 mm from the central wall region of the three surrounding rods. A similar approach was followed for the bare edge subchannels as shown in Figure 5.3. Here again the distance from the walls of the locations close to the walls is approximately 1.0 mm. These patterns of locations were chosen so that approximately one third of these locations are situated at the vicinity of the wall region and they are uniformly spread all over the subchannel area. When the wire-spacer was present in a given subchannel, some necessary distortion of these patterns occured as shown in Figure 5.3.

In order to minimize the time required to collect all these data the following procedure was followed:

(a) Set the probe at the subchannel location desired.

(b) Set the flow rate at Re=316. Make sure that isothermal conditions have been established and that $T_{in}=T_{out}$. Measure bridge voltage E.

(c) Set the flow rate at Re equal 158 and 80 respectively and repeat step (b).

(d) Zero the flow and measure E_0. Use this value for all data reduction corresponding to the position chosen in step (a).

(e) Choose a new probe location and repeat steps (b,c,d).

Note that it is more time consuming to accurately place the probe in a new location than to select a new flow rate and establish steady state conditions for a new voltage measurement. Therefore, the above procedure is the least time consuming.

Finally one problem had to be resolved, namely the problem of the calibration curve drift (equation 5.2) during the course of the above measurements which lasted more than ten days. Dirt accumulation, chemical corrosion and possible scratches on the surface of the miniature conical probe significantly altered the behavior of our HFA system during the day-to-day operation and, sometimes, even within the same day. The main cause of this drift was the formation of tiny air bubbles within certain "pockets" (or nucleation sites) on the probe surface, created by the above phenomena. The drift was partially alleviated by carefully brushing out dirt, corrosion products or tiny air bubbles, at least once a day, using a soft brush. However the need of recalibrating the HFA system remained. Transfering the HFA probe from its place in the driving mechanism at the upper plenum to the calibration apparatus and vice versa was a very time consuming process. It was decided therefore to employ an "in-situ" calibration procedure in order to calibrate the probe without relocating it to the calibration apparatus. The following steps were followed in order to establish the "in-situ" calibration technique.

(a) The probe was calibrated first using the calibration apparatus of Figure 5.5. The calibration were $\sqrt{V}$ versus $(E/E_0)^2$ of Figure 5.7 was constructed.

(b) Immediately after completion of the above step, the HFA was transfered and installed in the probe driving mechanism at the rod bundle upper plenum. No electrical cable was disconnected and connected again in order to avoid any change in the cable resistance. The probe was placed at a reference location within subchannel 27. The reference location was chosen so that it would be easily accessible, as follows: it is the location close to the center of subchannel 27 where maximum voltage E (and consequently velocity) is measured for Re=316. For this position, the z,r and θ coordinates were recorded. Each time the reference was reaccessed, the z coordinate was kept the same. However, the r and θ coordinates were sometimes slightly different due to the fact the (a) the probe support mechanism is not perfectly rigid and (b) the position of maximum velocity is not unique within our HFA resolution.

(c) With the probe at the reference location, the Reference Location Calibration Curve (RLCC) is constructed as follows: For each flow meter setting, the reference location velocity is estimated using the bridge voltage measurement E and the HFA calibration curve of Figure 5.7. The resulting RLCC is given in Figure 5.8.

Note that the RLCC once constructed does not drift as long as the bundle geometry remains the same. In order to check and, if necessary, recalibrate our HFA system the opposite system procedure is followed: The probe is placed at the reference location and for each flow meter setting the velocity V is estimated using the RLCC. The HFA calibration curve was

then reconstructed using this velocity estimate and the corresonding E and E_o measurements.

The "in-situ" calibration procedure was performed at the beginning of a new series of data collection when the probe had not been operated for more than 12 hours. The probe conical surface was always cleaned first with a soft brush before calibration. It was found that while the slope of the $\sqrt{V} - (E/E_o)^2$ curve remained practically the same, the constant of equation 5.2 could change up to 20%.

5.3.2 Subchannel Velocity Data and Flow Split

Axial subchannel velocity measurements were performed at the exit plane of our 19-pin wire-wrapped bundle for all 48 subchannels and for three different Reynolds number cases, with the Re equal to 316, 158 and 80 respectively.

In order to get an estimate of the error involved in the subchannel velocity calculation (equal to the arithmetic average of a discrete number of local velocity measurements per subchannel, as discussed in 5.3.1), the average bundle velocity V_b^{HFA} was estimated from HFA measurements as follows:

$$V_b^{HFA} = \left(\sum_{k=1}^{48} A_k \, V_k^{HFA}\right)/A_b' \tag{5.3}$$

where

$$A_b' = \sum_{k=1}^{48} A_k \tag{5.4}$$

A_k is the real area of a given subchannel k and it is estimated using the geometrical data of Figure 5.3.

$$\text{Also} \qquad V_k^{HFA} = \left(\sum_{\ell=1}^{N_k} V_{k,\ell}^{HFA} \right) / N_k \qquad (5.5)$$

where $V_{k,\ell}^{HFA}$ is a local measurement within subchannel k and N_k is equal to the total number of locations sampled in the subchannel k.

It was found that $A_b' = 50.13\ cm^2$. This value is only slightly higher than the real bundle cross-section area $A_b = 48.46\ cm^2$ which is calculated based on the flat-to-flat distance and the rod and wire diameter (see chapter 2).

In Table 5.1 the values of the summation $\sum A_k V_k$ are presented separately for interior, edge and corner subchannels and for all three Re number cases. The values of the velocity ration V_b^{HFA} / V_b^{FM} are also presented, where V_b^{FM} is based on the flow meter measurement and calculated as the ratio of the measured volumetric flow rate over A_b. Note that in all cases this ratio is higher than one. This was expected since as discussed in paragraph 5.3.1 most of the sampled location per subchannel (approximately the two thirds of them) lie at that region of the 2-dimensional velocity profile where the velocity is expected to exhibit a local maximum (see Figure 5.3). In estimating V_b^{HFA}, there are two kinds of errors involved:

(a) the discretization error, resulting in higher estimates of V_b and (b) the random error which accounts for all other errors (HFA calibration curve error, RLCC error, uncertainty of a location selection, etc.). An estimate of the order of magnitude of the random error can be obtained from the data scattering of the V_b^{HFA} / V_b^{FM} ratio, which according to Table 5.1 is of order of 12.0%. Note that for laminar flows this ratio is

TABLE 5.1 Flow Split Data

Case	Re	$\sum A_i V_i$ (cm^3/sec)	$\sum A_e V_e$ (cm^3/sec)	$\sum A_c V_c$ (cm^3/sec)	V_b^{HFA}/V_b^{FM}	X_2
1	316	59.38	72.95	11.8	1.123	1.120
2	158	29.15	38.64	5.16	1.137	1.146
3	80	13.53	17.0	2.31	1.024	1.121

TABLE 5.2 Flow Split Data by Chen, Ip and Todreas (C-4) with P/D = 1.25 and Re ≈ 640

H/D	X_2
24	1.24
48	1.19

expected to be constant so that the above data scattering indicate the presence of a random error. More data are needed in order to determine whether this 12.0% is a high or a low estimate of the random error. At this point is reasonable to assume from equation 5.3 that the random error of V_k estimation is also of order of 12.0%.

In Figure 5.9 some subchannel velocity data are presented for a continuous row of subchannels (see also Figure 5.2 for subchannel numbering convention). For reducing the data of Figure 5.9, V_b was taken equal to V_b^{HFA}. Note that in estimating the V_k^{HFA}/V_b^{HFA} ratio only the random error is involved since the discretization error is canceled out. Therefore, the total error of V_k/V_b estimation is expected to be of order of 12+12=24%. Referring to Figure 5.9 the following remarks can be made:

(a) The presence of the wire-spacer within an interior subchannel causes a substantial velocity drop which is higher for lower Reynolds numbers.

(b) At the edge subchannels the velocity is generally higher than the velocity in the interior ones. This velocity difference tends to increase with decreasing Reynold's number.

In general the velocity profiles tend to become flatter with increasing Reynolds number. These trends have been established under turbulent flow conditions (C-8). In our velocity data, the Re effects on the velocity magnitude lie well within the estimated random error bars for these data. Therefore more data are needed before these trends can be fully supported.

Based on the data of Table 5.1 the flow split parameter X was calculated. The flow split for the edge subchannels is defined as

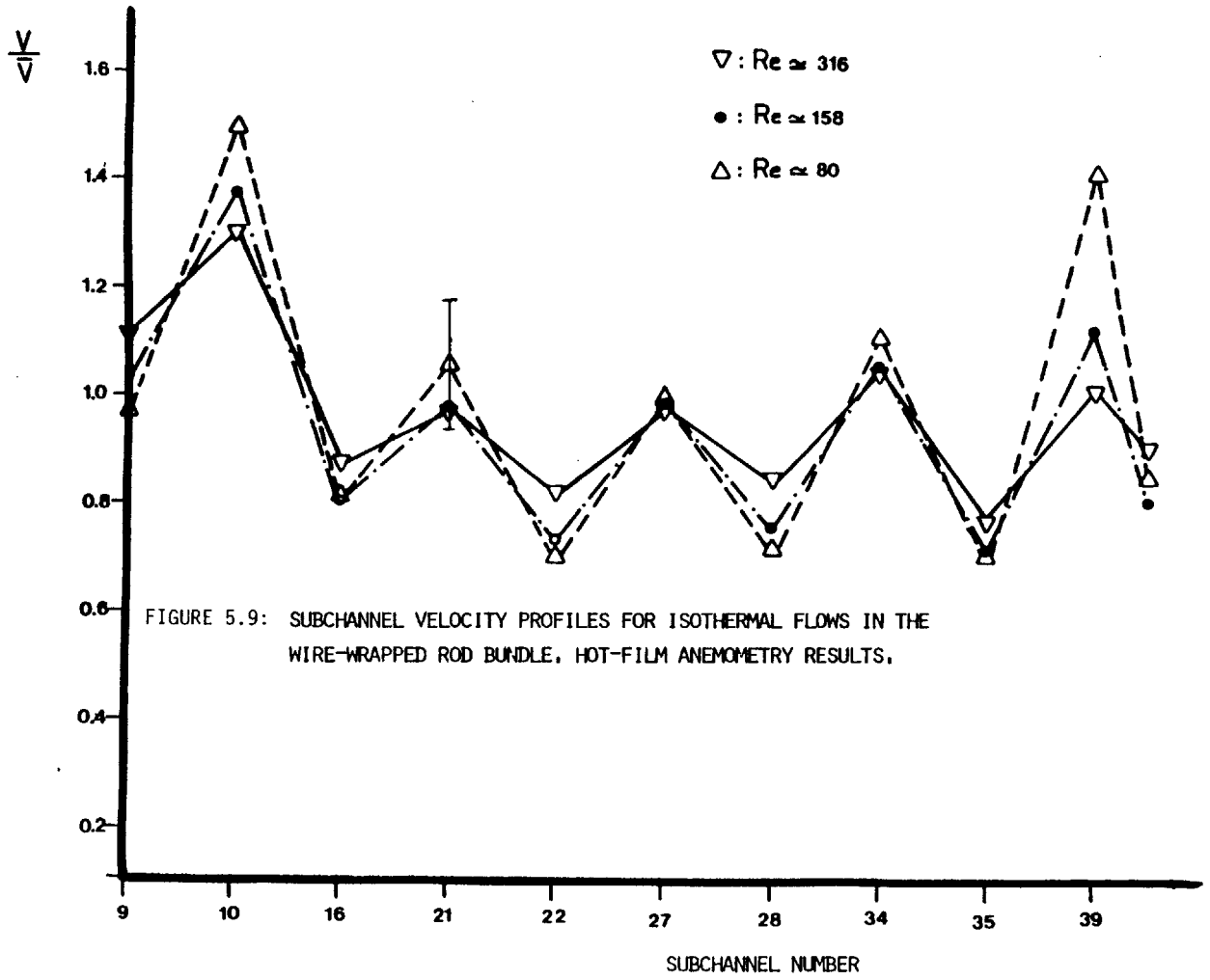

FIGURE 5.9: SUBCHANNEL VELOCITY PROFILES FOR ISOTHERMAL FLOWS IN THE WIRE-WRAPPED ROD BUNDLE. HOT-FILM ANEMOMETRY RESULTS.

follows:

$$X_2 = \frac{\sum_{}^{edge} A_k V_k^{HFA}}{\sum_{k=1}^{48} A_k V_k^{HFA}} \tag{5.6}$$

where the summation in the nominator of equation 5.6 is performed over the edge subchannels only. The flow split parameters for interior and corner subchannels are similarly defined. The edge flow split parameters for the three Reynolds number cases are presented in Table 5.1. According to this data, X_2 is of order of 1.12 to 1.15. No definite trend with the Reynolds number can be established from these data. Note that the velocity data of Figure 5.9 indicate that X_2 increases with the Re number decreased. However, as discussed earlier, due to the large error involved, this latter trend cannot be fully supported.

There is only one other experimental work presenting laminar flow split data. Chen, Ip and Todreas (C-4) used a laser doppler anemometer to measure the axial velocity profile for the edge subchannels of a 61-pin wire-wrapped bundle with P/D = 1.25. Two different H/D cases were explored. Table 5.2 summarizes their laminar flow split results. These results show that X_2 increased with H/D decreasing and that the order of magnitude of X_2 for H/D equal to 35 (which corresponds to our geometry) is 1.22 to 1.23. This estimate is around 9.0% higher than our estimate. Given the magnitude of the random error involved in the velocity estimation (± 12% in our case) this deviation is well within the experimental error expected. However, we expect that Chen's, et al. flow split results are overestimated due to the following reasons. Their subchannel average

velocites were calculated as an arithmetic average of 32 to 42 local measurements per subchannel. Most of these local points were distributed in the center of the edge subchannels as was the case in this work. It is expected therefore that the edge velocity is overestimated. In contrast with our work, the bundle volumetric flow rate required in the denominator of equation 5.6 was estimated using flow meter measurements. Consequently the systematic error in the numerator of equation 5.6 is not canceled by a similar systematic error in the denominator (as is the case in this work), yielding higher X_2 estimates.

5.4 Exit Subchannel Temperature Measurements

Subchannel temperature measurements were performed at the exit plane of the 19-pin wire-wrapped bundle. The subchannel average temperature was estimated as the arithmetic average of local temperature measurements, performed at the same locations as in the velocity measurement case. (see Figure 5.3).

Five different runs were performed for various levels of the Gr_q/Re parameter. In all cases the power skew was kept constant and equal to 5:1. Runs T1 and T2 are presented in Figure 5.10 and runs T3, T4, and T5 in Figure 5.11. The flow rate was 3.1×10^{-4} m^3/sec for runs T1 and T2 and $1.24 \times 10^{-4} m^3$/sec for runs T3, T4 and T5. Referring to Figure 5.2, the high power rods are the three peripheral rods next to subchannels 4 and 1. The three rods next to subchannels 42 and 39 are the low power rods. For all runs in Figures 5.10 and 5.11 the power of a high power rods is given. The power of a low power rod then is $\dot{q}_{max}/5$. For example in run T1 all high power rods are rated at 1000 W. Each of the four rods next to the

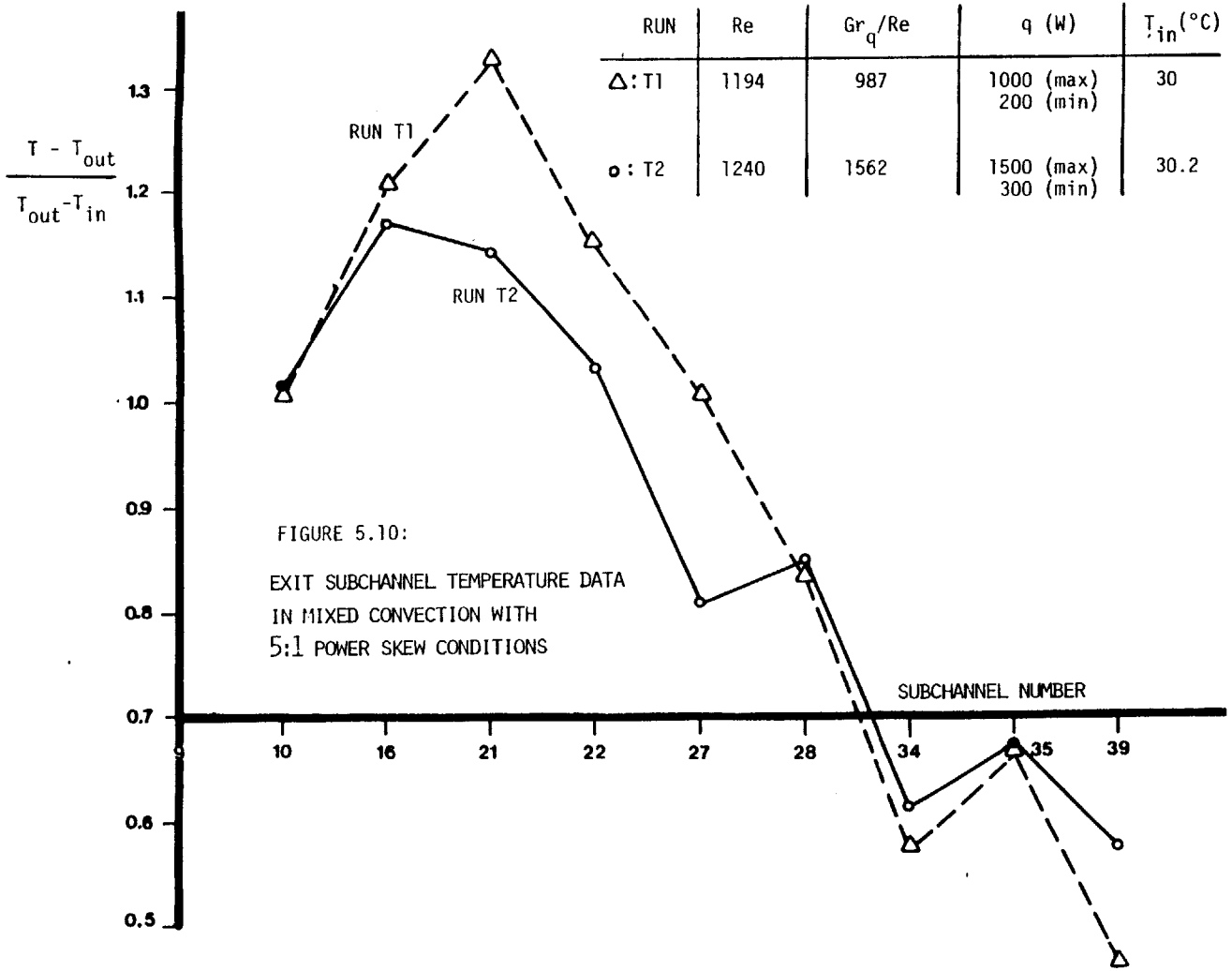

FIGURE 5.10:

EXIT SUBCHANNEL TEMPERATURE DATA
IN MIXED CONVECTION WITH
5:1 POWER SKEW CONDITIONS

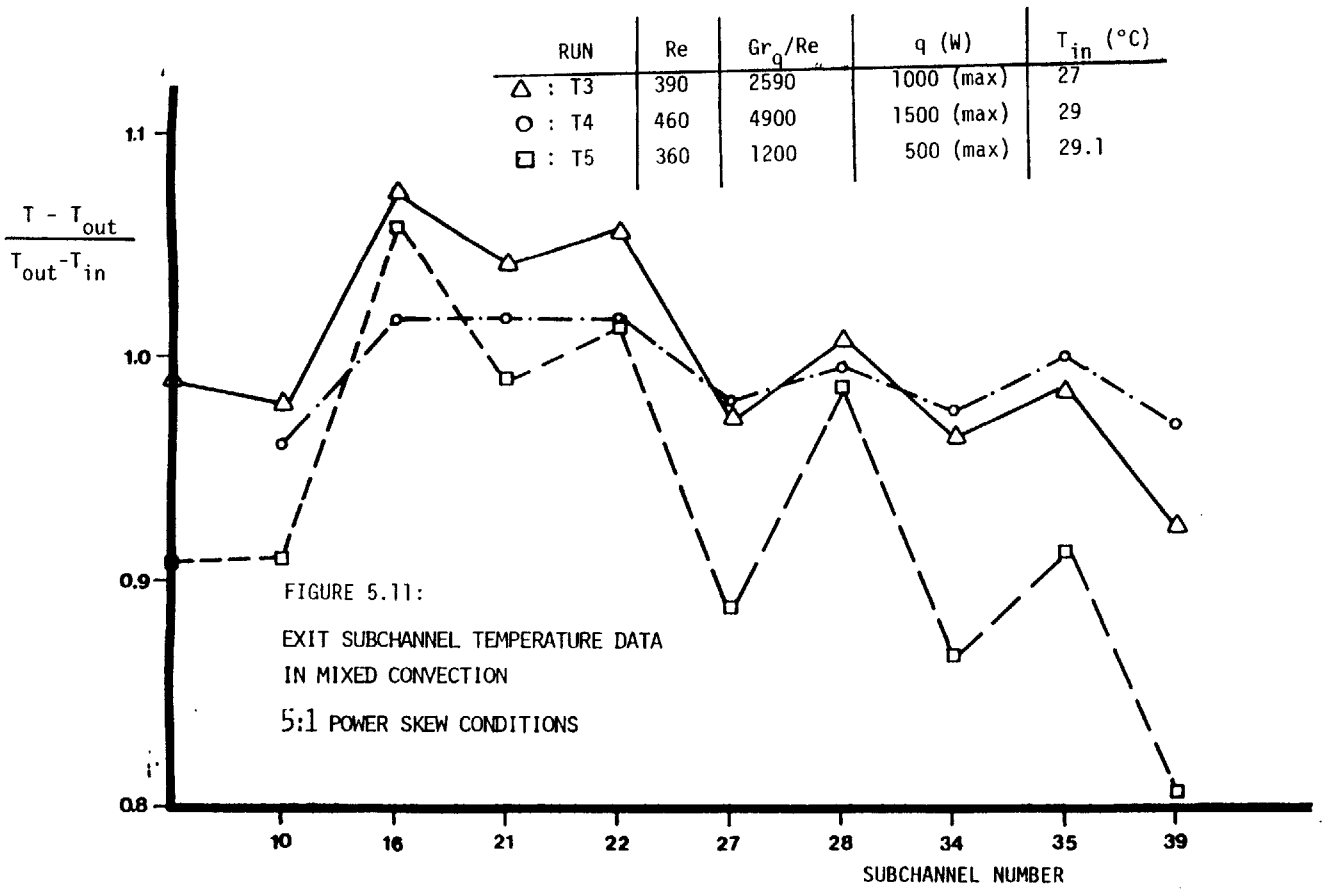

FIGURE 5.11:

EXIT SUBCHANNEL TEMPERATURE DATA
IN MIXED CONVECTION

5:1 POWER SKEW CONDITIONS

high power rods are rated at 800W. The next five rods are rated at 600W, the next four rods at 400W and finally the three low power rods are rated at 200W each.

The Gr_q and the Re numbers were calculated based on bundle average temperature, average heat flux and bundle flow rate.

Referring to Figure 5.10 observe that run T2 exhibits a flatter temperature profile than run T1 which corresponds to lower Gr_q/Re number. This trend was expected since it is well known that increasing buoyancy forces reduce the peaks in the temperature profile. From Figure 3.8 observe that flows with Gr_q/Re at the vicinity of 1500 correspond to the onset of mixed convection regime. Hence Run T2 with Gr_q/Re around 987 is still expected to be in the forced convection regime.

Runs T3, T4 and T5 are made at lower flow rates with Re ~ 400. Here the temperature profiles are in general flatter than those in runs T1 and T2. In addition these profiles become flatter with increasing Gr_q/Re. For the interior subchannels the temperature profile experiences a dip when the wire-spacer is present. This dip is more pronounced at lower Gr_q/Re numbers.

Runs T1 through T5 were tested against MIT criterion for onset of recirculation (S-4). In the flow recirculation regime, the flow at the low power region stagnates or even reverses direction while the flow at the high power region experiences further acceleration. The application of this criterion indicated that recirculation did not occur in any of our runs. Figure 5.12 illustrates the two cases most susceptable to flow recirculation on MIT flow regime map. The large horizontal error bar for run T4 is due to the fact that low Reynold's number (less than 800)

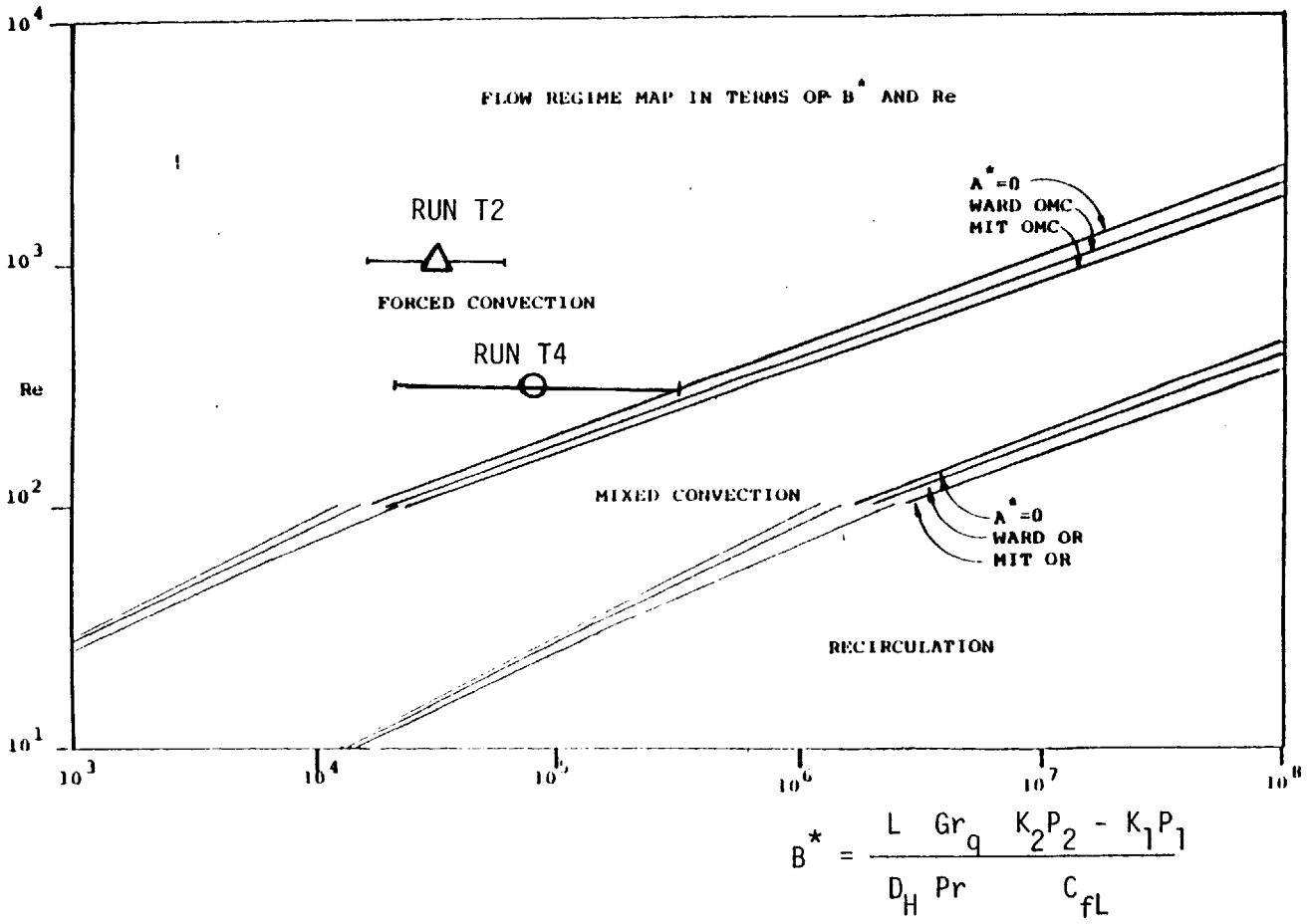

FIGURE 5.12: RUNS T2 AND T4 PLACED ON MIT'S FLOW REGIME MAP.
(The Map is taken from reference S-4)

cases are not covered by Symolon's graph solutions. It was necessary therefore to extrapolate these graphic solutions down to the 400 Reynolds number range.

A significant level of turbulence was present in all of our runs. For steady state temperature measurements, with average temperature around 40°C, the temperature variation due to turbulence phenomena was 5.0 to 10.0°C. It is expected therefore that considerable amount of turbulence mixing (induced by the buoyancy effects) occurs between adjacent subchannels. Currently there is no models to predict the onset of buoyancy induced turbulence or the amount of turbulence mixing in wire-wrapped or bare rod bundles.

MIXED CONVECTION AND HYDRODYNAMIC MODELING OF FLOWS IN ROD BUNDLES

by

APOSTOLOS EFTHIMIADIS

Mech.-Elec. Engr. Dipl., National Technical University of Athens
(1978)

M.S., Purdue University
(1980)

Submitted to the Department of
Nuclear Engineering
in Partial Fulfillment of the
Requirements of the Degree of

DOCTOR OF PHILOSOPHY

at the

June 1984

Signature of Author Signature redacted
Department of Nuclear Engineering
April 30, 1984

Certified by Signature redacted
Professor Neil E. Todreas
Thesis Supervisor

Accepted by Signature redacted
Allen F. Henry
Chairman, Department Graduate Committee

CHAPTER 6

SUBCHANNEL ANALYSIS FOR TRIANGULAR WIRE-WRAPPED ROD BUNDLES

6.1 Introduction

In this chapter we discuss the formulation of the subchannel analysis equations for bare and wire-wrapped triangular rod arrays. The subchannel analysis approach was originally introduced for rectangular bare rod arrays in order to perform thermohydraulic analysis in Light Water Reactor fuel elements. Certain simplifying assumptions that were made for the square array case cannot directly be extended for the case of triangular wire-wrapped rod bundles. Here we discuss the implications of the wire-wrapped spacer in the subchannel analysis formulation. Certain recommendations are made for improvements in the formulation of the pressure terms and of various geometrical parameters.

In addition the porous-body approach formulation is also discussed and compared with the subchannel analysis approach. The most important advantages of the subchannel analysis over the porous body approach are outlined.

6.2 The Subchannel Analysis Conservation Equations

The mass, momentum and energy balance conservation equations in integral form are (see for example (R-2) or (T-1))

$$\text{Continuity: } \frac{\partial \langle \rho \rangle}{\partial t} + \frac{1}{V} \int_{A_f} \rho \vec{v} \cdot \hat{n} dA = 0 \tag{6.1}$$

$$\text{Momentum: } \frac{\partial}{\partial t} \langle \rho \vec{v} \rangle + \frac{1}{V} \int_{A_f} \rho \vec{v} (\vec{v} \cdot \hat{n}) dA = \tag{6.2}$$

$$\langle\rho\rangle\vec{g} + \frac{1}{V}\int_{A_f}(-p\hat{n} + \overline{\overline{\tau}}\cdot\hat{n})dA + \frac{1}{V}\int_{A_{fs}}(-p\hat{n} + \overline{\overline{\tau}}\cdot\hat{n})dA$$

Energy: $$\frac{\partial}{\partial t}\langle\rho h\rangle + \frac{1}{V}\int_{A_f}\rho h(\vec{v}\cdot\hat{n})dA =$$

$$\frac{1}{V}\left\langle\frac{dp}{dt}\right\rangle + \frac{1}{V}\int_{A_f}k_e\langle\hat{n}\cdot\vec{\nabla}T\rangle dA - \frac{1}{V}\int_{A_{fs}}\vec{q}\cdot\hat{n}dA + \frac{1}{V}\langle\Phi\rangle \quad (6.3)$$

where V, A_f, A_{fs} are shown in Figure 6.1

$\vec{v}$ = velocity

$\hat{n}$ = unit vector normal to A_f and A_{fs}

h = enthalpy

$\overline{\overline{\tau}}$ = stress tensor

k_e = the effective fluid thermal conductivity

Φ = the dissipation rate of mechanical energy into heat per per unit volume

The brackets $\langle\ \rangle$ indicate volume averaging:

$$\langle\psi\rangle = \frac{1}{V}\int_V \psi dV$$

In the Lumped Parameter (LP) approach, these integral conservation equations are discretized over a certain computation grid. Figure 6.2 illustrates different nodelization schemes that have been used in triangular rod bundle analysis. Grids (a) through (e) are a tailored along orthogonal (cartesian) coordinates and are used in the porous body approach. Grid (f) corresponds to the numerical mesh that has been used for the mass, axial momentum and energy balance equations in the subchannel analysis approach. In application the axial momentum mesh is staggered in the axial direction with respect to the energy and mass

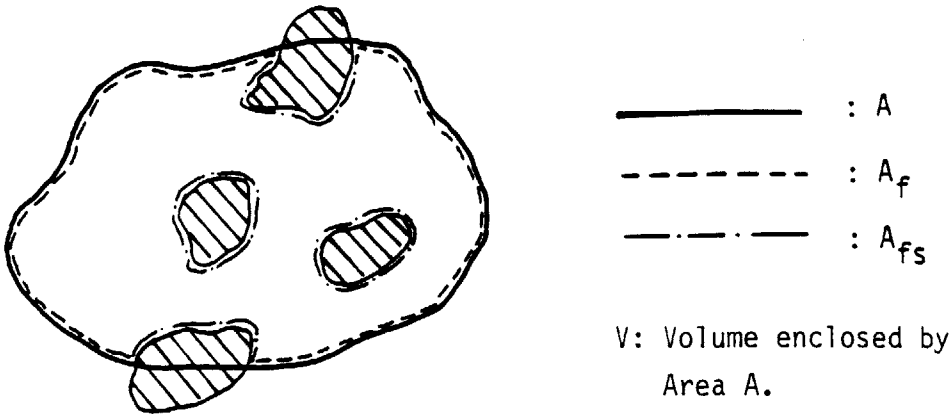

FIGURE 6.1: CONTROL VOLUME AND BOUNDING SURFACE AREA DEFINITIONS.

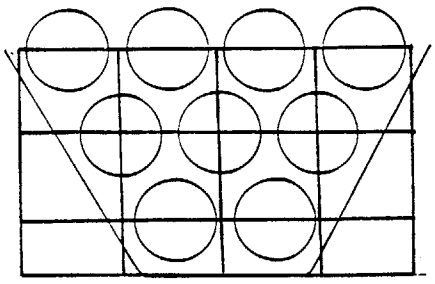

(a) FULL-PIN MESH GEOMETRY

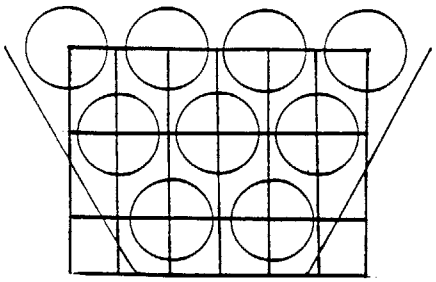

(b) HALF-PIN MESH GEOMETRY

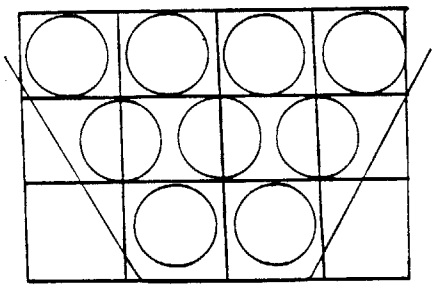

(c) FULL-PIN MESH GEOMETRY

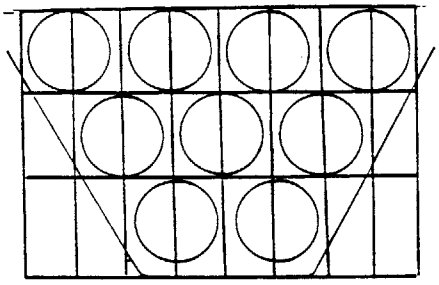

(d) HALF-PIN MESH GEOMETRY

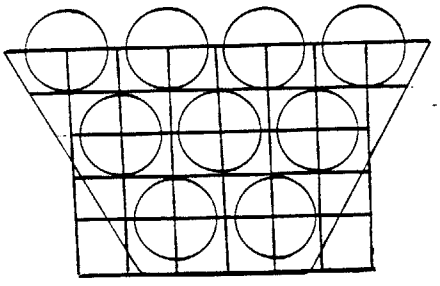

(e) QUARTER-PIN MESH GEOMETRY

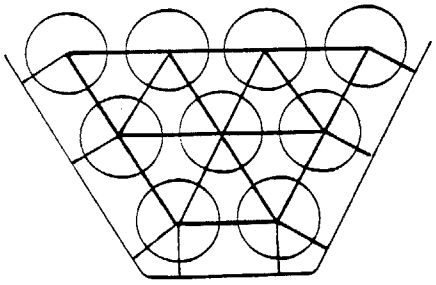

(f) SUBCHANNEL ANALYSIS MESH GEOMETERY

FIGURE 6.2 POROUS BODY AND SUBCHANNLE ANALYSIS MESHES FOR TRIANGULAR ROD ARRAYS.

balance equation grid. Also the lateral momentum numerical grid is staggered in the horizontal direction. Typical mass balance and lateral momentum balance control volumes (CV) for the subchannel analysis approach are given in Figure 6.3.

The intergral equations 6.1, 6.2 and 6.3 can be discretized on the CVs of Figure 6.3 to give the subchannel analysis equation. Todreas (T-1) derived the subchannel analysis equations for square rod arrays based on the more general porous body equations (for the latter see for example (T-1) or (S-8)). The subchannel equations were presented in the following form:

Continuity:

$$\underset{(1)}{A_{fi}\frac{\partial}{\partial t}\langle\rho_i\rangle} + \underset{(2)}{\frac{\Delta \dot{m}_i}{\Delta z}} = \underset{(3)}{-\sum_{j=1}^{J} W_{ij}} \tag{6.4}$$

Axial Momentum:

$$\underset{(1)}{\frac{\partial}{\partial t}\langle\dot{m}_i\rangle} + \underset{(2)}{\sum_{j=1}^{J} W_{ij}\{w^*\}} + \underset{(3)}{\frac{\Delta(\dot{m}_i w_i)}{\Delta z}} = \tag{6.5}$$

$$\underset{(4)}{A_{fi}\langle\rho\rangle g_z} - \underset{(5)}{A_{fi}\frac{\Delta\{p\}}{\Delta z}} - \underset{(6)}{\sum_{j=1}^{J} W'^{M}_{ij}(w_i - w_j)} - \underset{(7)}{\frac{F_{iz}}{\Delta z}}$$

Transverse Momentum:

$$\underset{(1)}{\frac{\partial}{\partial t}(W_{ij})} + \underset{(2)}{\frac{\Delta}{\Delta x'}(W_{ij}\{u\})} + \underset{(3)}{\frac{\Delta}{\Delta z}(W_{ij}\{w\})} = \tag{6.6}$$

$$\underset{(4)}{-\left(s_{ij}\frac{\Delta}{\Delta x'}\{p\}\right)} - \underset{(5)}{\frac{F_{ix}}{\Delta x'\Delta z}}$$

Energy:

$$\underset{(1)}{A_{fi}\frac{\partial}{\partial t}[\langle\rho h\rangle_i]} + \underset{(2)}{\frac{\Delta}{\Delta z}[\dot{m}_i h_i]} = \underset{(3)}{(q_i')_{rb}} \qquad (6.7)$$

$$\underset{(4)}{-\sum_{j=1}^{J} W^{*H}_{ij}[h_i - h_j]} \underset{(5)}{-\sum_{j=1}^{J} W \{h^*\}_{ij}} + \underset{(6)}{A_{fi}\langle\frac{dp_i}{dt}\rangle}$$

where

z = axial direction

x = transverse direction

w = local axial velocity

u = local transverse velocity

A_{fi} = total axial cross sectional subchannel area coincident to the area of the coolant flow

$\dot{m}_i$ = flow rate for the subchannel $i = \int_{A_{fi}} \rho w dA$

$\{\ \}$ = indicates intrinsic surface averaging (intrinsic stands for coolant flow area)

$w_i = \{w\}$

W_{ij} = transverse mass flow rate per unit length $= \{\rho u\}\, s_{ij}$

s_{ij} = thickness of gap between subchannels i and j s_{ij} = P-D (for nominal geometry)

p = pressure

$w^* = \frac{\{\rho w u\}}{\{\rho u\}}$

F_{ix}, F_{iz} = total force on the fluid at x,z direction due to fluid-solid interaction

$\Delta x'$ = transverse length equal to $\ell = \frac{2}{3}\frac{A_{fi}}{s_{ij}}$

h = enthalpy $= \frac{\{\rho h w\}}{\{\rho w\}}$

$h^* = \frac{\{\rho h u\}}{\{\rho u\}}$

$(\dot{q}_i')_{rb}$ = the equivalent dispersed heat source (or sink) per unit length

In order to account for the presence of the wire spacer an empirical model for the wire spacer forced crossflow of the following form has been often introduced.

$$W_{forced} = \pi(D+D_w)\ (s_{ij}/A_{fi})\ (\delta/\Delta z)\dot{m}_i \qquad (6.8)$$

where D is rod diameter and D_w is the wire spacer diameter, δ is an arbitrary parameter proportional to $\Delta z/H$, and H is the wire-wrap pitch. Subchannel flow areas and wetted perimeters are also adjusted to account for the presence of a wire wrap in the subchannel. The forced crossflow from equation 6.8 is then held constant while solving the transverse momentum equations for the remaining cross-flows. More detailed discussion of the various wire-spacer distributed resistance models will be given in Chapter 7.

6.3 Inherent Assumptions and Limitations of the Subchannel Approach

6.3.1 Introduction

In this paragraph the inherent assumptions or limitations of the subchannel analysis approach are examined with particular emphasis on wire-wrapped rod bundles geometry. Before that, we briefly discuss the most important features of fluid flows in wire-wrapped bundles.

6.3.2 Wire-Spacer Effects on the Flow Field

Lafay, Menant and Barroil (L-1) presented local pressure and peripheral velocity measurements in a 19-rod wire wrapped rod bundle with P/D = 1.188 and H/D = 18.75. Figure 6.4(a) gives the axial static pressure evolution along a peripheral edge subchannel for different mass flow

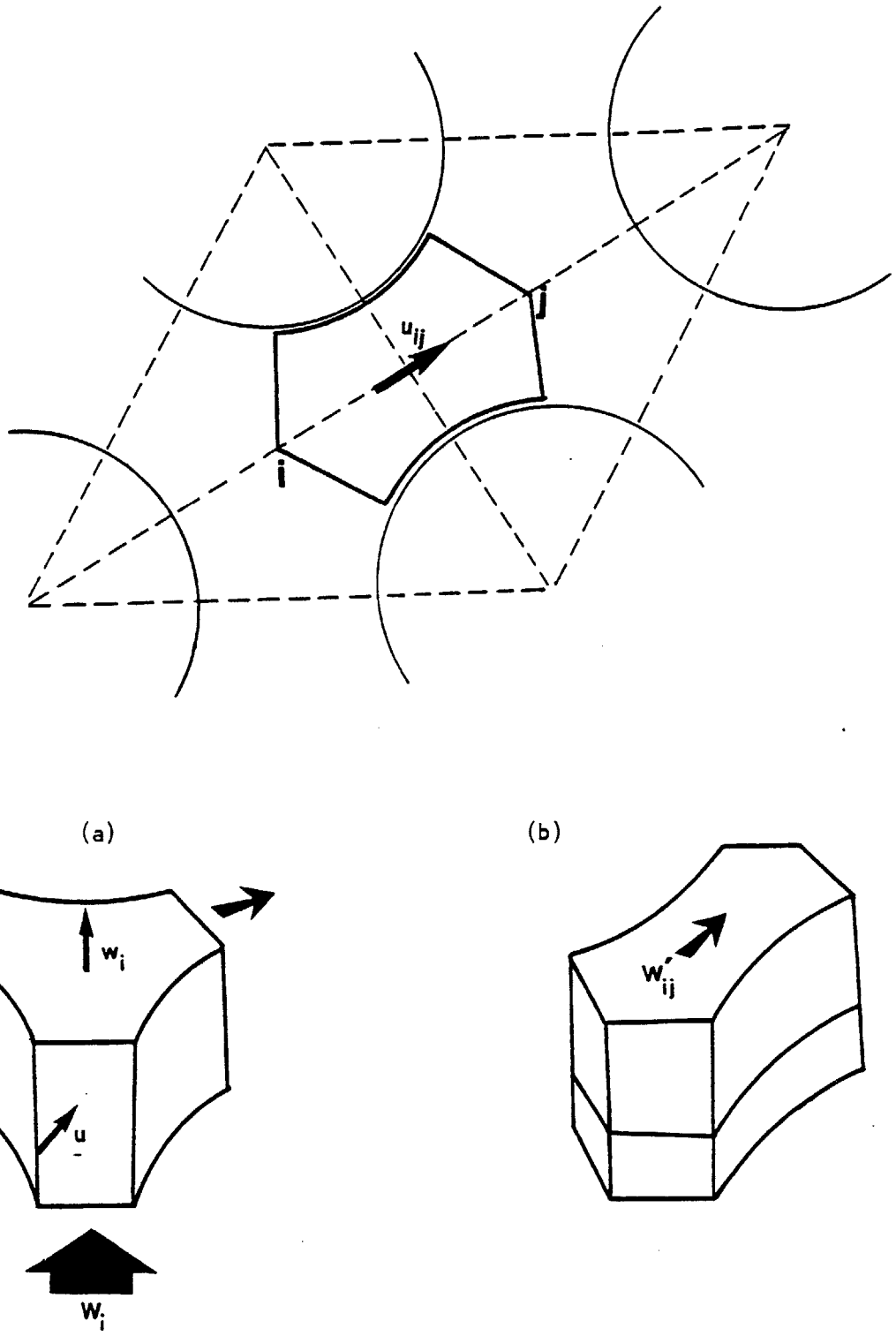

FIGURE 6.3: CONTROL VOLUMES FOR (a) AXIAL MOMENTUM EQUATION, (b) LATERAL MOMENTUM EQUATION.

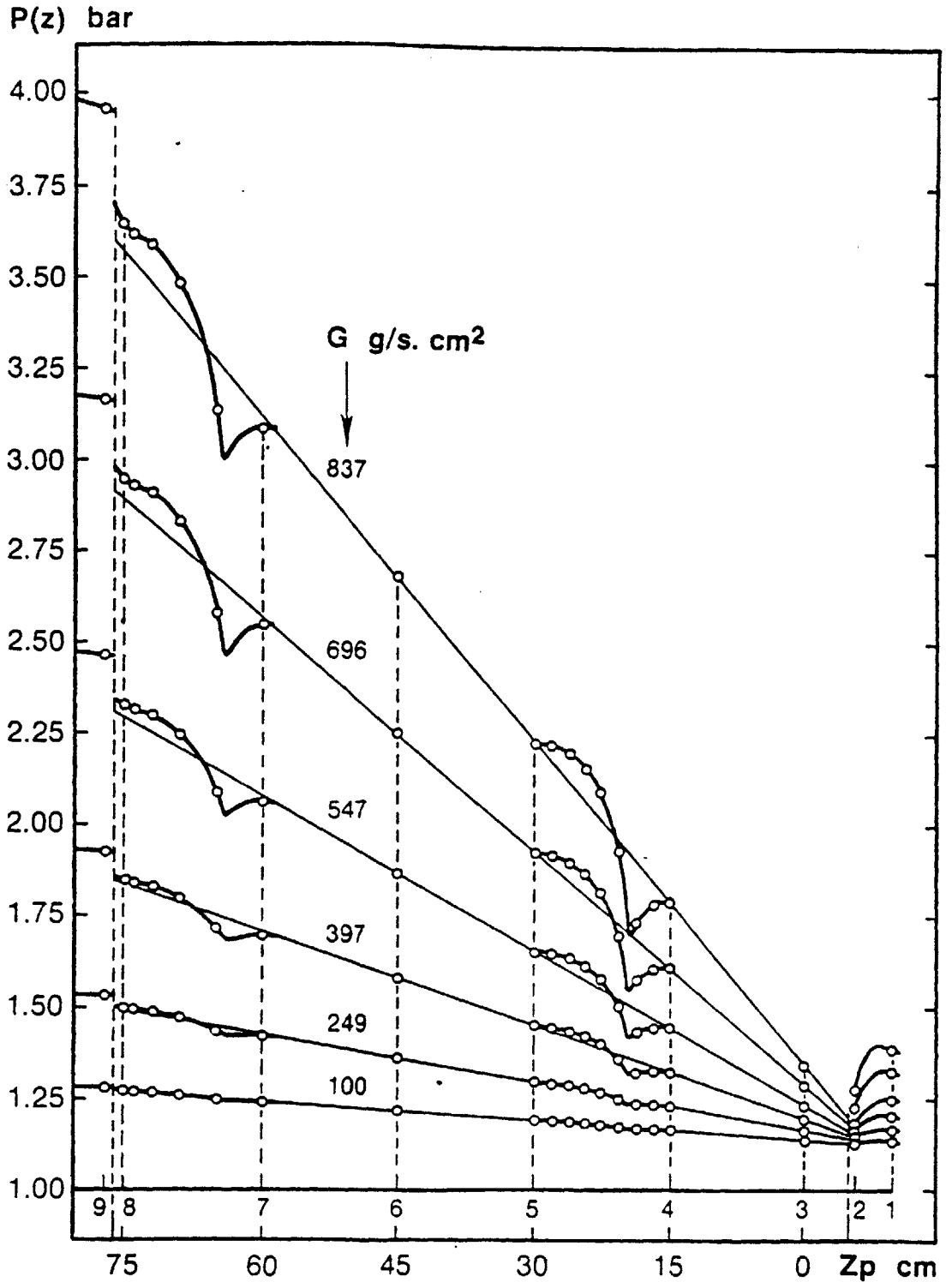

FIGURE 6.4(a) : AXIAL STATIC PRESSURE IN A PERIPHERAL EDGE SUBCHANNEL.
(Taken from reference B-5)

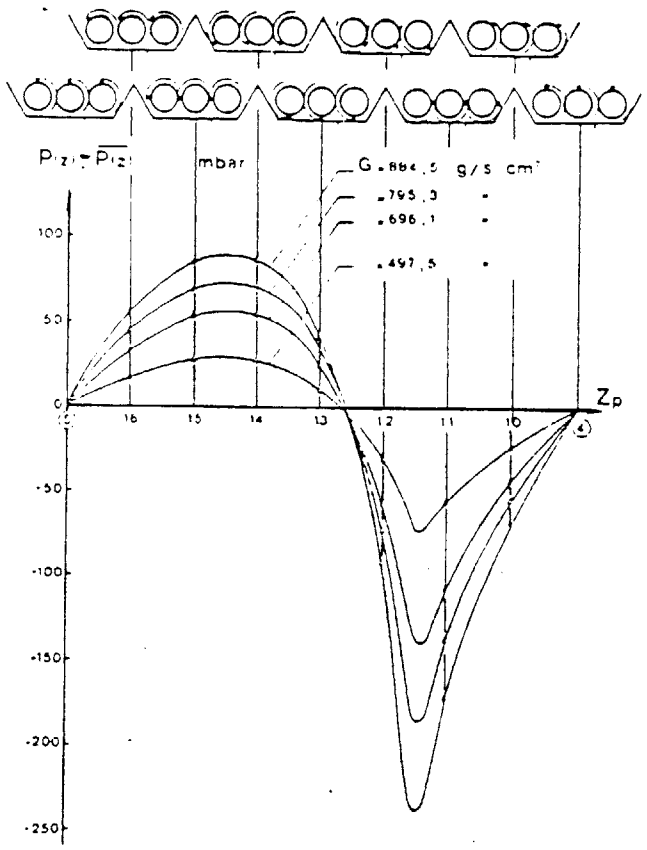

FIGURE 6.4(b) : STATIC PRESSURE DISTRIBUTION ALONG THE EDGE SUBCHANNELS FOR DIFFERENT FLOW RATES.
(Taken from reference L-1)

rates. Observe the local pressure disturbances when the wire spacer is present. Figure 6.4(b) gives a plot of these disturbances as $P(z)-\overline{P}(z)$ versus z where $\overline{P}(z)$ is the average pressure at a given axial level. For a given mass flow rate G the difference $(P(z)-\overline{P}(z))$ exhibits a sinusoidal-like profile stretching over one lead length. For locations upstream of the position where the wire-spacer is in the gap (location between points 12 and 13 of Figure 6.4(b)), the static pressure exhibits a hump. This is due to the decrease of the fluid velocity in the stagnating region upstream of the wire spacer. Downstream from the wire spacer the static pressure decreases, exhibiting a rather sharp trough, due to the formation of the wake (separated boundary layers) region there. Note that the maximum value of the static pressure decrease $(\overline{P}-P)$ in the wake region is approximately three times as large as the static pressure increase in the stagnating region. Figure 6.5, taken also from (L-1), shows the variations of the swirl velocity at the gaps of the peripheral subchannels. The swirl flow velocity here is given as $\overline{u}/\overline{V}$ where $\overline{V}$ is the average bundle velocity and $\overline{u}$ is the average transverse velocity at a peripheral gap. The swirl flow in the peripheral subchannels tends to follow the rotation of the wire spacer. However, this is only the case for the average transverse gap velocities. Doppler velocity measurements by Chen, Ip and Todreas (C-4) indicate that in some of the peripheral subchannels the transverse velocities may form recirculation regions. Finally, Figure 6.6 is a schematic of flow visualization studies at the peripheral subchannels. Lafey et al. noted that the flow downstream of the wire spacer (horizontal arrow) is almost axial. However, after the boundaries marked with a tilted vertical arrow, the swirl flow becomes larger (see Figure 6.5) and the flow is even more inclined than the wire spacer

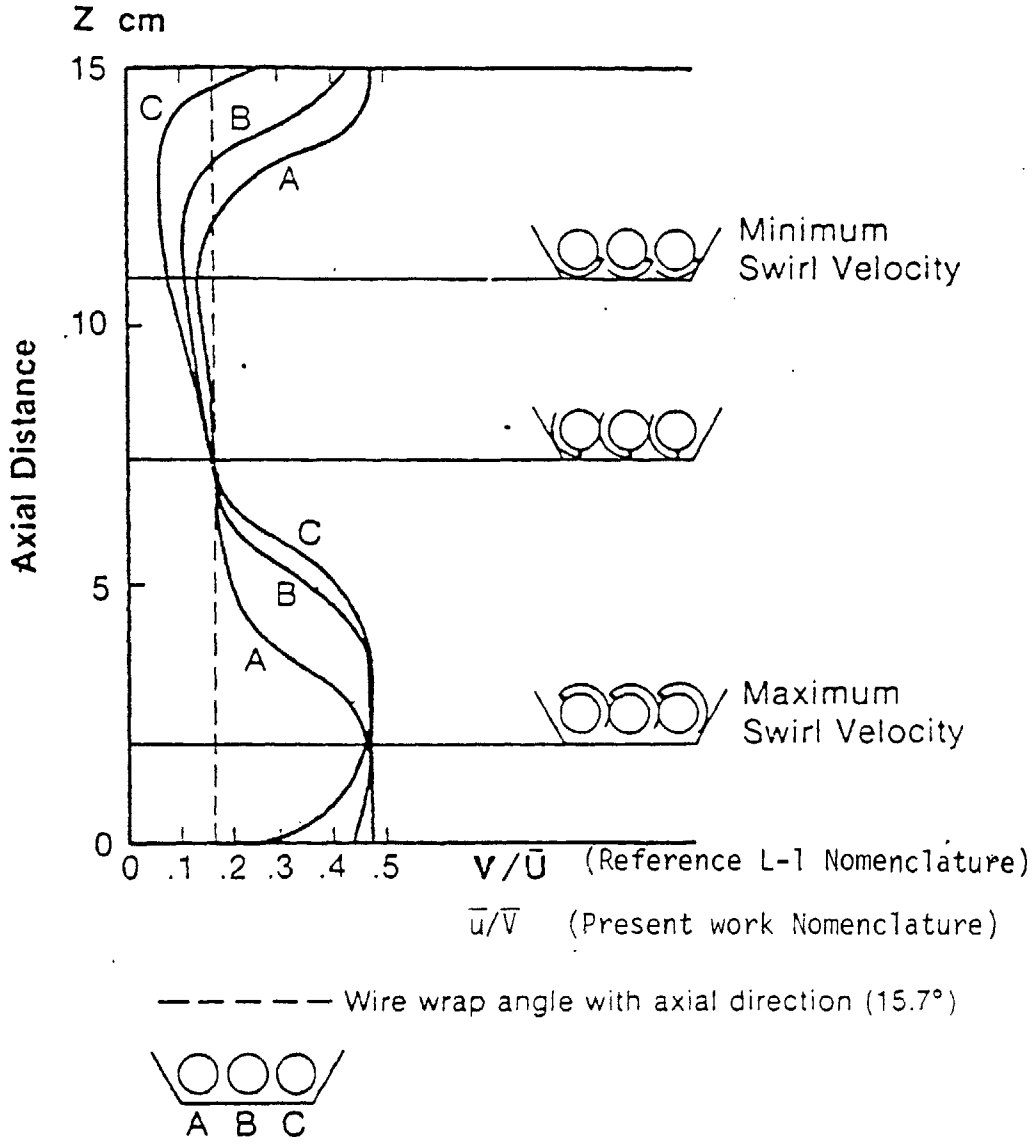

FIGURE 6.5: SIDE SUBCHANNEL FLOW SWEEPING DATA OVER AN AXIAL WIRE-WRAP PITCH. P/D = 1.19
(Taken from reference L-1)

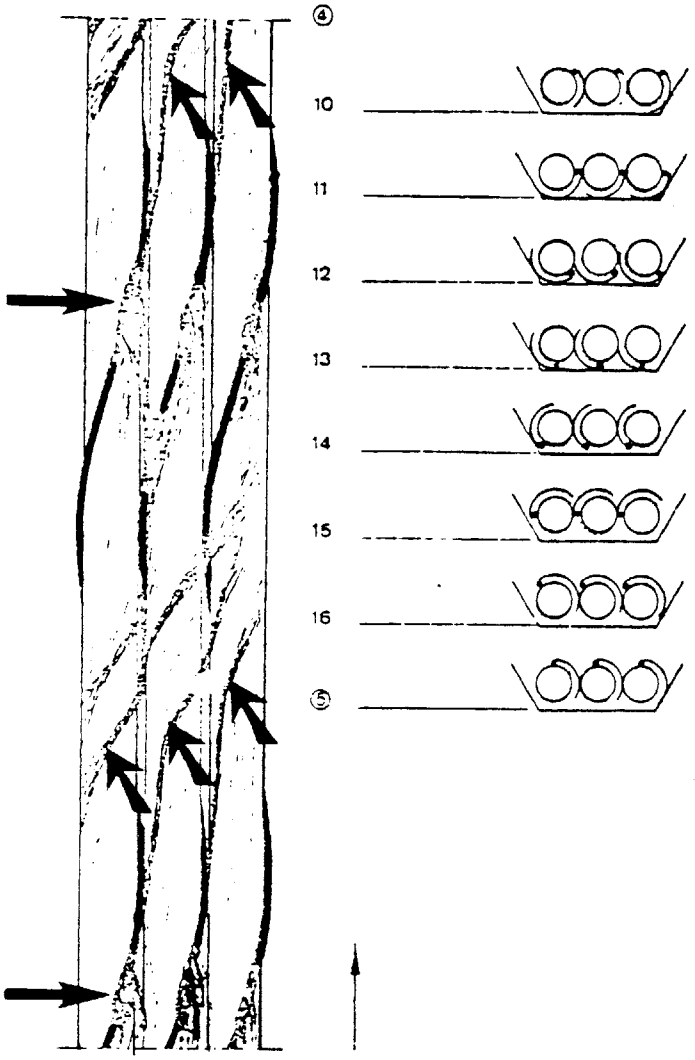

FIGURE 6.6: TYPICAL FLOW PATTERNS IN THE PERIPHERAL SUBCHANNELS.
(Taken from reference L-1)

itself. We speculate that the region exactly upstream of the horizontal arrows corresponds to separated regions (wakes). At the location indicated by the tilted arrow, the density gradients appearing in Figure 6.6 suggest that this is the location where the separated region is reattaching to the rod surface.

The above arguments can also be supported by the work of Sarno, Gori and Andalo (S-1). They performed local pressure and velocity measurements in a 19 rod bundle with water in turbulent flow. Figure 6.7 gives the static pressure distribution at the circumference of each rod at a given axial level. Note that for each rod there are two pressure zones, the high and the low one. Each zone stretches over approximately 180° of the rod circumference. The wire spacer itself lies in one of the two boundaries between the high and the low pressure regions. Referring to Figures 6.6 and 6.7 one can speculate that the low and high pressure a of Figure 6.7 correspond to the wake and stagnating regions of Figure 6.6 respectively.

Ohtake, Urawashi and Takahashi (O-1) performed local velocity measurements in a ~ 5:1 scale, turbulent air flow wire-wrapped rod bundle with P/D = 1.19 and H/D = 34.8. Figures 6.8 and 6.9 give some of their local transverse velocity fields for interior and peripheral channels respectively. Their results closely parallel the Westinghouse results (B-1). The heavy lines and the alphanumeral symbols in Figure 6.8 have been added for later discussion.

Finally, Figures 6.10 and 6.11 give detailed axial velocity field results from Westinghouse (B-1) and Lafey et al. (L-1) respectively. Note that in both figures the velocity variations are of the same order of magnitude.

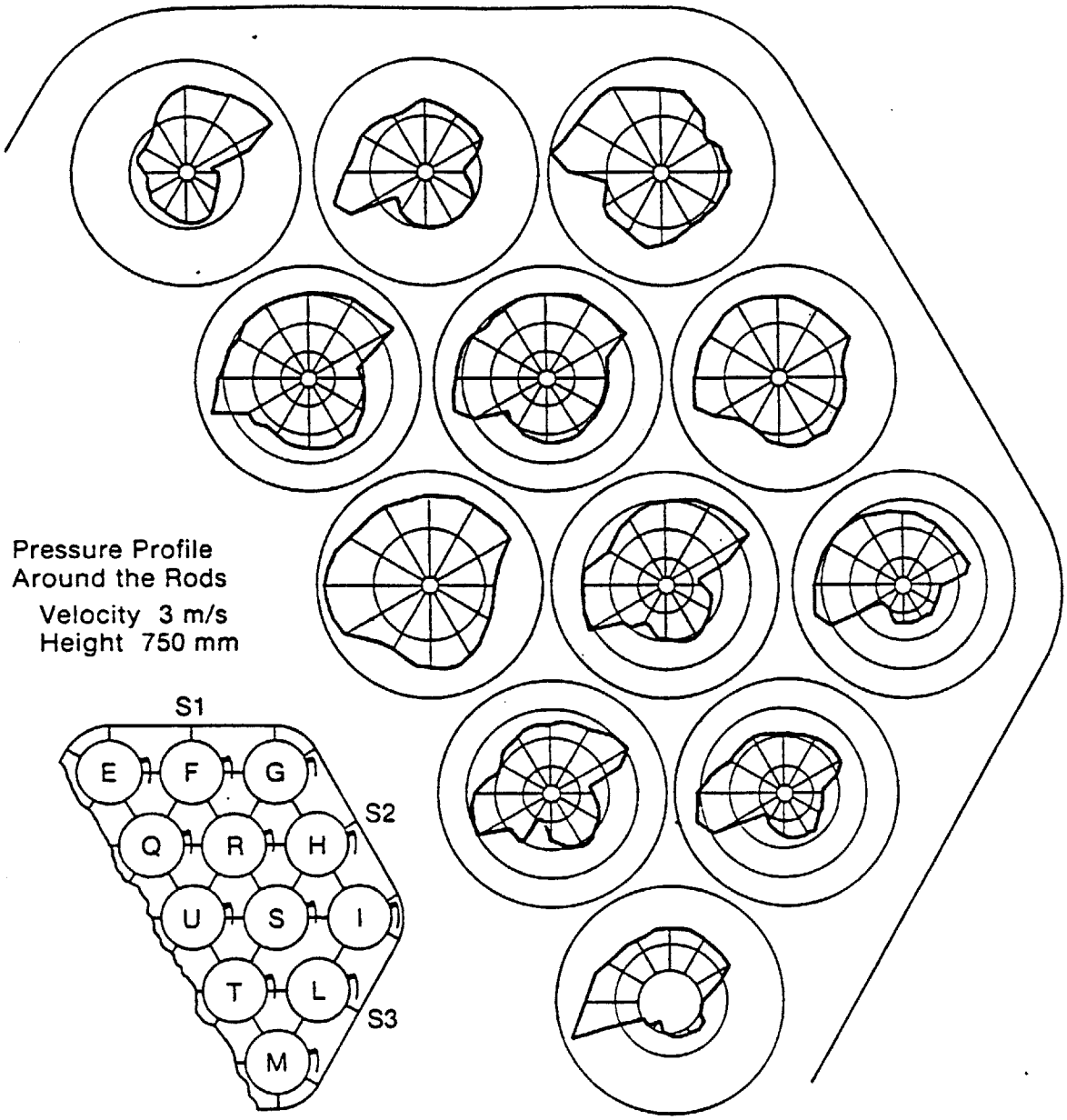

FIGURE 6.7: PRESSURE DISTRIBUTION AROUND WIRE-WRAPPED RODS.
P/D = 1.15 (Taken from reference B-5)

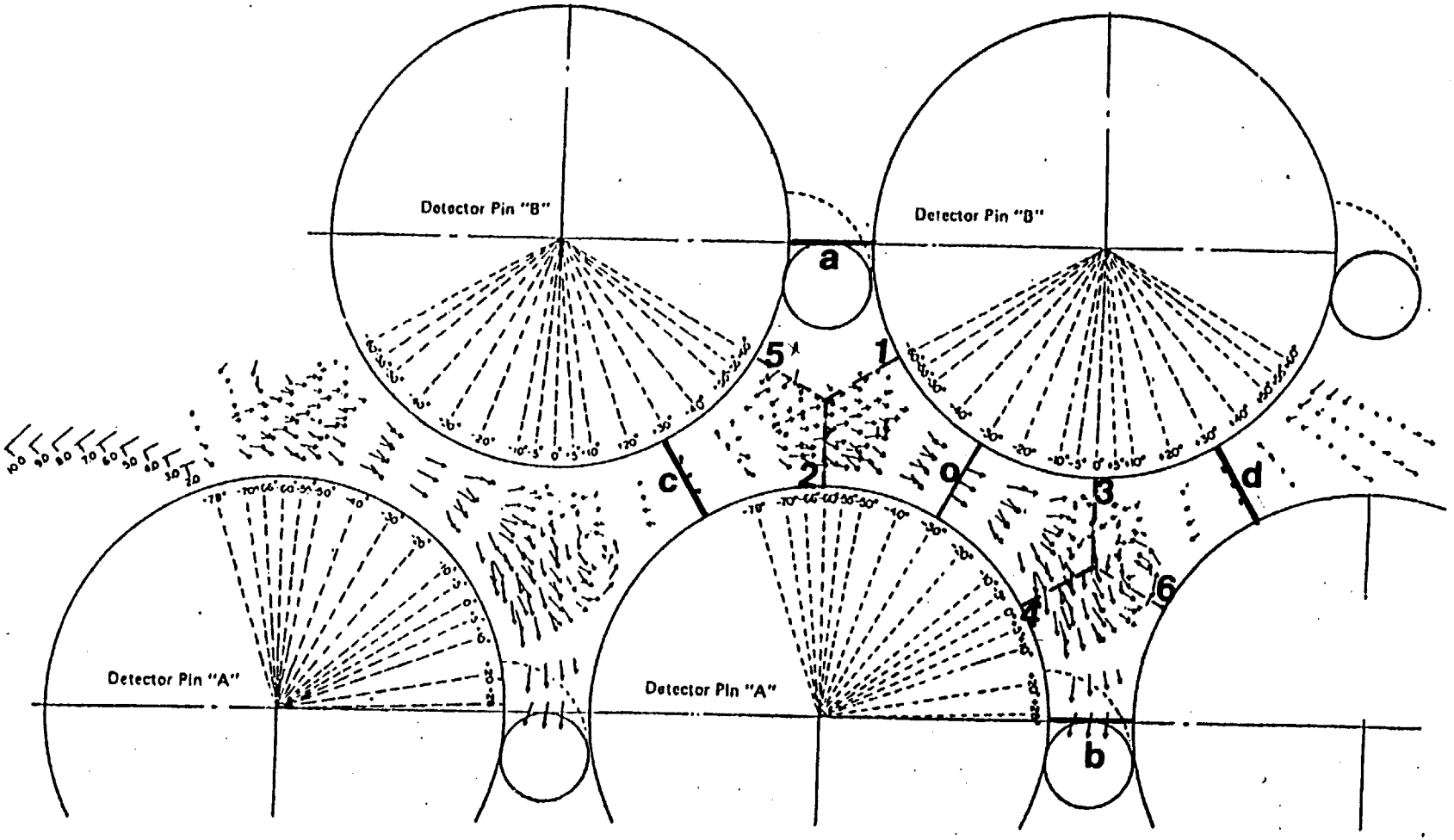

FIGURE 6.8: DETAILED LOCAL TRANSVERSE VELOCITY DATA FOR INTERIOR SUBCHANNELS. Re = 15000
(Taken from reference 0-1)

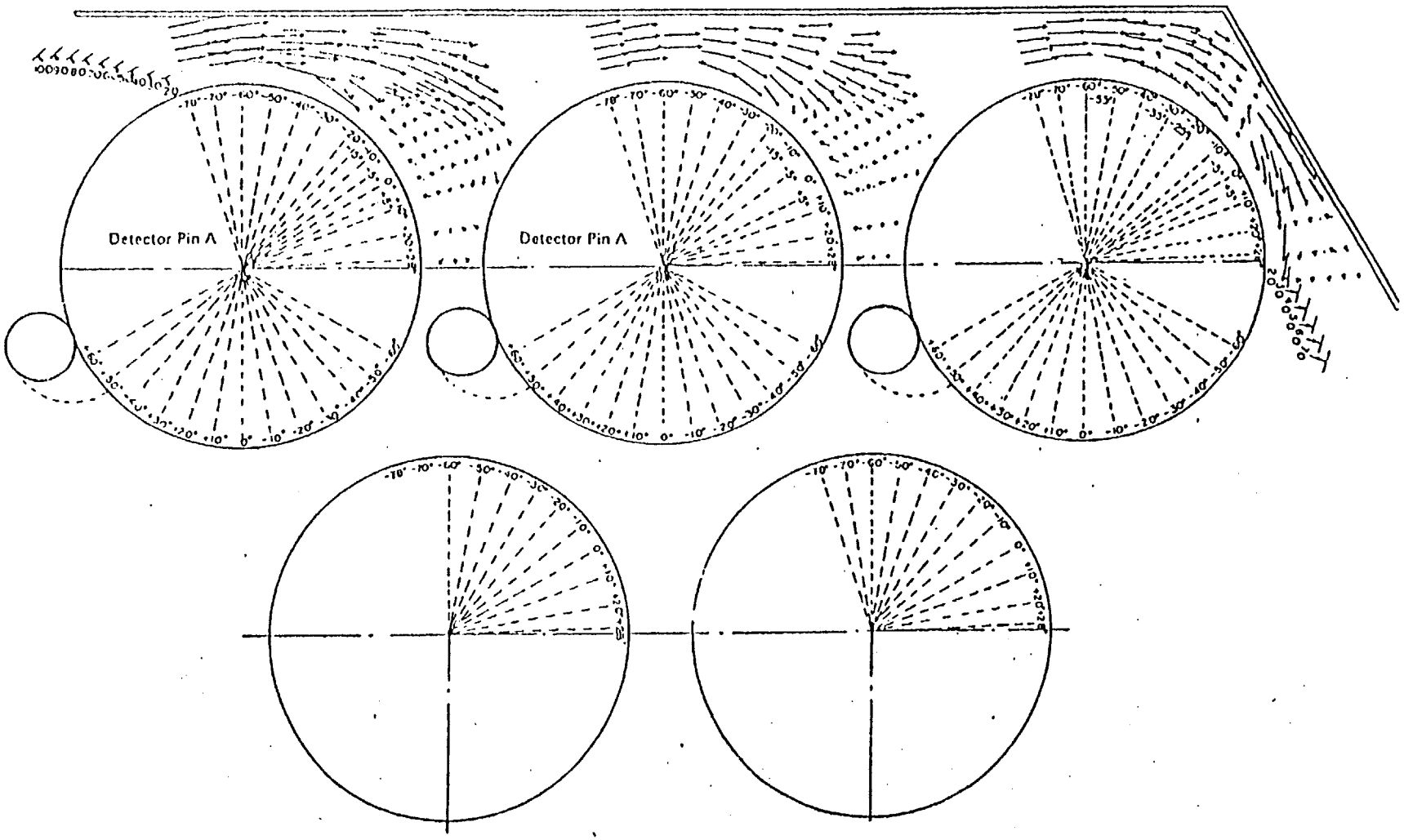

FIGURE 6.9: DETAILED LOCAL TRANSVERSE VELOCITY DATA FOR PERIPHERAL SUBCHANNELS. Re = 15000
(Taken from reference 0-1)

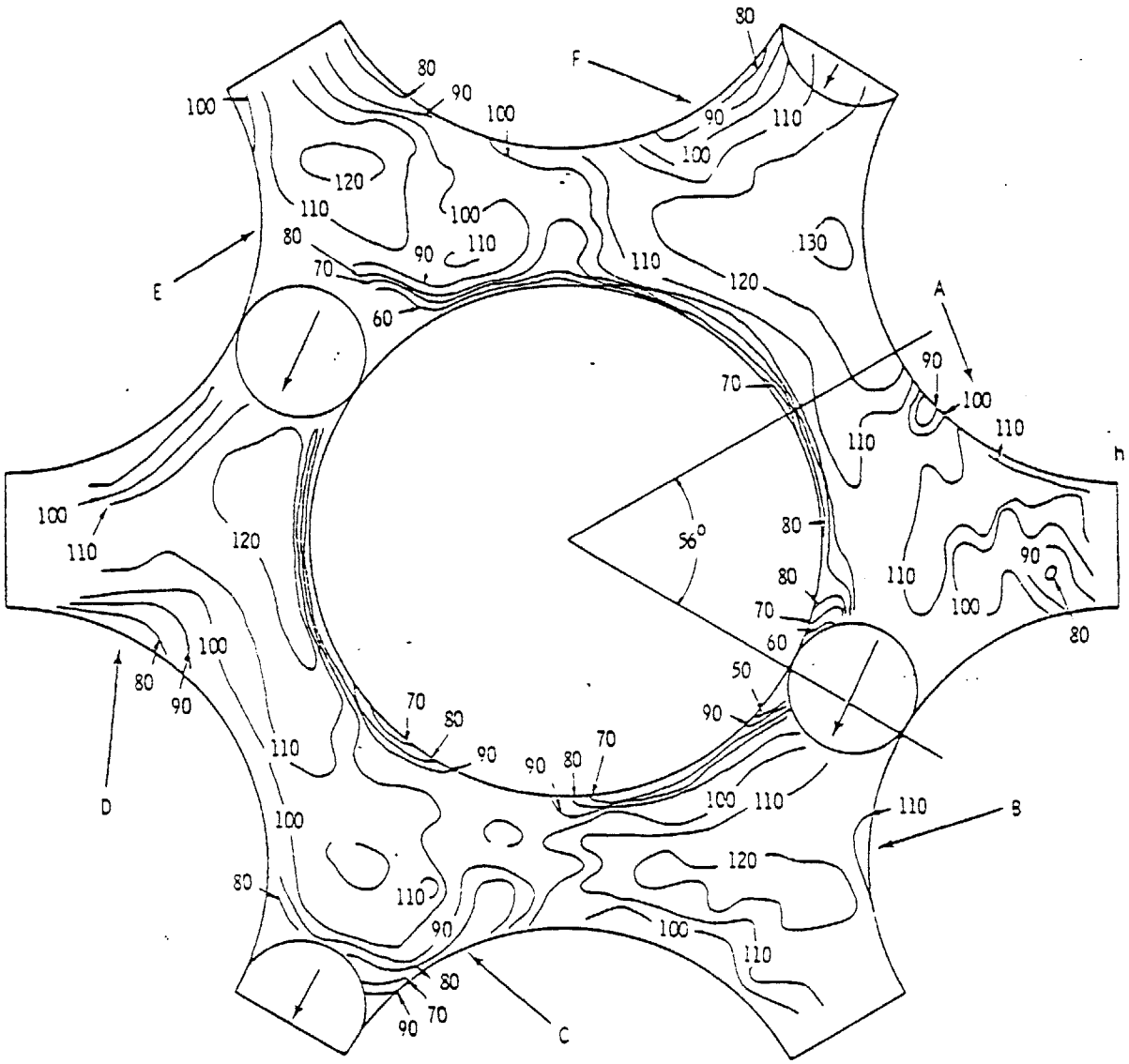

FIGURE 6.10: AXIAL VELOCITY DISTRIBUTION FOR INTERIOR SUBCHANNELS.
(Taken from reference B-1)

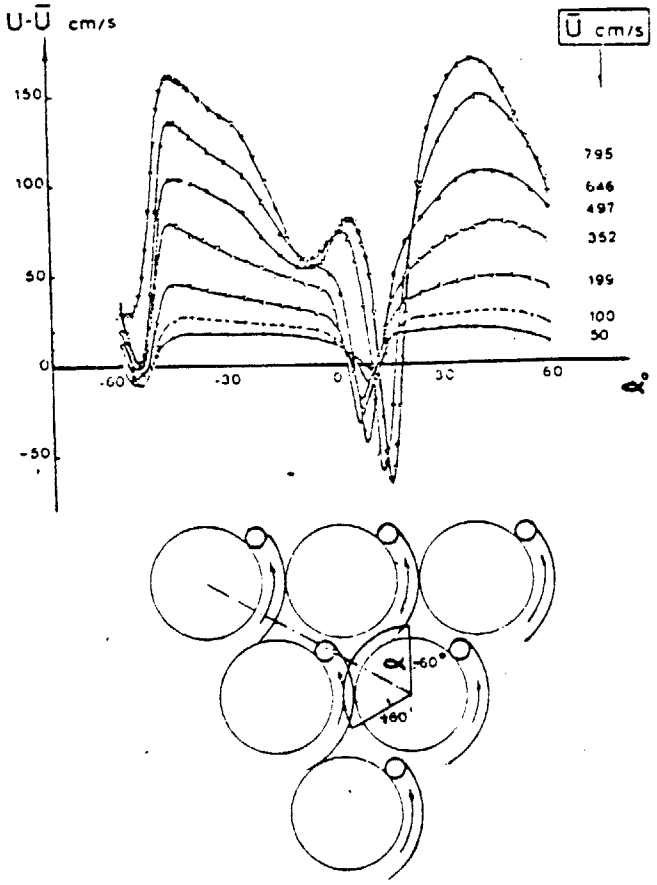

FIGURE 6.11: AXIAL VELOCITY DISTRIBUTION IN INTERIOR SUBCHANNELS.
(Taken from L-1)

Based on the above experimental findings and in particular on the visual observation reported in (L-1), we proposed in Figure 6.12 a schematic model for the flow stagnation region and the wake region around the wire-spacer. The stagnation region is defined as the region upstream the wire-spacer, whereas the wake region is formed downstream of the spacer.

Based on this physical description of the wire-wrap effects on the flow fields, we proceed to examine the validity of the subchannel analysis approach for wire-wrapped rod bundle analysis.

6.3.3 Subchannel Analysis Approximation and Limitations

6.3.3.1 The Convective Terms

The most important limitation of the subchannel analysis approach is the omission of the axial vorticity terms of the full momentum flux array:

$$\vec{V} \cdot \vec{V} = \begin{bmatrix} u\,u & \textcircled{u\,v} & u\,w \\ \textcircled{v\,u} & v\,v & v\,w \\ w\,u & w\,v & w\,w \end{bmatrix} \tag{6.9}$$

where u and v lay on a horizontal plane and w is the axial velocity.

The omitted terms are encircled in equation 6.9. Subchannel analysis in principle can introduce these terms for square rod array analysis (orthogonal gap directions). Theoretically though this is not true for triangular rod arrays since the gap directions do not lay on an orthogonal co-ordinate system.

For bare rod bundles this omission does not introduce serious errors even for predominately lateral flows. This can be explained with the help of Figure 6.13(a). It is seen that the momentum flux vector component:

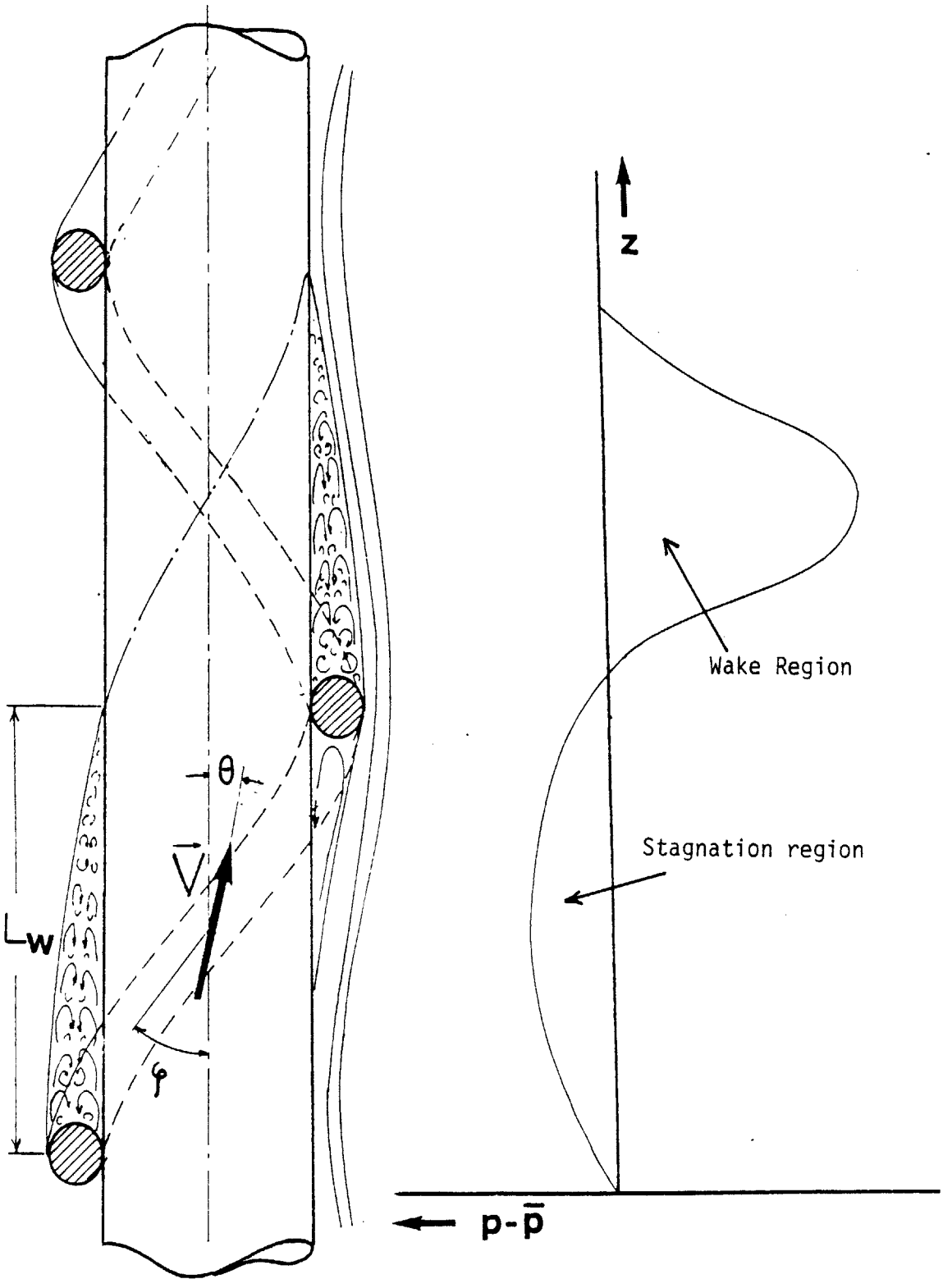

FIGURE 6.12: WAKE AND PRESSURE DISTRIBUTION FOLLOWING THE WIRE SPACER.

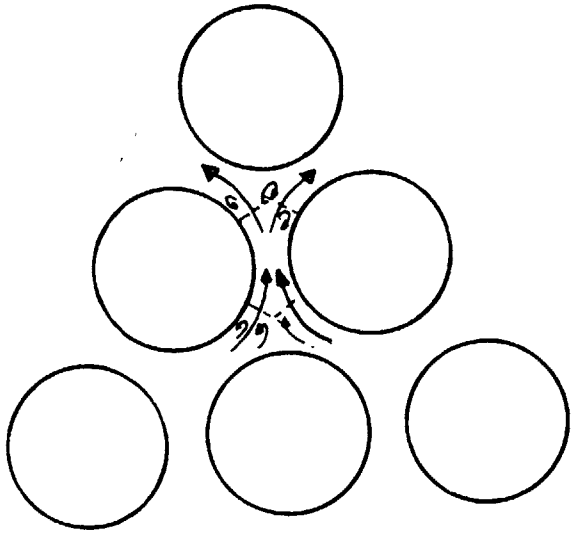

FIGURE 6.13(a): AXIAL VORTICITIES FOR LATERAL FLOWS IN BARE ROD BUNDLES.

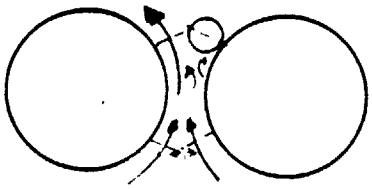

FIGURE 6.13(b): AXIAL VORTICITIES FOR LATERAL FLOWS IN WIRE-WRAPPED ROD BUNDLES.

$$uv = \int_{A_f,\ \text{horizontal}} \rho \vec{V} \cdot \vec{V}\, dA \qquad (6.10)$$

will be close to zero since the axial vorticities tend to be symmetric and counteracting each other. However, in the case of wire-wrapped rod bundles the axial vorticity momentum integral given by equation 6.10 is not expected to be negligible when the wire-spacer is close to the gap. (see Figure 6.13(b)). In this case, the axial vorticity momentum effects should be accounted on an empirical basis, since they cannot be modeled within the framework of the subchannel anaylsis approach.

One other term that is also usually omitted in the subchannel anaylsis approach is the u.u term in the lateral momentum equation (term (2) in equation 6.6)

The term (2) = $\frac{\Delta}{\Delta x'}(W_{ij}\{u\})$ is usually negligible in comparison with the term (3) = $\frac{\Delta}{\Delta z}(W_{ij}\{w\})$ in the case of bare rod bundles. However, this might not be the case for wire-wrapped rod bundles. This argument can be supported with the data of Figure 6.8. For the transverse control volume centered at gap (0), the momentum flux at the vertical side (4) is much larger than the fluxes at the rest of the sides (1), (2) and (3). Term (2) corresponds to the $\int_{A_f\ \text{vert.}} W_{ij}(\vec{V}\cdot n)\hat{dA}$ term of equation 6.2 and so order of magnitude analysis, using also Figure 6.8 gives:

$$(2) \sim \int_{A_f\ \text{vertical}} W_{ij}(\vec{V}\cdot\hat{n})dA \sim W_{ij}^2 \sim (0.1\ \overline{U}_b)^2 \quad ;$$

since the velocity across side 4 is approximately equal to the velocity at the gap b.

$\overline{U}_b$ = average bundle velocity

The term (3) corresponds to the $\int_{A_{f_{horiz.}}} W_{ij}(\vec{V}\cdot\hat{n})dA$ term and so

$$(3) \sim \int_{A_{f_{horizontal}}} W_{ij}(\vec{V}\cdot\hat{n})dA \sim W_{ij}\{w\} \sim$$

$$\sim 0.08\,\overline{U}_b \cdot \overline{U}_b$$

These comparisons indicate that

order of magnitude

(2) ~ (3)

Therefore, term (2) cannot be neglected.

However, the above result was based on a single axial level of the subchannel. It could be that on the average ($\Delta z \sim H/12$), the various components of term (2) cancel out.

Some subchannel codes treat term (2) in a quite empirical way. COBRA (S-2) for example adds vectorially the transverse momentum fluxes of the adjacent gaps (gaps (a), (b), (c) and (d) of Figure 6.8. The vector sum is multiplied with an arbitrary constant, to be estimated from data fit analysis. This vectorial sum can be visualized in Figure 6.14. All the vectors are projected on a reference direction which forms an angle β_1 with the gap of interest. However, for any reference angle the vectorial sum of momentum fluxes at gaps (a), (b), (c) and (d) of Figure 6.8 equals zero, since the momentum fluxes at gap pairs (a), (b), and (c), (d) are equal in magnitude and opposite in sign. On the contrary, the vectorial sum of the momentum fluxes on the vertical sides (1), (2), (3) and (4) of the transverse control volume is not zero, as was discussed above.

Unfortunately, the transverse velocities at sides (3), (4) and (6) cannot be calculated using the transverse velocities at gaps (0), (b) and (d) and the continuity equation. Additional empirical information is

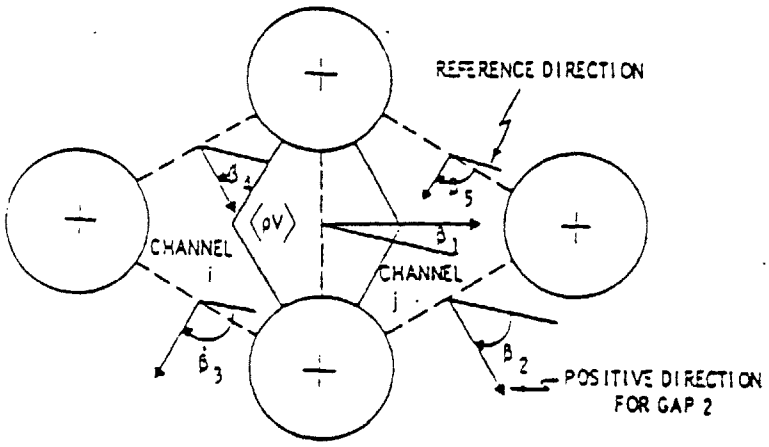

FIGURE 6.14: COBRA SCHEME FOR GAP REFERENCE ANGLES.
(Taken from reference T-1)

required for the magnitude and geometrical charactersitics of the axial vorticity within the subchannel (odb) of Figure 6.8. Until then, a more rigorous formulation of the term (2) cannot be developed.

6.3.3.2 The Pressure Terms

(a) Axial Momentum Equation

As it can be observed in equation (6.5), the pressure term is of the following form:

$$- A_{fi} \frac{\Delta[p]}{\Delta z} = - A_{fi} \frac{\langle p \rangle_u - \langle p \rangle_\ell}{\Delta z} \tag{6.11}$$

where u and ℓ stand for upper and lower control volume surface respectively. This formulation assumes that both the axial subchannel area and pressure vary linearly with axial length. In this case, the force F_w exerted by the fluid on the solids is given by:

$$F_w = \langle p \rangle_m \, (A^u_{fi} - A^\ell_{fi}) \tag{6.12}$$

where m stands for the middle section of a given control volume. Adding F_w, to the pressure force on the control volume F_p where F_p is given by:

$$F_p = - \langle p \rangle_u \, A^u_{fi} + \langle p \rangle_\ell \, A^\ell_{fi} \tag{6.13}$$

and dividing by Δz we get:

$$\frac{F_p + F_w}{\Delta z} = - \frac{A^m_{fi} \, (\langle p \rangle_u - \langle p \rangle_\ell)}{\Delta z} \tag{6.14}$$

Equation 6.14 is equivalent with the pressure term of equation 6.11.

In the wire-wrap case the linearity assumptions leading to the estimation of F_w in equation 6.12, are not valid any more. Both area and pressure vary non-linearly along the axis, when the wire-spacer is present. In Chapter 7 a non-linear model for estimating F_w in wire-wrap rod

bundles is presented. Since the wire-spacer/fluid force F_w is accounted in these models, which are introduced into the subchannel analysis equations via the distributed resistance terms (terms (7) and (5) in equations 6.5 and 6.6), the correct form of the pressure terms:

$$\text{Pressure Term} = \frac{-A^u_{f_i} \langle p \rangle_u + A^\ell_{f_i} \langle p \rangle_\ell}{\Delta z} \tag{6.15}$$

The only problem with this formulation is that it is succeptible to numerical instabilities when the initial guess of the pressure field is not "close enough" to the actual one. How "close" the initial guess of the pressure field should be, depends on solution algorithm. Most of the time the initial guess should bear some resemblance of the non-linear effects of the final solution, in order to obtain stable convergence of the solution algorithm.

(b) Transverse Momentum Equation.

The pressure term in Equation 6.6 can be written in the following form.

$$S_{ij} \frac{\Delta}{\Delta x} \{p\} = \frac{s}{\ell} (p_i - p_j) \tag{6.16}$$

The parameter s/ℓ is well established in the subchannel analysis literature and it physically represents the ratio of the gap size to the distance between two neighbor subchannels. In COBRA series of codes, s/ℓ is specified by the user. Higher values of s/ℓ will tend to downplay the convective terms effects in equation 6.6 in favor of the pressure term effects.

In the case of wire-wrapped rod bundles the formulation given in equation 6.16 is not correct. This can be explained with reference to

Figure 6.15, which gives a 3-dimensional view of the wire-spacer cross-section with the transverse momentum equation control volume. In this Figure, the wire is moving out of the control volume and physically blocks a portion of the vertical face, VKOX, of the control volume. This fact is not reflected in equation 6.16. A more appropriate form would be:

$$\text{Pressure Term} = \frac{\sqrt{3}}{2} \frac{S_{ij}}{Vg} \left(A_{c,i} \langle p_i \rangle - A_{c,j} \langle p_j \rangle \right) \qquad (6.17)$$

where V_g is the control volume and $A_{c,i}$ and $A_{c,j}$ are given in Figure 6.15 as follows:

$$A_{c,i} = (SPYGS) + (PYZTP)$$

$$A_{c,j} = (KUWOK) + (VXOKV)$$

and $\sqrt{3}/2$ stands for COS(60°).

Note that for the case of Figure 6.15, $A_{c,i}$ is larger than $A_{c,j}$ since part of the $A_{c,j}$ surface is blocked by wire-spacer. This pressure term formula therefore corresponds to a variable s/ℓ situation for each individual gap and offers a geometrical modeling of the wire-spacer blockage effect.

Here again this approach is also susceptible to numerical instability problems as the authors found here at MIT working on the ASFREMIT numerical program. To avoid these problems one can use the following formula:

$$\text{Pressure term} = \frac{\sqrt{3}}{2} \frac{S_{ij}}{V_g} \frac{(A_{c,i} + A_{c,j})}{2} (\langle p_i \rangle - \langle p_j \rangle .) \qquad (6.18)$$

In equation 6.18 volume porosity effects are correctly modeled through the use of the V_g parameter. V_g does not include the volume of the wire-spacer. In contrast with equation 6.17, equation 6.18 does not fully account for surface blockage (or surface porosity) effects in the pressure

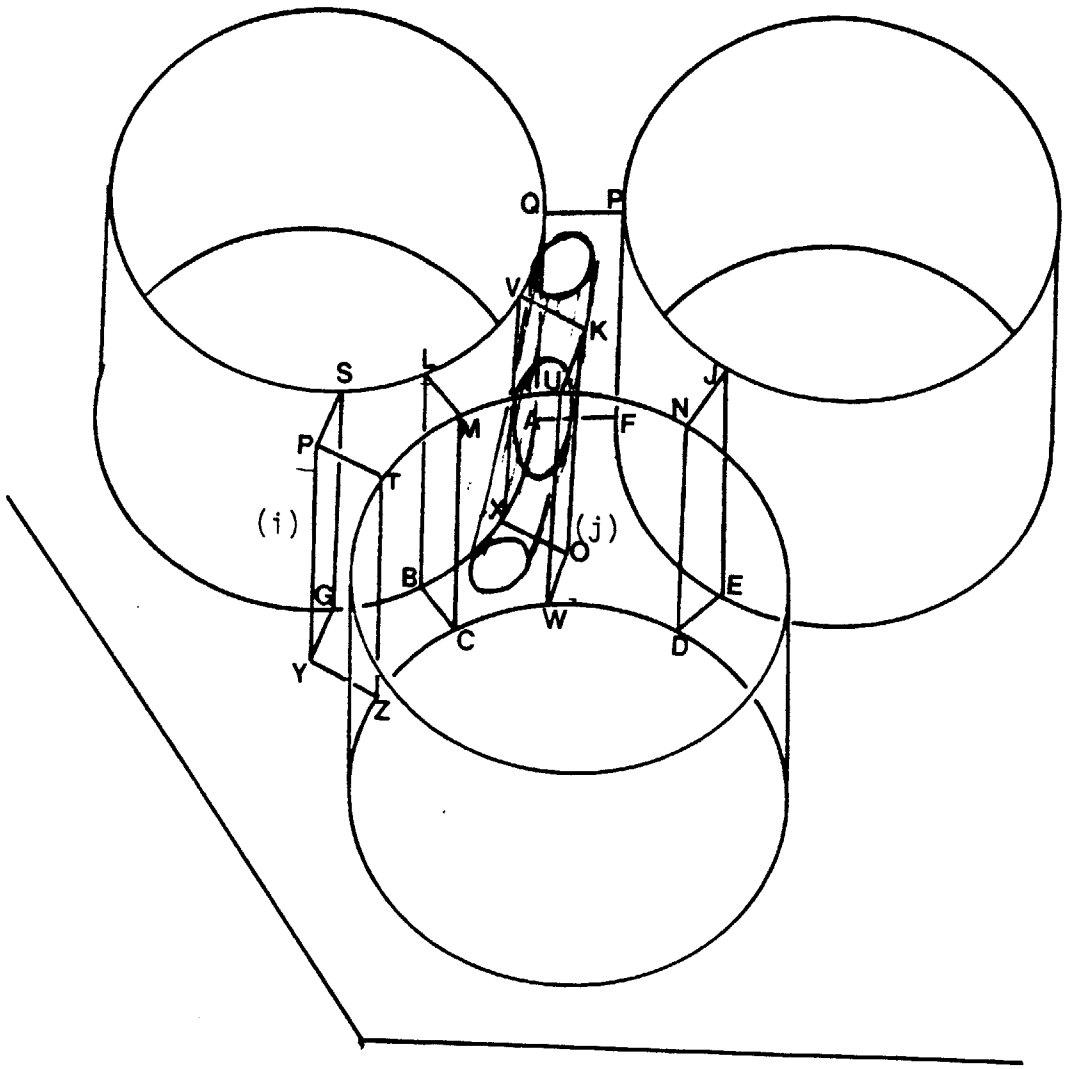

FIGURE 6.15: A 3-DIMENSIONAL VIEW OF A SUBCHANNEL AND A GAP.

term. Note that an empirical coefficient may still be needed in equation 6.18 to account for the momentum terms, as discussed in 6.3.3.1.

6.3.3.3. The Distributed Resistance Terms

The distributed Resistance terms (7) and (5) of equations 6.5 and 6.6 respectively are directly affected by the presence of the wire spacer. Due to geometrical asymmetries created by the wire-spacers, the models for terms (7) and (5) have to be individually tailored for each gap or subchannel control volume. It is through these terms that the fundamental flow characteristics due to helicoid spacers are established. Chapter 7 presents our Distributed Resistance Models (DRMs) for wire-spacers in rod bundles. In Chapter 8, these models are tested against the experimental data and the importance of the wire-spacer effects and the convective and pressure terms is also assessed.

6.4 Subchannel Analysis versus Porous Body Approach.

The numerical mesh of Figures 6.2(f) and 6.3 used in the subchannel analysis approach is one out of a practically infinite number of meshes that can be configured over rod bundles. Figure 6.2 gives some typical numerical meshes that are used in the porous body approach. The "porous body" definition refers to all thermo-hydraulic numerical programs which employ orthogonal coordinate systems (cartesian or cylindrical) to discretize the integral balance equations 6.1, 6.2 and 6.3.

The main consideration in the porous body approach is cost versus accuracy. The quarter-pin mesh geometry of Figure 6.2(e) requires more computational effort than the full-pin mesh geometry of Figures 6.2 (a) and (c). Referring to Figure 6.2 it is observed that the subchannel analysis mesh is a little more fine than the full-pin mesh and much coarser

than the half-pin mesh geometrics.

For square arrays, Rowe (R-4) compared both approaches (subchannel versus porous body) and found them almost equivalent. (The subchannel approach neglects the axial vorticity momentum terms). Note that for the square array case the subchannel mesh becomes orthogonal. Similar conclusions were independently drawn by Todreas (T-1). In triangular rod arrays however the two approaches differ substantially regarding the way and location where the axial and lateral velocities are defined. As it can be seen from Figure 6.2 all porous body mesh configurations do not coincide with the subchannels and gaps as defined in 6.2(f). The following remarks can be made:

(a) Since the subchannel is physically confined by the presence of three neighboring rods, it is expected in general that the axial velocity profiles will be flatter within the same subchannel than within an area of a typical porous body control volume.

(b) The same is true for the lateral velocities since in subchannel control volumes, lateral velocities are defined at the gaps between two neighbor rods. It is generally expected that the lateral velocities are more flat and oriented towards one or the other direction than in any other lateral surface of any porous body control volume.

(c) Remarks (a) and (b) are also true for the case of cylindrical porous body meshes.

Remarks (a) and (b) above indicate that in porous body methods the error of discretizing non-linear integral terms is higher. This can be explained as follows:

let $u = \bar{u} + u'$; u,w : velocities.

$w = \bar{w} + w'$

where -- is a spatially averaging operator and $\bar{u}' = \bar{w}' = 0$.

Then the non-linear $\overline{uw}$, which appears when discretizing the integral momentum equations 6.2, is approximated as follows:

$$\overline{uw} = (\bar{u} + u')(\bar{w} + w') = (\overline{uw} + \bar{u}w' + \bar{w}u' + u'w')$$

or $$\overline{uw} = \bar{u}\bar{w} + \overline{u'w'}$$

Usually the term $\overline{u'w'}$ is neglected and

$$\overline{uw} \sim \bar{u}\,\bar{w}$$

However, the higher the non-uniformity of velocities u and w over the area where averaging takes place, the higher the value of the $\bar{u}'\bar{w}'$ term and the higher the error introduced by neglecting it. This is particularly true in the case of wire-wrapped rod bundles where the presence of the helicoid spacer enhances non-uniformities in the velocity, pressure and temperature field.

An additional advantage of the subchannel approach also stems directly from remarks (a) and (b) above. Most of the constitutive relations for friction factors in rod bundles are derived based on the subchannel axial and lateral velocities. Therefore these relations can be directly applied in subchannel analysis meshes whereas some adaptation work is usually required for the porous body approach. In the later case some additional error is introduced for both coarse or fine porous body meshes. In summary, the subchannel analysis mesh utilizes more ordered and oriented velocity vectors than those in the porous body approach in

the case of triangular array rod bundles.

Two of the most important porous body type of codes that have been used for LMFBR subassembly studies are COMMIX-1 (S-8) and THERMIT (K-2). The Cartesian coordinate system is used in both these codes. However for square rod arrays, porous body and subchannel analysis codes are almost equivalent in terms of mathematical formulation and numerical mesh geometry while this is not the case for triangular rod arrays. Figure 6.2 gives the various mesh configurations that may be used in the porous body type of analysis. In D-2, COMMIX-1 predictions for the cross-flow field using a quarter-pin mesh has been reported. In this work, COMMIX failed to predict a consistent unidirectional flow field in the peripheral subchannels, as experimental results indicate. Similar results were obtained in E-4 using the THERMIT code with $\Delta z = H/6$ and a full-pin mesh. Admittedly in both these cases the presence of the wire-spacer was taken into account only in the volume and surface porosities of the numerical mesh whereas standard bare rod friction factor models were employed. However similar work with the subchannel analysis code ASFRE did succeed in predicting a unidirectional swirl flow with standard bare rod friction factor models. (N-1).

Based on the above theoretical discussion and current experience with subchannel and porous body codes, the subchannel analysis approach appears to be a more appropriate tool for dealing with wire-wrapped triangular rod arrays.

CHAPTER 7

THE DISTRIBUTED RESISTANCE MODELS (DRM)

7.1 Introduction

In this chaper we present a general method to formulate the Distributed Resistance Models (DRM) for flows in wire-wrapped rod bundles. The models include laminar, transition and turbulent flow conditions and can treat 3-dimensional velocity fields.

At first the state-of-the-art in Distributed Resistance Modeling of Wire-Wrap Bundles is reviewed. Then the integral representation of the proposed DRMs is given together with a schematic break down of all DRM components. Subsequently the DRMs are formulated for three increasingly complex rod bundle geometries:

(a) bare rod bundles

(b) rod bundles with displacers*

(c) wire-wrapped rod bundles

The above procedure facilitates the task of physically explaining the proposed DRMs for wire-wrapped rod bundles. The formulation of the models is general enough so that the DRMs can be easily adopted for any mesh size length Δz less than H/6, where H is the wire-wrap lead length.

7.2 Literature Review

Early efforts to account for the presence of the wire-wrap spacer in rod bundles were made in COBRA-IIIC subchannel analysis code by Rowe (R-2). The effect of the wire-spacer was accounted in two different ways:

---

*A displacer is a wire-wrapped spacer with $H/D \to \infty$.

(a) All geometrical parameters were modified accordingly (wetted perimeters, hydraulic diameters, etc)

(b) In all gaps where the wire-spacer was present moving from subchannel (i) to subchannel (j) some flow from the subchannel (i) was directed to subchannel (j). This forced cross-flow caused by the presence of the wire spacer was estimated as follows:

$$W_{ij}^{forced} = \frac{\pi(D + D_w)\ S}{A_i}\ \frac{\delta}{\Delta z}\ m_i \qquad (7.1)$$

where D_w is the wire-spacer diameter, S is the gap width, A_i is the area of the subchannel, m_i is the subchannel (i) flow rate and δ is an arbitrary parameter to be calibrated from the data. From equation 7.1 it is seen that W_{ij}^{forced} is a fraction of m_i which is proportional to the total wire-spacer caused blockage (equal to $\pi(D + D_w)S$) over the subchannel flow area A_i. Apparently this "forcing function" type cross-flow model is based solely on continuity considerations and does not account for momentum effects. In other words, the forced cross-flow model provides flow inputs and <u>not</u> resistance inputs. Similar "forcing function" type models were used in a number of subchannel analysis codes (see section 8.2). All of them have the same fundamental problem: Since they do not account for flow resistance due to the wire-spacer in a correct way, their arbitrary constant δ needs to be recalibrated each time some flow or geometrical parameter changes.

In order to avoid this problem, a new generation of wire-wrap models have been developed, based on the Distributed Hydraulic Resistance con-

cept. Here the wire-spacer is accounted for by using additional resistance terms in both the axial and lateral momentum equations. Early work along these lines was performed at MIT which focused on developing DRMs for the ENERGY series of codes for both turbulent (C-1) and laminar (B-4) flow conditions. These DRMs were particularly tailored for axial mesh size Δz equal H.

Davis (D-1) developed DRMs for the SABRE subchannel analysis code, valid for Δz equal to H/6 and for turbulent flow conditions. There are no open literature results illustrating the testing of this model against data. LeGuez (L-2) extended Davis's model for Δz equal to H/24 and reported satisfactory predictions of the WARD data (R-1). However, the essentials of their DRM have not been made available.

All of the above DRMs were developed for predominately axial flows under turbulent conditions. Here we develop an approach to include both predominately axial (along the rods) and predominately lateral (normal to the rods) flows. Laminar flow conditions are also considered. In what follows, the DRM is outlined, clearly stating all new ideas introduced in this work. Despite the fact that the models are particularly developed for the subchannel analysis approach, the models can be also extended to porous body approach numerical programs.

7.3 Integral Representation of the DRMs

In Chapter 6 the correspondence between the terms of the integral momentum equation and those of the subchannel analysis momentum equation were discussed. The distributed resistance $\vec{F}_{DR}$, which includes the friction and form drag forces at the solid-liquid interfaces was given as:

$$\vec{F}_{DR} = \int_{A_{sf}} (-p\hat{n} + \langle \bar{\bar{\tau}}.\hat{n} \rangle)\, dA \qquad (7.2)$$

form drag — friction drag

where A_{sf} is the solid-fluid interface within a given subchannel volume V, $\bar{\bar{\tau}}$ is the stress tensor at A_{sf} and $\hat{n}$ is a unit vector normal to A_{sf}. For a bare rod bundle, A_{sf} is equal to the surface area of the rods A_R. For rod bundles with wire-wrap spacers or displacers:

$$A_{sf} = A_R + A_W \qquad (7.3)$$

where A_W is the surface of the wire-wrap spacer or the displacer within the control volume. Therefore, equation 7.2 can be written as:

$$\vec{F}_{DR} = \int_{A_R} (-p\hat{n} + \langle \bar{\bar{\tau}}.\hat{n} \rangle)\, dA + \int_{A_W} (-p\hat{n} + \langle \bar{\bar{\tau}}.\hat{n} \rangle)\, dA \qquad (7.4)$$

or

$$\vec{F}_{DR} = \vec{F}_R + \vec{F}_W$$

Figure 7.1 illustrates a wire-wrapped rod where axis is rotated at an arbitrary angle to the vertical. This figure demonstrates the principal directions, along which all important parameters will be defined. The $\hat{n}$'s represent the unit vectors which are defined by Figure 7.1 as follows:

$\hat{n}_H$ and $\hat{n}_V$: horizontal and vertical

$\hat{n}_L$ and $\hat{n}_A$: lateral and axial (with respect to the rod bundles axis)

$\hat{n}_T$ and $\hat{n}_N$: tangential and normal (with respect to the wire-wrap or displacer direction)

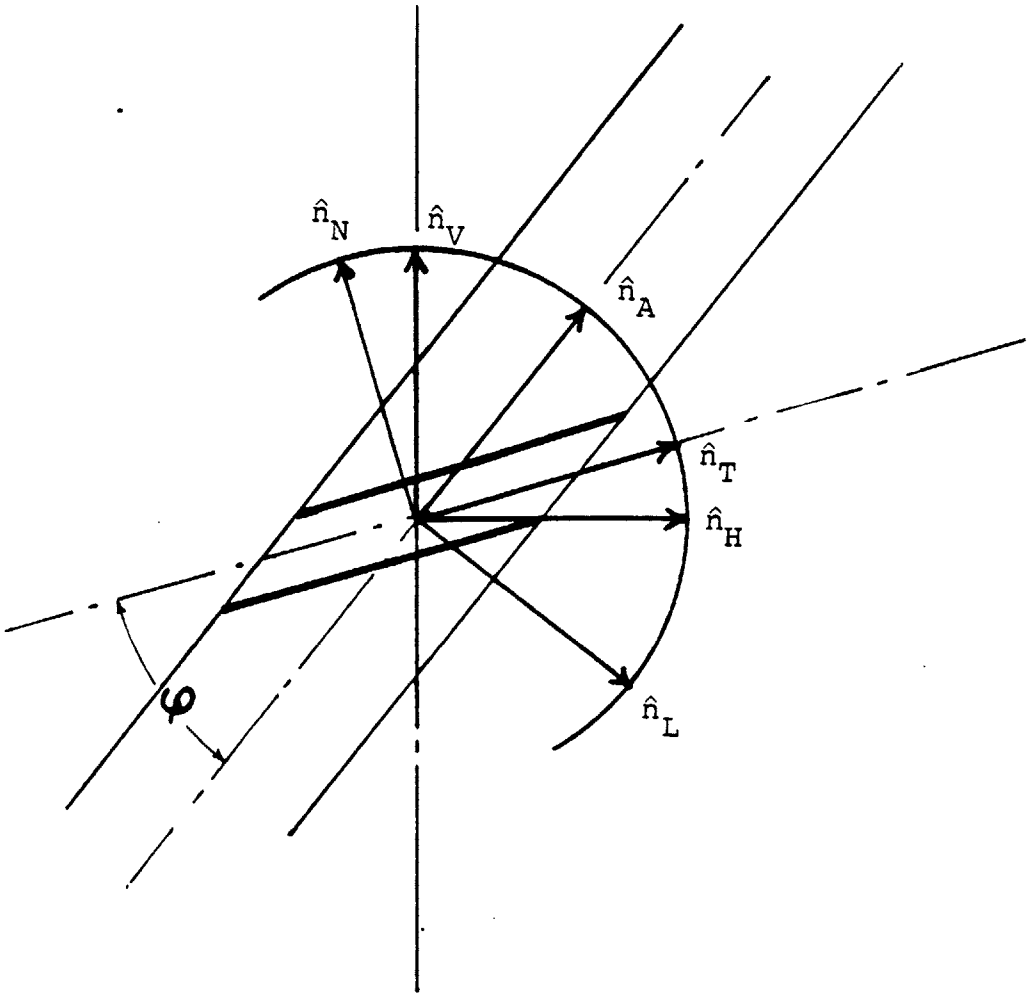

FIGURE 7.1: DEFINITION OF UNIT VECTORS DIRECTIONS.

For the wire-wrap spacer, the $(\hat{n}_T, \hat{n}_N)$ coordinate system rotates along the wire spacer while the $(\hat{n}_H, \hat{n}_V)$ and $(\hat{n}_L, \hat{n}_A)$ coordinate systems remain fixed for a given subchannel. For the displacer, $\hat{n}_T \equiv \hat{n}_A$ and $\hat{n}_N \equiv -\hat{n}_L$. The horizontal and vertical directions are not involved in the DRM. However, in most cases, the axis of the rod bundle is vertical, so that $\hat{n}_A = \hat{n}_V$ and $\hat{n}_L = \hat{n}_H$. Nevertheless, the DRM will be developed for the more general case of $\hat{n}_A \neq \hat{n}_V$ and $\hat{n}_L \neq \hat{n}_H$.

As will become clear later, it is convenient to further decompose the $\vec{F}_R$ component of $\vec{F}_{DR}$ along the axial and lateral directions and the $\vec{F}_W$ component along the tangential and normal directions respectively.

$$\vec{F}_R = \vec{F}_R^A + \vec{F}_R^L \tag{7.5}$$

$$\vec{F}_W = \vec{F}_W^T + \vec{F}_W^N \tag{7.6}$$

Using the definitions which have been presented, the following relations are true where <.> stands for the vectorial inner product.

$$|\vec{F}_R^A| = \langle \vec{F}_R \cdot \hat{n}_A \rangle = \int_{A_R} \langle \langle \bar{\bar{\tau}} \cdot \hat{n} \rangle \cdot \hat{n}_A \rangle \, dA \tag{7.7}$$

$$|\vec{F}_R^L| = \langle \vec{F}_R \cdot \hat{n}_L \rangle = \int_{A_R} (- p \langle \hat{n} \cdot \hat{n}_L \rangle + \langle \langle \bar{\bar{\tau}} \cdot \hat{n} \rangle \cdot \hat{n}_L \rangle) \, dA \tag{7.8}$$

$$|\vec{F}_W^T| = \langle \vec{F}_W \cdot \hat{n}_T \rangle = \int_{A_W} \langle \langle \bar{\bar{\tau}} \cdot \hat{n} \rangle \cdot n_T \rangle \, dA \tag{7.9}$$

$$|\vec{F}_W^N| = \langle \vec{F}_W \cdot \hat{n}_N \rangle = \int_{A_W} (- p \langle \hat{n} \cdot \hat{n}_N \rangle + \langle \langle \bar{\bar{\tau}} \cdot \hat{n} \rangle \cdot \hat{n}_N \rangle) \, dA \tag{7.10}$$

Note that the form drag term is zero in both $\vec{F}_R^A$ and $\vec{F}_W^T$ components (see equations 7.7 and 7.8). This is true since in these cases both $\langle \hat{n}\cdot\hat{n}_A \rangle \Big|$ over A_R and $\langle \hat{n}\cdot\hat{n}_T \rangle \Big|$ over A_W are zero. In contrast, the components F_R^L and F_W^N consist of both friction and form drag. Note that equations 7.7 and 7.8 are completely analogous to equations 7.9 and 7.10 respectively.

Figure 6.15 displays a wire wrap spacer within the axial momentum control volume. A schematic representation of the rod surface and the wire-spacer projected onto a vertical plane is given in Figure 7.2 The the subchannel velocity $\vec{v}$ makes an angle θ_v from the vertical due to the presence of the wire spacer. Figure 7.3a clarifies how the velocity $\vec{v}$ can be broken down into u, w or v_T , v_N velocity components. These velocity components satisfy the following relationships:

$$v_T = w \cos \phi + u \sin \phi \tag{7.11}$$

$$v_N = w \sin \phi - u \cos \phi \tag{7.12}$$

The positive directions are defined in accordance with the unit vectors of Figure 7.1.

Figure 7.3b shows the distributed resistance forces that are experience by the solid walls (rod and wire spacer) due to fluid motion. The components of Figure 3b that are encircled correspond to those given by equations 7.7 through 7.10 respectively. It is for these four components, F_R^A, F_R^L, F_W^T, F_W^N, that distributed resistance models (DRMs) will be developed as a function of P/D (pitch-to-diameter ratio), H/D (wire-wrap lead length-to-diameter ratio), and Reynolds number Re.

The axial and lateral momentum equations of the subchannel analysis approach require DR forces along the axial and lateral directions respec-

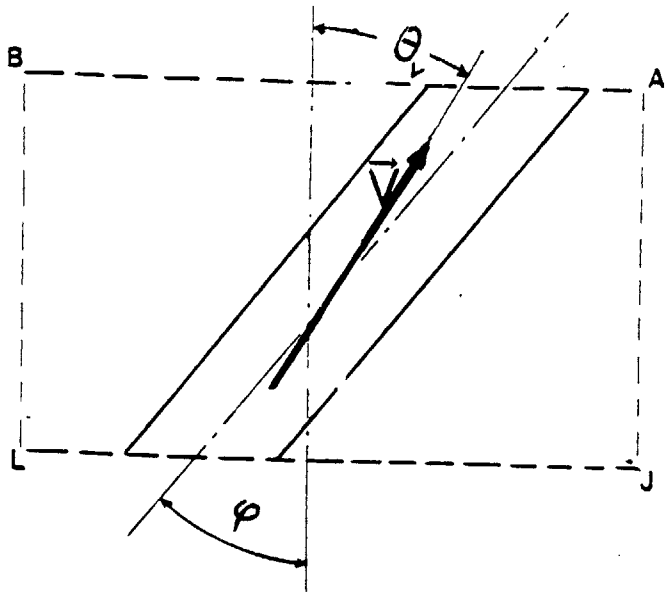

FIGURE 7.2: SIDE (ABLJ) OF FIGURE 6.15, UNRAVELED ON A VERTICAL PLANE.

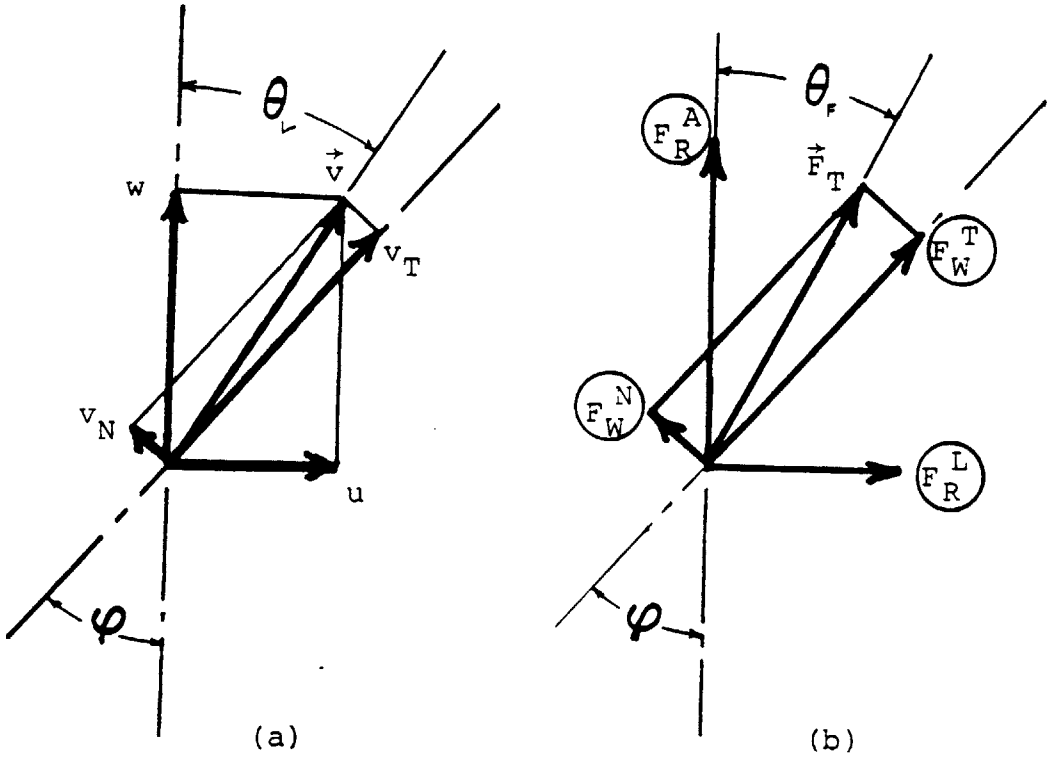

FIGURE 7.3: (a) VELOCITY COMPONENTS; (b) DRAG COMPONENTS.

tively. These forces can be expressed in terms of the above DRMs as follows:

$$F^{A}_{TOT} = F^{A}_{R} + F^{T}_{W} \cos \phi + F^{N}_{W} \sin \phi \tag{7.13}$$

$$F^{L}_{TOT} = F^{L}_{R} + F^{T}_{W} \sin \phi - F^{N}_{W} \cos \phi \tag{7.14}$$

For each individual subchannel (interior, edge, corner, with or without spacer present), the above force balance will be written. In the following paragraphs, we present DRM formulations for various subchannel geometries.

7.4 DRMs for Bare Rod Bundles

7.4.1 Introduction

In this chapter we discuss the most important correlations for axial and lateral flows in bare rod bundles. Suggestions are also made for drag calculations in the case of inclined flows in bare rod bundles. These models will be modified later in order to account for the presence of displacers and wire-wrap spacers.

Here we consider two kinds of subchannels:

(a) Subchannels in bare rod bundles

(b) Subchannels in displacer or wire-wrapped rod bundles which do not contain any spacer within the axial control volume under consideration.

In the latter case, in order to develop a unified bare rod DRM, we assume that the flow regime in the given subchannel (laminar, transition, turbulent) can be determined solely on the basis of the averaged subchannel properties (velocity, pressure, temperature). However, this is not

generally true. The most apparent deviation from the above assumption is the formation of high vorticity regions (wakes) downstream from the spacers of neighboring subchannels. These wakes, depending on geometric considerations, might be shed in the subchannel under consideration and, therefore, they might directly influence the fluid-solid interactions there. Neighboring spacers may also affect the onset of transition to turbulence, the turbulence scale, and the onset of instability in the spacer-free subchannel. These latter effects, though, are of secondary importance in comparison with the wake effect. In this report, in order to simplify the DRM formulation, we stick with the above assumption which can be stated in another way as follows: "It is sufficient to account for the wake effects only within the subchannel in which they were generated." We designate this assumption as a First-Order Approximation.

We next present the best available information on pressure drop in bare rod bundles for axial and lateral flows under laminar and turbulent flow conditions.

7.4.2 Friction Drag of Axial Flows

As equation 7.7 indicates, the axial drag component F_R^A caused by an axial flow consists of only frictional forces. From the steady-state integral momentum balance in channels, F_R^A can be directly derived as

$$F_R^A = \tau_W P_W \Delta z = - \Delta p_f A_c \qquad (7.15)$$

where P_W is the wetted perimeter, A_c is the cross-sectional area of the channel and Δp_f is the fraction of the total pressure drop Δp that corresponds to the friction forces. Then

$$\tau_W = - \frac{A_c}{P_W} \frac{\Delta p_f}{\Delta z} = - \frac{De}{4} \frac{\Delta p_f}{\Delta z} \tag{7.16}$$

Therefore, it is possible to make use of the large number of frictional pressure drop correlations that are available in the literature to calculate the wall shear stress and the axial drag.

7.4.2.1 Laminar Flow

The pressure drop will be expressed in terms of a friction factor by the well known expression:

$$\frac{\Delta p_f}{\Delta z} = - f_M \frac{1}{De} \rho w | w | \tag{7.17}$$

where Δz is an axial length, De is the subchannel hydraulic diameter, and w is the axial velocity, averaged over the subchannel cross-section, f_M is the Moody friction factor. Note that the Fanning friction factor f_F is equal to:

$$f_F = \frac{1}{4} f_M \tag{7.18}$$

Sparrow and Loeffler (S-6) gave the Fanning friction factor for axial laminar flows in rod bundles as a function of P/D, as Figure 7.4 indicates. Their result was based on numerical calculations for fully developed flow in both infinite triangles and square rod arrays, and hence apply only to interior subchannels.

Rehme (as reported by Shah and London (S-7)) performed detailed finite difference calculations for finite triangular and square arrays, including the presence of the surrounding square or hexagonal wall respectively. Again the flow was laminar and fully developed. Rehme distinguished among interior, edge, and corner subchannels, and he presented the corresponding $K_M = f_M \cdot Re_{De}$ parameter in tabular form (see S-7) as a func-

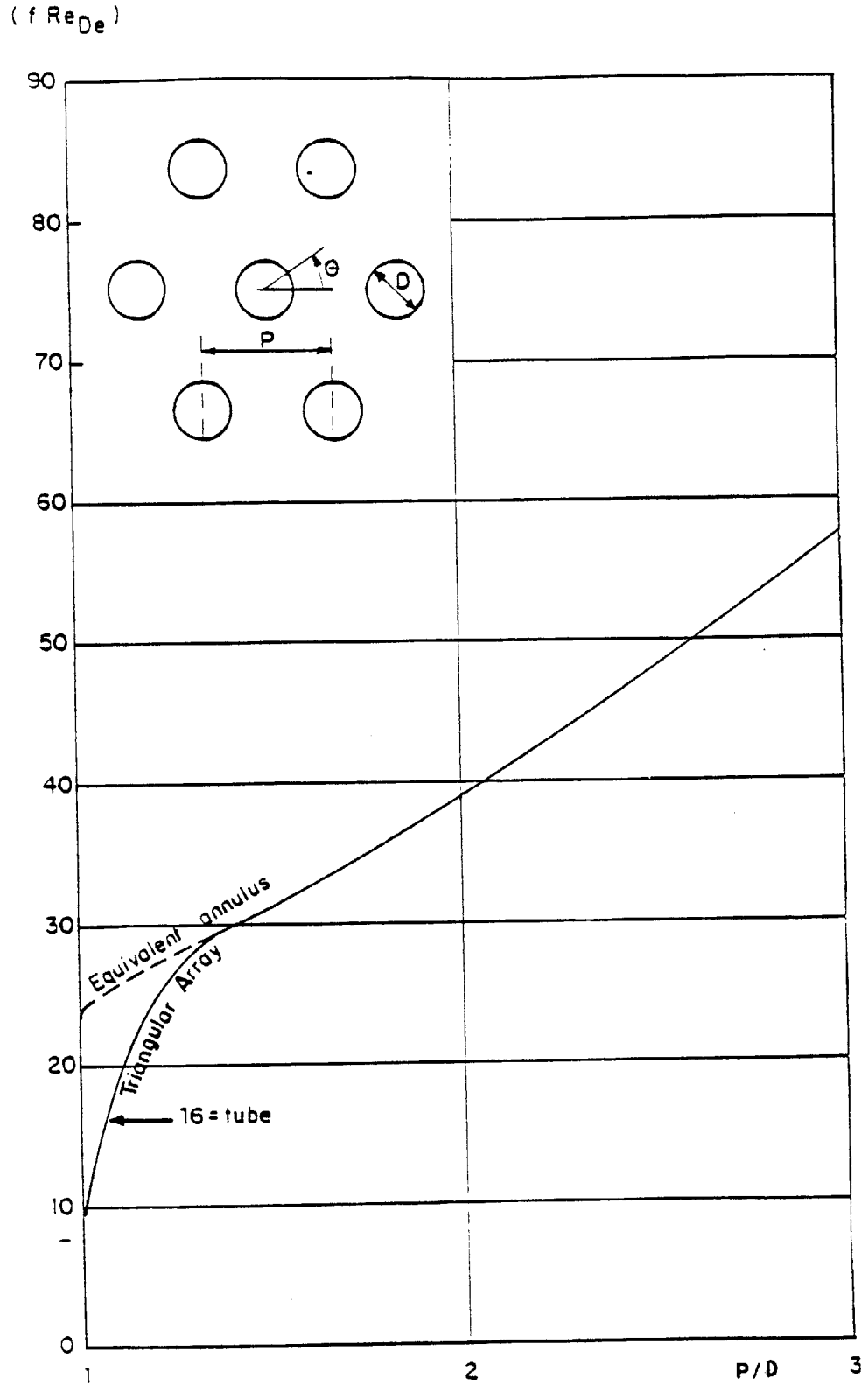

FIGURE 7.4: FRICTION COEFFICIENTS FOR FULLY DEVELOPED LAMINAR FLOW PARALLEL TO AN ARRAY FO CIRCULAR TUBES.
(Taken from reference S-6)

tion of P/D. For the edge subchannels, he accounted also for the effect of the W/D parameter (see Figure 7.7 for definition of W).

Cheng (C-6) has performed a least squares curve fit for Rehme's K_M parameter, which was presented in tabular form in (S-7). Cheng used the following polynomial curve fit:

$$K_M = a + b_1 \left(\frac{P}{D} - 1\right) + b_2 \left(\frac{P}{D} - 1\right)^2 \tag{7.19}$$

The values of the a, $b_1$amd b_2 parameters for the interior, edge, and corner subchannels are given in Table 7.1. Using the parameter K_M as calculated from equation 7.19, the Moody friction factor can be given as follows:

$$f_M = \frac{K_M}{Re_{De}} \tag{7.20}$$

Therefore, equations 7.19, 7.20 and Table 7.1 constitute a simple way for direct calculation of bare rod subchannel friction factors in laminar, fully developed flows.

For developing, laminar flows, i.e., in flows within the entrance region of a channel, the following pressure drop correlation is widely used (W-6):

$$\frac{p_1 - p(z)}{(\rho/2)w^2} = f_M \frac{z}{De} + K(z) \tag{7.21}$$

where p_1 is the inlet pressure and K(z) is the incremental pressure drop number, sometimes called the pressure defect. This last term characterizes the cumulative additional pressure drop caused by the entrance effects over the fully developed flow pressure drop. The function K(z) is given in (W-6) only for flows in pipes and parallel plates. The total

TABLE 7.1. Coefficients of equation 7.19.

	$1.0 < P/D < 1.1$ (or W/D)			$1.1 < P/D < 1.5$ (or W/D)		
	a	b_1	b_2	a	b_1	b_2
Interior	26.00	888.2	- 3334.	62.97	216.9	- 190.2
Edge	26.18	554.2	- 1480.	45.30	256.4	- 271.2
Corner	26.98	1636.	-10050.	87.26	38.59	- 55.12

TABLE 7.2 Characteristic Hydrodynamic Parameters of Noncircular Laminar Pipe Flow (H-2)

Cross Section	Geometry	D_e	K_M	K (∞)	$\frac{L_e}{De\ Re}$
Circle	Diameter d	d	64	1.25	0.057
Square	Side a	a	56.9	1.43	0.033
Rectangle	a/b = 2	2/3a = 4/3b	62.2	1.38	0.028
(sides a,b)	a/b = 5	1/3a = 5/3b	76.3	0.931	0.019
Two-dimensional	Height h	2h	96	0.674	0.011
channel					
Equilateral triangle	Side a	0.577a	53.3	1.69	0.040
Concentric annulus	d_i/d_o=0.05	$0.95d_o$=19d_i	86.3	0.830	0.021
(outer diameter d_o,	d_i/d_o=0.1	$0.9d_o$=9d_i	89.4	0.784	0.019
inner diameter d_i)	d_i/d_o=0.5	$0.5d_o$=d_i	95.2	0.688	0.012
	d_i/d_o=0.75	$0.25d_o$=0.33d_i	95.9	0.678	0.011
	d_i/d_o=1	d_o - d_i	96	0.674	0.011

pressure drop within the hydrodynamic entrance length L_e is characterized by the parameter $K(\infty)$. Typical values of $K(\infty)$ and L_e are given in Table 7.2 (taken from (H-2)).

To the author's knowledge, there is no correlation on pressure drop for developing flows in rod bundles. For the purpose of the present work then, one has to rely on results for other geometries in order to estimate the K(z) function for rod bundles. The following general formula for K(z), suggested by Shah (see (S-7), p. 399), should be used:

$$K(z^+) = 3.44(z^+)^{1/2} + \frac{K(\infty) - C_d K_M (z^+)^{-1} - 3.44(z^+)^{1/2}}{1 + C_d (z^+)^{-2}} \qquad (7.22)$$

where $z^+ = z / (DeRe_{De})$ and C_d is a geometry dependent parameter which ranges from 0.29×10^{-4} to 2.9×10^{-4} (S-7). For a given geometry of Table 7.2 (and therefore for a given value of C_d), equation 7.22 matches the analytical solutions with less than ± 3.0 percent error. In our case, we have no basis upon which to establish the value of C_d is. We arbitrarily choose $C_d = 1 \times 10^{-4}$.

In order to estimate the value of $K(\infty)$ for rod bundles, plot the data of Table 7.2 as shown in Figure 7.5. Observe that the values of $K(\infty)$ are well correlated in terms of the K_M parameter for all kinds of geometries. For rod bundles, K_M is given from equation 7.20. Therefore, we recommend the use of Figure 7.6 for $K(\infty)$ estimation.

With $K(z^+)$ known, the pressure drop within a subchannel can be calculated as follows:

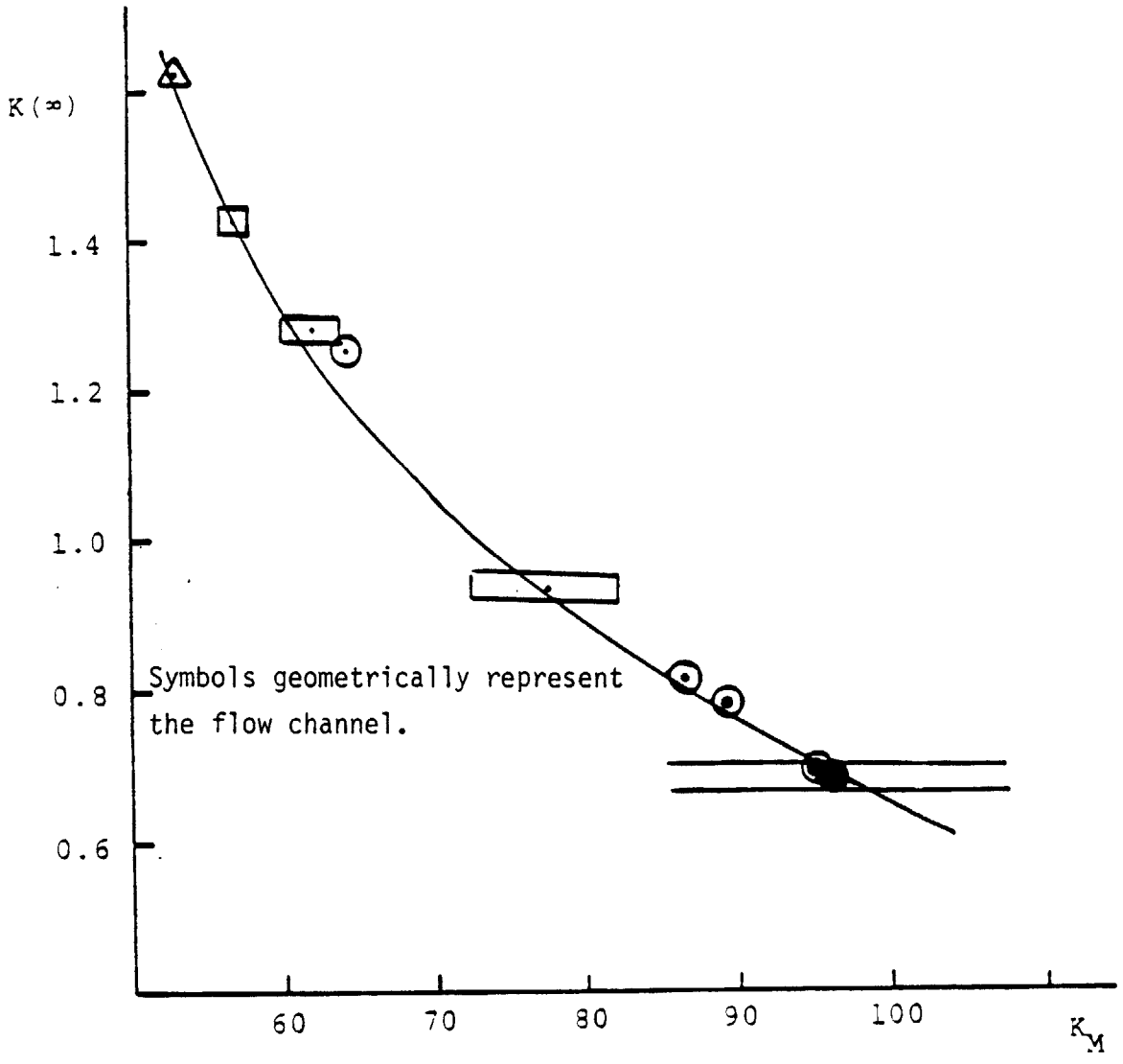

FIGURE 7.5: HYDRODYNAMIC ENTRANCE PRESSURE DEFECT AS A FUNCTION OF K_M FOR VARIOUS CHANNEL GEOMETRIES.

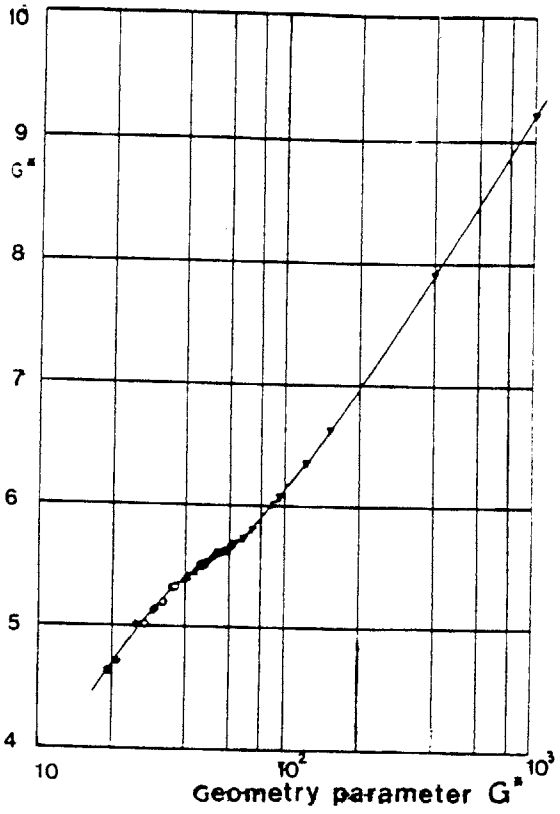

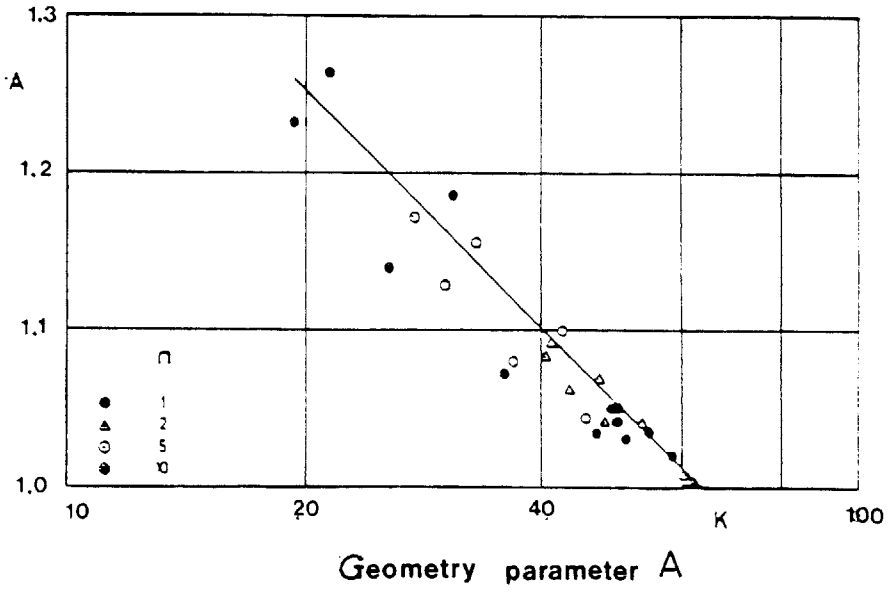

FIGURE 7.6: GEOMETRY FACTORS G^* AND A OF REHME'S CORRELATION.
(Taken from reference R-3)

$$\frac{p(z_1) - p(z_2)}{\rho w^2/2} = f_M \frac{(z_2 - z_1)}{De} + \{K(z_2^+) - K(z_1^+)\} \qquad (7.23)$$

In order to verify or improve the above methods to estimate K(z), K(∞) and C_d for rod bundles, one may use the BODYFIT code (C-3). This numerical program, developed at Argonne National Lab., performs 3-dimensional distributed, thermal-hydraulic analysis of rod bundles. It has been tested with overall satisfactory results against rod bundle velocity and temperature data, under isothermal and mixed convection conditions (E-1).

7.4.2.2 Turbulent Flow

Many correlations have been suggested to calculate friction factors for turbulent flows in bare rod bundles. Cheng (C-6) compared the methods of Deissler, Ibragimov, Dwyer, Malak and Rehme (G*-method) against data with P/D ranging from 1.0 to 1.5. He concluded that Rehme's G*-method and Dwyer's method performed better than the others against both interior subchannel or bundle averaged pressure drop data. Since the G*-method can be applied to any type of channel (including edge and corner subchannels) whereas Dwyer's method is restricted to interior subchannels, the G*-method is recommended for this work. The friction factor f_M is calculated as follows:

$$\sqrt{\frac{8}{f_M}} = A\,[2.5 \ln Re \sqrt{\frac{f_M}{8}} + 5.5] - G^* \qquad (7.24)$$

where parameters A and G* are given in Figure 7.7 as a function of the K_M parameter which is equal to:

$$K_M = (f_M\, Re_{De})_{laminar} \qquad (7.25)$$

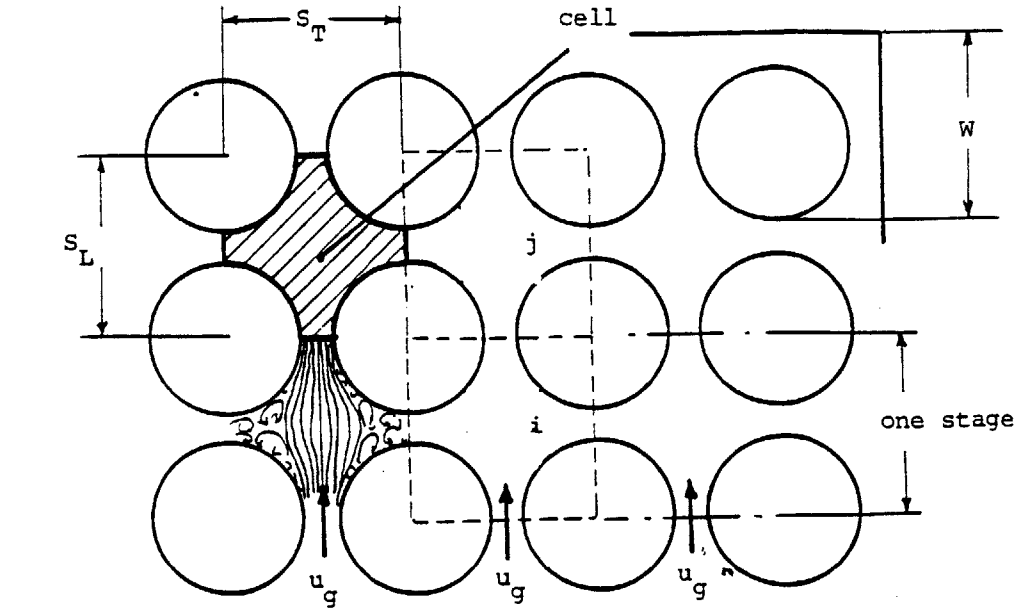

(a)

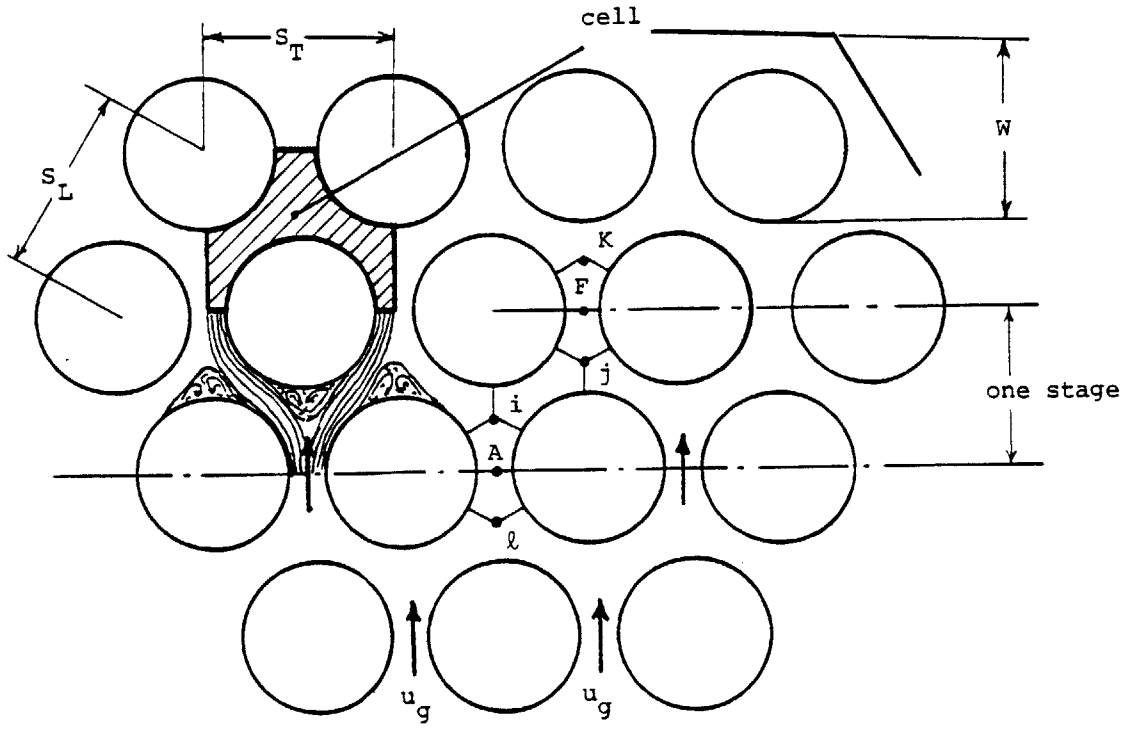

(b)

FIGURE 7.7: CROSS-FLOWS IN BARE ROD BUNDLES; GEOMETRICAL AND FLOW CHARACTERISTICS FOR (a) SQUARE AND (b) TRIANGULAR ROD ARRAYS.

K_M is the only "external" parameter that is needed in the G*-method. Rehme (R-3) has validated his method by comparing it against data from various channel geometries. In the case of bare rod bundles, equation 7.19 can be used to calculate K_M's for each subchannel (interior, edge, and corner) separately.

For developing turbulent flow in rod bundles, the situation is very little understood. Schmidt and Zelding (W-6) found that the K(z) function given in equation 7.21 is a weak function of Re number for flows in pipes and parallel plates. They also found that for pipes and channels, the value of $K(\infty)$ decreases less than 10 percent when the Reynolds number increases from 10^2 to 10^4. It is reasonable and conservative, therefore, to employ here the laminar flow results of paragraph 7.4.2.1.

Again we recommend that the BODYFIT numerical program be used, employing the k-ε model option, to check both the value of $K(\infty)$ and the shape of the $K(z^+)$ function in turbulent flows.

7.4.3 Friction and Form Drag in Lateral Flows

Here we examine simultaneously laminar and turbulent flows since all available correlations have been presented that way. Figures 7.7a and 7.7b give the layouts of square and triangular rod arrays respectively. At the left of both figures, the characteristic features of the flow field are depicted. Both cases exhibit a core region where the flow is more or less orderly oriented, and a wake region where the flow has separated and flow recirculation of some characteristic frequency has been established. In Figure 7.7, the definition of one <u>stage</u> of a rod row and of a <u>cell</u> is also given. Applying the integral momentum equation to a cell, then:

$$F_R^L = \Delta p_L^S \cdot A_g \tag{7.28}$$

where F_R^L is the total drag force on the cell solids, A_g is the gap area (for a given axial length), and Δp_L^S is the lateral pressure drop over one row stage due to friction and form drag. Several remarks are in order.

(a) For square arrays, the following is true: (see Figure 7.7)

$$\Delta p_L^S = p_i - p_j \tag{7.27}$$

where p_i and p_j are the corresponding subchannel pressures. Consequently, any models for Δp_L^S are directly applicable for the subchannel analysis analysis transverse momentum equation.

(b) For triangular arrays, equation 7.27 does not hold. By inspection of Figure 7.7b, we get:

$$\Delta p_L^S = (p_A - p_i) + (p_i - p_j) + (p_j - p_F) \tag{7.28}$$

or since

$$(p_A - p_i) + (p_j - p_F) = (p_\ell - p_i)$$

then

$$\Delta p_L^S = (p_\ell - p_i) + (p_i - p_j) = \Delta p_{\ell,i} + \Delta p_{i,j} \tag{7.29}$$

Equation 7.29 indicates that models for Δp_L^S cannot be directly applied to the transverse momentum equation of the subchannel analysis since models for $\Delta p_{i,j}$ are required.

(c) For triangular arrays, an equation similar to equation 7.28 is valid for the lateral CV drag forces:

$$F_R^L = F_{R_{\ell,i}}^L + 2\, F_{R_{i,j}}^L \cos 60°$$

or

$$F_R^L = F_{R_{\ell i}}^L + F_{R_{i,j}}^L \tag{7.30}$$

where $F_{R_{i,j}}^L$ is the drag on the solid surfaces enclosed by the transverse control volume between subchannel i and j.

Let us now present one of the first and the most widely used pressure drop correlations for the transverse flows in rod bundles. It is the Gunter-Shaw correlation (G-4) which is written in the following form:

$$\frac{\Delta p_L}{L} = f_L \frac{1}{D_V} \rho \frac{u_g^2}{2} \left(\frac{D_V}{S_T}\right)^{0.4} \left(\frac{S_L}{S_T}\right)^{0.6} \tag{7.31}$$

where L is the lateral length of a number of stages, u_g is the average gap velocity and S_T, S_L are indicated on Figure 7.7. The volume equivalent diameter D_V is:

$$D_V = \frac{4V_f}{A_W} \tag{7.32}$$

where V_f is the total fluid volume and A_W is the total wetted surface of a cell. In addition

$$f_L = \begin{cases} 180 \,/\, Re_{D_V} & ; \text{ laminar flow} \\ 1.92 \,/\, Re_{D_V}^{0.145} & ; \text{ turbulent flow} \end{cases} \tag{7.33}$$

where

$$Re_{D_V} = \rho \, D_V \, u_g \,/\mu \tag{7.34}$$

The Gunter-Shaw correlation has been recently tested against new data and correlations in (E-2). It was found that the correlation performed satis-

factorily, particularly for laminar flows where the data exhibit a wider scatter. Due to its simplicity and generality, the Gunter-Shaw correlation will be chosen for this work.

Recently, ZuKauskas and Ulinskas (see article in (H-2), vol. 2) made a very comprehensive study on developing effects of transverse flows in rod bundles. Their data showed that the pressure drop in the first one or two stages is different from the average pressure drop occuring over stages away from the inlet. They suggested the following formula:

$$\Delta p_L^{\text{m-th stage}} = c_m \, \Delta p_L \tag{7.35}$$

where Δp_L is given by equations similar to 7.31 and c_m is given in Figure 7.8, as a function of m and Re_{D_V}.

It is now important to suggest a correlation for pressure drop between two adjacent subchannels $\Delta p_{i,j}$ as remark (c) above indicates. In Appendix A.7.1, we prove that the Gunter-Shaw formula is still valid when applied to a transverse momentum equation CV of the subchannel analysis. Furthermore, we recommend the use of the c_m coefficient of Equation 7.35 with m equal to one. This latter proposition, though, is not true for rod bundle flows predominantly in the transverse direction. Here the analyst should be very careful to account for flow developing effects in the transverse direction using c_m values from Figure 7.8.

7.4.4 Friction and Form Drag for Inclined Flows

In this case the average velocity vector $\vec{v}$ forms an angle θ_V with the bundle axis direction (parallel direction). Obviously $\tan \theta_V = w/u$ and $|\vec{v}| = (u^2 + w^2)^{1/2}$. The question that naturally arises here is whether it is possible to apply the previously suggested models in each direction

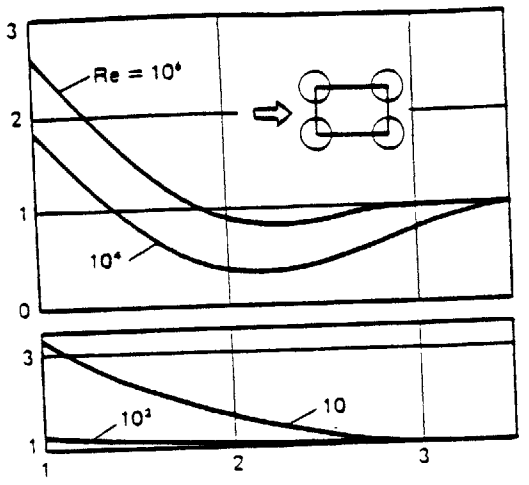

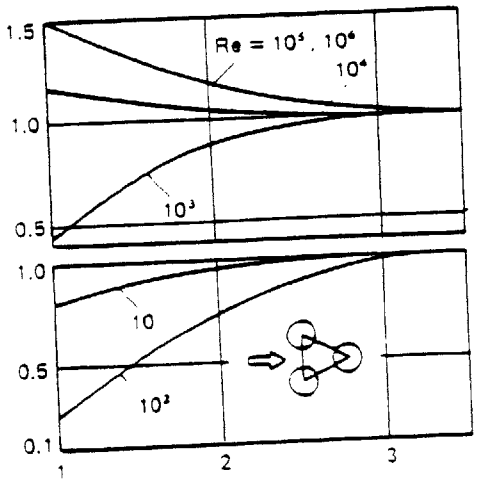

FIGURE 7.8: CROSS-FLOW DEVELOPING PARAMETER C_m AS A FUNCTION OF NUMBER OF STAGES m. (Taken from reference H-2)

separately as if the flow was purely axial or lateral. The following principle (called by some authors the principle of independence) has been established (see (W-6), p. 362) for the simple case of laminar flow over a yawed cylinder. If u,v are the velocity components normal to the cylinder axis and w is the velocity component parallel to the cylinder axis, then it is easily shown that u and v can be calculated independently of w. On the other hand though, the velocity component w does depend on u and v, and it can be derived from the following equation:

$$u \frac{\partial w}{\partial x} + v \frac{\partial w}{\partial y} = \nu \frac{\partial^2 w}{\partial y^2} \tag{7.36}$$

where x/y are the tangential/normal directions to the surface of the cylinder. Both are normal to the cylinder axis. From this relationship, it is apparent that w(x,y,z) depends on both parallel and normal components of the free stream velocity plus the geometrical characteristics of the submerged body.

In summary, u and v velocity components are independent of w, whereas w is dependent on u and v. It is therefore appropriate to call this the "semi-independence" principle instead of the "independence" principle. Based on this "semi-independence" principle, one should expect that the lateral drag of flow over a cylinder should be a function of u, v and D only, as if the flow were purely lateral. This latter postulate was verified experimentally for turbulent flow conditions by Groehn (K-1). In contrast, the drag in the axial direction is expected to be influenced by the magnitude of both axial and lateral velocity components.

In the more complicated case of inclined flows in rod bundles the semi-independence principle is not generally valid. Ebeling-Koning and

Todreas (see (E-3)) performed an extensive literature review and comparisons of pressure drop (or drag) models for inclined flows in bare rod arrays. They found that most of the models do a fairly good job for the range of the data that they were developed to predict. A new model was proposed to cover a wide range of experimental conditions as follows:

$$F^{A}_{TOT} = \frac{A_w}{8} f_A \left(\left| \vec{V} \right| \right) \rho \left| \vec{V} \right| w \tag{7.37}$$

$$F^{L}_{TOT} = \frac{A_w}{8} f_L \left(\left| \vec{V}_g \right| \right) \rho \left| \vec{V}_g \right|^{0.6} \left| u_g \right|^{0.4} u_g \tag{7.38}$$

where $\vec{V}$ is the average fluid velocity, $\vec{V}_g$ is the fluid velocity at the gap and w and u_g are defined in Figure 7.9. A_w is the wetted surface within a given control volume, f_A and f_L are friction and form drag coefficients for axial and lateral flows respectively. In this work f_A is estimated through Rehme's correlation and f_L by the Gunter-Shaw correlation. Also for simplicitly, equation 7.38 is slightly modified to give:

$$F^{L}_{TOT} = \frac{A_w}{8} f_L \left(\left| \vec{V}_g \right| \right) \rho \left| u_g \right| u_g \tag{7.39}$$

Model (7.39) was also tested in (E-3) and gave satisfactory results.

7.5 DRMs for Rod Bundles With Displacers

7.5.1 Introduction

As discussed earlier, the displacers are cylindrical wires with diameter D_W which is less than or equal to (P-D). Figure 7.10 presents a triangular rod array with displacers placed at -45° from the reference line. The displacers may be placed at any angle from 0° to 360°.

The purpose of this section is to study the pressure drop charac-

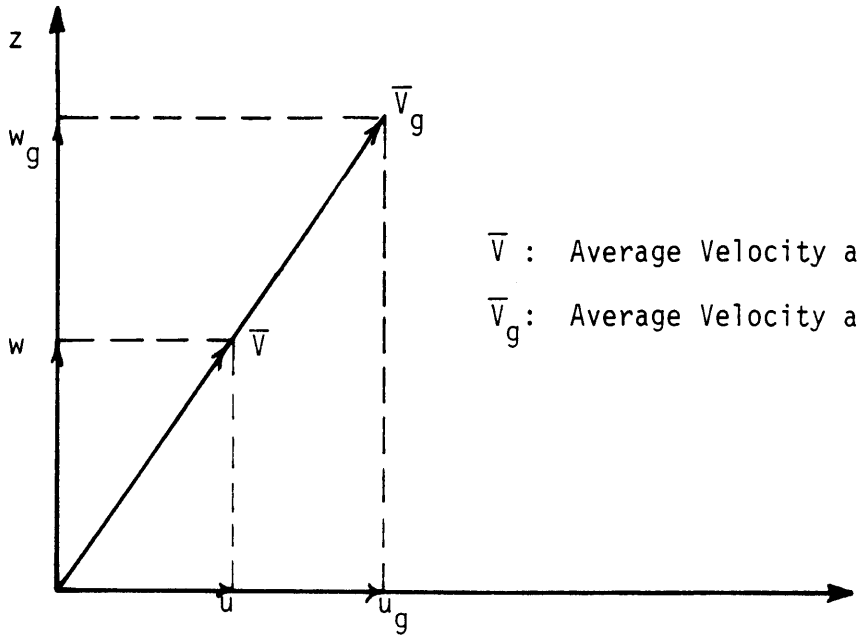

FIGURE 7.9: SUBCHANNEL AND GAP AVERAGED VELOCITIES.

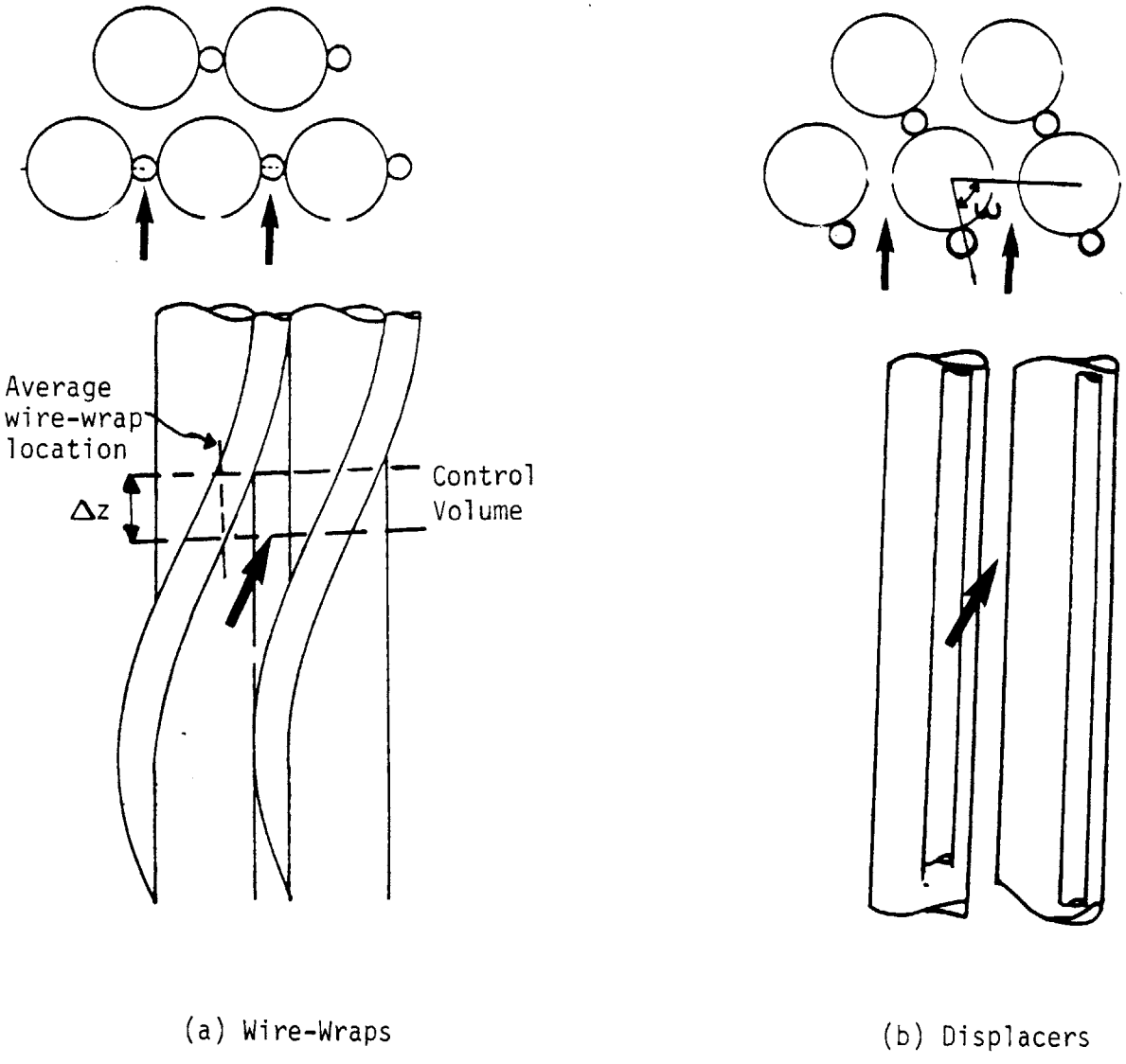

(a) Wire-Wraps

(b) Displacers

FIGURE 7.10: GEOMETRICAL COMPARISONS OF WIRE-WRAP SPACERS AND DISPLACERS.

teristics of rod bundles with displacers as an intermediate step toward the modeling of wire-wrapped rod bundles. The motivation stems from the fact that for sufficiently small axial mesh size Δz ($\Delta z < \frac{H}{12}$) and for predominately lateral flows, the wire-wrap spacer within a given subchannel resembles a slightly tilted displacer at the same angular position. Therefore, models developed for rod bundles with displacers might be easily extended to wire-wraps. In the case of predominately axial flows, the direct extension of the displacer models to the wire-wrap models is not as straightforward as in the case of predominately lateral flows.

7.5.2 Axial Flows

For the subchannel depicted in Figure 7.11 the friction drag forces on the surface of the rods and displacer F_R^A and F_W^A respectively will be given from:

$$F_{TOT}^A = F_R^A + F_W^A = A_c' f \frac{\Delta z}{D_e''} \rho \frac{w^2}{2} \tag{7.40}$$

where

$$D_e'' = 4A_c'/P_W' \tag{7.41}$$

$$A_c' = A_c - \pi D_w^2/4 \tag{7.42}$$

$$P_W' = P_W + \pi D_W \tag{7.43}$$

and A_c and P_W are the bare rod subchannel cross-section and wetted perimeter respectively.

$$A_c = \frac{D^2}{4} \left[\sqrt{3} \left(\frac{P}{D}\right)^2 - \frac{\pi}{2}\right] \tag{7.44}$$

$$P_W = \pi D/2 \tag{7.45}$$

The friction factor f can be estimated by extending Rehme's correla-

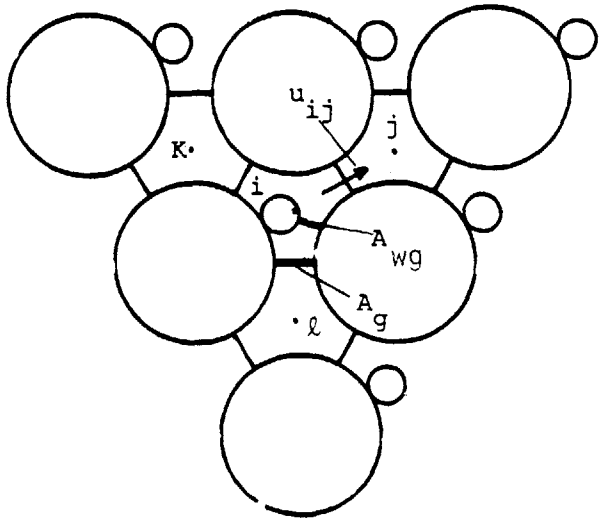

FIGURE 7.11: DISPLACERS AT 30° AND RELEVANT GAP DEFINITIONS.

tions for laminar and turbulent flows given in Section 7.4. In both cases, the laminar flow parameter K_M, given from equation 7.19, needs to be estimated. K_M is formulated for bare rods only and it is a function of P/D. For rod arrays with displacers, we suggest the following approach in order to estimate f:

(a) Calculate an equivalent $(P/D)_{eq}$ using 7.44 with A_c' replacing A_c:

$$\left(\frac{P}{D}\right)^2_{eq} = \frac{4}{\sqrt{3}} \left(\frac{A_c'}{D^2} + \frac{\pi}{8}\right)$$

or

$$\left(\frac{P}{D}\right)^2_{eq} = \left(\frac{P}{D}\right)^2 - \frac{\pi}{\sqrt{3}} \left(\frac{P}{D} - 1\right)^2 \qquad (7.46)$$

(b) Estimate K_M from equation 7.19 using $(P/D)_{eq}$ and $Re = \frac{\rho D_e'' w}{\mu}$

(c) Estimate f based in K_M and $Re_{D_e''} = \rho D_e'' w/\mu$.

This approach is being tested experimentally by Kune (K-3). However, since the presence of the displacer does not alter the structure of the flow patterns (i.e., it does not create wakes or intensify the turbulence), we do not expect appreciable differences in the axial friction data of the displacer laminar flows due to the large scatter that the data exhibit in low pressure drop measurements.

Finally, we estimate the drag forces F_R^A and F_W^A individually as follows:

$$F_R^A = \frac{P_W}{P_W'} F_{TOT}^A \text{ and } F_W^A = \frac{P_W' - P_W}{P_W'} F_{TOT}^A \qquad (7.47)$$

Equations 7.40 and 7.47 give:

$$F_R^A = \frac{f}{8} P_W \Delta z \rho w^2 \tag{7.48}$$

$$F_W^A = \frac{f}{8} (P_W' - P_W) \Delta z \rho w^2 \tag{7.49}$$

7.5.3 Lateral Flows

Here the situation is not so straight forward as before. The reason is that the presence of the displacer might significantly alter the structure of the wakes and of the vorticity within them, as Figure 7.12 indicates. This may render the Gunter-Shaw correlation inappropriate for estimating the total lateral drag in a given control volume.

We proceed here in a heuristic way to suggest correlations for F_R^L and and F_W^L lateral drag on rod surfaces and displacer respectively. The proposed correlations are:

(a) Use modified Gunter-Shaw correlation for the total lateral drag

$F_{TOT}^L = F_R^L + F_W^L$

$$F_{TOT}^L = f_L \frac{1}{D_{V'}''} \rho \frac{u_{mg}^2}{2} \left(\frac{D_{V'}''}{S_T}\right) \left(\frac{S_L}{S_T}\right)^{0.6} \cdot E(\omega) \tag{7.50}$$

where

$$D_{V'}'' = \frac{4V'}{A_W'}$$

and " ' " (prime) indicates that the presence of the displacer is accounted for. The velocity u_{mg}^2 is defined at the minimum gap among A_g and A_{wg} (see Figure 7.11).

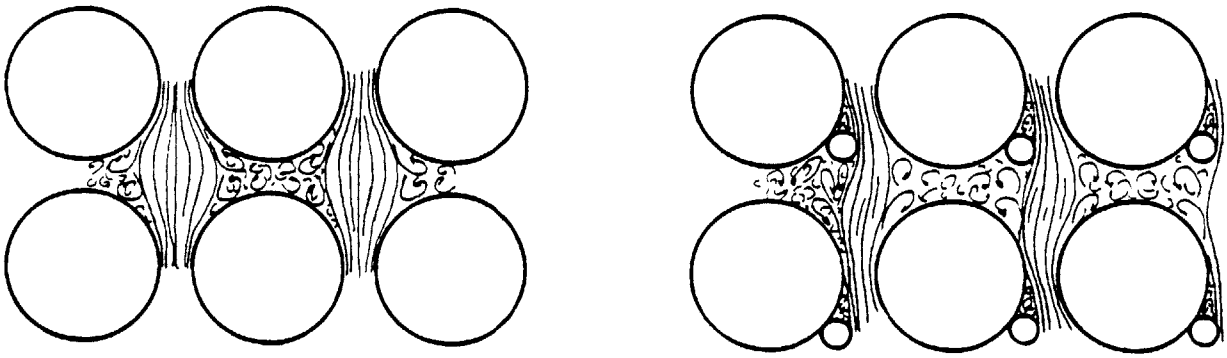

(a) Rectangular Array

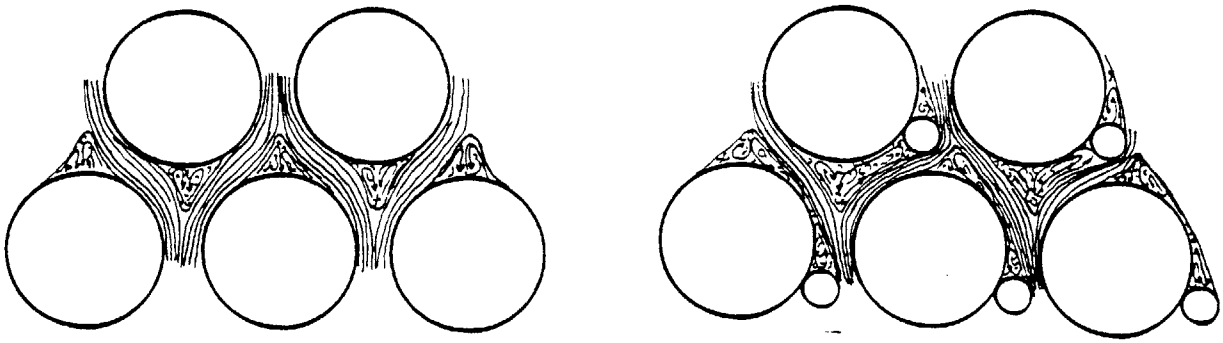

(b) Triangular Array

FIGURE 7.12: THE EFFECT OF THE DISPLACER IN THE WAKE DISTRIBUTION OF CROSS-FLOWS IN ROD BUNDLES.

$$u_{mg} = \begin{cases} u_g A_g / A_{wg} & ; \quad A_{wg} < A_g \\ u_g & ; \quad A_{wg} \geq A_g \end{cases} \tag{7.51}$$

The function $E(\omega)$ accounts for lateral drag changes due to flow structure alteration that are caused by the presence of the displacer. ω is the angular position of the displacer from a reference position. $E(\omega)$ should also be a function of the displacer diameter-to-diameter ratio, P/D and the Reynolds number. Experiments are currently being performed at MIT (K-3) in order to determine the E parameter as function of the displacer angular position ω.

(b) To estimate F_W^L amd F_R^L we propose the following correlations:

$$F_W^L = D(\omega) \frac{(A_W' - A_W)}{A_W'} F_{TOT}^L \tag{7.52}$$

$$F_W^L = \left[1 - \frac{D(\omega)\ (A_W' - A_W)}{A_W'} \right] F_{TOT}^L \tag{7.53}$$

where $D(\omega)$ is a new function that accounts for the non-uniform distribution of the wakes among the rod surfaces and the displacer. It is expected, though, that $D(\omega) \sim 1.0$.

7.6 DRMs for Wire-Wrapped Rod Bundles

7.6.1 Introduction

In this section, the displacer models of the previous section are extended to the more general case of the wire-wrap spacer. The wire-wrap can be tilted to any angle with respect to the axial direction and this tilt is characterized by the wire lead-to-diameter ratio H/D. The displacer may be considered as wire-wrap spacer with $H/D \to \infty$.

Consequently, all models developed here are valid for the displacers also in the limiting condition $H/D \to \infty$.

In contrast to the displacer or bare rod bundle situations, friction and form drag models require as inputs both axial and lateral velocities, w and u respectively even for "purely" axial flows. In other words, in order to calculate the axial drag within a control volume (CV), one needs to know both w and u (averaged axial and lateral velocities). This coupled flow field analysis makes the general modeling of wire-wrapped rod bundles quite elaborate. Flow pattern and wake distribution maps for each particular CV geometry are required for drag calculations as a function of u and w. Unfortunately, no such information or data exist in the literature. Consequently we proceed in a heuristic way, building up the wire-spacer modes as an extension of the displacer models (whenever possible), clearly identifying all assumptions made.

7.6.2 General Wire-Wrap Modeling

In this section, we examine collectively all drag components, namely F_R^A, F_R^L, F_W^T, and F_W^N. The models developed here are valid for both axial and transverse momentum equation control volumes (CV).

7.6.2.1 F_R^A and F_W^T Components

Here we follow the arguments presented in Section 7.4.4 for axial pressure drop (or drag) calculations for inclined flows in bare rod bundles. Generalizing these concepts we define two "axial" directions, the axial and tangential. Based on Rehme's correlation, define the following drag function:

$$R(v) = \frac{A_W' f_M(v)}{8} \rho v |v| \tag{7.54}$$

where $f_M(v)$ is the Moody friction factor based on Rehme's theory, and A_W' is the wetted flow area of the channel (including the presence of the wire-spacer). The F_R^A and F_W^T components will be given as follows:

$$F_R^A = R\left(\sqrt{w^2 + u^2}\right) \cdot \left(\frac{A_W}{A_W'}\right) \cdot \cos\theta \tag{7.55}$$

$$F_W^T = R\left(\sqrt{w^2 + u^2}\right) \cdot \left(1 - \frac{A_W}{A_W'}\right) \cdot \cos\left(\phi - \theta\right) \tag{7.56}$$

where A_W is the rod surface area and A_W' is the total wetted solid surface area enclosed by the reference CV. Note that when the wire-spacer is not present within a given CV, then $A_W' = A$ and $F_W^T = 0$. Three key assumptions were employed in deriving equations 7.55 and 7.56:

(a) The friction drag along the "parallel" directions can be estimated by projecting the friction drag along the velocity direction on these parallel direction.

(b) The friction drag along any direction can be estimated using Rehme's friction factor correlations.

(c) The total friction drag is uniformly distributed among the rod and wire-spacer surfaces.

7.6.2.2 F_R^L and F_W^N components

Here things ae much more complicated. Assumption (c) is not generally valid as pointed out in Section 7.5.2. There the D function was introduced to account for the uneven distribution of the wakes. In this case though, D is not only a function of u, P/D and ω as it is in the case of rod bundles with displacers, but also a function of w and H/D. We

distinguish between two different cases:

(1) The flow is predominantly lateral. This case is an extension of the case of lateral flows in rod bundles with displacers. Introduce now the G(v) function based on the Gunter-Shaw correlation:

$$G(v) = \frac{A_W' f_G(v)}{8} \rho \mid v \mid v \left(\frac{D_V''}{S_T}\right) \left(\frac{S_L}{S_T}\right)^{0.6} E(\omega) \tag{7.57}$$

where $f_G(v)$ is given from equation 7.33.

Making use of the independence principle for the cross-flow friction and form drag, take:

$$F_R^L = G(u)\ D_1(\omega)\ \left(\frac{A_W}{A_T}\right) \tag{7.58}$$

$$F_W^T = G(v_N)\ \left[1 - D_1(\omega)\ \frac{A_W}{A_T}\right] \tag{7.59}$$

where $D_1(\omega)$ may be different from the $D(\omega)$ function introduced in equation 7.52, but certainly close to one too.

(2) The flow is predominantly axial. This is the most interesting and most frequent case. Typical directions of the velocity component vectors are given in Figure 7.3b. The directions of Figure 7.3b are defined as positive. Note that the projection vector of the $\vec{v}_n$ vector on the lateral axis is directed opposite direction to the of $\vec{u}$ vector. Conversely, for the case of predominantly transverse flows, both these directions are expected to coincide. The wake distribution for the above cases is expected to be quite different. Consequently, equations 7.58 and 7.59, which were based on the predominantly lateral flow assumption, might not be valid here. We present a heuristic alternative set of equations:

$$F_R^L = \frac{A_W' f_G(v_g)}{8} \rho \mid u \mid u \left(\frac{D_V''}{S_T}\right) \left(\frac{S_L}{S_T}\right)^{0.6} \tag{7.60}$$

$$F_W^N = f_n \rho \frac{v_N^2}{2} \cdot D_W \cdot \Delta z / \cos \phi \tag{7.61}$$

where

$$f_n = \left(\frac{A_g}{A_{mg}}\right)^2 \left[1 + \frac{D_2}{Re^{2/3}}\right] \quad , A_{mg} = A_{wg} \tag{7.62}$$

$Re = D_W \cdot v_N / \nu$ and D_W is the wire-spacer diameter.

The particular form of Equation 7.62 is suggested, based on the following reasoning. The bracketed term equals the drag coefficient C_D of free stream flows over cylinders (W-6) with $D_2 \simeq 10$. The $A_g/A_{mg})^2$ term accounts for the fact that the flow is confined and this term characterizes the rapid increase of the lateral velocity in the minimum gap area. The minimum gap area A_{wg} is defined in Figure 7.11 for average angular position of the wire spacer within a given cell.

7.6.2.3 w and u estimation

For the axial momentum equation CV(i) we take $w = w_i$, where w_i is the subchannel axial velocity and $u = (u_{\ell i} + u_{ik})/2$; where $u_{\ell i}$ and u_{ik} are the cross-flow velocities for the entrance and exit gap of the wire-spacer respectively. Similarly for the transverse momentum equation CV between subchannels i and j, take $w = (w_i + w_j)/2$ and $u = u_{ij}$.

The above wire-wrap models have to be tailored for each subchannel and gap geometry on an individual basis. Note that for a given subchannel number, the various subchannels at different axial locations exhibit different geometry patterns due to varying position of the wire-spacer. In the next section we examine all different subchannel and gap geometries and develop a logic to classify these geometries in terms of the subchannel or gap number and its axial position.

CHAPTER 8

THE COMPUTER PROGRAM ASFREMIT

8.1 Introduction

In this chapter the computer program ASFREMIT is presented. ASFREMIT is a single-phase thermo-hydraulic numerical program which is an extension of the computer program ASFRE, developed by PNC (Y-1). The basic new features in ASFREMIT are the development and utilization of a new distributed resistance model (see Chapter 7) and of new attribute functions to numerically implement the resistance models into the code. The code is currently limited to an axial numerical mesh (or subchannel) size Δz equal to H/12, where H is the wire wrap lead length. This Δz size was selected as a compromise between axial resolution and execution speed. H/12 is the minimum Δz required to obtain satisfactory resolution of the pseudo-periodic phenomena caused by the wire wrapped spacer. On the other hand, given the large number of subchannels usually involved in LMFBR subassembly calulations, smaller values of Δz would render the execution speed prohibitedly low. However both the hydraulic resistance models and the attribute functions can be easily modified to cover other desired Δz sizes (H/24 or even H/6, H/2)

Since the distributed resistance models have been presented in Chapter 7, here the general structure of ASFREMIT and the general logic to implement numerically these models is outlined. Finally some preliminary calibration/validation runs of ASFREMIT are perfomed against data presented in this thesis or available in the literature. We start with a literature review of similar numerical programs.

8.2 Literature review

LMFBR subassembly analysis and simulation have attracted considerable attention all over the world. A large number of numerical programs have been published which are capable of handling wire-wrap spacers. These programs may be classified according to the following characteristics.

(a) subchannel analysis versus porous body approach.

(b) size of the axial thickness of the numerical mesh Δz.

(c) forcing function versus distributed resistance wire-wrap modeling.

Several subchannel analysis codes have been developed for LMFBR subassembly analysis (COBRA (R-2), THI3D (S-8), SABRE (D-1) SABRE-CEA (L-2), ORRIBLE(W-1),ASFRE (Y-1), ENERGY (K-4).)

The subchannel conservation equations employed in COBRA-IV were given in Chapter 6. In order to account for the presence of the wire spacer, COBRA-IV introduced a semi-empirical model for the forced crossflow induced by the wire-spacer as discussed in Chapter 7. Similiar "forcing function" type of the wire-spacer models are employed in ORRIBLE and ASFRE.

Basehore and George (B-8) compared COBRA-IV with various local velocity data. The COBRA-IV code required calibration of four input parameters:

* the turbulent mixing coefficient, β
* the turbulent crossflow resistance factor, K_{ij}
* the effective fraction of pitch length for forced crossflow, δ
* the transverse momentum geometry factor, S_{ij}/ℓ

In COBRA-IV the models for the hydraulic resistance remain the same for every subchannel or gap and K_{ij} accepts only one value for all subchannels. Figure 8.1 compares the COBRA-IV predictions with the WARD data (R-1). The values of the input parameters for optimum data fit are also given. Note that some deviations exist, particularly in the - 30° to 90° region. Figure 8.2 compares the code against the MIT laser doppler velocity data for the peripheral subchannels (C-4). Note the large deviations observed for different values of the K_{ij} parameter. As the authors admit (B-8), it does not appear that both data sets (WARD, MIT) can be accurately matched by the same set of input parameters. The authors suggest that the COBRA wire wrap model needs further improvement in order to obtain point by point match with several velocity data sets, for both blanket and fuel assemblies and for laminar and turbulent flow.

A forced crossflow model similar to that in COBRA is included by Wei (W-4) in FULMIX-II. Wei also gives some references for recommended values of the parameter δ for different geometries (P/D and H/D varying). However, no comprehensive validation effort of a recommended set of input parameters appears to have been published.

In ASFRE and ORRIBLE, the forced crossflow due to the wire wrap has a continuous rather than a discrete representation. The ASFRE wire-wrap model is:

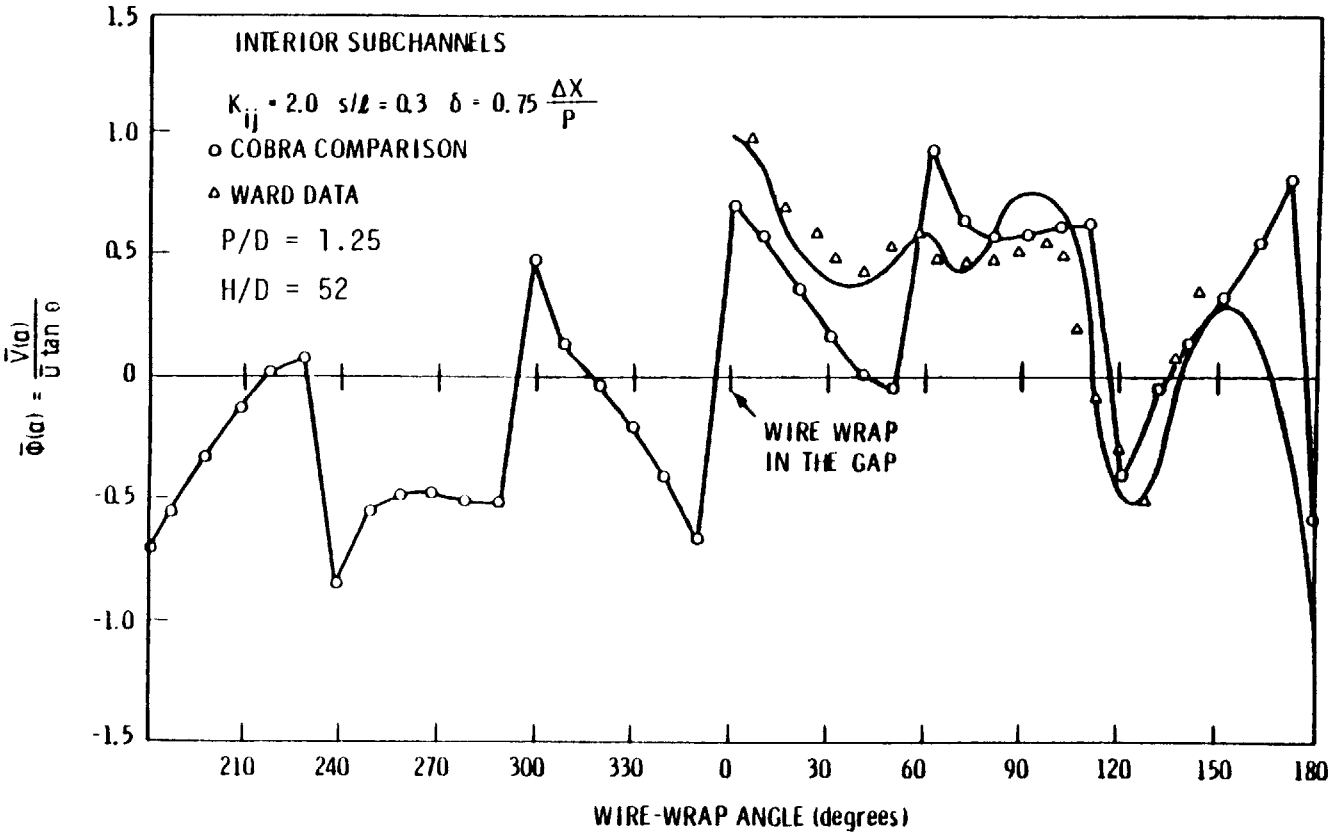

FIGURE 8.1. COBRA COMPARISONS WITH THE WARD DATA FOR TURBULENT FLOW CONDITIONS
(Taken from reference B-8)

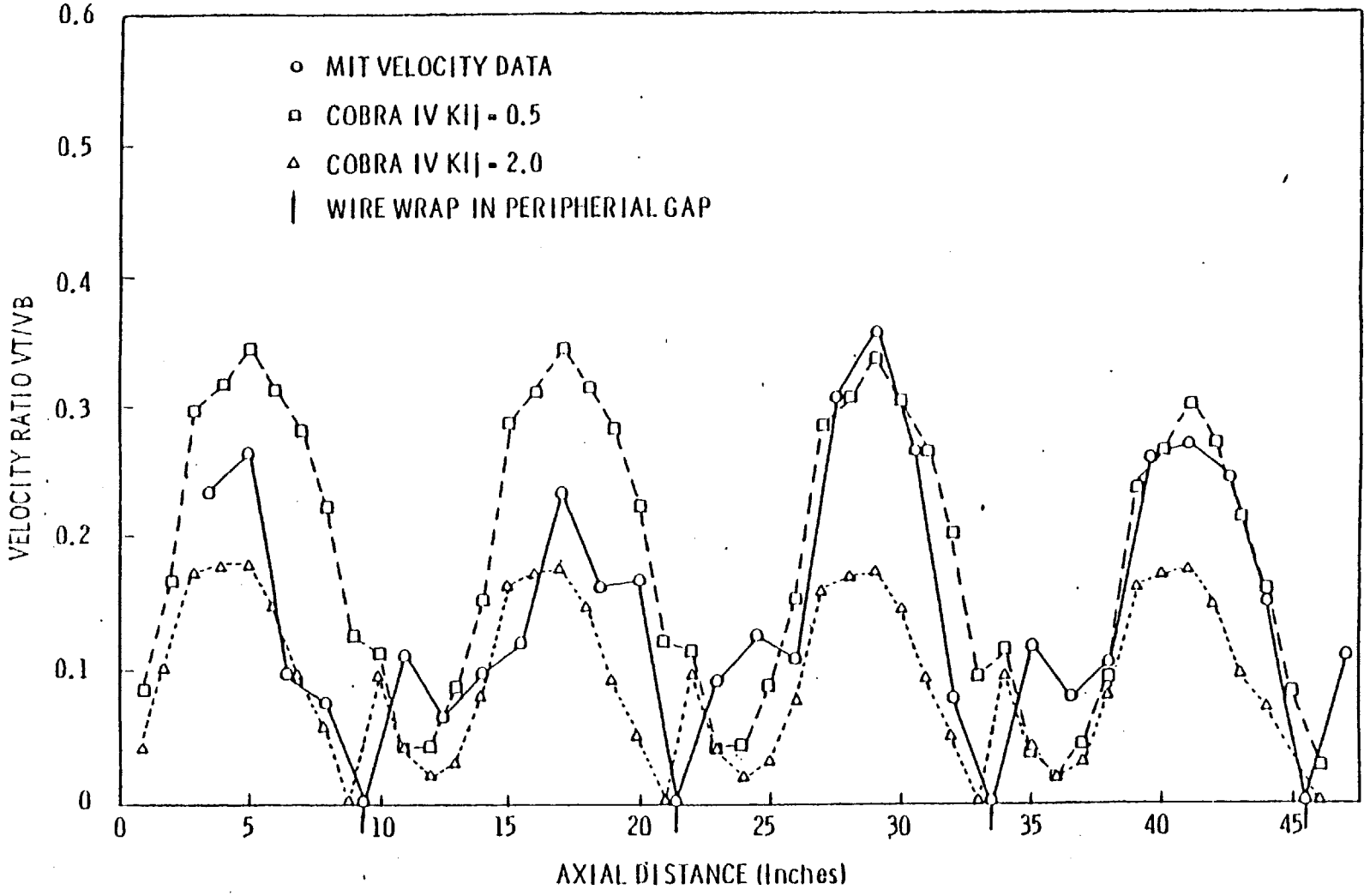

FIGURE 8.2. COBRA COMPARISONS WITH THE MIT LASER DOPPLER SWIRL FLOW VELOCITY DATA.
(Taken from reference B-8)

$$W_{forced} = \begin{cases} c_s \pi (D+D_w) \dfrac{S'_{ij}(z)}{A_{fi}(z)} \dot{m}_i \dfrac{1+\cos(3\theta/2)}{2}, & |\theta| \leq \dfrac{\pi}{3} \\ 0, & |\theta| > \dfrac{\pi}{3} \end{cases}$$

where S'_{ij} is the projected horizontal length of the wire spacer on the gap at a given axial level z, and A_{fi} is now a function of z. ASFRE employs, besides the above model, correct geometrical representations of the axial flow areas $A_{fi}(z)$, the wetted perimeter $P_w(z)$ and $S_{ij}(z)$ accounting for the presence of the wire wrap. ORRIBLE employs two forced crossflow models, one for an interior and a second for a peripheral gap. These models are similar to that used is ASFRE.

All wire-wrap models reviewed so far are of a forced crossflow type. Their underlying concept is that of providing flow input instead of a hydraulic resistance input. Further the subchannel equations exhibit only minor differences among various subchannel codes. Therefore, one does not expect any of the above codes to have inherently better predictive capabilities than the others.

A qualitatively different approach has been followed by Davis in the SABRE subchannel code (D-1). The model is based on the assumption that the effects of the wire-wrap can be represented solely by its direction and its resistance characteristics. Thus, the model does not account for the geometrical differences in cross sectional area and perimeter due to the presence of a wire-wrap. These differences though are included in the derivation of the distributed resistance models for the momentum equations. The SABRE

distributed resistance models for the momentum equations. The SABRE model was developed for one Δz equal to H/6 and its similar in concept with the models developed for one lead length by Chiu, Rohsenow and Todreas (C-1) and Burns, Rohsenow and Todreas (B-4). These later models were formulated for axial mesh size Δz equal to H and implemented in the ENERGY series of codes.

Recently additional work on SABRE was performed at CEA by Le Gouez (L-2). The former SABRE wire-wrap model was adopted on a H/24 axial mesh size. Satisfactory predictions of the WARD data were presented. However, the essentials of the wire spacer model are not available at this time.

In this section, we present the implementation of the Distributed Resistance Model (DRM) given in Chapter 7, into the ASFRE subchannel code.

8.3 General Structure of ASFREMIT

8.3.1 New Features in ASFREMIT

The general structure of ASFREMIT closely parallels that of the original ASFRE code. Figure 8.3 outlines the building blocks of ASFREMIT code. The fractional time step method (a variation of the ADI method) is used to numerically solve the subchannel conservation equations. In the first half-time step, the horizontal direction is treated implicitly and the axial direction explicitly. The opposite is true for the second half-time step. Figure 8.4 outlines the momentum equation solution scheme which is similar to SIMPLE (P-2).

The most important new features of ASFREMIT are:

(a) The wire wrap geometrical characteristics are taken into account in all geometrical parameters of the subchannel analysis formulation. Subchannel and gap volumes, axial and lateral surfaces have been modified accordingly. All relevant geometrical calculations are performed in subroutine H12WG listed in Appendix A.8.1. This subroutine requires that the axial length of the computational mesh should be equal to H/12 (H: the wire-wrap lead length) and that the starting position of the wire-wrap forms an angle of -15° with the reference gap (see Figure 8.5).

(b) All references to the forcing function model have been eliminated. In ASFREMIT, the wire-wrap effect on the velocity fields in both the Axial (A) and Lateral (L) directions is accounted through the spatially varying distribution of the resistance forces.

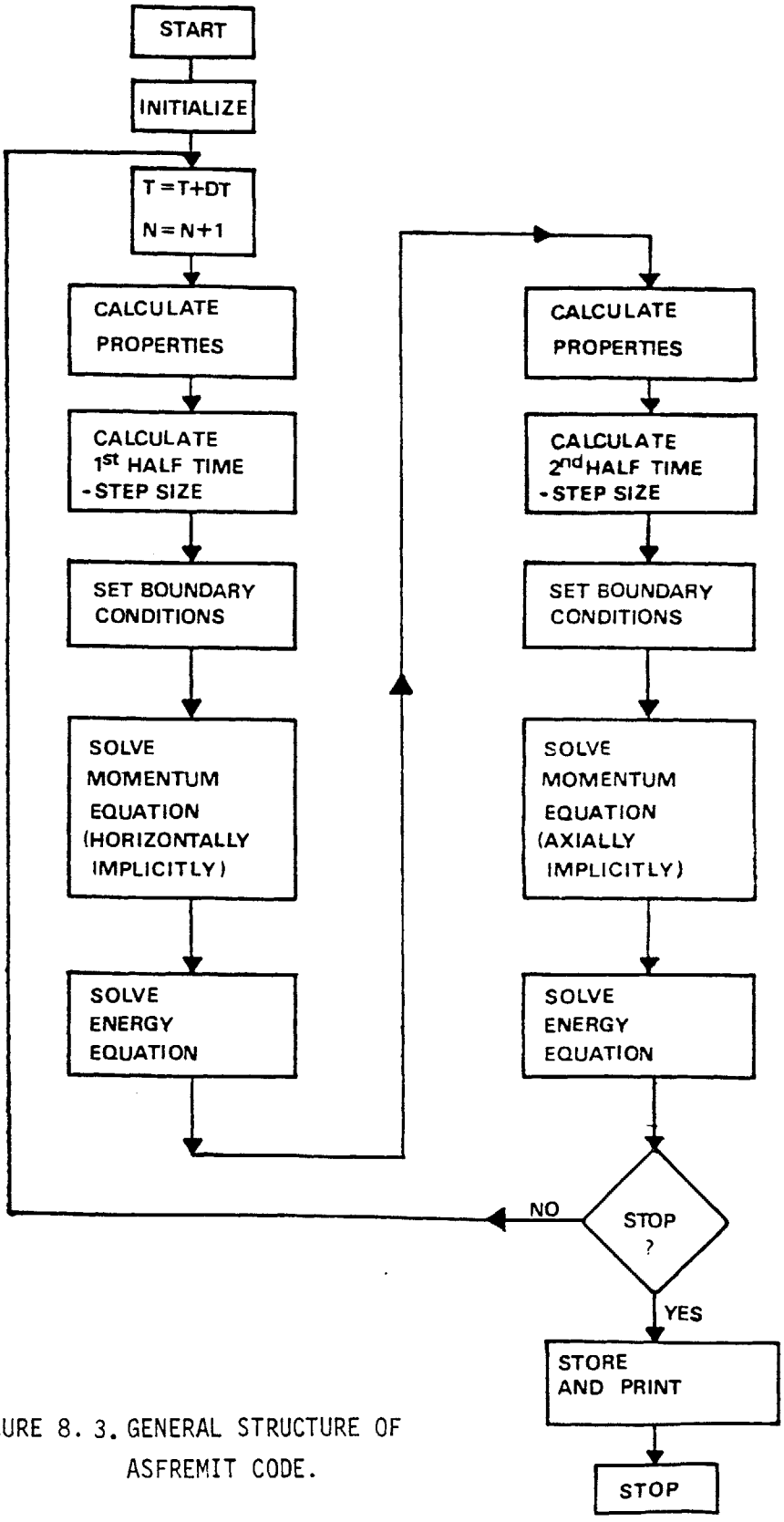

FIGURE 8. 3. GENERAL STRUCTURE OF ASFREMIT CODE.

MOMENTUM EQUATION SOLUTION SCHEME

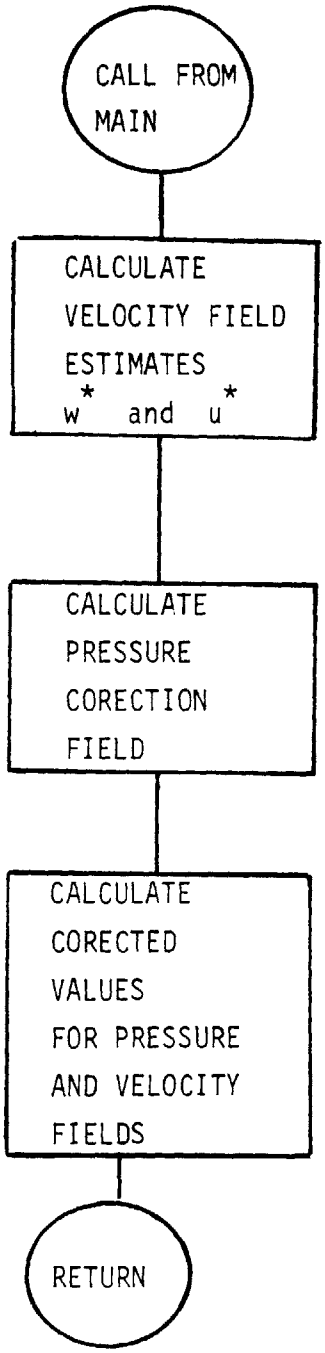

FIGURE 8.4. MOMENTUM EQUATION SOLUTION SCHEME.

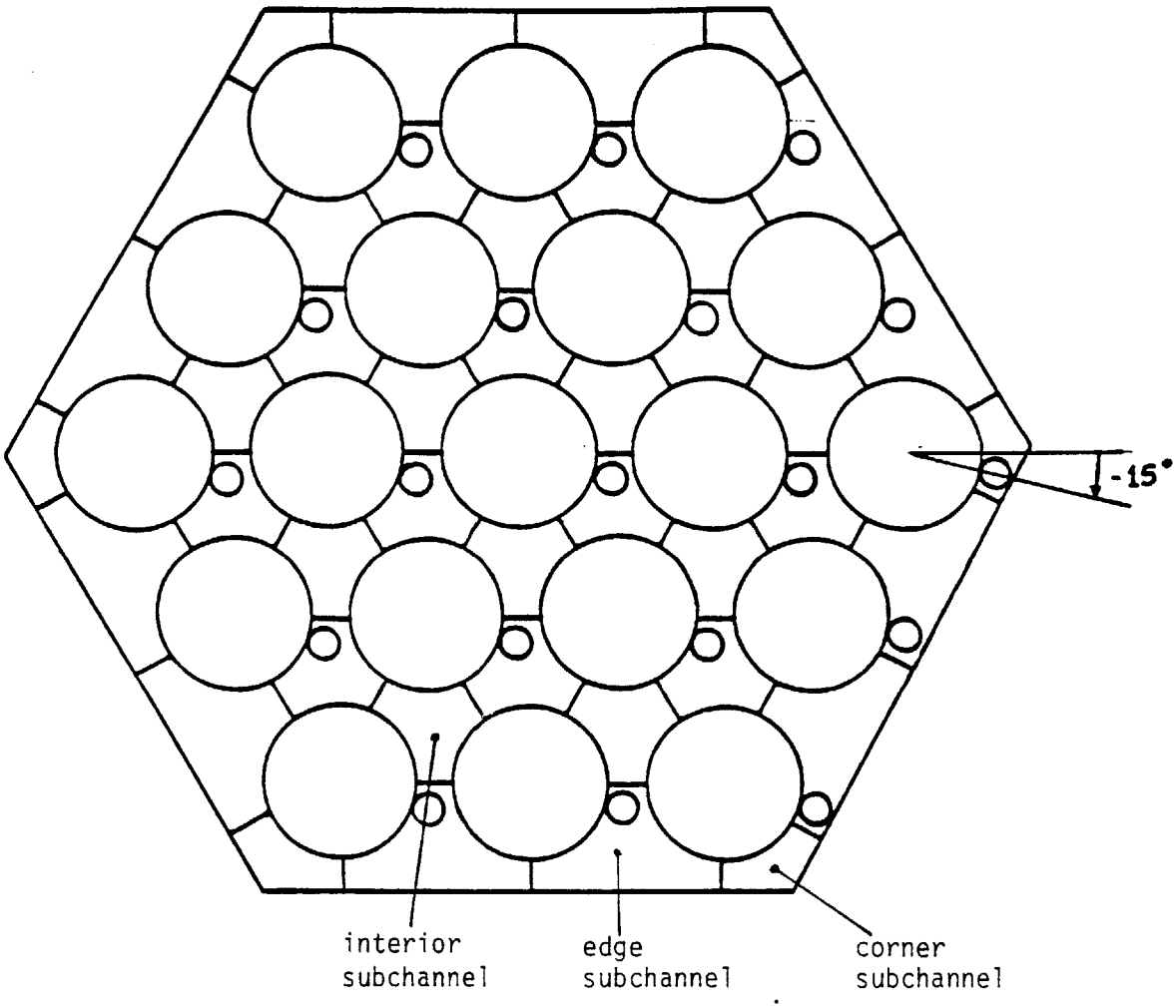

FIGURE 8.5. Initial lower position of the wire spacer.

(c) The solution scheme of ASFREMIT is identical to that of ASFRE. However, the source terms due to the distributed resistance are quite different. Subroutines WLADI1, WLADI2 and ULCALC that are used to calculate the "predictor" velocities $\hat{w}$ and $\hat{u}$ are modified accordingly. These subroutines are listed in Appendix A.8.2.

(d) The old Blasius (axial) and Gunter-Shaw (crossflow) friction factor calculations have been replaced with our new DRM models. Recall that our models are formulated for Δz equal to H/12. Subroutines DRMA and DRML estimate the resistance forces along the axial direction for a subchannel and the lateral direction for a gap respectively. There subroutines are listed in Appendix A.8.1.

8.3.2 The Distributed Resistance Models

The numerical implementation of the DRMs will be discussed here in terms of the solution of the axial momentum equation in the first half time step. The exact form of the discretized momentum equation can be found in (Y-1). Here we outline only the new features. Let (i) be a certain subchannel at an axial location ℓ of the staggered mesh. Then, following Patankar (P-2), we write the equation in the following form:

$$\underset{(1)}{a_{i,\ell}\hat{w}_{i,\ell}} + \underset{(2)}{\sum_j a_{j,\ell}\hat{w}_{j,\ell}} = \underset{(3)}{b} + \underset{(4)}{A_{i,\ell}(P_{i,\ell-1} - P_{i,\ell})} - \underset{(5)}{(S_E^A + S_I^A \cdot \hat{w}_{i,\ell})} \tag{8.1}$$

where j's are the neighbor subchannels of subchannel i. Terms (1) and (2) of the equation (8.1) contain the sought for predicted velocities $\hat{w}$ and they represent the implicit terms. Terms (3) and

(4) contain all discretized terms of the momentum equation that are treated explicity. (Previous time step or iteration values are used for the velocities or pressures). Term (5) contains what is called the source terms. Here these source terms represent the DRMs in the axial direction. Term (5) of ASFREMIT replaces the old resistance terms of ASFRE.

Note that the source term contains a constant part S_E^A which is treated "explicitly" and a variable part $S_I^A \hat{w}_{i,\ell}$ which is treated "implicity". Here the term explicit means that old time step values are employed to estimate S_E^A . The term "implicit" refers to the use of $\hat{w}_{i,\ell}$ whereas the parameter S_I^A is still estimated at the old time step.

Equation 8.1 is finally written as:

$$(a_{i,\ell} + S_I^A)\hat{w}_{i,\ell} + \sum_j a_{j,\ell}\,\hat{w}_{j,\ell} = b + A_{i,\ell}(P_{i,\ell-1} - P_{i,\ell}) - S_E^A \qquad (8.2)$$

Note that to ensure stability (as much as possible) the S_I^A parameter has to be positive. Both the S_E^A and S_I^A parameters are provided by subroutine DRMA. The following FORTRAN notation is used:

$$S_E^A = \text{FAVEX}$$

$$S_I^A = \text{FAVIM} \qquad (8.3)$$

Similarly the lateral momentum equation for a gap k between two neighbor subchannels i and j is expressed as:

$$(c_{k,\ell} + S_I^L)\,\hat{u}_{k,\ell} + c_{k,\ell-1}\hat{u}_{k,\ell-1} + c_{k,\ell+1}\hat{u}_{k,\ell+1} = d \pm C_{k,\ell}(P_{i,\ell} - P_{j,\ell}) - S_E^L \qquad (8.4)$$

where again S_I^L and S_E^L are calulated in subroutine DRML using the following FORTRAN notation:

$$S_E^L = \text{FLVEX}$$
$$S_I^L = \text{FLVIM} \qquad (8.5)$$

8.3.3 Distributed Resistance Models (DRM) Formulation

Subroutines DRMA and DRML are used to calculate the hydraulic resistance per unit volume for the solution of the axial and lateral momentum equation respectively, as follows:

$$\text{DRMA} : \quad F_V^A = (F_R^A + F_W^T \cos\phi + F_W^N \sin\phi)/V_S \qquad (8.6)$$

$$\text{DRML} : \quad F_V^L = (F_R^L + F_W^T \sin\phi - F_W^N \cos\phi)V_G \qquad (8.7)$$

where F_R^A, F_R^L, F_W^T, F_W^N and ϕ are schematically shown in Figure 7.3, and V_S and V_G are the subchannel and gap fluid volumes respectively. The models that are currently in use in AFREMIT for the above hydraulic resistances are presented in Table 8.1.

The exact values of the geometrical parameters A_W, D_V, V_S and V_G are calculated in subroutine H12WG for different geometry patterns (combinations of subchannels or gap kinds and wire-spacer position, see Section 8.4) as a funtion of P/D and H/D. Subroutine DRMA or DRML performs the following tasks.

I. Identifies the subchannel or gap type and the relative position of the wire-spacer (pattern). Selects the proper geometrical parameters.

TABLE 8.1. SUMMARY OF EQUATIONS USED FOR THE DISTRIBUTED RESISTANCE MODEL.

$$F_R^A = \frac{f_A}{8} A_w \rho V^2 \cos\theta \qquad (T.1)$$

$$F_W^T = \frac{f_A}{8} (A' - A)\rho V^2 \cos(\phi-\theta) \qquad (T.2)$$

where

$$f_A = f_A(Re_v\ a) = \begin{cases} a/Re_v & ; \quad Re < 600 \\ 0.3166/Re_v^{0.25} & ; \quad Re > 2{,}000 \\ a/600\cdot(1-\psi) + \dfrac{0.316}{1000^{0.25}}\psi & ; \text{ otherwise} \end{cases} \qquad (T.3)$$

$$\text{where } \psi = \frac{(Re_v - 600)}{1200}$$

$$Re_v = D\,\rho\,|v|/\mu$$

a: Rehme's coefficient of laminar flow

$$F_W^N = C.D_w \frac{\Delta z}{\cos\phi} \rho |V_N| V_N = C \frac{D_w \Delta z}{\cos\phi} \rho V^2 |\cos(\phi-\theta)| \cos(\phi-\theta) \qquad (T.4)$$

$$F_R^L = \frac{f_L}{8} A_w \rho |u| u \qquad (T.5)$$

$$f_L = 180/Re_u \quad ; \quad Re_u < 200 \text{ or } Re_v < 400 \qquad (T.6)$$

$$f_L = 2.25/Re_u^{0.145} \quad ; \quad \text{otherwise}$$

$$Re_u = D_V \rho |u|/\mu$$

A_w : Subchannel or gap wetted area

A_w' : Subchannel or gap wetted area including the wire-wrap

$D_V = 4\,V_f/A_w'$

V_f: fluid volume in subchannel or gap

Δz : axial dimension of numerical mesh

D_w : wire-spacer diameter (uniform)

C : constant to be dtermined by calibration against data.

II. Estimates for the given subchannel or gap the values of w and u to be used in the models of Table 8.1. For the axial momentum equation (subroutine DRMA) the following velocities are used (see Figure 8.6).

$$w = w_i \tag{8.8}$$

$$u = u_{k1,\ell-1}/2.0 + u_{k1,\ell}/2.0 \tag{8.9}$$

Note that the axial momentum equation cell is staggered upwards with respect to the mass balance cell.

For the lateral momentum equation (subroutine DRML) the following velocities are used: (see Figure 8.7)

$$w = (w_{i,\ell}+w_{i,\ell+1}+w_{j,\ell}+w_{j,\ell+1})\ /4.0 \tag{8.10}$$

$$u = \begin{cases} u_{k,\ell}; \text{ case (a)} \\ u_{k,\ell}/2.0; \text{ case (b)} \end{cases} \tag{8.11}$$

III. Calculates the total hydraulic resistances F^A_{TOT} (in DRMA) and F^L_{TOT} (in DRML) using equations 8.6 and 8.7 respectively and the models of Table 8.1. As discussed in the previous paragraph, each individual resistance component F^A_R, F^L_R, F^T_W, F^N_W is decomposed into "implicit" and "explicit" components. This is made possible since, as Table 8.1 indicates, each resistance component is proportional to V^2 where

$$V^2 = w^2 + u^2$$

For example, the F^A_R component can be written:

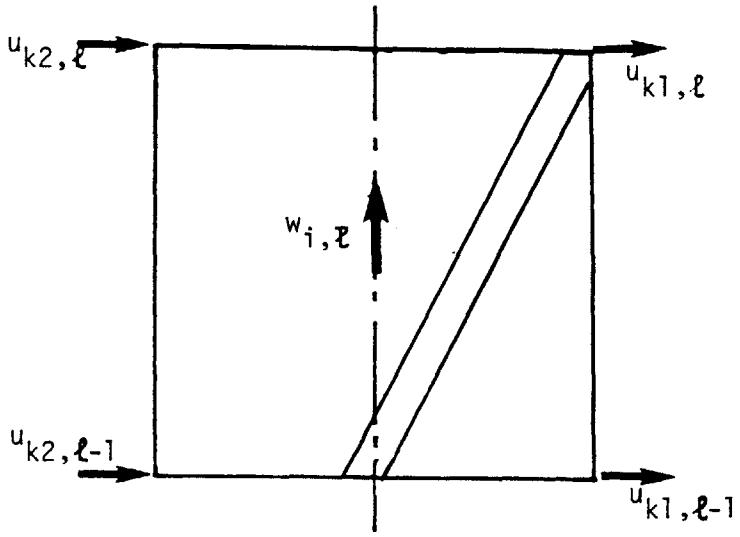

FIGURE 8.6. Typical wire-wrap pattern arising in axial momentum equation control volume. (subchannel)

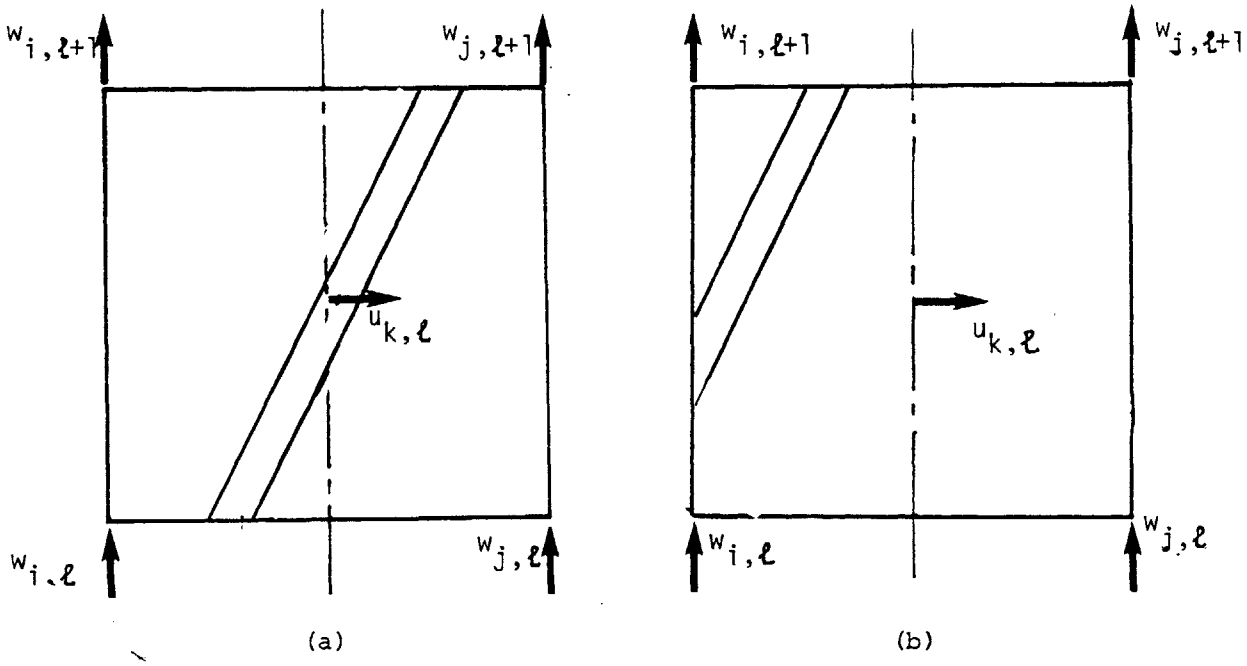

FIGURE 8.7. Typical wire-wrap patterns arising in the tranverse momentum equation control volume. (gap).

$$F_R^A = \frac{f_A}{8} A_w \rho \cos\theta \, w^2 + \frac{f_A}{8} A_w \rho \cos\theta \, u^2 \qquad (8.12)$$

or

$$F_R^A = \text{FRAIM} * w + \text{FRAEX} \qquad (8.13)$$

Note that FRAIM is always positive since $\cos\phi.w$ has the same sign with w^2. Therefore FRAIM > 0 and hence Patankar's stability criterion is satisfied.

The F_R^L component in DRML subroutine is treated similarly.

$$F_R^L = \text{FRLIM} * u \text{ (implicit term only)} \qquad (8.14)$$

Note that in subroutine DRMA, the "w" components are treated implicity and the "u" components explicitly. The opposite is true for subroutine DRML.

Resistance components F_W^T and F_W^N are included in both the DRMA and DRML subroutines. In the case of DRMA they are written as:

$$F_W^T = \text{FWTIM} * w + \text{FWTEX}$$

$$F_W^N = \text{FWNIM} * w + \text{FWNEX}$$

In this case FWTIM might be both positive or negative. If F_W^T is negative then the following Fortran statements are executed:

```
FWTEX = FWTEX + FWTIM * w
FWTIM = 0.0
```

In other words all source terms generated by F_W^T are treated explicitly. Similar steps are followed in DRML subroutine. Finally note that:

$$S_E^A = FAVEX = (FRAEX + FWTEX\cos\phi + FWNEX\sin\phi)/V_S$$

$$S_I^A = FAVIM = (FRAIM + FWTIM.\cos\phi + FWNIM.\sin\phi)/V_S$$

and

$$S_E^L = FLVEX = (FRLIM + FWTEX.\sin\phi - FWNIM.\cos\phi)/V_G$$

$$S_I^L = FLVIM = (FLVIM + FWTIM.\sin\phi - FWNIM.\cos\phi)/V_G$$

8.3.4 ASFREMIT Initialization

Experiences to now with ASFREMIT indicates that some high flow runs may diverge, despite all precautions taken for the treatment of the source terms. This is due to the fact that ASFREMIT initializes the velocity field as follows:

$w_{i,\ell} = \text{const.}$ for all i,ℓ's

$u_{k,\ell} = 0$ for all k,ℓ's

Thus the initial guess results in extremely large source terms in the lateral momemtum equation at high flow rates, (high w's). One remedy is to start ASFRE with low values of the coefficient C in equation (T.4 in Table 8.1) and increase it progressively as the iterations proceed. However since this approach may be time consuming it is not currently used. Instead use is made of the "forcing function" approach during the first 5 to 10 iterations. The lateral momentum equation is <u>not</u> solved when the wire spacer is close <u>to</u> or <u>at</u> the gap (Figure 8.9(a) and 8.9(b). In this case we assign:

$$u_{k,\ell} = \begin{cases} w\cos\phi\ ; & \text{case (a) , Figure 8.7} \\ w\cos\phi/2; & \text{case (b) , Figure 8.7} \end{cases}$$

The axial momentum equation is always solved without any change. With this initialization procedure, convergence was always achieved in the high Reynolds' runs we have performed to date.

8.4 Numerical Implementation of the Distributed Resistance Models.

8.4.1 Introduction

In this paragragh we develop a method to calculate S_E^A, S_I^A or S_E^L, S^L (see paragraph 8.3.3) for a given subchannel or gap. In order to do so, we need to know:

(a) the specific geometrical configuration of the particular subchannel Control Volume.

(b) the specific axial and lateral velocities involved for this particular configuration.

Both the geometrical parameters (hydraulic diameters, wetted perimeters, gap size, wire position, ect.) and the relevant velocities are needed as inputs in the DRM's presented in Table 8.1 (see also Chapter 7). In this section we develop a methodology to tackle this problem in an efficent way. Before presenting the whole identification logic, some subchannel or gap attributes have to be defined, namely subchannel or gap kinds, patterns and types as well as the gap attribute gap orientation. In addition some definitions of attribute functions have to be discussed namely the

FORTRAN functions LC(I.J) and ICB(M,I) that were introduced in ASFRE code together with the functions ITBL (I,L), ITBL1(K,L), NADJ(I,L) and NADJ1(K,L), introduced in this work.

8.4.2. Kinds and Patterns of Subchannels or Gaps.

Figure 6.3 shows the control volumes (CV) employed for the solution of the axial and lateral momentum equations respectively. As it has been already stated in this work the axial mesh size Δz of subchannels and gaps is taken equal to H/12 were H is the wire-wrap lead length. Within this axial length, the wire-spacer spans an angle of 30° rotation along the axial direction. Note that the wire-spacer rotates counter-clockwise for an observer situated at the top of the rod and observing the wire-spacer move from the bottom to the top.

We define three subchannel kinds namely interior (i) edge (e) and corner (c) subchannels. These terms are widely used in the rod bundle literature and they are illustrated in Figure 8.5.

To define subchannel patterns note clearly that for the solution of the axial momentum equation, the subchannels are defined on a staggered mesh, which is different than the mass or energy balance numerical mesh. The staggered mesh can be constructed by a $\Delta z/2$ upward displacement of the reference (mass,balance) mesh. It is obvious then that the lowest intersection of the wire-spacer with the staggered mesh should occur at the 0° location.

Figure 8.8 (a) examines the relative positions of the wire-spacer within an interior Axial Momentum equation CVs (AMCV or subchannels). The following situations exist:

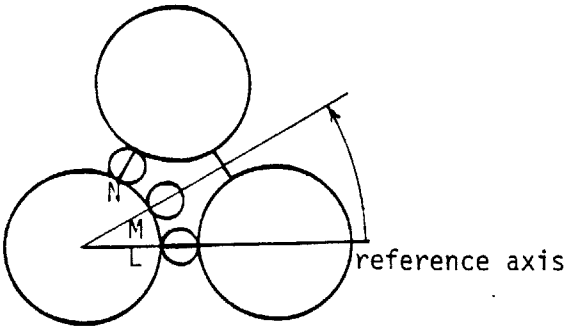

(a) INTERIOR SUBCHANNEL

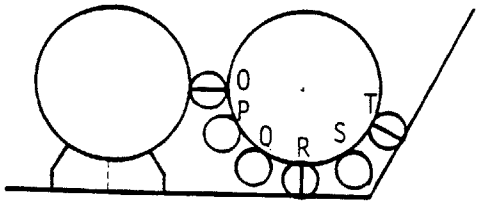

(b) EDGE AND CORNER SUBCHANNEL

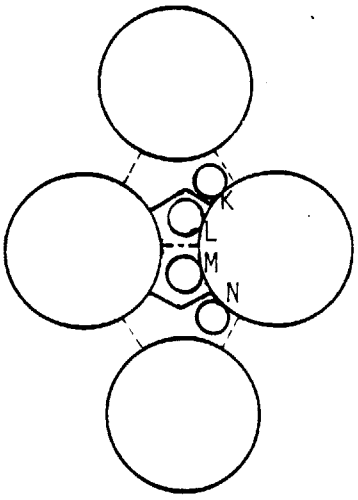

(c) (i-i) GAP

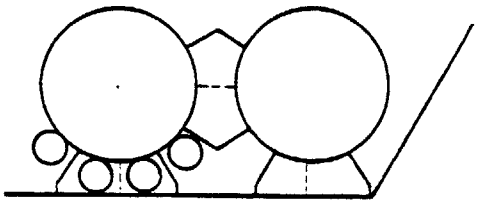

(d) (i-i), (e-e), and (e-c) GAPS

FIGURE 8.8 . PATTERN DEFINITION FOR SUBCHANNELS AND GAPS.

1. Spacer entering subchannel (i), moving from position L to M (or from $\omega = 0°$ to $\omega = 30°$)
2. Spacer leaving subchannel (i), moving from position M to N (or from $\omega = 30°$ to $\omega = 60°$)
3. Spacer not intersecting subchannel (i).

Note that the subchannel geometrical characteristics (hydraulic diameter, wetted perimeters and areas, etc.) are identical for situations 1 and 2 above. Therefore, not counting situation 3, which corresponds to a bare subchannel geometry, the number of geometrical patterns (situations with different geometrical characteristics) is one. We name this pattern, pattern (1).

Following the same procedure, observe that in the case of edge AMCVs, there exist two geometrical patterns. Referring to Figure 8.8 (b), pattern (2) corresponds to the wire-wrap rotations from position O to P, and from position Q to R (corresponding to ω's from 180° to 210°, and from 240° to 270°, respectively). Pattern (3) corresponds to wire-wrap rotation from P to Q (210° to 240°). Similarly in the case of corner AMCVs, a single, (4), pattern exists, corresponding to rotations from R to S and from S to T of Figure 8.8 (b).

We turn now to the transverse momentum equation control volumes (TMCV or gaps). Note that the gaps are located within the reference mesh and not within the staggered mesh. Therefore the cross-sections of the gap horizontal surfaces and the wire-wrap spacers occur at different angles than those arising in the subchannel case. In order

to make things easier, we define two kinds of gaps: (see Figures 8.8 (c) and (d))

First kind : interior-interior (i-i)

interior-edge (i-e)

Second kind: edge-edge (e-e)

edge-corner (e-c)

Again the words interior, edge and corner refer to the neighbor subchannels adjacent to the gap. Refering to Figure 8.8 (c) (First kind gap) observe that two geometrical patterns arise. We define pattern (1) as the configuration arising when the wire spacer is exactly at the center of a first kind gap (moving from point L to point M). Pattern (3) is defined when the wire spacer enters or exits from this gap (see Figure 8.11 (d)). Patterns (2) and (4) are defined respectively for a second kind gap.

For these subchannel and gap pattern definitions, the geometrical parameters that are used in the models of Table 8.1 (hydraulic diameters, volumes, areas, etc.) can be calculated. These calculations are performed in subroutine H12WG in Appendix A.8.1. as a function of P/D, H/D and wire-spacer diameter.

8.4.3. The Identification Problem-Attribute Functions

Here we define the general identification problem. For a given control volume (subchannel or gap) we identify:

(a) the geometrical configuration (pattern) associated with it, and

(b) the relevant neighbor control volumes (when the CV on hand is not bare.)

In order to explain the above more clearly, let us give some useful definitions. The definitions presented in this work consist of an extension to those employed in the ASFRE subchannel analysis program [Y-1]. Index I indicates a given subchannel, as shown in Figure 5.2. For a 19-pin bundle, there are a total of 42 subchannels. Index L marks the axial location of a given subchannel or gap. Since $\Delta z = H/12$, the subchannel (I,L) has the same geometric characteristics as subchannel (I,L+12). We introduce a new index, LW, which runs from 1 to 12 and is defined as follows:

$$LW = MOD(L,12) = L - [L/12]*L \tag{8.17}$$

In identifying geometrical patterns in a subchannel, we need to only specify indices I and LW (instead of L).

Index K indicates a specific gap (see Figure 5.2). In a 19-pin rod bundle, there are 60 gaps connecting the corresponding subchannels. The FORTRAN function KCHAN gives the gap number as a function of the neighbor subchannels I and J:

$$K = KCHAN(I,J) \tag{8.18}$$

Since there is a one-to-one correspondence between K and (I,J), equation 8.18 might be used to determine the neighbor subchannels I,J of a given gap K.

Finally, the FORTRAN function LC(I,M)-- where M=1, 2 or 3-- gives the neighbor subchannels for a given subchannel I. In order to calculate the neighbor gaps, one should use the KCHAN(I,J) function with J = LC(I,M).

So far, we have presented only the ASFRE approach for completely specifying the neighbor control volumes given I (for subchannels) or K (for gaps). We now present the concept of gap direction as it is employed in ASFRE.

Figure 8.9 defines the gap directions for all kinds of gaps (i-i, i-e, e-e, e-c). It defines also the ICB(M,I) function as being equal to the gap direction from the I-th subchannel toward the LC(I,M) subchannel. (Note that the direction from the LC(I,M) to I-th subchannel has an opposite sign number.)

The function ICB(M,I) can be used to identify the various types of subchannels and gaps. Two subchannels or gaps are of the same type when they have the same gap directions.

Figure 8.9 marks all subchannels with a Roman numeral which indicates the type of subchannel. As can be seen, the interior subchannels are of two types: Type I (for which ICB(M,I) equals 1, -2, or 3) and Type II (where ICB(M,I) equals -1, 2, or -3). Table 8.2 gives the definitions of the various types of subchannels in terms of the ICB function. Table 8.3 gives the various types of gaps

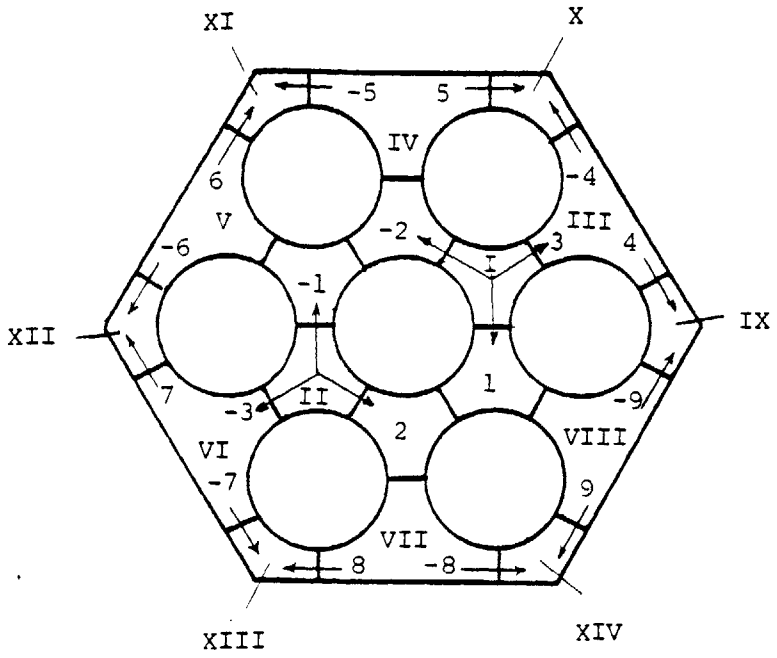

FIGURE 8.9. ICB(M,I) FUNCTION DEFINITION AND SUBCHANNEL TYPES.

TABLE 8.2. TYPES OF SUBCHANNELS (AMCVs) AND ORIENTATIONS.

Type	Subchannel Kind	ICB(M,I) Values
I	interior	1, -2, 3
II	"	-1, 2, -3
III	edge	-3, -4, 4
IV	"	1, -5, 5
V	"	2, -6, 6
VI	"	3, -7, 7
VII	"	-1, -8, 8
VIII	"	-2, -9, 9
IX	corner	9, -4, 0
X	"	4, -5, 0
XI	"	5, -6, 0
XII	"	6, -7, 0
XIII	"	7, -8, 0
XIV	"	8, -9, 0

TABLE 8.3. TYPES OF GAPS (TMCVs) AND GAP ORIENTATIONS.

Type	Gap Kind	Gap Orientation
I	(i-i), (i-e)	1
II	"	2
III	"	3
IV	(e-e), (e-c)	4
V	"	5
VI	"	6
VII	"	7
VIII	"	8

as a function of the gap orientation (absolute value of the gap direction).

Having established the concepts of kind and type for subchannels or gaps, Tables 8.4 and 8.5 are discussed which determine, (a) whether the wire-spacer is present or not at a given Control Volume and if yes (b) the relative position and the relevant gap along which DRM force balances will be performed. The input of these tables are (a) subchannel or gap type given by tables 8.2 and 8.3 respectively, (b) the LW parameter given by equation 8.17. These tables are defined in ASFREMIT using the FORTRAN attribute function names ITBL(ITYPE,LW) and ITBL1(ITYPE,LW) respectively (see subroutine H12WG).

We now explain the output provided by these attribute functions. In both cases a zero entry indicates that the subchannel or gap is bare, i.e. free from any spacer. In case that the entry is different than zero the signed number in Table 8.4 indicates the gap orientation (as defined in Figure 8.9) along which the wire enters to or exits the subchannel on hand. This rule is not valid in case of edge subchannels when the entry number is 50. This indicates that the wire spacer is in the middle of an edge subchannel (arc PQ of Figure 8.8 (b)). A similar convention is followed in the case of gap control volumes of Table 8.5. The only difference is the different decades used for each number. For example a 10 entry indicates that the wire spacer enters the gap with orientation of 10 (arc KL of Figure 8.8 (c)). Similarly entries 1 and 100 correspond to middle (arc LM) and exit (arc MN) position of

TABLE 8.4. SUBCHANNEL IDENTIFICATION TABLE

	Interior		Edge						Corner					
	I	II	III	IV	V	VI	VII	VIII	IX	X	XI	XII	XIII	XIV
1	0	-1	50	0	0	0	+1	50	-9	0	0	0	0	0
2	-1	0	-4	-1	0	0	0	2	-4	0	0	0	0	0
3	-2	0	-4	50	0	0	0	0	0	-4	0	0	0	0
4	0	-2	50	-5	-2	0	0	0	0	-5	0	0	0	0
5	0	-3	-3	-5	50	0	0	0	0	0	-5	0	0	0
6	-3	0	0	50	-6	-3	0	0	0	0	-6	0	0	0
7	1	0	0	1	-6	50	0	0	0	0	0	-6	0	0
8	0	1	0	0	50	-7	1	0	0	0	0	-7	0	0
9	0	2	0	0	2	-7	50	2	0	0	0	0	-7	0
10	2	0	0	0	0	50	-8	50	0	0	0	0	-8	0
11	3	0	0	0	0	3	-8	-9	0	0	0	0	0	-8
12	0	3	3	0	0	0	50	-9	0	0	0	0	0	-9

TABLE 8.5. GAP IDENTIFICATION TABLE

	GAP								
	Interior-Interior Edge-Interior			Edge-Edge Edge-Corner					
LW	Type I	Type II	Type III	Type IV	Type V	Type VI	Type VII	Type VIII	Type IX
1	-1	0	0	-40	0	0	0	0	-900
2	-100	-20	0	-4	0	0	0	0	0
3	0	-2	0	-400	-50	0	0	0	0
4	0	-200	-30	0	-5	0	0	0	0
5	0	0	-3	0	-500	-60	0	0	0
6	10	0	-300	0	0	-6	0	0	0
7	1	0	0	0	0	-600	-70	0	0
8	100	20	0	0	0	0	-7	0	0
9	0	2	0	0	0	0	-700	-80	0
10	0	200	30	0	0	0	0	-8	0
11	0	0	3	0	0	0	0	-800	-90
12	-10	0	300	0	0	0	0	0	-9

the wire spacer. In general when $10 < |ITBL1| < 100$ the wire spacer enters the gap (as it moves from bottom to top) whereas for $|ITBL1| < 10$ or $100 < |ITBL| < 1000$ the spacer is in the middle or exits from the gap respectively.

Using Table 8.4 and the ICB(M,I) and LC(I,J) functions, one can find the relevant gap K for a given subchannel. Using this gap K, the magnitude of the lateral velocity u of Figure 7.2 (a) can be estimated as explained in paragraph 8.3.3. In order to obtain the sign for u consider the following.

Figure 8.10 (a) shows three successive neighboring subchannel surfaces (belonging to the same rod and being at the same axial level). The dotted lines indicate the surface area of the relevant gaps. Referring to Figure 8.10 (a), take:

K1 = KCHAN(I,I1)

K2 = KCHAN(I,12)

We now introduce a new function as follows:

$$ISIGN(I,J) = -ISIGN(J,I) = \begin{cases} 1; & I<J \\ -1; & I>J \end{cases}$$

According to ASFRE, the positive direction of lateral velocity U(K), is indicated by the $\hat{n}_{I\to J}$ unit vector which is directed from subchannel I to subchannel J when $I < J$. If $J < I$, then the positive direction is given by $\hat{n}_{J\to I}$. In this report, as Figure 8.10 (a) indicates, the positive direction of the lateral velocity is defined by the right hand rule, given by unit vector n_L. It can then be shown that:

(a)

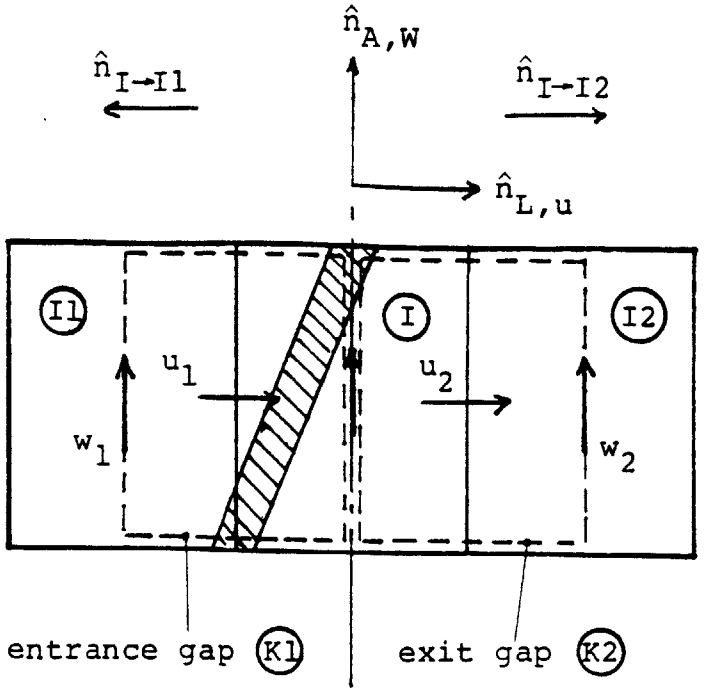

(b)

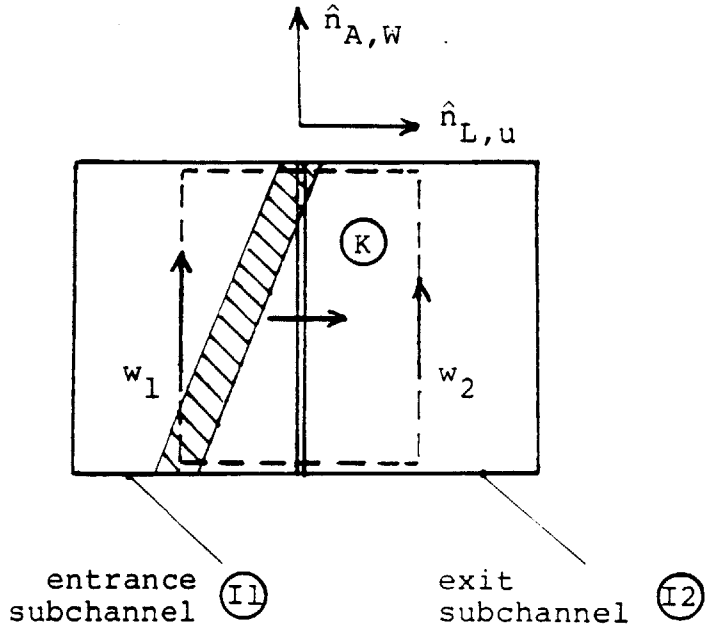

FIGURE 8.10.

Unit Vector Direction Definition and Relevant Velocities for (a) Subchannels and (b) Gaps

$$\hat{n}_L(I,J) = \text{IPORT}*\text{ISIGN}(I,J)\hat{n}_{I\to J} \tag{8.19}$$

where

$$\text{IPORT} = \begin{cases} -1; \text{ entrance gap} \\ 1; \text{ exit gap} \end{cases} \tag{8.20}$$

Applying eq. 8.19 to Figure 8.10 (a), take:

entrance gap $\quad u_1 = -\text{ISIGN}(I,I1)\ U(K1)$ (8.21)

exit gap $\quad u_2 = \text{ISIGN}(I,I2)\ U(K2)$ (8.22)

In a similar way for transverse momentum equation considerations, we obtain u as follows (see Fig. 8.10 (b)):

$$u = \text{ISIGN}(I1,I2)\ U(K) \tag{8.23}$$

where I1 is the subchannel from which the wire-spacer is coming, and I2 is the subchannel toward which the spacer is going (as we move up).

Finally, Figure 8.11 gives a summary of the velocity and pattern identification problem as described in this section. In the case of subchannels, the left branch of Figure 8.11 from "subchannel kind to crossflow velocities" is performed in subroutine H12WG. The attribute function NADJ(I,L) is constructed there, which gives the adjacent subchannel J and the sign of the corresponding lateral velocity for a given subchannel I. In the case of gaps, the same branch of Figure 8.11 is implemented within subroutine DRML directly. The branch of Figure 8.11 "Kind to geometrical parameters" is implemented within subroutines DRMA and DRML for subchannels and gaps respectively.

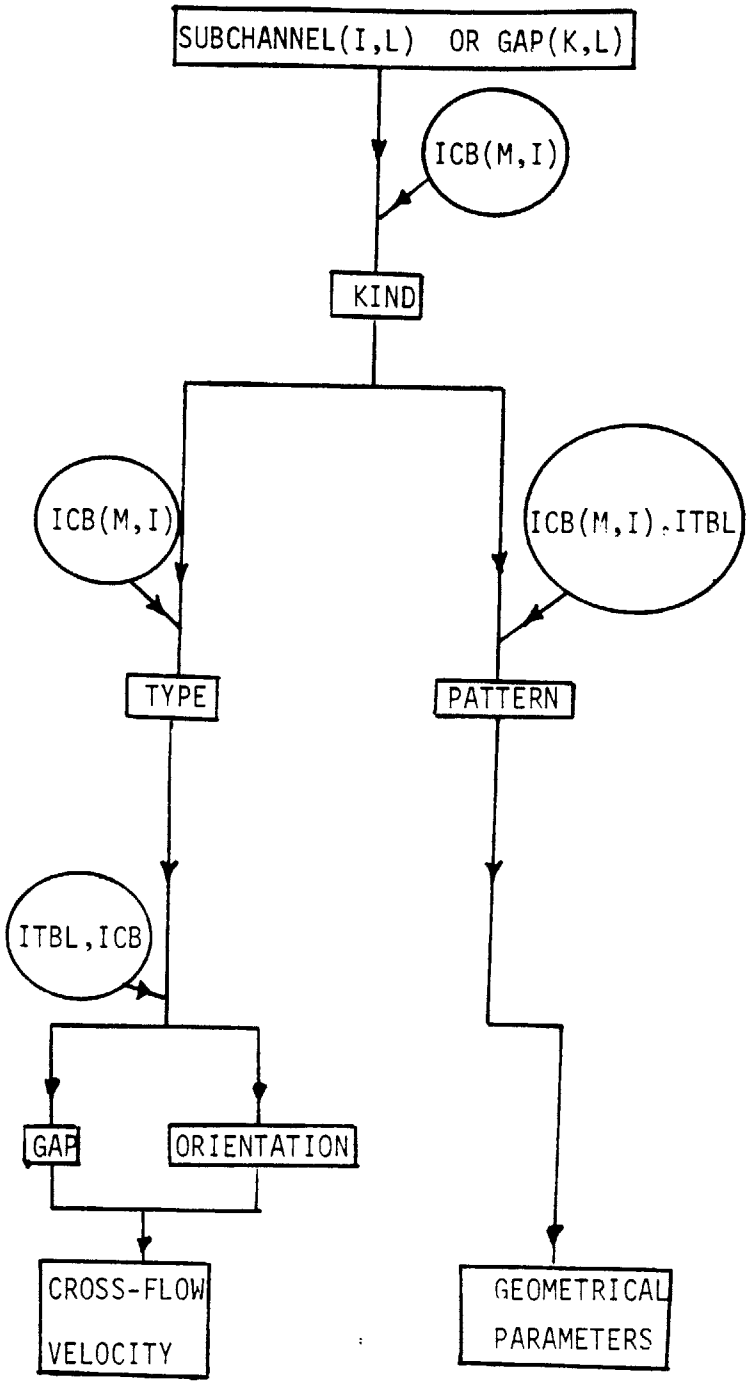

FIGURE 8.11. CROSS-FLOW VELOCITY AND GEOMETRICAL PARAMETER SELLECTION LOGIC FOR A GIVEN SUBCHANNEL OR GAP.

8.5 ASFREMIT Calibration and Comparisons with Experimental Data.

8.5.1 Introduction

In this section, the distributed resistance models (DRMs) incorporated in ASFREMIT code, are calibrated and tested against experimental data in both isothermal and mixed convection flows. The ASFREMIT constants that are to be determined by calibration are presented and discussed in deatail. Subsequently, the various data predictions are presented. Numerical convergence and subchannel formulation problems are identified and future research on these issues is proposed.

8.5.2. ASFREMIT Calibration Constants.

The only input parameter that is left to be determined from calibration studies is the parameter C given in equation (T-4) of Table 8.1.

As discussed earlier we propose the following model for C.

$$C = CON\left(\frac{A_g}{A_{mg}}\right)^n \left(1 + \frac{10}{R_e^{0.33}\, D_W}\right) \tag{8.24}$$

where A_g is the gap between the heated rods, A_{mg} is the minimum gap between the wire spacer and the adjacent rod and D_W is the wire spacer diameter. The constants CON and n will be the calibration constants. For each particular pattern arising in subchannels and gaps the ratio A_g/A_{mg} is calculated as a function of P/D. Figure 8.12 indicates the various average positions of the

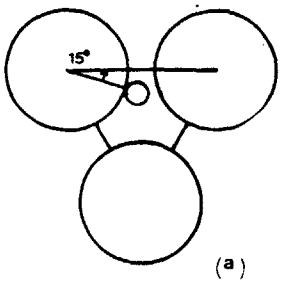

(a)
Subchannel patterns 1 and 2.

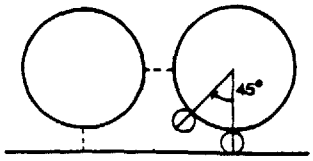

(b)
Subchannel number 3

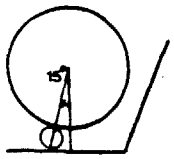

(c)
Subchannel number 2 and 4

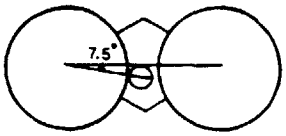

(d)
Gap pattern 1

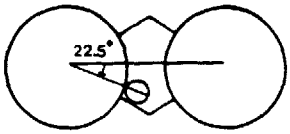

(e)
Gap pattern 3

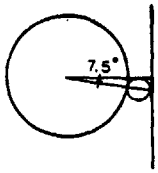

(f)
Gap pattern 2

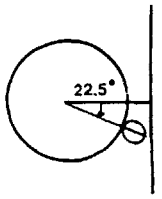

(g)
Gap pattern 4

FIGURE 8.12. AVERAGE POSITION OF THE WIRE-WRAP SPACER FOR THE VARIOUS SUBCHANNEL AND GAP PATTERNS.

wire spacer corresponding to the various subchannel and gap patterns. For the cases of Figure 8.12, the values of the area ratio (A_g/A_{mg}) are given by the following equations:

Case (a): RATS (1) = 30.3 (1-D/P)

RATS (2) = RATS (1)

Case (b): RATS (3) = (1-1.707 D/2P) /0.293

Case (c): RATS (4) = 58.7 (1-D/P)

Case (d): RATG (1) = 117.9 (1-D/P)

Case (e): RATG (2) = 233.78 (1-D/P)

Case (f): RATG (3) = 14.07 (1-D/P)

Case (g): RATG (4) = 26.27 (1-D/P)

Note that the S and G letters above signify subchannel and gap respectively. From Figure 8.12 note also that in the subchannel cases, there is not a one-to-one correspondance between subchannel patterns and the indices 1 to 4 of the FORTRAN function RATS.

Our preliminary calibration work, based on the Westinghouse data for fuel bundles (B-1) yielded the following values for the parameter CON of equation 8.24:

CASE OF FIGURE 8.12	CON
(a)	1.0
(b)	1.0
(c)	1.0
(d)	0.4
(f)	0.2
(g)	1.1
(h)	0.7

In all cases, the parameter n was taken equal to one. These values for CON and n were subsequently used in all comparisons of ASFREMIT with experimental results. In ASFREMIT the values of CON are read in the code in subroutine H12WG from the input file which is defined by the user.

8.5.3. ASFREMIT Comparisons with Isothermal Flow Data.

In this paragraph, the current version of ASFREMIT is compared against three different sets of experimental data in wire-wrapped rod bundles:

(a) Local, lateral velocities at the gaps provided by Westinghouse (R-2)

(b) Lateral swirl flow data at the peripheral subchannels. (Lafay et al (L-1))

(c) Subchannel axial velocity data at low Reynolds flows. (current work).

ASFREMIT was originally tested against turbulent flow data despite the fact that the primary emphasis of this work is in low Reynold's flows where laminar or transition flow regime in expected. The reason for this is the availability of local crossflow velocity data under turbulent flow conditions obtained by Roidt et al (R-2). No such data are available in laminar flows.

Figure 8.13 presents the Westinghouse data (B-1) for crossflows in large model bundle with P/D equal to 1.25 and H/D equal to 52. The model-to-prototype scale was 11:1 for the fuel out-of-pile experiments. This scale allowed detailed axial and transverse velocity measurements at the gaps between two adjacent rods. The working fluid was air and the flow was always turbulent. Some of their results for the crossflow at an interior subchannel gap are given in Figure 8.13. The average crossflow function is defined as follows:

$$\bar{\phi}\ (\alpha) = \frac{\bar{u}(\alpha)}{\bar{V}_A \tan\phi} \tag{8.26}$$

where $\bar{V}_A$ is the average subchannel axial velocity through the whole test section, $\bar{u}(\alpha)$ is the mean crossflow velocity at the gap averaged over the gap thickness, and ϕ is the angle between the wire spacer direction and the fuel rod axis. The $\bar{\phi}$ function (not to be confused with the ϕ angle) is always measured at the gap. The angle α is directly proportional to the axial distance z. For a given gap, define α to be zero when the wire-spacer is the gap.

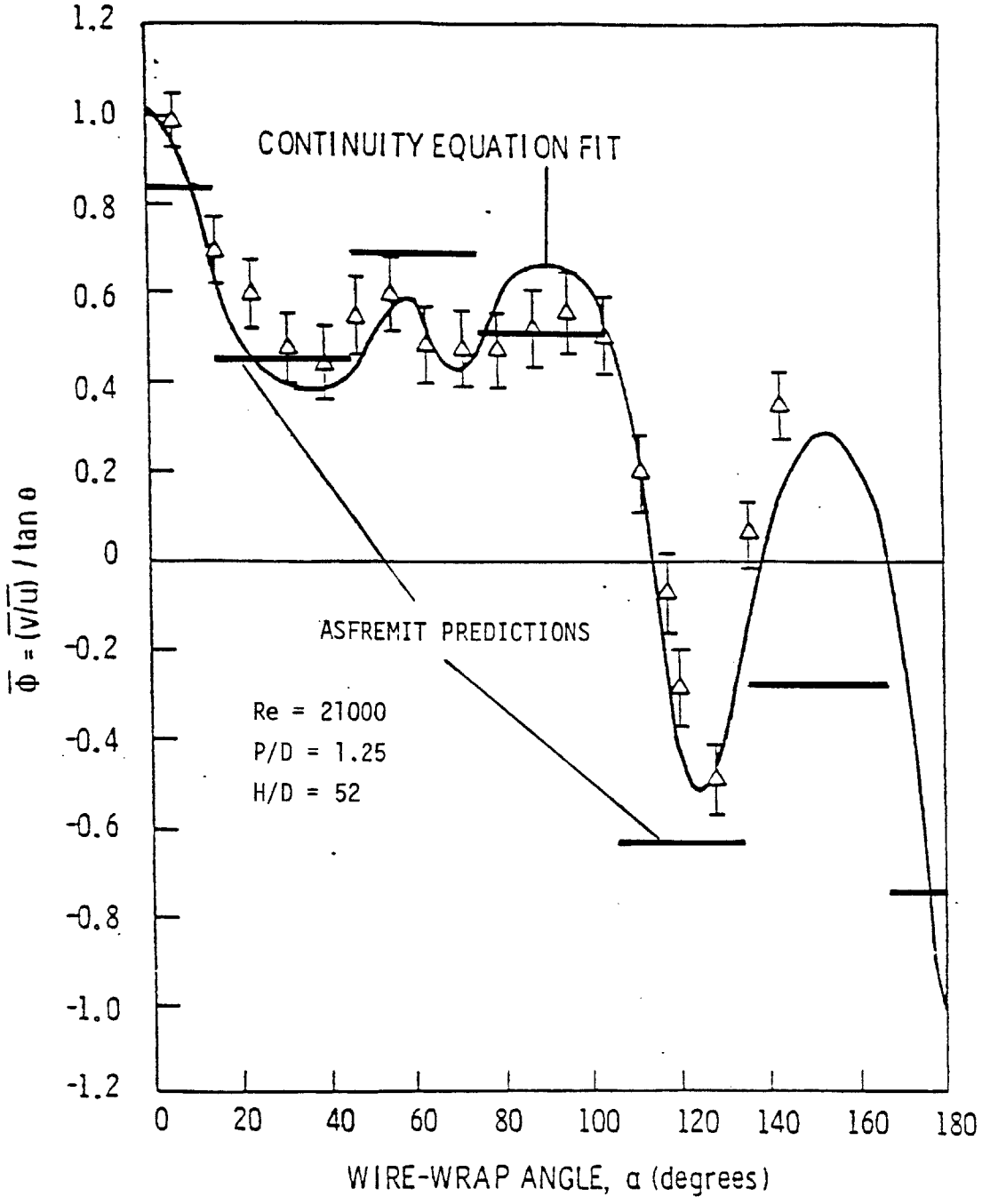

FIGURE 8.13. WARD LATERAL VELOCITY DATA AND ASFREMIT PREDICTIONS AS A FUNCTION OF THE WIRE-WRAP ANGLE.

Then for the same gap and at distance Δz downstream from the flow:

$$\alpha = 2\pi \frac{\Delta z}{H} \tag{8.27}$$

where H is the wire-spacer lead length. The data in Figure 8.13 are anti-symmetric for $180° \leq \alpha \leq 360°$. The solid curve in Figure 8.13 represent a best fit application of the relationship (from conservation of mass):

$$\overline{\phi}(\alpha) = \overline{\phi}(\alpha + 60°) - \overline{\phi}(\alpha + 120°),\ 0° < \alpha < 60° \tag{8.28}$$

which would hold if there were negligible variations in the mean subchannel axial velocities with α. (See B-1 for details.)

The thick solid horizontal bars in Figure 8.13 gives the ASFREMIT predictions for the same P/D and H/D values and for water flow at Re equal to 21,000. Predictions are satisfactory when the wire wrap angle α lies between 0° and 105°. However, for α moving from 105° to 135° the crossflow is overpredicted whereas for α in the 135° to 165° interval, ASFREMIT fails to predict the "flow reversal" as indictated by the data. We attribute this latter problem to the formulation of the pressure and convective terms of the ASFRMIT subchannel momentum equations. This can be explained with the help of Figure 8.14 (a). The crossflow in gap K will be determined by two counteracting effects. The wire spacer, being at 144° and moving from subchannel (i) to subchannel (j) will tend to "push" the flow along the same direction (from (i) to (j)). In

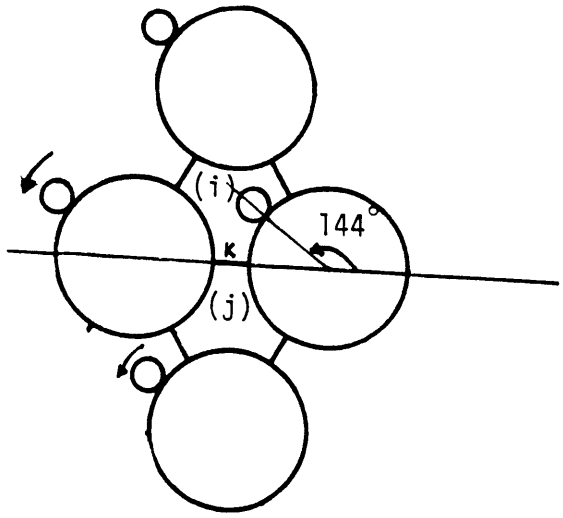

FIGURE 8.14(a). WIRE-SPACER AT 144°.

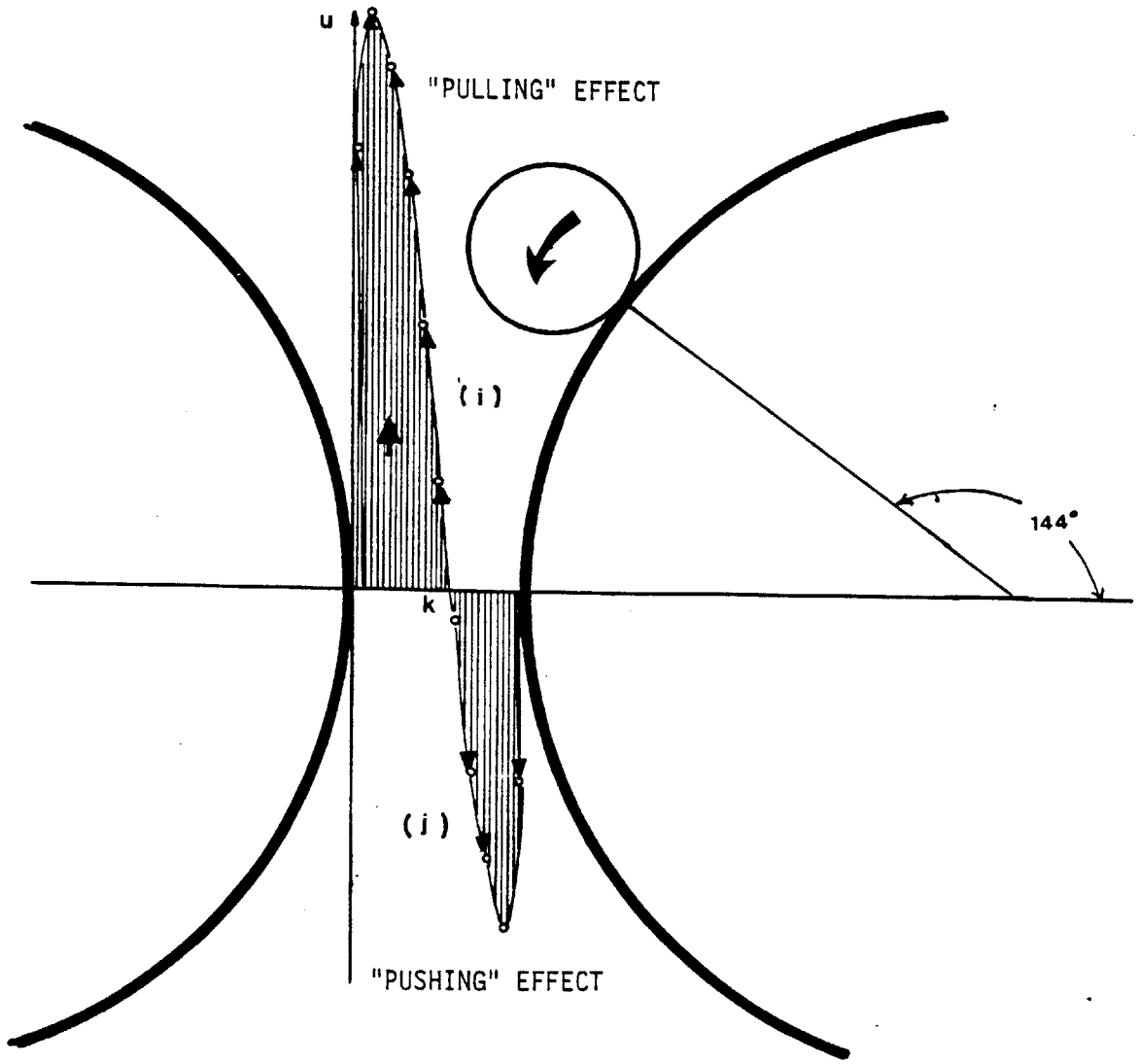

FIGURE 8.14(b)

WARD LATERAL VELOCITY DATA AT THE GAP FOR WIRE POSITION AT 144°

DEMONSTRATING THE "PULLING" AND "PUSHING" EFFECTS OF THE INCOMING SPACER ON THE GAP CROSS-FLOW.

contrast due to the presence of the wire spacer in the center of subchannel (i), the surrounding axial velocity field increases its magnitude resulting in a local drop of the pressure around the wire. This high velocity region in the vicinity of the wire-wrap was clearly observed in our Hot Film Anemometry studies at the exit plane of our wire-wrapped bundle. These latter phenomena will create a "pulling" effect causing some crossflow moving from (j) to (i). Figure 8.14 (b) gives the local lateral velocity profile data obtained by the Westinghouse experiments (B-1). The arrows indicate the magnitude of the lateral velocity taken along the gap using a pitot-static tube. In this Figure both the "pushing" and "pulling" effects are clearly indicated by the crossflow velocity profile. Our distributed hydraulic resistance models account for the pushing effects only. Therefore these models are incapable to produce any "pulling" effect. This latter effect can be correctly accounted for through the pressure and convective terms of the lateral momentum equation. As it can be seen from Figure 8.1 the COBRA code has been more successful in predicting the pulling effects. This can be explained on the basis of COBRA's steady state lateral momentum equation:

$$\underbrace{\frac{\Delta(u^{*}W_{ij})}{\Delta x}}_{\substack{\text{convective}\\ \text{term}}} = \underbrace{\frac{S}{\ell}(p_i - p_j)}_{\substack{\text{pressure}\\ \text{term}}} - \underbrace{F_{ij}}_{\substack{\text{resistance}\\ \text{term}}} \qquad (8.29)$$

The parameter S/ℓ is given as an input to the code. In case of Figure 8.1 it was taken equal to 0.3. The S/ℓ parameter can be

understood as a weighting factor of convective and pressure forces. The lower its value, the more emphasis is placed in the convective terms which in turn enhance the pulling phenomenon. This latter effect can be illustrated with the help of Figure 8.15. Here all conditions are similar to those of Figure 8.1 except the S/ℓ parameter which is smaller and equal to 0.1. Comparing Figure 8.1 and 8.15 it is clearly seen that for α between 120° and 165° the pulling effects are much more pronounced in the COBRA predictions of Figure 8.15 where the S/ℓ parameter is the smaller.

In order to achieve the same behavior with the ASFREMIT code, both the axial and the lateral momentum equations were modified to account for the presence of the wire spacer in all geometrical parameters as indicated in equation 6.18. Unfortunately, these changes rendered the code numerically unstable with most of the runs diverging in the first ten iterations. Given the cost/execution speed limitations of our computer facilities, it was decided not to pursue any further exploration of the numerical problems. Instead more ASFREMIT comparisons were performed with other data under different geometrical or flow conditions.

Lafay et al (L-1) performed local lateral flow (swirl flow) velocities measurements at the peripheral gaps of a 19-pin wire-wrapped bundle using a hydrogen bubble technique. These data are presented in Figure 8.16 together with the ASFREMIT predictions for the center gap at one hex edge. (The predictions are given by the triangles). It is observed that there is a qualitative agreement

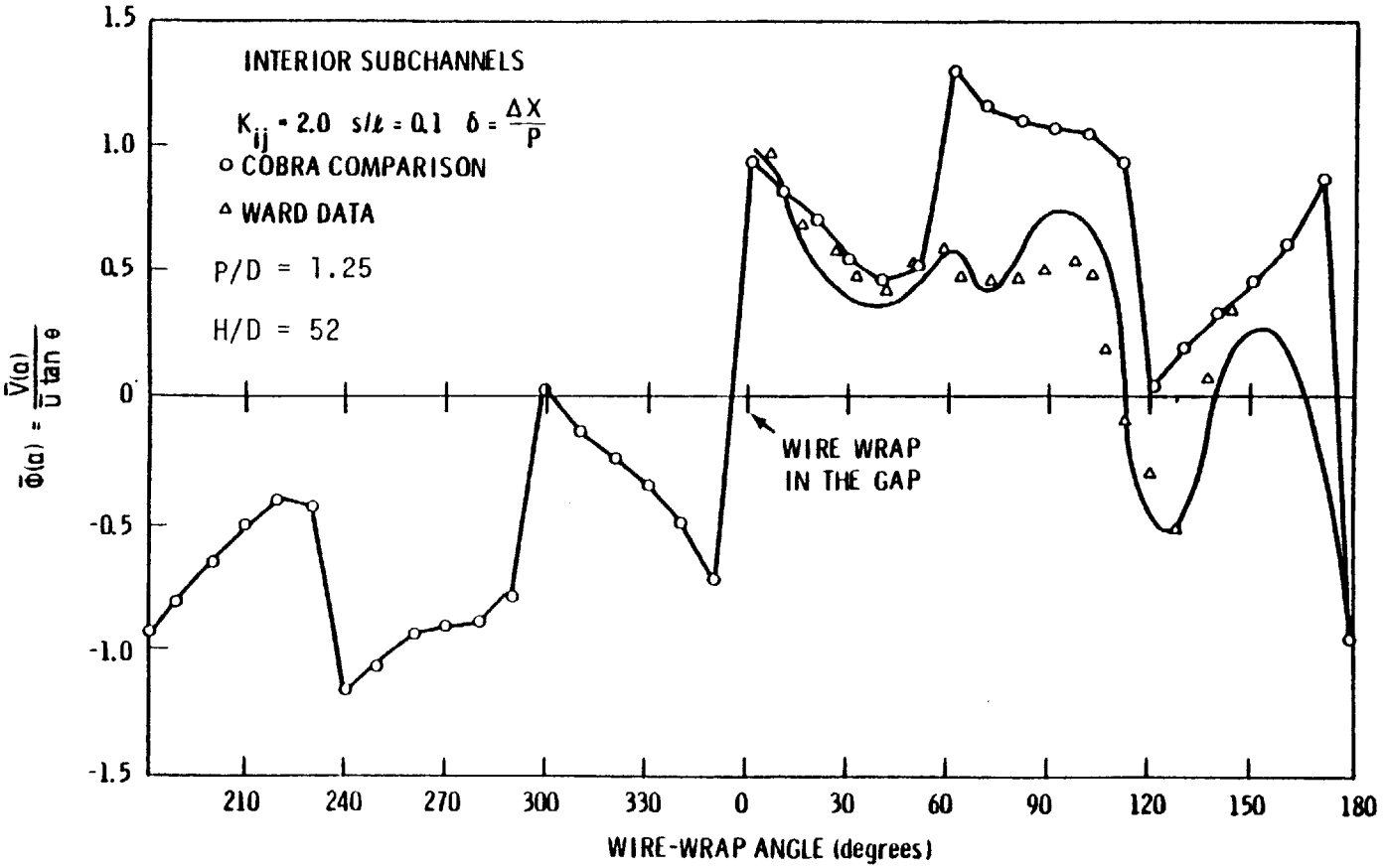

FIGURE 8.15. COBRA COMPARISONS WITH THE WARD DATA FOR TURBULENT FLOW CONDITIONS. (Taken from reference B-8)

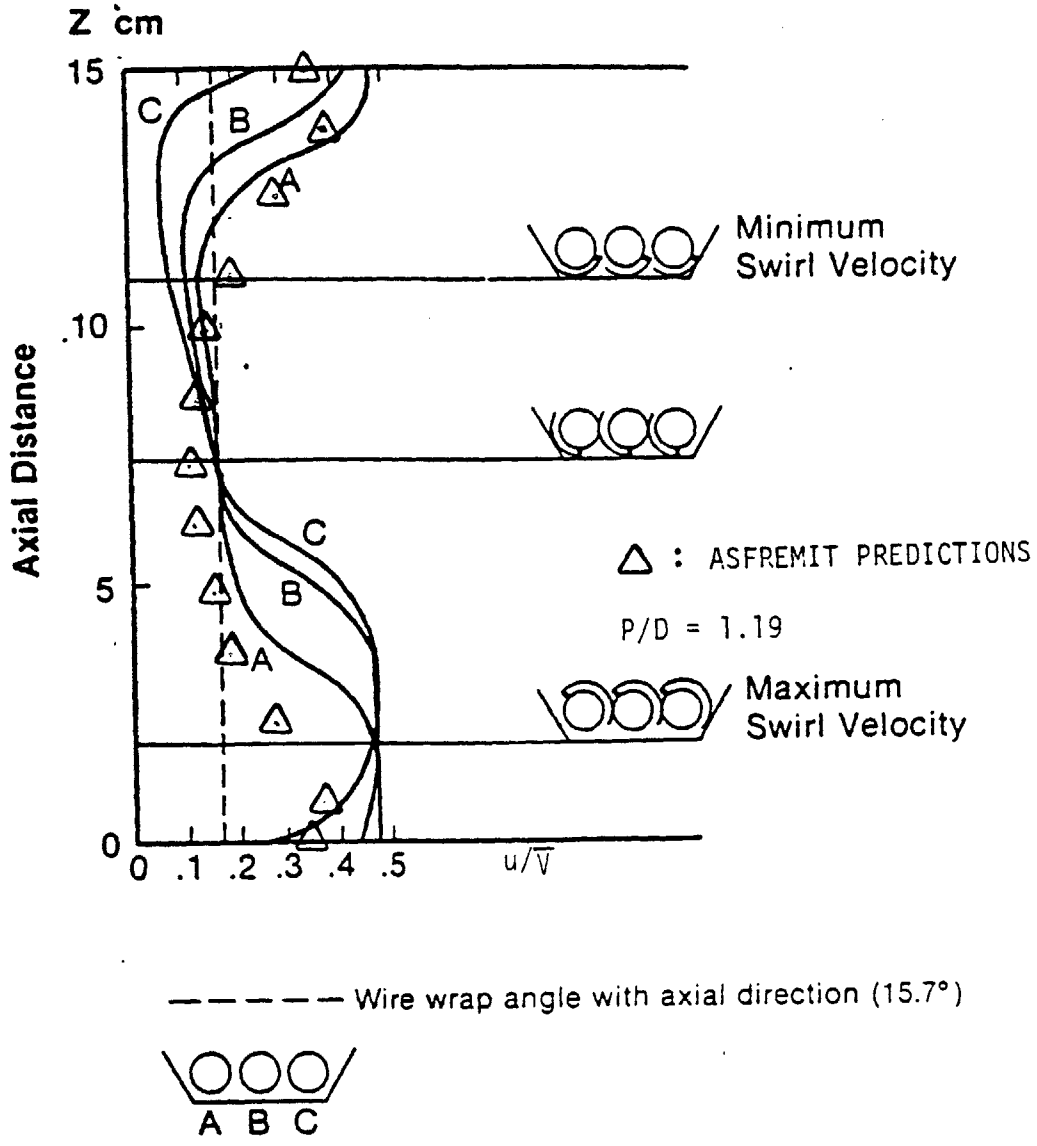

FIGURE 8.16. LAFAY'S SWIRL FLOW DATA AND ASFREMIT PREDICTIONS FOR A CENTRAL PERIPHERAL GAP, AS A FUNCTION OF THE AXIAL LOCATION Z.

between the predictions and the data. However, deviations may be as much as by factor of two.

ASFREMIT was also compared against our axial velocity data in laminar flows. Figure 8.17 plots out HFA data at the exit plane of the 19-pin wire-wrapped bundle against the ASFREMIT prediction. (For subchannel identification see Figure 5.2). In Figure 8.18, ASFREMIT is compared against another series of subchannels of the same experimental run. Overall the agreement between predictions and data is satisfactory. For the subchannels 29 and 25 (Figure 8.18) the data are overpredicted by as much as 20%. Note that these HFA data were taken at a horizontal plane at the exit region of the rod bundle while ASFREMIT predictions represent an axial average over H/12 wire-wrap lead length. Also note that due to construction problems, the areas of subchannels 25 and 15 were made 10 to 15% larger than the average edge subchannel area.

8.5.4 ASFREMIT Comparisons with Mixed Convection Temperature Data

Some preliminary comparisons of ASFREMIT versus temperature data under low flow mixed convection conditions with power skew are presented in this paragraph. The data were obtained in the present work in Chapter 5.

Figure 8.19 corresponds to Run T1 with power skew equal to 5:1 (subchannels 9,4,1,2 at high power) Re equal to 1194 and Gr_q/Re 987. This run conditions correspond to the onset of mixed convection effects. Both data and prediction exhibit a sharp temperature gradient corresponding to the high power skew ratio. Note that

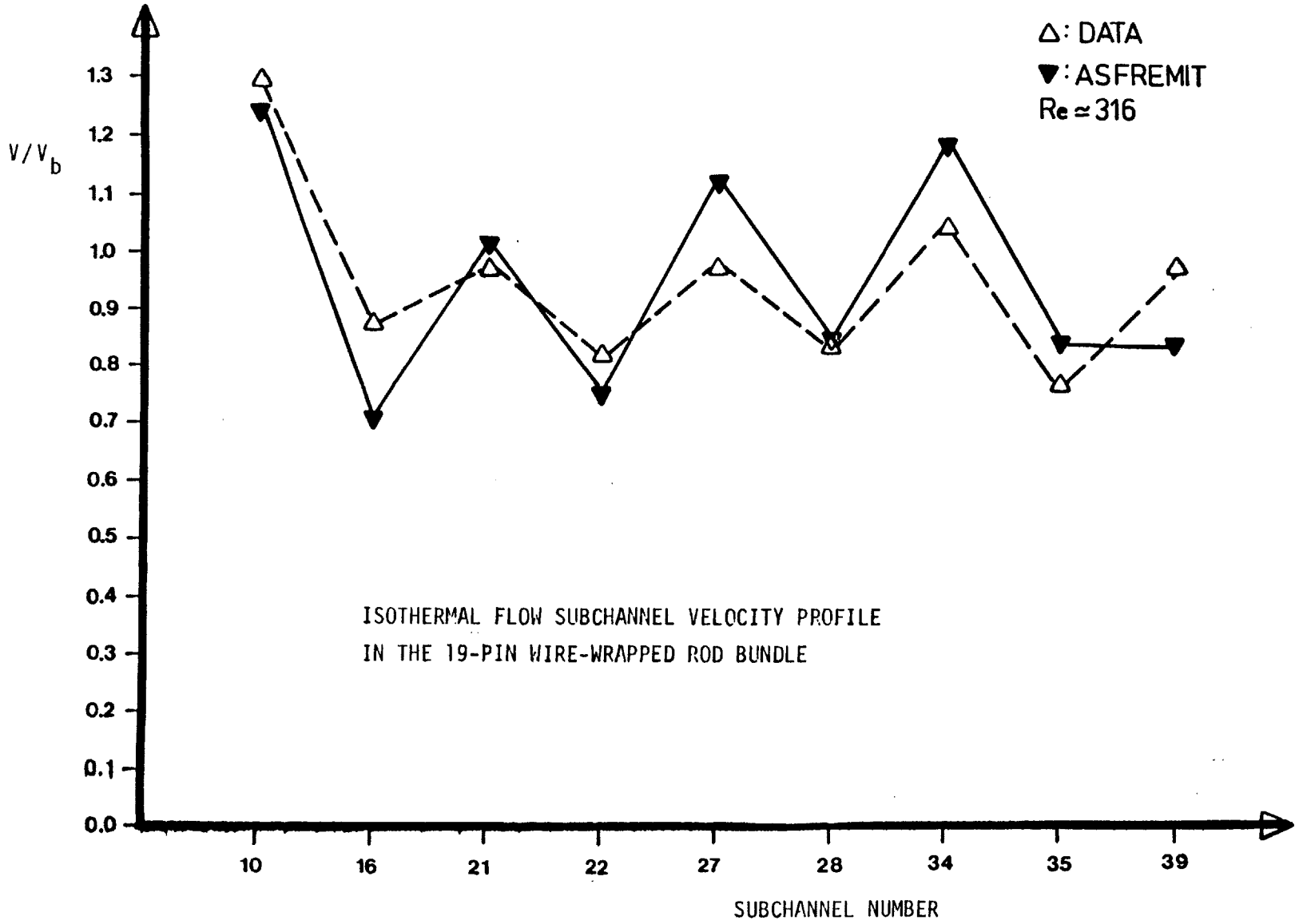

FIGURE 8.17. ASFREMIT COMPARISONS WITH SUBCHANNEL AXIAL VELOCITY DATA FOR ISOTHERMAL FLOWS.

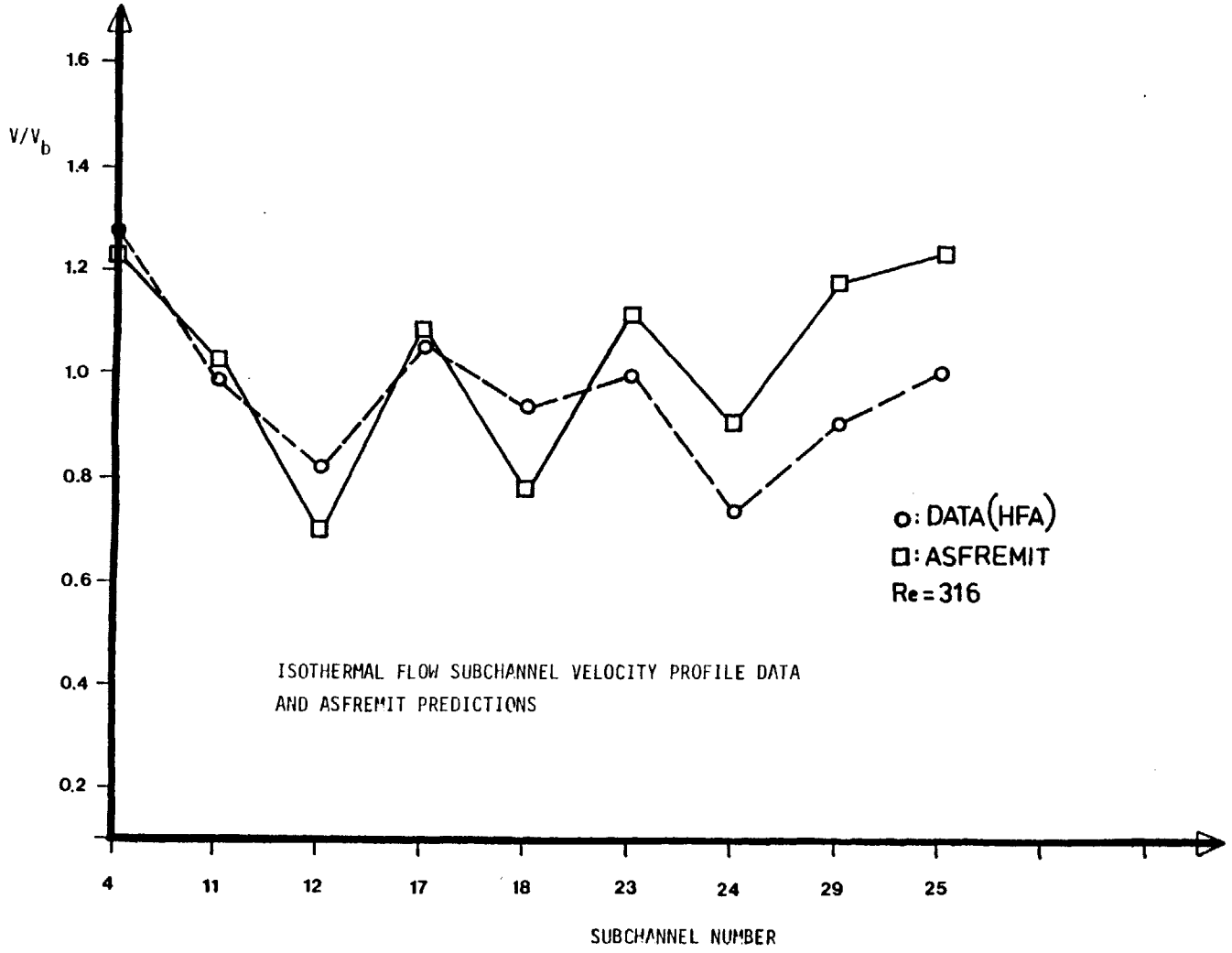

FIGURE 8.18 ASFREMIT COMPARISONS WITH SUBCHANNEL AXIAL VELOCITY DATA FOR ISOTHERMAL FLOWS.

ASFREMIT fails to predict the temperature "dip" that the data show in subchannel 34. This may be caused by the smoothing effects of the H/12 axial temperature averaging performed by ASFREMIT.

Figure 8.20 corresponds to Run T2 with the same power skew as above but Re=1240 and Gr_q/Re=1568. Here the mixed convection effects are more prominent and the profile of the temperature data is flatter than that in case T1. ASFREMIT prediction follows qualitative these trends but in an unsatisfactory way. The reason is that this ASFREMIT calculation is not converged and represents the results of the 50th iteration of the solution algorithm. For reasons that are not clear at this stage the code diverged in the subsequent iterations. Figure 8.20 reflects an energy imbalance i.e., ASFREMIT prediction shows more energy input than the data, so it probably is not converged. Therefore more work on the solution algorithim of ASFREMIT is needed before more calibration/validation work can be performed.

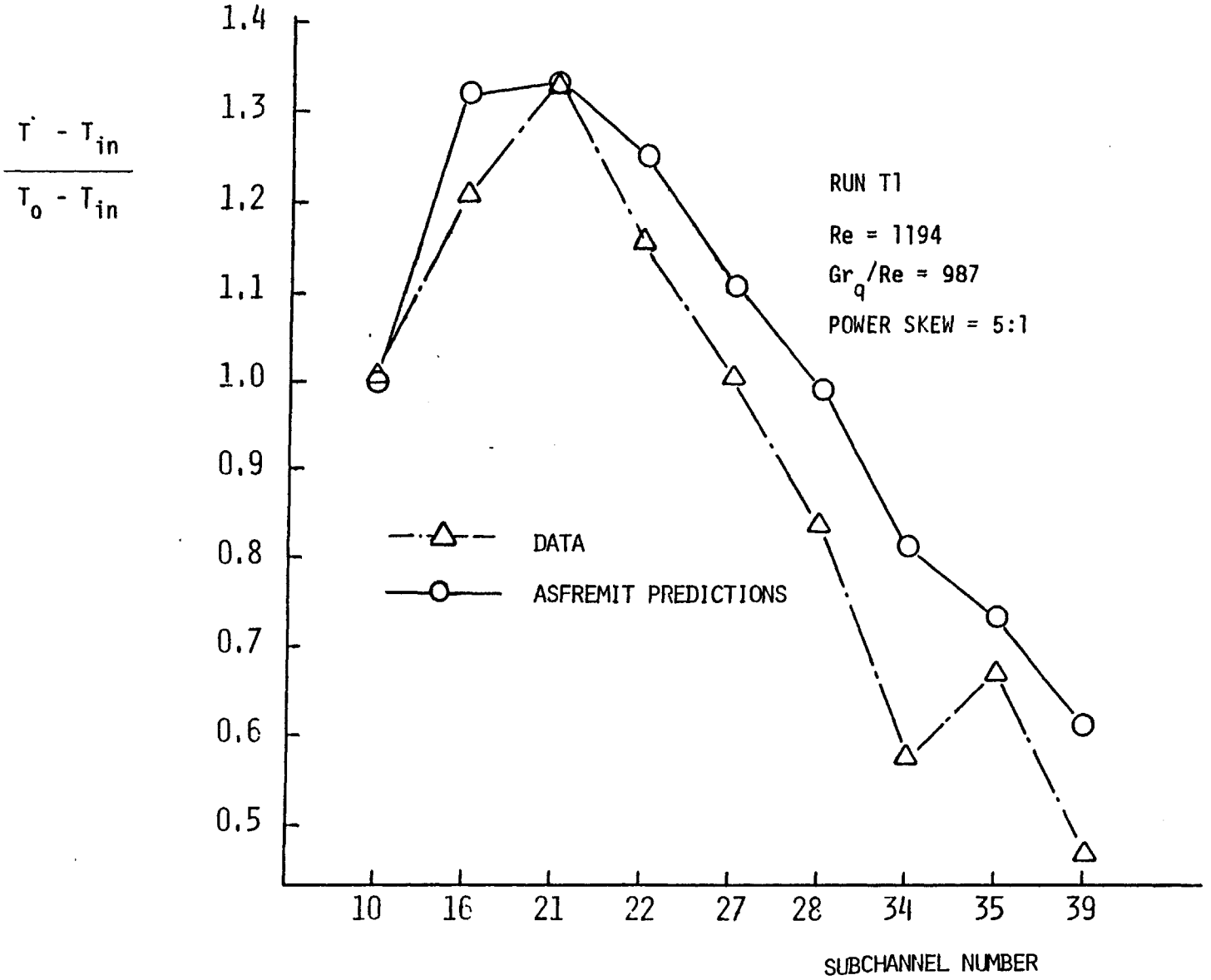

FIGURE 8.19. ASFREMIT COMPARISONS WITH MIXED CONVECTION SUBCHANNEL TEMPERATURE DATA.

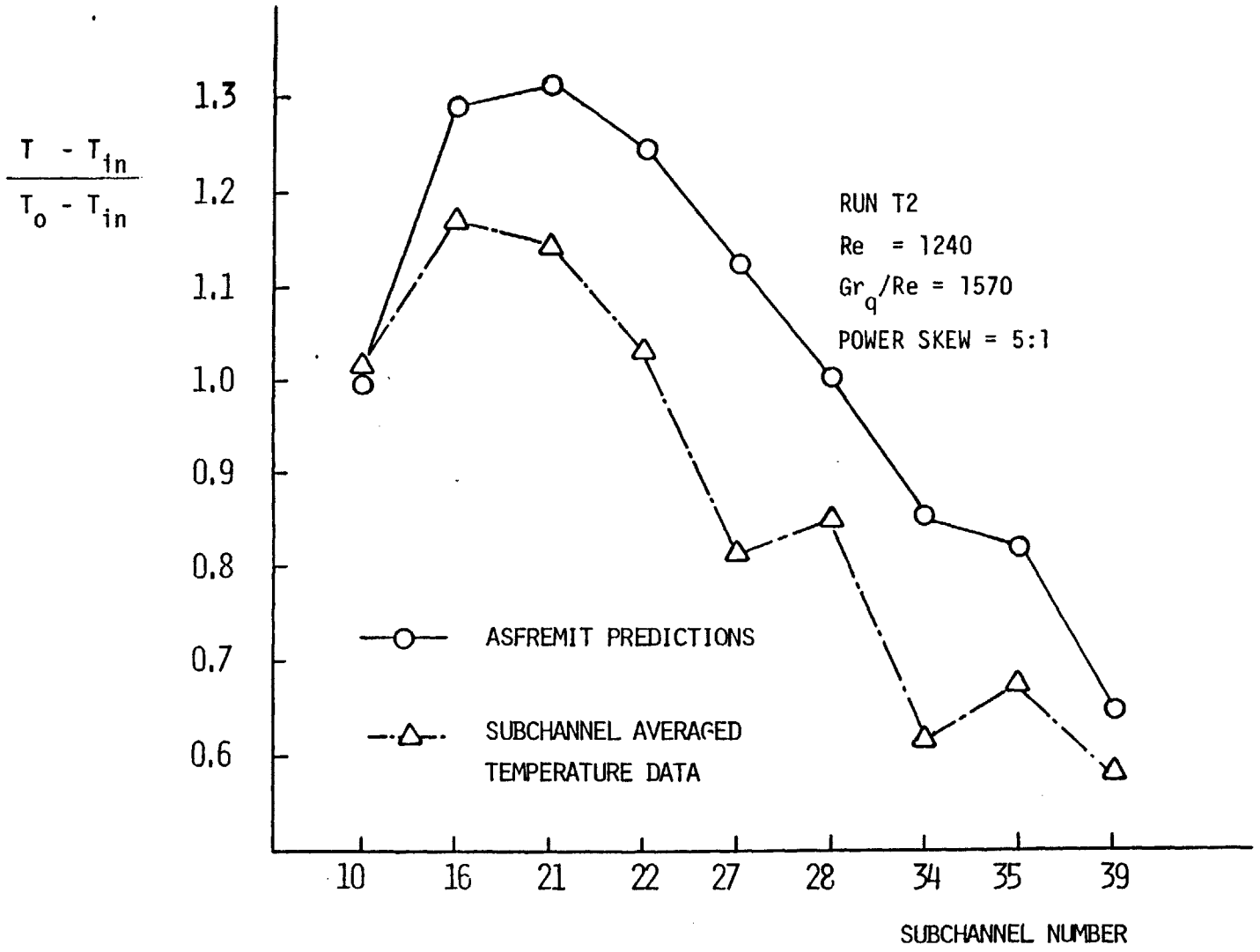

FIGURE 8.20. ASFREMIT COMPARISONS WITH MIXED CONVECTION SUBCHANNEL TEMPERATURE DATA. ASFREMIT SOLUTION IS NOT FULLY CONVERGED.

CHAPTER 9

CONCLUSIONS AND RECOMMENDATIONS FOR FUTURE WORK

9.1 Introduction

In this work the following general Tasks have been completed

Task I. Fundamentals of Low Reynolds Mixed Convection in Rod Bundles

Mixed Convection phenomena for vertical low Reynold's number flows have been investigated both experimentally and analytically. Data were obtained in both bare and wire-wrapped rod bundles. Empirical correlations for heat transfer coefficients under the above conditions were derived.

Task II. Subchannel Analysis for Wire-Wrapped Rod Bundles

The advantages and limitations of the subchannel analysis approach for thermo-hydraulic analysis of wire-wrapped rod bundles have been studied. Flow resistance models were developed to account for the specific geometry of the wire-wrapped bundle. Attribute functions were developed to incorporate these models as the ASFREMIT subchannel analysis code.

Task III. Data Base for Code Validation

Subchannel velocity and temperature data were obtained at the exit region of a 19-pin wire-wrapped rod bundle under low Reynold's number Flow Mixed Convection conditions. These data may directly be used for validation/verification studies of subchannel analysis or porous body numerical programs.

Task IV. Preliminary Model Validation Studies

Model validation studies were performed using the data of Task III

plus other data available in the literature.

In what follows the most important accomplishments and conclusions are outlined. Recommendations for future experimental, analytical and numerical work are suggested based on the limitations of our current data and our predictive capabilities for low Reynold's number mixed convection flows.

9.2 Conclusions

9.2.1 Mathematical Formulation of the Mixed Convection Problem

The non-dimensional differential equations and the corresponding boundary conditions for fully developed laminar mixed convection flows in vertical ducts were formulated. It was shown that under these conditions, the mixed-to-forced friction factor coefficient ratio and the Nusselt number depend on the Gr_q/Re ratio, the duct geometry and the shape function of the boundary conditions for heat flux or temperature distribution.

9.2.2 Experimental and Measurement Techniques

(a) Bundle Design and Construction

A 19-pin wire-wrapped rod bundle was designed and constructed. All rods could be individually heated to 2 KW using 19 variac autotransformers. For low Reynold's flow rates ($Re < 800$) mixed convection flows could be established with Gr_q/Re values as high as 2.4×10^4. The major design innovation in this work was the fact that the upper plenum was made free from any piercing rods, so that instrumentation could be easily placed there to perform detailed local subchannel measurements at the exit region of the rod bundle. A second design innovation consisted of designing a leak proof lower plenum to allow penetration of the heated

rods from the bottom of the test section.

(b) Pressure Drop Measurements

A method was established to measure low flow pressure drop under mixed convection conditions. It was found that thermal transients in the manometer tubes as well as in the manometer itself may significantly deteriorate the accuracy of the measurement. Special insulation and procedural techniques were employed to minimize this error. The accuracy achieved in this work for pressure ΔP measurements in mixed convection was ± 30%. The accuracy of subsequent data based on experience from this work has been improved to ± 12%.

(c) Instrumented Rod Measurements

In order to perform heated rod wall temperature measurements an Instrumented Rod (IR) was designed and constructed. The IR allowed temperature measurements along the interior side of its heated wall (wall thickness 0.53 mm) at any axial or azimuthal location. Standard copper-constantine thermocouples were used with accuracy of ± 0.5°F.

(d) Hot-Film Anemometry (HFA) Measurements

A HFA technique was established to measure local subchannel axial velocities. To calibrate the HFA probe, a transversing cylindrical tank mechanism was designed and constructed. In order to achieve higher accuracy and minimize calibration time, an "in-situ" HFA calibration method was developed. The resulting velocity measurement random error was less that ± 8.0 % for isothermal flows.

9.2.3 Experimental Results and Semi-empirical Correlations

(a) Low Reynold's Number Isothermal Pressure Drop

The low Reynold's number isothermal pressure drop and friction factor coefficient data obtained here closely parallel other data available in the literature. The friction factor data obtained in the MIT 4 x 4 pin square array bare rod bundle (with P/D equal 1.25) were well predicted by Rehme's correlation:

$$f_o = 82.4/Re_{De} \quad ; \qquad Re_{De} < 1000$$

where the constant 82.4 corresponds to the particular value of P/D = 1.25.

The friction factor data in our 19-pin wire-wrapped bundle were correlated by the following empirical formula:

$$f_o = 28.8/Re_{De}^{0.83} \qquad Re_{De} < 1000$$

(b) Buoyancy-Induced Instability Phenomena

Despite the fact that the Reynold's number was kept below 1,000, extensive instability phenomena were observed in both the bare and wire-wrapped bundles. Thermal plumes (buoyancy-induced instabilities) were more pronounced at higher values of Re and Gr_q/Re parameters. For Re ~ 200 and $Gr_q/Re \sim 10^4$, subchannel temperature fluctuations were recorded of the order of ± 8.0%. The intensity of these fluctuations depended on both Re and Gr_q/Re parameters.

(c) Mixed Convection Friction Factors

The mixed-to-forced convection friction factor coefficient ratio f/f_o under the same Reynold's number conditions was an increasing function of Gr_q/Re. It was also found that for higher Re values (around 1000) the

f/f_o ratio was slightly lower although the more recent data reported in Figure 3.8 taken with improved accuracy did not show a Re affect. All of our f/f_o versus Gr_q/Re data were significantly lower than the corresponding circular tube data as well as the 91-pin wire-wrapped bundle data reported in M-1. We are currently examining the unheated wall effect in order to explain these differences.

(d) Mixed Convection Heat Transfer Coefficients

The ratio Nu/Nu_o (mixed-to-forced convection Nusselt number ratio under the same Reynold's number) exhibited a similar behavior to f/fo. The following empirical formula was derived, based on our experimental results:

$$Nu/Nu_o = 0.39\ (Gr_q/Re)^{0.178}$$

when $Re < 400$ and $Gr_q/Re < 10^4$

For higher values of Re and Gr_q/Re the Nu/Nu_o ratio exhibited a slight decrease with increasing Gr_q/Re. This can be attributed on relaminarization effects of turbulence, already present for Reynold's number larger than 200 to 300.

(e) Temperature Profile in Mixed Convection

Buoyancy effects tended to smooth out radial temperature gradients in both the fluid (subchannel) region and solids (heated rod walls). The subchannel temperatures were measured at the exit region of the wire-wrapped bundle. Various Gr_q/Re values and power skew conditions were examined. In all cases, for higher Gr_q/Re values, flatter intersubchannel temperature profiles were obtained under the same power skew conditions. These data can be directly used to validate/calibrate lumped

parameter analysis numerical programs under mixed convection and power skew conditions.

Similar buoyancy induced phenomena were observed for the heated rod wall temperature measurements using the Instrumented Rod (IR) in a 19-pin array. A parameter c was defined as follows:

$$c = (T_w(z)^{max} - T_w(z)^{min}) \; / \; (\dot{q}" \; k_w/R)$$

where $T_w(z)$ is the IR wall temperature at a given axial location z, min and max refer to the minimum and maximum azimuthal temperatures respectively, $\dot{q}"$ is the IR surface heat flux and k_w is the IR wall thermal conductivity. The parameter c was always decreased with increasing Gr_q/Re. This behavior should be attributed to the increasing flattening of the subchannel temperature profiles when buoyancy effects become more pronounced. For the range of experimental conditions examined in this work, the parameter c was always less than 0.1 for uniform rod power distribution.

(f) Subchannel Axial Velocity Profiles in Isothermal Flows

Subchannel axial velocity data in isothermal flows were obtaind at the exit region of the wire-wrapped bundle using the Hot-Film Anemomety (HFA) technique. Each subchannel area was scanned with the HFA probe so that 10 to 13 velocity readings per subchannel at different points were taken. The subchannel velocity then was estimated as the average of these readings. All 48 subchannels were scanned and average subchannel velocities were estimated for three different Reynold's numbers; 320, 160, and

78. Velocites in the edge subchannels were always higher than the velocities in the interior ones and they were increased with increasing Reynold's number. For Re ~ 160 the edge flow split was around 1.14. Our velocity data can be used to validate hydraulic resistance models in lumped parameter numerical programs.

9.2.4 Physical Modeling and Numerical Simulation

(a) Distributed Resistance Models for Wire-Wrapped Bundles

Hydraulic resistance models were developed to account the presence of the wire-wrap spacer in the rod bundle. These models are of "Distributed Resistance" type and give the axial and transverse momentum equation flow resistances as a function of subchannel geometry and flow direction. The models are general enough to cover a wide range of geometrical parameters (P/D, H/D), flow regime (laminar, turbulent) and mixed convection effects. These models are applicable to both subchannel analysis and porous body approaches.

(b) The Computer Code ASFREMIT

The above hydraulic resistance models were incorporated into an existing subchannel analysis numerical program (ASFRE) for the particular case of axial mesh size Δz equal to H/12, where H is the wire-wrap lead length. Atribute functions were developed to establish correspondence between each individual computational cell (of both axial and momentum equations) and the set of hydraulic resistance models pertaining to a specific set of geometrical patterns.

(c) Preliminary Results of ASFREMIT

The new models, as implemented in conclusion (b) above, were tested against turbulent flow data available in the literature as well as against

our own isothermal and mixed convection low Reynold's number data. An initial calibration of the model constants has been completed. The models satisfactorily predicted the swirl flow under turbulent flow conditions. Comparisons with the Westinghouse data for gap crossflows indicated that pressure terms in the axial and transverse momentum equations need to be reformulated to account for the presence of the wire-spacer. Comparisons with our low Reynold's number isothermal or mixed convection flow data gave satisfactory results. However numerical convergence problems prevented completion this task.

9.3 Recommendations for Future Work

9.3.1 Introduction

In this section we discuss all questions that still remain open and formulate proposals for accomplishing future work to resolve these questions. In additions we propose work on new problems which emerged during the course of this work. In what follows, the proposals are grouped into three different areas namely, experimental, analytical and computational.

9.3.2 Experimental work

(a) Heat Transfer Analysis in Laminar/Transistion Mixed Convection

The scope of this work is to extend our initial wall temperature distribution data by placing the Instrumental Rod (IR) in edge and corner subchannels. Experiments should be run under various power skew conditions and empirical correlations formulated for the average heat transfer coefficients and the parameter

$$c = (T_w^{max} - T_w^{min}) / (\dot{q}'' \, k_w/R)$$

In particular for the parameter c, work should be performed under forced-to-mixed convection experimental conditions where c is expected to attain its maximum value.

(b) Pressure Drop in Laminar/Transition Mixed Convection

The effect of Reynold's number on friction factor coefficients in mixed convection has to be further examined for both bare and wire-wrapped rod bundles. The power skew effect on pressure drop should also be considered.

(c) Subchannel Axial Velocity Profiles in Mixed Convection

The applicability of our Hot Film Anemometry calibration technique for isothermal flows should be extended to mixed convection flows. For this purpose, an on-line calibration technique for the HFA bridge output versus temperature needs to be developed. Subchannel axial velocity data should be obtained at the exit region of the wire-wrapped bundle under mixed convection conditions. These data may be used for code validation/calibration under such conditions.

(d) The Effects of Inter-Assembly Heat Transfer

The effect of inter-assembly heat transfer on pressure drop and temperature gradients in both fluid and solids (see (a) and (b) above) should be examined. To simulate inter-assembly heat transfer phenomena, an external cooling channel should be constructed to cool an arbitrary side of the hexagonal wrapper tube. Using this external cooling channel, inter-assembly heat transfer coefficients can be obtained under both forced and mixed convection conditions.

(e) Turbulence Mixing in Low Reynold's Mixed Convection

Our experimental work indicated that temperature fluctuations under

mixed convection/recirculation conditions may be as high as ± 8.0% for Reynold's number less than 600. Since current turbulence mixing models for rod bundles do not apply in such conditions future work should be done in this field. From an experimental point of view flow instability maps should be constructed as a function of Gr_q and Re numbers. In addition Fast Fourier transform analysis of termperature signals will determine the appropriate time and length scale of the turbulence fluctuations caused by the buoyancy induced thermal plumes.

9.3.3 Analytical Work

(a) Pitch-to-diameter Ratio Effects on f/fo and Nu/Nu_o

Analytical studies for fully developed mixed convection flows in bare rod bundles show that there is a strong P/D effect on f/f_o or Nu/Nu_o functional relationship with Gr_q/Re. Since this effect is implicity hidden in the boundary conditions of the conservation differential equation, it is proposed to develop a simple explicit P/D factor to modify the equivalent annulus f/fo correlation with Gr_q/Re based on the concept of the hydraulic diameter.

(b) Turbulence Mixing Models in Low Reynold's Mixed Convection

Based on the experimental data of 9.3.2 (e) turbulence mixing models should be developed. These models can be directly used in porous body or subchannel analysis codes. Work should be conducted in both bare and wire-wrapped bundles.

9.3.4 Numerical Work

(a) Formulation of Subchannel Analysis Equations

As discussed earlier the subchannel momentum equations in ASFRE should be reformulated in order to account for the correct surface and

volume porosities, in particular for the lateral momentum equation. An S/l parameter, similar to that used in COBRA code should be introduced to supplement the step already accomplished of incorporating wire-wrap geometry into the convective and pressure terms of the momentum equations.

(b) The Solution Algorithm

The main numerical problem arising during the implementation of the new distributed hydraulic resistance models is that the solution algorithm diverges when large values are assigned to the multiplying constants of the models. Work has to be pursued in this area in order to develop a more stable solution algorithm than that currently employed in ASFRE. Several options should be considered.

1. Eliminate the second half time step of the ADI method keeping only the first half-time step.
   (SIMPLE algorithm)
2. Use under relaxation techniques in the first half time step in order to estimate in more realistic way the pressure correlation terms.
3. Introduce the SIMPLER solution algorithm (Patankar, 1979).

REFERENCES

B-1 Bartholet, R.G., et al., "Clinch River Breeder Reactor Plant. 11:1 Scale Wire Wrapped Rod Bundle Air Flow Tests, Interior Subchannels," WARD-D-108, Westinghouse, November 1975.

B-2 Bartholet, R.G., et al., "CRBRP. 11:1 Scale Wire Wrapped Rod Bundle Air Flow Test, Hot Film Anemometer Experiments," WARD-D-0161, Westinghouse, October 1976.

B-3 Bartholet, R.G., et al., "CRBRP. 11:1 Scale, Wire Wrapped Rod Bundle Air Flow Test, Side Subchannels," WARD-D-0129, Westinghouse, January 1976.

B-4 Burns, K.J., Rohsenow, and Todreas, N.E., "Laminar/Transition Sweeping Flow Mixing Model for Wire Wrapped LMFBR Assemblies," DOE/ET/37240-81TR, Nuclear Engineering Department, M.I.T., July 1980.

B-5 Bishop, A.A. and Todreas, N.E., "Hydraulic Characteristics of the Wire Wrapped Rod Bundles," Nucl. Eng. Des., 62 (1980), pp. 271-293.

B-6 Bartzis, J.G., and Todreas, N.E., "Hydrodynamic Behavior of a Rod Bundle," COO-2245-48TR, M.I.T. January 1977.

B-7 Bosy, B.J. and Khan, H., "Fabrication Details for Wire Wrapped Fuel Assembly Components," M.I.T., Report, COO-2245-27TR, Revision 1, September 1978.

B-8 Basehore, K.L. and George, T.L. "COBRA-IV Comparison with the WARD 11:1 Scale LMFBR Air Flow Tests," PNL-2923, UC-79e, Battelle, March 1979.

B-9 Bishop, A. A., Willis, J.M. and Markley, R.A., "Effects of Buoyancy on Laminar Vertical Upward Flow Friction Factors in Cylindrical Tubes," Nucl. Eng. & Design, 62, pp. 365-369, 1980.

C-1 Chiu, C., Rohsenow, W.M., and Todreas, N.E., "Turbulent Sweeping Flow Mixing Model for Wire Wrapped LMFBR Assemblies," COO-2245-55TR, Nuclear Engineering Department, M.I.T., April. 1978.

C-2 Chuang, M.C., Carelli, M.D., Bach, C.W., and Killimayer, J.S., "Three-Dimensional Thermal-Hydraulic Analysis of Wire-Wrapped Rods in Liquid-Metal Fast Breeder Reactor Core Assemblies," Nucl. Sci. Eng., 64, 1977, pp. 244-257.

C-3 Chen, G. C-J., Sha, W.T., Doria, M.L. Schmitt, R.C., and Thompson, J.F., "BODYFIT-IFE: A Computer Code for Three-Dimensional Steady-State/Transient Single-Phase Rod Bundle, Thermal-Hydraulic Analysis," ANL Report, NUREG/CR-1874, November 1980.

C-4 Chen, Y.B., Ip, K., and Todreas, N.E., "Velocity Measurements in Edge Subchannels of Wire Wrapped LMFBR Fuel Assemblies," COO-2245-11TR, Nuclear Engineering Department, MIT, September 1974.

C-5 Coeffe, Y. and Todreas, N., "Formulation of the Fluid-Solid Interaction Force for Multi-Dimensional Two-Phase Flow within Tube Arrays," Nuclear Eng. and Des., 58, pp. 383-391, 1980.

C-6 Cheng, S.K., "Bare Rod Subchannel Friction Factors," in Report No. DOE/ET/37240-100, Progress Report 9/82-11/82, Nuclear Engineering Department, M.I.T., December 1982.

C-7 Carajilescov, P., and Todreas, N.E., "Experimental and Analytical Study of Axial Turbulent Flows in an Interior Subchannel of a Bare Rod Bundle," Trans. ASME. Ser. C 98-2, May 1976.

C-8 Cheng, S.K., and Todreas, N.E., "Fluid Mixing Studies in a Hexagonal 37 Pin Wire-Wrapped Bundle," Report No. DOE/ET/37240-96TR, February 1982.

D-1 Davies, A.L., "Personal Communication," 1981.

D-2 Domanus, H.M., Shah V.L., Sha W.T.," Applications of the COMMIX Code Using the Porous Medium Formulation", Nuclear Engineering and Design 62, 81-100, 1980.

D-3 Dring, R.P. and Gebhart B., "Hot-Wire Anemometer Calibration for Measurements at Very Low Velocity," Journal of Heat Transfer, ASMF, May 1969.

E-1 Efthimiadis, A., Rohsenow, W.M., Todreas, N.E., and Wang, S.F., "Investigation of Developing Vertical Mixed Convection Flow in a Square Array of Cylindrical Rods," International Conference of Heat and Mass Transfer at Munich, Federal Republic of Germany, September 1982.

E-2 Ebeling-Koning, D.B., Robinson, J.T. and Todreas, N.E., "Hydrodynamic Prediction of Multi-Dimensional Single- and Two-Phase Flow in Rod Arrays," Progress Report, 5/82-12/82, DOE/ER/12075-IPR, Nuclear Engineering Department, MIT, January 1983.

E-3 Ebeling-Koning, D.B., "Hydrodynamics of Single and Two-Phase Flow in inclined Rod Arrays", PhD Thesis, Department of Nuclear Engineering, Massachusetts Institute of Technology, February 1984"

E-4 Efthimiadis, A., "A porous body approach to hydrodynamic modeling of wire-wrapped rod bundles," unpublished work, MIT 1981.

E-5 Engel, F.C., Markley, R.A., Bishop, A.A., "The Effects of Radial Heat Flux Gradients and Flow Regimes on the Peak Sodium Temperature Rise in Wire-Wrapped Rod Bundles," ANS Topical Meeting, Kiamesha Lake, September 1982.

F-1 Fontana, M.H., et al., "Temperature Distribution in the Duct Wall and at the Exit of a 19 Rod Simulated LMFBR Fuel Assemble (FFM Bundle 24)," Nuclear Technology, Volume 24, November 1974.

G-1 Greene, T.E. and Todreas, N.E., "Development and Evaluation of Techniques for Thermal-Hydraulic Analysis of LMFBR Fuel Assemblies," M.S. Thesis, Department of Nuclear Engineering, M.I.T., September 1980.

G-2 Greene, H.L. and Scheele, G.F., "Effect of Fluid Viscosity on combined Free Forced Convection Phenomena in Vertical Pipes," AICHE Journal 16, No. G, November 1970.

G-3 Gruszczynski, M.J. and Viskanta, R., "Heat Transfer from a Vertical Tube Bndle under Natural Circulation Conditions," Proceedings of the 1983 ASME-JSME Thermal Engn. Confr., Vol. III, New York, 1983.

G-4 Gunter, A. Y. and Shaw, W.A., "A General Correlation of Friction Factors of Various Types of Surfaces in Crossflow," ASME Trans., Vol 67, 1945.

H-1 Hallman, T.M., "Experimental Study of Combined Forced and Free Laminar Convection in a Vertical Tube," Technical Note, NASA TN, D-1104, December 1961.

H-2 Handbook of Heat Exchangers, Hemisphere Publishing Corporation, 1983.

H-3 Hollasch, K. and Gebhart, B., "Calibration of Constant-Temperature Hot-Wire Anemometers at Low Velocities in Water with Variable Fluid Temperature," Journal of Heat Transfer, ASME, February 1972.

J-1 Japikse, D., "Advances in Thermosyphon Technology," Advances in Heat Transfer, Academic Press, Vol. 9, 1973.

K-1 Kakac, S., Bergles, A-E. and Mayinger, F., Heat Exchangers, Hemisphere Publishing Corporation, 1981.

K-2 Kelly J.E. and Kazimi, M.S., "Development and Testing of the Three-Dimensional Two-Fluid Computer Code THERMIT for LWR Transient Analysis." MIT-EL-79-096, 1979.

K-3 Kune, S., Efthimiadis, A., Ro, T.S., Todreas, N.E., "An experimental correlation for crossflow pressure drop in rod bundles with displacers", to be published as an MIT Topical Report.

K-4 Khan, E.V., Rohsenow, W.M., Sonin, A.A., and Todreas, N.E., "A Porous Body Model for Predicting Temperature Distribution in Wire Wrapped Fuel Rod Assemblies," Nucl. Sci. Eng. and Des. 35, 1975.

K-5 Kemeny, G.A. and Somers, E.V., "Combined Free and Forced-Convective Flow in Vertical circular Tubes-Experiments with Water and Oil," ASME Journal of Heat Transfer, November 1962.

L-1 Lafay, J., Menant, B., and Barroil, J., "Local Pressure Measurements and peripheral Flow Visualization in a Water 19-Rod Bundle Compared with FLICA IIB Calculations: Influence of Helical Wire-Wrap Spacer System," AIChE-ASME Heat Transfer Conference, San Francisco, ASME paper 75-HT-22, August 1975.

L-2 Le-Guez J.M., "Development Work on SABRE Code," 10th Meeting of the LMBWG, Karlsruhe, October 1982.

M-1 Mawatari, K., Namekawa, F., Handa, N., Kasahara, F. and Ishida, Y., "Natural Circulation Decay Heat Removal Experiments and Analysis in an LMFBR Fuel Assembly," Int'l. Topical Meeting on LMFBR Safety, Lyons, France, July 1B-21, 1982.

M-2 Morris, R.H. et al., "Single-Phase Sodium Tests in a 61-Pin Full-Length Simulated LMFBR Fuel Assembly-Record of Phase 1 Experimental Data for THORS Bundle 9, ORNL/TM-7381, August 1980.

N-1 Ninokata, H., Personal communication to A. Efthimiadis, 1983.

O-1 Ohtake, T., Urawashi, S., and Takahashi, K., "Velocity Measurements in the Subchannel of the Wire-Spaced Subassebly," Nuclear Technology, Volume 30, September 1976.

P-1 Patch, L., Roidt, R.M., Carelli, M.D., and Markley, R.A., "Experimental Studies of Flow Distribution in a Wire-Wrapped LMFBR Blanket Assembley," paper included at "Fluid Flow and Heat Transfer Over Rod Bundles," Winter Annual Meeting of ASME, New York, December 1979.

P-2 Patankar, S.V., "Numerical Heat Transfer and Fluid Flow," Hemisphere Publishing Corporation, 1980.

R-1 Roidt, R., Carelli, M.D., and Markley, R.A., "Experimental Investigation Of the Hydraulic Field in Wire-Wrapped LMFBR Core Assemblies," Nucl. Eng. Des., 62, 1980.

R-2 Rowe, D.S., "COBRA-IIIC: A Digital Computer Program for Steady-State and Transient Thermal-yydraulic Analysis of Nuclear Fuel Elements," BNWL-1695, Battelle Pacific Northwest Laboratories, Richlan, WA, March 1973.

R-3 Rehme, K., "Simple Method of Predicting Friction Factors of Turbulent Flow in Non-Circular Channels," Int. J. of Heat and Mass Transfer, 16, pp. 933-950 (1973).

R-4 Rowe, D.S., "A Review of Porous Media Modeling for Rod-Bundle Hydraulic Analysis", Appendix C in" Khan, E.U.," LMFBR In-Core Thermal-Hydraulics: The State of the Art and U.S. Research and Development Needs", PNL Laboratory, PNL-3337, UC-32, Battelle, April 1980.

R-5 Ramn, H., Johannsen, K., "Combined Forced and Free Laminar Convection in Vertical Rod Bundles with Longitudinal Flow," ASME paper, 77-HT-44, August 1977.

R-6 Rehme, K., "Experimental Techniques for Low-Reynolds Forced Convection in Tube Bundles with Longitudinal Flow," Kernforschunggszentrum Karlsruhe, Institut für Neutronephysik und Reaktortechnik, D 7500 Karlsruhe, Federal Republic of Germany.

R-7 Rohsenow, W.M., and Choi, H.Y., "Heat, Mass and Momentum Transfer," Prentice-Hall Inc., 1961.

S-1 Sarno, A., Gori, P., and Andalo, G., "Local Pressure and Velocity Measurements in a Water 19-Rod Bundle Using a Wire Wrap Spacer System," Specialists' Meeting on "Thermodynamics of FBR Fuel Subassemblies Under Nominal and Non-nominal Operating Conditions," Karlsruhe, February 1979.

S-2 Steward, C.S., Wheeler, C.L., Cena, R.J. McMonagle, C.L. Cuta, J.M., and Trent, D.S., "COBRA-IV: The Model and the Method," BNWL-2214, Battelle, PNL, July 1977.

S-3 Stephens, M.J. et al., "the Design, Development and Calibration of a Thermocouple Probe for the Measurement of Surface Temperature Distribution in Rod Clusters," Berkeley Nuclear laboratories, RD/B/N2514, October 1973.

S-4 Symolon, P.D., "Mixed Convection in Rod Bundles," Ph.D. Thesis, MIT, August 1982.

S-5 Spencer, D.R. and Markley, R.A., "Friction Factor Correlation for 217 Pin Wire Wrap Spaced LMFBR Fuel Assemblies," Trans. Amer. Nucl. Soc., 39, 1014, 1980.

S-6 Sparrow, E.M. and Loeffler, Jr., A.L., "Longitudinal Laminar Flow Between Cylinders," J. Heat Transfer, 83, pp. 415-422, (1961).

S-7 Shah, R.K. and London, A.L., Laminar Flow Forced Convection in Ducts, Academic Press, 1978.

S-8 Sha, W.T., "An Overview of Rod-Bundle Thermal-Hydraulic Analysis", Nuclear Design and Engineering, Vol. 62, Nos. 1-3, December 1980.

S-9 Stephen, M.J. et al., "The Design, Development and Calibration of a Thermocouple Probe for the Measurement of Surface Temperature Distributions in Rod Clusters,"RD/B/N2514, RPC/HT/N(73)19, Berkeley Nuclear Laboratories, October 1973.

T-1 Todreas, N.E., 22.313 Class Notes, Nuclear Engineering Department, M.I.T., January 1982.

T-2 Todreas, N.E. and Efthimiadis, A., "Mixed Convection Testing and Analysis of Wire-Wrapped Bundles," Department of Nuclear Engineering, MIT Report No. PNC/MIT-1, February 1982.

T-3 Todreas, N.E. and Efthimiadis, A., "Mixed Convection Testing and Analysis of Wire-Wrapped Bundles," Department of Nuclear Engineering, MIT Report No. PNC/MIT-2, May 1982.

T-4 Todreas, N.E. and Efthimiadis, A., "Mixed Convection Testing and Analysis of Wire-Wrapped Bundles," Department of Nuclear Engineering, MIT Report No. PNC/MIT-3, August 1983.

T-5 Todreas, N.E. and Efthimiadis, A., "Mixed Convection Testing and Analysis of Wire-Wrapped Bundles," Report No. PNC/MIT-4, Department of Nuclear Engineering, MIT, November 1982.

T-6 Todreas, N.E. and Efthimiadis, A. "Mixed Convection Testing and Analysis of Wire-Wrapped Bundles., Report No. PNC/MIT-5, Nuclear Engineering, M.I.T., March 1983.

T-7 Todreas, N.E., and Efthimiadis, A., "Mixed Convection Testing and Analysis of Wire-Wrapped Bundles," Progress Report No. PNC/MIT-6, June 1983.

T-8 Todreas, N.E., and Efthimiadis, A., "Mixed Convection Testing and Analysis of Wire-Wrapped Bundles", Progress Report No. PNC/MIT-7 August 1983.

T-9 Todreas, N.E., Efthimiadis, A., Okada, T. and Ro, T-S., "Mixed Testing and Analysis in Wire-Wrapped Bundles," Progress Report No. PNC/MIT-9, Nuclear Engineering, MIT, February 1984.

W-1 Wantland, J.L. "ORRIBLE - A Computer Program for Flow and Temperature Distribution in 19-Rod LMFBR Fuel Subassemblies," Nuclear Technology, Volume 24, November 1974.

W-2 Wang, S-F and Todreas, N.E., "Experimental Investigation of Laminar, Mixed Convection in a Square Array of Bare Rods," M.I.T. Report, DOE/ET/37240-88TR, February 1981.

W-3 Wong, C-N, "Wire Wrapped Rod Bundle Heat Transfer Analysis for LMFBR: Distribution Parameter Approach," Ph.D. Thesis, Department of Nuclear Engineering, M.I.T., October 1981.

W-4 Wei, J.P., "Thermal-Hydraulic Evaluation of Advanced Wire-Wrap Assemblies," AIChE Symp., Series No. 164, 73, 1977.

W-5 Wantland, J.L., "ORRIBLE - A Computer Program for Flow and Temperature Distribution in 19-Rod LMFBR Fuel Subassemblies," Nuclear Technology, Vol. 24, November 1974.

W-6 White, F.M., Viscous Fluid Flow, McGraw-Hill, 1974.

W-7 Wang, S.-F., "Natural Convection Effects in Isolated and Interconnecting Subchannels of a Reactor Fuel Assembly," Ph.D. Thesis, Department of Nuclear Engineering, MIT, January 1981.

W-8 Wang, Song-Feng, Rosenow, W.M., Todreas, N.E., "Steady Laminar Fully-Developed Mixed Convection in Finite Rod Arrays", COO-2245-74TR, MIT, February 1980.

W-9 Wendling, M. Ricque, R. and Martin, R., "Mixed Convection with Sodium", in "Progress in Heat and Mass Transfer," Vol. 7, Pergamon Press, 1973.

Y-1 Yoshikawa, N., Ishimaru, J., Tamura, S., Ninokata, H., and Hirata, N., "ASFRE: A Computer Code for Single-Phase Subchannel Thermal Hydraulic Analysis of LMFBR Single Subassembly," PNC Report, PNC N941 81-74, April 1981.

Y-2 Yang, J.W., "Heat Transfer and Fluid Flow in Regular Rod Arrays with Opposing Flow", ASME, December 1979.

Y-3 Yang, J.W., "Analysis of Combined Convection Heat Transfer in Infinite Rod Arrays," Heat Transfer, 1978, National Research Council of Canada, Ottawa (1978), Volume 1, pp. 49-54.

APPENDIX A.3.1

Correlation of Gr_q/Re with Gr (M-1)

In M-1, the folowing Gr number is used:

$$Gr = \frac{g \beta (T_e - T_{in}) De^3}{\nu^2} \tag{1}$$

where T_e is the exit temperature of the fluid at the exit of the heated zone. Then:

$$T_e - T_{in} \simeq \frac{\dot{q}''_w P_w L}{\dot{m} C_p} \tag{2}$$

where L is the heated length. Substituting (2) in (1):

$$Gr = \frac{g \beta \dot{q}''_w D_c^4}{k\nu^2} \cdot \frac{L}{De} \cdot \frac{P_w \mu}{4 \dot{m}} \cdot 4 \frac{k}{\mu C_p}$$

or
$$Gr = 4 \frac{Gr_q}{R_e} \frac{1}{Pr} \frac{L}{De} \tag{3}$$

Since L = 93.0 cm, De = 0.326 cm, and Pr ~ 3.0 (for $\bar{T} \simeq 60°C$) then:

$$Gr \simeq 380 \frac{Gr_q}{Re} \tag{4}$$

APPENDIX A.3.2

Pressure Drop Estimation Under Mixed Convection

Figure 3.4 shows a schematic of our test section and the differential pressure measuring device (electronic manometer). The objective is to measure the pressure drop due to friction between axial levels (1) and (2) in Figure 3.4. Assume that the temperature of the water in the tubes that connect the manometer with the test section is equal to the inlet temperatures T_o. The static pressure balance equation for the manometer gives

$$\Delta p_M = p_1 - p_2 - \rho_o g H \tag{1}$$

where p_1, p_2 are the static pressures at points (1) and (2) and Δp_M is the reading (in Torrs) at the electric manometer. In isothermal flows, the Bernoulli equation for the test section gives:

$$p_1 = p_2 + \rho_o g H + (\Delta p)_f^{iso} \tag{2}$$

where $(\Delta p)_f^{iso}$ is the frictional pressure drop in isothermal flows. Substituting (2) into (1) take:

$$\Delta p_M = (\Delta p)_f^{iso} \tag{3}$$

Eq. (3) says that in isothermal (or forced convection) flows, the reading of the manometer corresponds directly to the frictional presure drop. However, if the fluid in the manometer tubes has a density of ρ_M (different than ρ_o), then:

$$\Delta p_M = (\Delta p\ )_f^{iso} + (\rho_0 - \rho_M) g H \tag{4}$$

In mixed convection cases (MC), the Bernoulli equation has the following form:

$$p_1 + \rho_1 u_1^2 = p_2 + \rho_2 u_2^2 + \int_{z_1}^{z_2} \rho(z) g \, dz + (\Delta P_f)^{MC} \tag{5}$$

or

$$p_1 - p_2 = \rho_1 u_1^2 \left(\frac{\rho_1}{\rho_2} - 1\right) + \int_{z_1}^{z_2} \rho(z) g \, dz + (\Delta P_f)^{MC} \tag{6}$$

Here we have made use of the continuity equation:

$$\rho_1 u_1 = \rho_2 u_2$$

Substituting (6) into (1) take:

$$(\Delta p_f)^{MC} = (\Delta p_M)^{MC} - \rho_1 u_1^2 \left(\frac{\rho_1}{\rho_2} - 1\right) + \int_{z_1}^{z_2} [\rho_0 - \rho(z)] g \, dz \tag{7}$$

In laminar forced convection and mixed convection flows in our bundle, the velocity ranges from 2 to 10 cm/sec. Therefore the inertia term in equation (7) can be neglected. Using the following definitions:

$$\overline{\rho}_M = \frac{1}{V_M} \int_{V_M} \rho \, dV \tag{8}$$

where V_M is the volume of the manometer tubes

and

$$\overline{\rho}_{1,2} = \frac{1}{H} \int_{z_1}^{z_2} \rho(z) \, dz \tag{9}$$

equation 7 is written as follows:

$$\Delta p_f^{MC} = \Delta p_M^{MC} + H\, g(\bar{\rho}_M - \bar{\rho}_{1,2}) \qquad (10)$$

This is the requred form.

Up to now it was assumed that the temperature of the water within the vertical part of the manometer tubes (see Figure 3.4) remains constant. Therefore, we should make sure that the increasing temperatures within the test section (during the heat-up transient) do not affect this vertical part of the tubes. In order to achieve that, the horizontal part of the manometer tubes should be long enough so that the time that it takes for the heat to diffuse all along the horizontal part is longer than the total transient time (~10 min). Rough calculations using the formula

$$L \sim \sqrt{\alpha t}$$

where α is the water thermal diffusivity ($\alpha \sim 10^{-6}$ to 10^{-7} m^2 /sec) and for t = 20 minutes, indicate that the horizontal length L should be of the order of 4 cm. Therefore for L ~ 10 to 20 cm the above assumption should be readily satisfied.

APPENDIX A.4.1

Gruszczynski and Viskanta Heat Transfer Correlation

In this appendix the heat transfer correlation of Gruszczynski and Viskanta is recasted in terms of the Gr_q/Re parameter. The above authors used the following Grashof number in correlating their data:

$$\overline{Gr} = g\,\beta(\overline{T}_w - \overline{T}_f)\,D_e^3/\,\nu^2 \tag{1}$$

where $\overline{T}_w$ and $\overline{T}_f$ are the wall and fluid temperatures respectively, averaged over the total bundle length including the entrance length. They proposed the following correlation:

$$\overline{N}_u = 0.0667\ \overline{Re}^{0.80}\ Pr^{0.43} \qquad 80 < Re < 300 \tag{2}$$

Since the flow in the bundle was driven through natural circulation, $\overline{Re}$ was a function of $\overline{Gr}$. It was experimentally found that:

$$\overline{Gr}\ \overline{Pr} = 575\ \overline{Re}^{1.12} \qquad 80 < Re < 650 \tag{3}$$

Defining $\dfrac{\overline{Gr}_q}{\overline{Re}} = \dfrac{\overline{Gr}\ \overline{Nu}}{\overline{Re}}$ and using (3) and (2) take:

$$\frac{\overline{Gr}_q}{\overline{Re}} \simeq 38.3\ \frac{\overline{Re}^{0.92}}{\overline{Pr}^{0.57}} \tag{4}$$

Eliminating the parameter Re from equation (2) and (4) take:

$$\overline{Nu} = 2.8 \times 10^{-3}\ \left(\frac{\overline{Gr}_q}{\overline{Re}}\right)^{0.87}\ \overline{Pr}^{0.49} \tag{5}$$

APPENDIX A.4.2

The Ra_D Dimensionless Number

In this Appendix the Ra_D number is expressed in terms with the Gr_q/Re parameter.

From equation 1.30 take:

$$4\ Gr_q = Re\ Pr\ \frac{\partial T^*}{\partial z^*} \cdot Gr_{\Delta T} \tag{1}$$

$$\text{Since } Gr_{\Delta T} = \frac{\beta\ g\ (T_1 - T_o)\ D_e^3}{\nu^2} \tag{2}$$

$$\text{and} \qquad Gr_D = \frac{\beta\ g\ (T - T_o)\ D^3}{\nu^2} \tag{3}$$

$$\text{then} \qquad Gr_D = Gr_{\Delta T}\ \frac{T - T_o}{T_1 - T_o}\ \left(\frac{D}{De}\right)^3 = Gr_{\Delta T}\ T^*\ \left(\frac{D}{De}\right)^3 \tag{4}$$

$$\text{by definition } Ra_D = Gr_D\ Pr\ \frac{\partial T^*/\partial z^*}{T^*}\ \frac{D}{De} \tag{5}$$

Using equations (4) and (1), equation (5) is written as follows:

$$Ra_D = 4\ \frac{Gr_q}{Re}\ \left(\frac{D}{De}\right)^4 \tag{6}$$

APPENDIX A.7.1

Validation of Gunter-Shaw Correlation for a Single Gap of Triangular Rod Arrays

For triangular rod arrays, the Gunter-Shaw correlation, (G-S), given by equation 7.31, is applied over one or multiple stages of rod rows, as shown in Figure 7.7(b). The total presure drop, $p_A - p_F = \Delta p^S$ (see Figure 7.7(b)), can be obtained as follows:

$$\frac{\Delta p^S}{L} = C\, u_g^{2-a} \tag{1}$$

where C is a proportionality constant (given by the G-S correlation)

$$L = P \cos 30 = \frac{\sqrt{3}P}{2} \tag{2}$$

and

$$a = \begin{cases} 1; & \text{laminar flow} \\ 0.145; & \text{turbulent flow} \end{cases} \tag{3}$$

According to the G-S correlation, u_g is the maximum velocity at any gap. So, acording to Figure 7.7(b)

$$u_g = u_{\ell,i} = u_{j,k} \tag{4}$$

From continuity, take:

$$u_{ij} = \frac{1}{2}\, u_{\ell,i} = \frac{1}{2}\, u_g \tag{5}$$

Also, from eqs. 7.29 and (1):

$$\Delta p_{\ell,i} + \Delta p_{i,j} = C\, L\, u_g^{2-a} \tag{6}$$

Now, assume that

$$\Delta p_{\ell,i} \sim u_{\ell,i}^{2-a} \tag{7}$$

$$\Delta p_{i,j} \sim u_{i,j}^{2-a} \tag{8}$$

From equations 4, 5, 7 and 8 take

$$\frac{\Delta p_{\ell,i}}{\Delta p_{i,j}} = 2^{2-a} \tag{9}$$

From equations 9 and 6 obtain

$$\Delta p_{i,j} = \frac{2L}{3} C \frac{3 + 2^{2-a}}{2(1+2^{2-a})} \left(\frac{u_g}{2}\right)^{2-a} \tag{10}$$

$$\Delta p_{\ell,i} = \frac{2L}{3} C \frac{3}{2(1+2^{a-2})} u_g^{2-a} \tag{11}$$

Since $L_{i,j} = L_{\ell,i} = \frac{2}{3} L$ (see Figure 7.7(b)), equations 10 and 11 give:

$$\Delta p_{i,j}/L_{i,j} = C \frac{3}{2(1+2^{a-2})} u_{i,j}^{2-a} \tag{12}$$

$$\Delta p_{\ell,i}/L_{\ell,i} = C \frac{3}{2(1+2^{a-2})} u_{\ell,i}^{2-a} \tag{13}$$

Note that C is the same for all three control volumes, namely the gaps ℓ-i and i-j as well as the cell volume. Equations 12 and 13 indicate that for triangular rod arrays, the G-S correlation is still valid over a gpa control volume if it is multiplied by the factor

$$M = \frac{3}{2(1+2^{a-2})} \tag{14}$$

In laminar flows, a=1 and $M_L = 1$. In turbulent flows, a = 0.145 and $M_T = 1.175$. Therefore, the G-S friction factor coefficient given by equation

7.33 has to be multiplied by M, yielding

$$f'_L = Mf_L = \begin{cases} 1.80/Re_{D_v} ; & \text{laminar flow} \\ 2.25/Re_{D_v}^{0.145} ; & \text{turbulent flow} \end{cases} \qquad (15)$$

APPENDIX A.8.1

Subroutines H12WG, DRMA, DRML, FRIFAC.

```
      SUBROUTINE H12WG(PW)
      IMPLICIT REAL*8(A-H,O-Z)
C
C
C     THIS SUBROUTINE CALCULATES THE GEOMETRICAL INPUT PARAMETERS
C     FOR THE WIRE-SPACER HYDRAULIC RESISTANCE MODELS AS THEY ARE
C     EMPLOYED IN SUBROUTINES DRMA AND DRML.
C
C
C     THE AXIAL NUMERICAL MESH LENGTH EQUALS H/12
C
C=== COMMON ==========================================================
      COMMON /GMT/      NCHAN          ,NCHANM          ,LMAX
     1 ,LMAXM           ,KMAX          ,ICB(3,42)       ,LC(42,3)
     2 ,KCHAN(42,42)  ,THETA(31)      ,IBD(42)         ,ITYPE(42)
     3 ,NHALF           ,RP            ,WT              ,GAP(60)
     4 ,PITCH(60)      ,DZ(31)         ,ZCHNL(32)       ,DS(60)
     5 ,DHW(42,31)     ,DHU(60,31)     ,A(60,31)        ,AC(60,31)
     6 ,B(42,31)       ,D(60,31)       ,VS(42,31)       ,VC(60,31)
     7 ,VW(42,31)      ,NWRAP          ,MWRAPT(18)      ,IWRAP(18)
      COMMON /OPT/      IVFLAG         ,ITFLAG          ,IFFLAG
     1 ,IBLCK           ,IWIRE         ,IGRID           ,ICFLAG
      COMMON /WIR/      WDIA(19)       ,WS              ,WL
     1 ,WAREAN          ,WSUR          ,BET             ,DBET
     2 ,KNEARP(60,2)   ,INEARP(42,3)  ,CS              ,C(60,31)
     3 ,H               ,COEM(42)
      COMMON /WGIP/  NADJ(42,12),DVBS(4),DVPS(4),AWBS(4),AWPS(4),
     1  PHI,DW,RATS(4),RATG(4),DELZ,DVBG(4),DVPG(4),AWBG(4),AWPG(4),
     2  ALAM(4),BB(4),DD(4),PWB(4),PWD(2),CFWN,PIT,NADJ1(9,12)
C=== COMMON ==========================================================
C
      DIMENSION PW(42)
C
      DIMENSION ITBL(14,12),ITBL1(9,12)
      DATA ((ITBL(I,J),J=1,12),I=1,14)/
     1  0,-1,-2,0,0,-3,1,0,0,2,3,0,
     2 -1,0,0,-2,-3,0,0,1,2,0,0,3,
     3  50,-4,-4,50,-3,6*0,3,
     4  0,-1,50,-5,-5,50,1,5*0,
     5  3*0,-2,50,-6,-6,50,2,3*0,
     6  5*0,-3,50,-7,-7,50,3,0,
     7 -1,6*0,1,50,-8,-8,50,
     8 -9,50,-2,6*0,2,50,-9,
     9  -9,-4,10*0,
     A  0,0,-4,-5,8*0,
     B  4*0,-5,-6,6*0,
     C  6*0,-6,-7,4*0,
     D  8*0,-7,-8,2*0,
     E  10*0,-8,-9/
      DATA ((ITBL1(I,J),J=1,12),I=1,9)/
     1 -1,-100,3*0,10,1,100,3*0,-10,
     2  0,-20,-2,-200,3*0,20,2,200,0,0,
     3  3*0,-30,-3,-300,3*0,30,3,300,
     4 -40,-4,-400,9*0,
```

```
     5  2*0,-50,-5,-500,7*0,
     6  4*0,-60,-6,-600,5*0,
     7  6*0,-70,-7,-700,3*0,
     8  8*0,-80,-8,-800,0,
     9 -900,9*0,-90,-9/
C
C    CALCULATE THE NADJ(I,LW) FUNCTION, LW=1,12
C
      DO 400 I=1,NCHAN
      IF(ICB(3,I) .EQ. 0) GO TO 200
      IF(IABS(ICB(1,I)).GT.3 .OR. IABS(ICB(2,I)).GT.3) GO TO 100
C
C    INTERIOR SUBCHANNELS
C
      ISUM=ICB(1,I)+ICB(2,I)+ICB(3,I)
      NTYPE=1
      IF(ISUM .LT. 0) NTYPE=2
      GO TO 300
C
C    EDGE SUBCHANNELS
C
  100 NTYPE=MAX0(IABS(ICB(1,I)),IABS(ICB(2,I)))-1
      GO TO 300
C
C    CORNER SUBCHANNELS
C
  200 NTYPE=MIN0(IABS(ICB(1,I)),IABS(ICB(2,I)))+6
      MUL=IABS(ICB(1,I))*IABS(ICB(2,I))
      IF(MUL .EQ. 36) NTYPE=9
  300 CONTINUE
C
C
      DO 380 LW=1,12
      IF(ITBL(NTYPE,LW) .EQ. 0) GO TO 360
      IF(ITBL(NTYPE,LW) .EQ. 50) GO TO 370
      DO 310 M=1,3
      NICB=IABS(ICB(M,I))
      IF(NICB.GT.3 .AND. ICB(3,I).NE.0) GO TO 305
      IF(IABS(ICB(M,I)) .EQ. IABS(ITBL(NTYPE,LW))) GO TO 320
      GO TO 310
  305 LP1=LW+1
      IF(LP1 .EQ. 13) LP1=1
      JSG=-1
       IF(ITBL(NTYPE,LW) .EQ. ITBL(NTYPE,LP1)) JSG=1
      JTBL=ITBL(NTYPE,LW)*JSG
      IF(ICB(M,I) .EQ. JTBL) GO TO 320
  310 CONTINUE
  320 J=LC(I,M)
      IPORT=-1
      IF(ICB(M,I) .EQ. ITBL(NTYPE,LW)) IPORT=1
      NSGN=1
      IF(I .GT. J) NSGN=-1
      NADJ(I,LW)=J*IPORT*NSGN
      GO TO 380
```

```
  360 NADJ(I,LW)=0
      GO TO 380
  370 NADJ(I,LW)=1000
  380 CONTINUE
  400 CONTINUE
      DO 410 I=1,9
      DO 410 J=1,12
      NADJ1(I,J)=ITBL1(I,J)
  410 CONTINUE
C
C   ESTIMATE GEOMETRICAL CHARECTERISTICS
C
      PAI=3.141592
      DW=WDIA(1)
      PHI=DATAN((2.0*RP+DW)*PAI/H)
      WRS=DW/2.0
      WRL=0.5*DW*DSQRT(H**2+(2.0*PAI*(RP+WRS))**2)/H
      DELZ=H/12.0
      WAREA=PAI*WRS*WRL
      WAREAZ=PAI*DW**2/4.0/DSIN(PHI)
      PIT=PITCH(1)
      WPER=4.0*(0.9827*WRL+0.311*WRS+0.2867*WRS**2/WRL)
      BB(1)=PIT**2*SQRT(3.0)/4.0-PAI*RP**2*0.5
      BB(2)=(RP+DW)*PIT-PAI*RP**2*0.5
      BB(3)=BB(2)
      BB(4)=(RP+DW)**2/SQRT(3.0)-PAI*RP**2/6.0
      DD(1)=PIT**2/2.0/SQRT(3.0)-PAI/3.0*RP**2
      DD(2)=PIT**2/4.0/SQRT(3.0)+(RP+DW-PIT/2.0)*PIT/SQRT(3.0)-
     1 PAI*RP**2/6.0
      PWB(1)=PAI*RP
      PWB(2)=PWB(1)+PIT
      PWB(3)=PWB(2)
      PWB(4)=PWB(1)/3.0+2.0*(RP+DW)/SQRT(3.0)
      PWD(1)=PAI*RP*2.0/3.0
      PWD(2)=RP*PAI/3.0+PIT/SQRT(3.0)
      VLFOV=DW**3/3.0/DSIN(2.0*PHI)
      WIRVOL=PAI*DW**2*DELZ/4.0/DCOS(PHI)-VLFOV
      WAWLF=H/8.0/PAI*DATAN(WRL/(RP+DW/2.0))
      WAW=WPER*(DELZ-WAWLF)
      WIRVL=PAI*DW**2*DELZ/2.0/DCOS(PHI)-VLFOV
      WAWL=WPER*(DELZ/2.0-WAWLF)
C
C
      DO 420 I=1,4
      AWBS(I)=PWB(I)*DELZ
      DVBS(I)=4.0*BB(I)/PWB(I)
      AWPS(I)=AWBS(I)+WAW
      IF(I .EQ. 3) AWPS(I)=AWBS(I)+WPER*DELZ
      VOLPS=BB(I)*DELZ-WIRVOL
      IF(I .EQ. 3) VOLPS=VOLPS+VLFOV
      DVPS(I)=4.0*VOLPS/AWPS(I)
  420 CONTINUE
C
      DO 430 I=1,2
```

```
      AWBG(I)=PWD(I)*DELZ
      DVBG(I)=4.0*DD(I)/PWD(I)
      AWPG(I)=AWBG(I)+WPER*DELZ
      VOLPG=DD(I)*DELZ-WIRVOL+VLFOV
      DVPG(I)=4.0*VOLPG/AWPG(I)
      AWBG(I+2)=AWBG(I)
      AWPG(I+2)=AWBG(I)+WAWL
      DVBG(I+2)=DVBG(I)
      VOL=DD(I)*DELZ-WIRVL
      DVPG(I+2)=4.0*VOL/AWPG(I+2)
  430 CONTINUE
C
C
C   CALCULATE LAMINAR FRICTION FACTOR COEFFICIENT CONSTANTS
C   BASED ON REHME'S CORELATION
C
C
      PODM1=PIT/2.0/RP-1.0
      IF((PODM1+1.0) .LT. 1.1) GO TO 440
      ALAM(1)=62.97+216.9*PODM1-190.2*PODM1**2
      ALAM(2)=45.30+256.4*PODM1-271.2*PODM1**2
      ALAM(3)=ALAM(2)
      ALAM(4)=87.26+38.59*PODM1-55.12*PODM1**2
      GO TO 450
  440 ALAM(1)=26.0+888.2*PODM1-3334.0*PODM1**2
      ALAM(2)=26.18+554.5*PODM1-1480.0*PODM1**2
      ALAM(3)=ALAM(2)
      ALAM(4)=26.98+1636.0*PODM1-10050.0*PODM1**2
C
C   ESTIMATE DRAG COEFFICIENTS FOR THE FWL COMPONENT
C
  450 PDPAR=1.0-1.0/PIT*2.0*RP
      READ(5,800) CON1,CON2,CON3,CON4,CON5,CON6,CON7
      WRITE(6,900) CON1,CON2,CON3,CON4,CON5,CON6,CON7
      RATS(1)=30.3*PDPAR/1.0*CON1
      RATS(2)=RATS(1)/1.0
      RATS(3)=(1.0-1.707*1.0*RP/PIT)/0.293/1.0*CON2
      RATS(4)=58.7*PDPAR/1.0*CON3
      RATG(1)=117.9*PDPAR/1.5*CON4
      RATG(2)=233.78*PDPAR/2.0*CON5
      RATG(3)=14.07*PDPAR/1.0*CON6
      RATG(4)=26.274*PDPAR/1.0*CON7
      CFWN=10.0
C
C   CALCULATE B(I,L) - A(K,L) - AC(K,L) - D(K,L)
C   DUE TO THE PRESENCE OF THE WIRE-SPACER
C
      DO 600 I=1,NCHAN
      IF(ICB(3,I) .EQ. 0) GO TO 520
      IF(IABS(ICB(1,I)).GT.3 .OR. IABS(ICB(2,I)).GT.3) GO TO 510
      ISUM=ICB(1,I)+ICB(2,I)+ICB(3,I)
      NTYPE=1
      IF(ISUM .LT. 0) NTYPE=2
      GO TO 530
```

```
  510 NTYPE=MAXO(IABS(ICB(1,I)),IABS(ICB(2,I)))-1
      GO TO 530
  520 NTYPE=MINO(IABS(ICB(1,I)),IABS(ICB(2,I))) +6
      MUL=IABS(ICB(1,I))*IABS(ICB(2,I))
      IF(MUL .EQ. 36) NTYPE=9
  530 CONTINUE
C
      DO 580 L=1,LMAX
      LW=MOD(L,12)
      IF(LW .EQ. 0) LW=12
      IF(ITBL(NTYPE,LW) .EQ. 0) GO TO 580
      B(I,L)=B(I,L)-WAREA
      DHW(I,L)=4.0*B(I,L)/(PW(I)+WPER)
  580 CONTINUE
  600 CONTINUE
C
C
      DO 700 I=1,NCHAN
      DO 690 M=1,3
      J=LC(I,M)
      IF(I .GT. J) GO TO 689
      K=KCHAN(I,J)
      KDIR=IABS(ICB(M,I))
      IF(KDIR .GT. 3) GO TO 610
      LTOP=2*KDIR-1
      LBOT=LTOP+6
      GO TO 620
  610 LTOP=2*(KDIR-3)
      LBOT=100
  620 CONTINUE
C
      DO 680 L=1,LMAX
      LW=MOD(L,12)
      IF(LW .EQ. 0) LW=12
      IF(LW.NE.LTOP .AND. LW.NE.LBOT) GO TO 680
      A(K,L)=A(K,L)-WAREAZ
      AC(K,L)=A(K,L)
      D(K,L)=D(K,L)-WAREA
      IF(L .EQ. LMAX) GO TO 680
      D(K,L+1)=D(K,L+1)-WAREA
  680 CONTINUE
  689 CONTINUE
  690 CONTINUE
  700 CONTINUE
  800 FORMAT(10X,7F10.2)
  900 FORMAT(//,7X,'CON1',6X,'CON2',6X,'CON3',6X,
     1  'CON4',6X,'CON5',6X,'CON6',3X,'CON7',/,7F10.2,///)
      RETURN
      END
```

```
      SUBROUTINE DRMA(I,L,RAV,VISCAV,FAVEX,FAVIM)
      IMPLICIT REAL*8(A-H,O-Z)
C
C   THIS SUBROUTINE CALCULATES THE AXIAL HYDRAULIC RESISTANCE ON THE
C   FLUID FLOW WITHIN A SUBCHANNEL OR GAP FOR BARE OR WIRE-WRAPPED
C                  ROD BUNDLES
C
C=== COMMON ============================================================
      COMMON /GMT/      NCHAN           ,NCHANM          ,LMAX
     1 ,LMAXM           ,KMAX           ,ICB(3,42)      ,LC(42,3)
     2 ,KCHAN(42,42)  ,THETA(31)       ,IBD(42)        ,ITYPE(42)
     3 ,NHALF           ,RP             ,WT              ,GAP(60)
     4 ,PITCH(60)      ,DZ(31)         ,ZCHNL(32)      ,DS(60)
     5 ,DHW(42,31)    ,DHU(60,31)     ,A(60,31)       ,AC(60,31)
     6 ,B(42,31)      ,D(60,31)       ,VS(42,31)      ,VC(60,31)
     7 ,VW(42,31)     ,NWRAP           ,MWRAPT(18)     ,IWRAP(18)
      COMMON /OPT/      IVFLAG          ,ITFLAG          ,IFFLAG
     1 ,IBLCK           ,IWIRE          ,IGRID           ,ICFLAG
      COMMON /VAR/      U6LN(60,31)   ,W6LN(42,31)   ,T6LN(42,31)
     1 ,P6N(42,31)    ,Q6LN(42,31)   ,R6LN(42,31)
      COMMON /WGIP/  NADJ(42,12),DVBS(4),DVPS(4),AWBS(4),AWPS(4),
     1  PHI,DW,RATS(4),RATG(4),DELZ,DVBG(4),DVPG(4),AWBG(4),AWPG(4),
     2  ALAM(4),BB(4),DD(4),PWB(4),PWD(2),CFWN,PIT,NADJ1(9,12)
C========================================================================
      PAI=4.0*DATAN(1.0D00)
      WS=W6LN(I,L)
      LW=MOD(L,12)
      IF(LW .EQ. 0) LW=12
      IF(ICB(3,I) .EQ. 0) GO TO 20
      IF(IABS(ICB(1,I)).GT.3.OR.IABS(ICB(2,I)).GT.3) GO TO 5
      GO TO 10
C
C   EDGE SUBCHANNELS
C
   5  IPAT=2
      IF(NADJ(I,LW) .EQ. 0) GO TO 100
       IF(NADJ(I,LW) .EQ. 1000) IPAT=3
      GO TO 30
C
C   INTERIOR SUBCHANNELS
C
  10  IPAT=1
      IF(NADJ(I,LW) .EQ. 0) GO TO 100
      GO TO 30
C
C   CORNER SUBCHANNELS
C
  20  IPAT=4
      IF(NADJ(I,LW) .EQ. 0) GO TO 100
C
C
  30  J1=IABS(NADJ(I,LW))
      EXPN=1.0
      IF(J1 .EQ. 1000) GO TO 40
```

```
       KSN=1
       IF(I .GT. J1) KSN=-1
       PRD=KSN*NADJ(I,LW)
CCC    IF(PRD .LT. 0.0) EXPN=1.3
       K1=KCHAN(I,J1)
       US=(U6LN(K1,L)+U6LN(K1,L-1))/2.0
       IF(NADJ(I,LW) .LT. 0) US=-US
       GO TO 50
   40  US=0.0
C
C
   50  VTS=DSQRT(WS**2+US**2)
       IF(VTS .LT. 1.0D-09) GO TO 90
       IF(DABS(WS) .LT. 1.0D-09) GO TO 60
       THET=DATAN(US/WS)
       IF(THET.LT.0.0 .AND. WS.LT.0.0) THET=THET+PAI
       IF(THET.GT.0.0 .AND. WS.LT.0.0) THET=THET-PAI
       GO TO 70
   60  THET=DSIGN(PAI/4.0,US)
C
C     CALCULATE THE FRA AND FWT COMPONENTS
C
   70  RES=DVPS(IPAT)*RAV*VTS/VISCAV
       CONS1=AWPS(IPAT)*FRIFAC(RES,ALAM(IPAT))*RAV/8.0
       CONS2=AWBS(IPAT)/AWPS(IPAT)
       FRAIM=CONS1*CONS2*WS*DCOS(THET)
       FRAEX=CONS1*CONS2*US**2*DCOS(THET)
       FWTIM=CONS1*(1.0-CONS2)*WS*DCOS(PHI-THET)
       FWTEX=CONS1*(1.0-CONS2)*US**2*DCOS(PHI-THET)
       IF(IWIRE .EQ. 6) GO TO 75
       IF(FWTIM .LT. 0.0) FWTEX=FWTEX+FWTIM*WS
       IF(FWTIM .LT. 0.0) FWTIM=0.0
C
C   CALCULATE THE FWN COMPONENT
C
   75  CONTINUE
       VNS=VTS*DSIN(PHI-THET)
       IF(DABS(VNS) .LT. 1.0D-09) GO TO 80
       REWN=DW*RAV*DABS(VNS)/VISCAV
       ICH=IABS(ICB(1,J1))+IABS(ICB(2,J1))
       IF(ICH .GE.7 .AND. IPAT.EQ.2) IPAT=4
       FFNS=RATS(IPAT)**EXPN*(1.0+CFWN/REWN**0.333)
       IF(ICB(3,I).NE.0 .AND. IPAT.EQ.4) IPAT=2
       CONS3=DSIN(PHI-THET)
       CONS4=FFNS*RAV*DW*DELZ/DCOS(PHI)/2.0*DABS(CONS3)*CONS3
       FWNIM=CONS4*WS
       FWNEX=CONS4*US**2
       IF(IWIRE .EQ. 6) GO TO 85
       IF(FWNIM .LT. 0.0) FWNEX=FWNEX+FWNIM*WS
       IF(FWNIM .LT. 0.0) FWNIM=0.0
       GO TO 85
   80  FWN=0.0
C
C    CALCULATE THE TOTAL AXIAL DRAG
```

```
C
   85 VOLSUB=DVPS(IPAT)*AWPS(IPAT)/4.0
      FAVIM=(FRAIM+FWTIM*DCOS(PHI)+FWNIM*DSIN(PHI))/VOLSUB
      FAVEX=(FRAEX+FWTEX*DCOS(PHI)+FWNEX*DSIN(PHI))/VOLSUB
      IF(IWIRE .NE. 6) RETURN
      IF(FAVIM .LT. 0.0) FAVEX=FAVEX+FAVIM*WS
      IF(FAVIM .LT. 0.0) FAVIM=0.0
      RETURN
   90 FAVIM=0.0
      FAVEX=0.0
      RETURN
C
C   BARE ROD BUNDLE
C
  100 FAVEX=0.0
      REBS=DVBS(IPAT)*RAV*DABS(WS)/VISCAV
      IF(REBS .LT. 1.0D-04) GO TO 110
      FTOTA=AWBS(IPAT)*FRIFAC(REBS,ALAM(IPAT))*RAV*DABS(WS)/8.0
      FAVIM=FTOTA/DVBS(IPAT)*4.0/AWBS(IPAT)
      RETURN
  110 FAVIM=0.0
      RETURN
      END
```

```
      SUBROUTINE DRML(K,L,I,J,M,RAV,VISCAV,FLVEX,FLVIM)
      IMPLICIT REAL*8(A-H,O-Z)
C
C   THIS SUBROUTINE CALCULATES THE LATERAL HYDRAULIC RESISTANCE ON THE
C   FLUID FLOW WITHIN A SUBCHANNEL OR GAP FOR BARE OR WIRE-WRAPPED
C                  ROD BUNDLES
C
C=== COMMON ============================================================
      COMMON /GMT/      NCHAN          ,NCHANM          ,LMAX
     1 ,LMAXM           ,KMAX          ,ICB(3,42)       ,LC(42,3)
     2 ,KCHAN(42,42)  ,THETA(31)      ,IBD(42)         ,ITYPE(42)
     3 ,NHALF           ,RP            ,WT              ,GAP(60)
     4 ,PITCH(60)      ,DZ(31)         ,ZCHNL(32)       ,DS(60)
     5 ,DHW(42,31)     ,DHU(60,31)     ,A(60,31)        ,AC(60,31)
     6 ,B(42,31)       ,D(60,31)       ,VS(42,31)       ,VC(60,31)
     7 ,VW(42,31)      ,NWRAP          ,MWRAPT(18)      ,IWRAP(18)
      COMMON /OPT/      IVFLAG         ,ITFLAG          ,IFFLAG
     1 ,IBLCK           ,IWIRE         ,IGRID           ,ICFLAG
      COMMON /VAR/      U6LN(60,31)   ,W6LN(42,31)   ,T6LN(42,31)
     1 ,P6N(42,31)     ,Q6LN(42,31)   ,R6LN(42,31)
      COMMON /WGIP/  NADJ(42,12),DVBS(4),DVPS(4),AWBS(4),AWPS(4),
     1  PHI,DW,RATS(4),RATG(4),DELZ,DVBG(4),DVPG(4),AWBG(4),AWPG(4),
     2  ALAM(4),BB(4),DD(4),PWB(4),PWD(2),CFWN,PIT,NADJ1(9,12)
C========================================================================
      PAI=4.0*DATAN(1.0D00)
      LW=MOD(L,12)
      IF(LW .EQ. 0) LW=12
      IGADI=ICB(M,I)
      NTYPE=IABS(IGADI)
      IWIDI=NADJ1(NTYPE,LW)
       IF(IWIDI .EQ. 0) GO TO 100
      MPROD=IWIDI*IGADI
      IF(MPROD .GT. 0) GO TO 10
      I1=J
      I2=I
      GO TO 20
   10 I1=I
      I2=J
   20 CONTINUE
      JSIGN=1
      IF(I1 .GT. I2) JSIGN=-1
C
C
      IPAT=1
      IF(NTYPE .GT. 3) IPAT=2
      IF(IABS(IWIDI) .GT. 9) IPAT=IPAT+2
      UG=U6LN(K,L)*JSIGN
      LU=L+1
      IF(L .EQ. LMAX) LU=L
C
C   ESTIMATE THE AXIAL VELOCITY MAGNITUDE
C
      IF(IPAT .GT. 2) GO TO 30
      WG=(W6LN(I,L)+W6LN(I,LU)+W6LN(J,L)+W6LN(J,LU))/4.0
```

```
      FDEL=1.0
      EXPL=1.0
      GO TO 40
   30 IW=11
CC    UG=UG/2.0
      IF(IABS(IWIDI) .GT. 99) IW=12
      WG=(W6LN(IW,L)+W6LN(IW,LU))/2.0
      FDEL=0.5
      EXPL=1
      IF(IW .EQ. 12) EXPL=1.5
   40 CONTINUE
      IF(IWIRE .NE. 5) GO TO 42
C
C    FORCING FUNCTION TYPE WIRE-SPACER MODEL
C    FOR INITIALIZATION OF THE U6LN VELOCITY FIELD
C
      FLVIM=1.0D32
      COEFF=-0.9D32
      IF(IPAT .GT. 2) COEFF=COEFF/2.0
      FLVEX=COEFF*DTAN(PHI)*WG*JSIGN
      RETURN
C
C   CALCULATE THE FWT COMPONNENT
C
  42  VG=DSQRT(WG**2+UG**2)
      IF(VG .LT. 1.0D-09) GO TO 90
      IF(DABS(WG) .LT. 1.0D-09) GO TO 44
      THETG=DATAN(UG/WG)
      IF(THETG.LT.0.0 .AND. WG.LT.0.0) THETG=THETG+PAI
      IF(THETG.GT.0.0 .AND. WG.LT.0.0) THETG=THETG-PAI
      GO TO 46
  44  THETG=DSIGN(PAI/4.0,UG)
   46 REVG=DVPG(IPAT)*RAV*VG/VISCAV
      FMD=FRIFAC(REVG,ALAM(1))
      CONS5=(AWPG(IPAT)-AWBG(IPAT))*FMD*RAV/8.0*DCOS(PHI-THETG)
      FWTEX=CONS5*WG**2*JSIGN
      FWTIM=CONS5*UG
      IF(IWIRE .EQ. 6) GO TO 48
      IF(FWTIM .LT. 0.0) FWTEX=FWTEX+FWTIM*UG*JSIGN
      IF(FWTIM .LT. 0.0) FWTIM=0.0
C
C   CALCULATE THE FWN COMPONENT
C
   48 CONTINUE
      VNG=VG*DSIN(PHI-THETG)
      IF(DABS(VNG) .LT. 1.0D-8) GO TO 50
      REWG=DW*RAV*DABS(VNG)/VISCAV
      FNG=RATG(IPAT)**EXPL*(1.0+CFWN/REWG**0.333)
      CONS6=DSIN(PHI-THETG)
      DELZP=DELZ*FDEL
      CONS7=FNG*RAV*DABS(CONS6)*CONS6*DW*DELZP/DCOS(PHI)/2.0
      FWNEX=CONS7*WG**2*JSIGN
      FWNIM=CONS7*UG
      IF(IWIRE .EQ. 6) GO TO 60
```

```
      IF(FWNIM .GT. 0.0) FWNEX=FWNEX+FWNIM*UG*JSIGN
      IF(FWNIM .GT. 0.0) FWNIM=0.0
      GO TO 60
   50 FWNEX=0.0
      FWNIM=0.0
C
C    CALCULATE THE FRL COMPONENT USING THE GUNTER-SHAW CORELATION
C
   60 IF(DABS(UG) .LT. 1.0D-08) GO TO 70
      REUG=REVG*DABS(UG)/VG
      FGS=180.0/REUG
      IF(REUG.GT.200.0 .OR. REVG.GT.400.0) FGS=2.25/REUG**0.145
      FRLIM=FGS*AWBG(IPAT)/8.0*RAV*DABS(UG)*DVPG(IPAT)/PIT*0.917
      GO TO 80
   70 FRLIM=0.0
C
C    CALCULATE THE TOTAL LATERAL DRAG
C
   80 VOLGAP=DVPG(IPAT)*AWPG(IPAT)/4.0
      FLVIM=(FRLIM+FWTIM*DSIN(PHI)-FWNIM*DCOS(PHI))/VOLGAP
      FLVEX=(FWTEX*DSIN(PHI)-FWNEX*DCOS(PHI))/VOLGAP
      IF(IWIRE .NE. 6) RETURN
      IF(FLVIM .LT. 0.0) FLVEX=FLVEX+FLVIM*UG*JSIGN
      IF(FLVIM .LT. 0.0) FLVIM=0.0
      RETURN
   90 FLVIM=0.0
      FLVEX=0.0
      RETURN
C
C    BARE ROD CASE
C
  100 FLVEX=0.0
      UG=U6LN(K,L)
      IPAT=1
      IF(NTYPE .GT. 3) IPAT=2
      IF(DABS(UG) .LT. 1.0D-08) GO TO 110
      LU=L+1
      IF(L .EQ. LMAX) LU=L
      WG=(W6LN(I,L)+W6LN(I,LU)+W6LN(J,L)+W6LN(J,LU))/4.0
      VG=DSQRT(WG**2+UG**2)
      REUB=DVBG(IPAT)*RAV*DABS(UG)/VISCAV
      REVB=REUB*DABS(VG/UG)
      FGB=180.0/REUB
      IF(REVB .GT. 200.000) FGB=2.25/REUB**0.145
      FTOTL=FGB*AWBG(IPAT)/8.0*RAV*DABS(UG)*DVBG(IPAT)/PIT*0.917
      FLVIM=FTOTL/DVBG(IPAT)*4.0/AWBG(IPAT)
      GO TO 120
  110 FLVIM=0.0
  120 CONTINUE
      RETURN
      END
C
C
C
```

```
      REAL FUNCTION FRIFAC*8(RE,A)
C
C   THIS FUNCTION CALCULATES THE FRICTION FACTOR COEFFICIENT
C   BASED ON REHME'S  THEORETICAL WORK.
C
C   THE LAMINAR-TRANSITION REYNOLDS NUMBER RELT=600
C   THE TRANSITION-TURBULENCE REYNOLDS NUMBER RETT=2000
C
      DATA RELT,RETT/6.0D02,2.0D04/
      IF(RE .LT. RELT) GO TO 10
      IF(RE .GT. RETT) GO TO 20
      PSI=(RE-RELT)/(RETT-RELT)
      FRIFAC=A/RELT*(1.0-PSI)+0.316/RETT**0.25*PSI
      RETURN
   10 FRIFAC=A/RE
      RETURN
   20 FRIFAC=0.316/RE**0.25
      RETURN
      END
```

APPENDIX A.8.2

Subroutines UCLCALC, WLADI1, WLADI2.

```
      SUBROUTINE ULCALC
      IMPLICIT REAL*8 (A-H,O-Z)
C
C              *****   ULCALC   *****
C +-------------------------------------------------------------------+
C |                                                                   |
C |  THIS SUBROUTINE SOLVES TRANSVERS MOMENTUM EQUATION, ASSUMING ZERO |
C |                                                                   |
C |  MOMENTUM FLUX TRANSPORT DIFFERENCES IN TRANSVERSE DIRECTION.     |
C |                                                                   |
C +-------------------------------------------------------------------+
C
C==== COMMON ========================================================
      COMMON /MAT/       AMT(42,42)    ,BMT(3,31)      ,Y(31)
      COMMON /GMT/       NCHAN           ,NCHANM         ,LMAX
     1 ,LMAXM           ,KMAX           ,ICB(3,42)      ,LC(42,3)
     2 ,KCHAN(42,42)  ,THETA(31)      ,IBD(42)        ,ITYPE(42)
     3 ,NHALF           ,RP             ,WT             ,GAP(60)
     4 ,PITCH(60)      ,DZ(31)         ,ZCHNL(32)      ,DS(60)
     5 ,DHW(42,31)    ,DHU(60,31)    ,A(60,31)       ,AC(60,31)
     6 ,B(42,31)      ,D(60,31)      ,VS(42,31)      ,VC(60,31)
     7 ,VW(42,31)     ,NWRAP          ,MWRAPT(18)     ,IWRAP(18)
      COMMON /CNT/       NSTEP           ,TIME           ,CRNT
     1 ,DTHLF           ,TMAX           ,NMAX           ,ITMAX
     2 ,NOUT            ,PEPS
      COMMON /BND/       INFLAW          ,MAXW           ,WXT(20)
     1 ,WDATA(20)       ,INFLAT         ,MAXT           ,TXT(20)
     2 ,TDATA(20)       ,INFLAP         ,MAXPO          ,MAXPI
     3 ,PXTO(20)        ,PXTI(20)       ,PODATA(20)     ,PIDATA(20)
     4 ,INFLAQ          ,MAXQ           ,QXT(20)        ,QDATA(20)
     5 ,PDIST(31)      ,QIN            ,SGM(42)        ,WIN
     6 ,TIN             ,PIN
      COMMON /BLK/       LBD             ,LBU            ,LBL(31)
     1 ,MESHBL          ,LBS(42,31)    ,LBCR(60,31)   ,RBLC
     2 ,CPBLC           ,CNDBLC         ,WBLK           ,TBLK
     3 ,SGMB(60)       ,DZBL
      COMMON /GRD/       DZGR            ,LGR(31)        ,MESHGR
     1 ,FLOSS(42,31)  ,JSPACE(42,31)
      COMMON /VAR/       U6LN(60,31)   ,W6LN(42,31)   ,T6LN(42,31)
     1 ,P6N(42,31)    ,Q6LN(42,31)   ,R6LN(42,31)
      COMMON /WRK/       DIVL(42,31)   ,DP6N(42,31)   ,T6LNP(42,31)
     1 ,W6LNT(42,31)  ,U6LNT(60,31)  ,UW6LN(60,31)  ,UP6LN(60,31)
      COMMON /LIQ/       CPLN(42,31)   ,VSCLXX(60,31)  ,VSCLZ(42,31)
     1 ,CNDLX(60,31)  ,CNDLZ(42,31)  ,CPIN           ,RIN
     2 ,VISCOS          ,VSCLZX(60,31)
C=====================================================================
C
      DATA               COEFFI          /1.0E+01/
      DATA               LPD             /9/
              LST =1
      IF(INFLAP.EQ.2) LST =2
              LEN =LMAX
      DO 2100 I =1,NCHAN
        DO 2100 M =1,3
```

```
            J =LC(I,M)
          IF(I-J) 1000,2100,2100
1000          K =KCHAN(I,J)
          DO 1100 L =1,LMAX
              BMT(1,L) =0.0
              BMT(2,L) =1.0
1100          BMT(3,L) =0.0
          DO 1700 L =1,LMAX
              LU =L+1
CC            TAUWL =FRIWLX(K,L,I,J)
              FRBS =0.0
            IF(L.NE.LBD .AND. L.NE.LBU) GO TO 1200
              KIJFL =LBS(I,LBD+1)*LBS(J,LBD+1)
            IF(KIJFL.EQ.1) FRBS =FRICBL(I,J,K,L)
1200        CONTINUE
              RAV =0.5*(R6LN(I,L)+R6LN(J,L))
      VISCAV=0.5*(VSCLZ(I,L)+VSCLZ(J,L))
      CALL DRML(K,L,I,J,M,RAV,VISCAV,FLVEX,FLVIM)
CC          TAUWIR =TAUWL*COEFFI/(DABS(UP6LN(K,L))+1.0D-06)*DABS(UP6LN(K
CC    1           ,L)-UW6LN(K,L))
CC            BMT(2,L) =BMT(2,L)+DTHLF*(TAUWL+FRBS)/RAV
CC            Y(L) =UP6LN(K,L)-DTHLF*(P6N(J,L)-P6N(I,L))/DS(K)/RAV
      BMT(2,L)=BMT(2,L)+DTHLF*(FLVIM+FRBS)/RAV
      Y(L)=UP6LN(K,L)-DTHLF*(P6N(J,L)-P6N(I,L))/DS(K)/RAV-DTHLF*FLVEX/
     1      RAV
CC          IF(A(K,L).LT.AC(K,L)) Y(L) =Y(L)-DTHLF*TAUWIR*UW6LN(K,L)/RAV
CC          IF(A(K,L).LT.AC(K,L)) BMT(2,L) =BMT(2,L)+DTHLF*TAUWIR/RAV
              VCX =VC(K,L)
            IF(L.GT.1) GO TO 1300
              Y(1) =Y(1)-DTHLF*VISCTM(DZ(1),D(K,1),VCX,VSCLZX(K,1),UP6LN
     1          (K,1),RAV)
            GO TO 1400
1300          UPX =UP6LN(K,L)-UP6LN(K,L-1)
              DZX =0.5*(DZ(L-1)+DZ(L))
              Y(L) =Y(L)-DTHLF*VISCTM(DZX,D(K,L),VCX,VSCLZX(K,L),UPX,RAV
     1          )
            IF(L.EQ.LMAX) GO TO 1700
1400          DX =D(K,LU)
              WX =0.5*(W6LN(I,LU)+W6LN(J,LU))
              UPX =UP6LN(K,LU)-UP6LN(K,L)
              DZX =0.5*(DZ(L)+DZ(LU))
              Y(L) =Y(L)+DTHLF*VISCTM(DZX,DX,VCX,VSCLZX(K,LU),UPX,RAV)
            IF(WX) 1500,1500,1600
1500          DUMY =DTHLF*CONVTM(DX,VCX,WX,1.0)
              BMT(3,L) =DUMY
              BMT(2,L) =BMT(2,L)-DUMY
            GO TO 1700
1600          VCU =VC(K,LU)
              DUMY =DTHLF*CONVTM(DX,VCU,WX,1.0)
              BMT(1,LU) =-DUMY
              BMT(2,LU) =BMT(2,LU)+DUMY
1700      CONTINUE
          DO 1800 L =1,LMAXM
              LU =L+1
```

```
            IF(LBS(I,L).EQ.1 .OR. LBS(J,L).EQ.1) BMT(1,L) =0.0
            IF(LBS(I,LU).EQ.1 .OR. LBS(J,LU).EQ.1) BMT(3,L) =0.0
            IF(LBCR(K,L).LE.0) GO TO 1800
              BMT(1,L) =0.0
              BMT(2,L) =1.0
              BMT(3,L) =0.0
              Y(L) =0.0
              U6LN(K,L) =0.0
1800        CONTINUE
            DO 1900 L =2,LMAXM
                LD =L-1
                LU =L+1
                JF =MAX(JSPACE(I,L),JSPACE(J,L))
              IF(JF.EQ.0) GO TO 1900
                BMT(1,L) =0.0
                BMT(1,LU) =0.0
                BMT(2,L) =1.0
                BMT(3,LD) =0.0
                BMT(3,L) =0.0
                Y(L) =0.0
                U6LN(K,L) =0.0
1900        CONTINUE
            CALL GAUSSJ(BMT,Y,LST,LEN,2)
            IF(INFLAP.EQ.2) U6LNT(K,1) =0.0
            DO 2000 L =LST,LMAX
                U6LNT(K,L) =Y(L)
2000        CONTINUE
2100    CONTINUE
        WRITE (LPD,100)
        DO 2300 M =1,30
                I1 =(M-1)*10+1
                I2 =M*10
          IF(I2.GT.KMAX) I2 =KMAX
          WRITE (LPD,110) (J,J=I1,I2)
          DO 2200 I =1,LMAX
            WRITE (LPD,120) I,(U6LNT(J,I),J=I1,I2)
2200      CONTINUE
          IF(I2.GE.KMAX) GO TO 2400
2300    CONTINUE
2400    CONTINUE
        RETURN
100     FORMAT (' ','U6LNT(JC,JZ) (VELOCITY) <ULCALC> ;AUXILIARY VELOCITY
       1FIELD OF TRANSVERSE FLOW')
110     FORMAT (/' ',5X,10I10/)
120     FORMAT (' ',I5,10(1PD10.3))
        END
```

```
      SUBROUTINE WLADI1
      IMPLICIT REAL*8 (A-H,O-Z)
C
C              *****   WLADI1   *****
C +-------------------------------------------------------------------+
C |                                                                   |
C |   THIS SUBROUTINE COMPUTES THE PSEUDO VELOCITIES ASSUMING         |
C |                                                                   |
C |   PRESSURES AT EACH NODE POINT BE THOSE AT PREVIOUS TIME STEP.    |
C |                                                                   |
C |   : IMPLICIT IN TRANSVERSE DIRECTION.                             |
C |                                                                   |
C +-------------------------------------------------------------------+
C
C==== COMMON ========================================================
      COMMON /MAT/       AMT(42,42)    ,BMT(3,31)       ,Y(31)
      COMMON /GMT/       NCHAN           ,NCHANM          ,LMAX
     1 ,LMAXM           ,KMAX            ,ICB(3,42)       ,LC(42,3)
     2 ,KCHAN(42,42)  ,THETA(31)       ,IBD(42)         ,ITYPE(42)
     3 ,NHALF           ,RP              ,WT              ,GAP(60)
     4 ,PITCH(60)       ,DZ(31)          ,ZCHNL(32)       ,DS(60)
     5 ,DHW(42,31)    ,DHU(60,31)     ,A(60,31)       ,AC(60,31)
     6 ,B(42,31)      ,D(60,31)       ,VS(42,31)      ,VC(60,31)
     7 ,VW(42,31)     ,NWRAP            ,MWRAPT(18)      ,IWRAP(18)
      COMMON /CNT/       NSTEP           ,TIME            ,CRNT
     1 ,DTHLF           ,TMAX            ,NMAX            ,ITMAX
     2 ,NOUT            ,PEPS
      COMMON /BND/       INFLAW          ,MAXW            ,WXT(20)
     1 ,WDATA(20)       ,INFLAT          ,MAXT            ,TXT(20)
     2 ,TDATA(20)       ,INFLAP          ,MAXPO           ,MAXPI
     3 ,PXTO(20)        ,PXTI(20)        ,PODATA(20)      ,PIDATA(20)
     4 ,INFLAQ          ,MAXQ            ,QXT(20)         ,QDATA(20)
     5 ,PDIST(31)      ,QIN             ,SGM(42)        ,WIN
     6 ,TIN             ,PIN
      COMMON /BLK/       LBD              ,LBU             ,LBL(31)
     1 ,MESHBL          ,LBS(42,31)     ,LBCR(60,31)    ,RBLC
     2 ,CPBLC           ,CNDBLC          ,WBLK            ,TBLK
     3 ,SGMB(60)       ,DZBL
      COMMON /GRD/       DZGR             ,LGR(31)         ,MESHGR
     1 ,FLOSS(42,31)  ,JSPACE(42,31)
      COMMON /VAR/       U6LN(60,31)   ,W6LN(42,31)   ,T6LN(42,31)
     1 ,P6N(42,31)    ,Q6LN(42,31)   ,R6LN(42,31)
      COMMON /WRK/       DIVL(42,31)   ,DP6N(42,31)   ,T6LNP(42,31)
     1 ,W6LNT(42,31)  ,U6LNT(60,31)  ,UW6LN(60,31)  ,UP6LN(60,31)
      COMMON /LIQ/       CPLN(42,31)   ,VSCLXX(60,31)  ,VSCLZ(42,31)
     1 ,CNDLX(60,31)  ,CNDLZ(42,31)  ,CPIN            ,RIN
     2 ,VISCOS          ,VSCLZX(60,31)
C=====================================================================
C
      DATA               LPD             /9/
      DATA               GRVTY           /9.8/
      DO 1900 L =2,LMAX
              LD =L-1
        DO 1000 I =1,NCHANM
```

```
                AMT(I,I) =1.0
                II =I+1
              DO 1000 J =II,NCHAN
                AMT(I,J) =0.0
                AMT(J,I) =0.0
1000        CONTINUE
                AMT(NCHAN,NCHAN) =1.0
            DO 1500 I =1,NCHAN
                VWX =VW(I,L)
                RAV =(1.0-THETA(L))*R6LN(I,LD)+THETA(L)*R6LN(I,L)
          VISCAV=(1.0-THETA(L))*VSCLZ(I,LD)+THETA(L)*VSCLZ(I,L)
                WX =DABS(W6LN(I,L))
                DHWX =DHW(I,L)
CC              TAUWL =FRIWLZ(RAV,WX,DHWX,I,L)
           CALL DRMA(I,L,RAV,VISCAV,FAVEX,FAVIM)
                JF =MAX(JSPACE(I,LD),JSPACE(I,L))
CC            IF(JF.EQ.1) TAUWL =0.0
           IF(JF.EQ.1) FAVEX=0.0
           IF(JF.EQ.1) FAVIM=0.0
CC              AMT(I,I) =AMT(I,I)+DTHLF*(TAUWL/RAV+FLOSS(I,L)*WX/2.0)
CC              Y(I) =W6LN(I,L)-DTHLF*(P6N(I,L)-P6N(I,LD))/(0.5*(DZ(LD)+DZ
CC     1           (L)))/RAV-DTHLF*GRVTY
           AMT(I,I)=AMT(I,I)+DTHLF*(FAVIM/RAV+FLOSS(I,L)*WX/2.0)
           Y(I)=W6LN(I,L)-DTHLF*(P6N(I,L)-P6N(I,LD))/(0.5*(DZ(LD)+DZ(L)))/RAV
          1      -DTHLF*GRVTY-DTHLF*FAVEX/RAV
            DO 1300 M =1,3
                J =LC(I,M)
              IF(J) 1300,1300,1100
1100            K =KCHAN(I,J)
                ACX =0.5*(AC(K,LD)+AC(K,L))
                UX =(1.0-THETA(L))*U6LN(K,LD)+THETA(L)*U6LN(K,L)
                KSN =ISIGN(1,I-J)
                FLK =UX*FLOAT(KSN)
              IF(FLK.LE.0.0) GO TO 1200
                DUMY =KSN*DTHLF*CONVTM(ACX,VWX,UX,1.0D00)
                AMT(I,J) =-DUMY
                AMT(I,I) =AMT(I,I)+DUMY
1200          CONTINUE
                DSX =(1.0-THETA(L))*DS(K)+THETA(L)*DS(K)
                VISX =VSCLXX(K,L)
                WX =W6LN(J,L)-W6LN(I,L)
                Y(I) =Y(I)+DTHLF*VISCTM(DSX,ACX,VWX,VISX,WX,RAV)
1300        CONTINUE
            IF(L.EQ.LMAX) GO TO 1400
                LU =L+1
                WU =0.5*(W6LN(I,L)+W6LN(I,LU))
                WX =W6LN(I,LU)-W6LN(I,L)
                BU =0.5*(B(I,L)+B(I,LU))
            IF(WU.LT.0.0) Y(I) =Y(I)-DTHLF*CONVTM(BU,VWX,WU,WX)
                Y(I) =Y(I)+DTHLF*VISCTM(DZ(L),BU,VWX,VSCLZ(I,L),WX,RAV)
1400            WX =W6LN(I,L)-W6LN(I,LD)
                WD =0.5*(W6LN(I,LD)+W6LN(I,L))
                BD =0.5*(B(I,LD)+B(I,L))
            IF(WD.GT.0.0) Y(I) =Y(I)-DTHLF*CONVTM(BD,VWX,WD,WX)
```

```
            Y(I) =Y(I)-DTHLF*VISCTM(DZ(LD),BD,VWX,VSCLZ(I,LD),WX,RAV)
1500    CONTINUE
        DO 1700 JJ =1,NCHAN
          IF(LBS(JJ,L).EQ.0) GO TO 1700
          DO 1600 KK =1,NCHAN
               AMT(JJ,KK) =0.0
1600           AMT(KK,JJ) =0.0
               AMT(JJ,JJ) =1.0
               Y(JJ) =0.0
          IF(L.EQ.LBD+1 .OR. L.EQ.LBU) Y(JJ) =WBLK
1700    CONTINUE
        CALL DECOMP(AMT,Y,IBD,NCHAN)
        DO 1800 I =1,NCHAN
               W6LNT(I,L) =Y(I)
1800    CONTINUE
1900  CONTINUE
      DO 2000 I =1,NCHAN
        IF(INFLAP.EQ.2) W6LNT(I,1) =W6LNT(I,2)
        IF(INFLAP.NE.2) W6LNT(I,1) =W6LN(I,1)
2000  CONTINUE
      WRITE (LPD,100)
      DO 2200 M =1,30
               I1 =(M-1)*10+1
               I2 =M*10
        IF(I2.GT.NCHAN) I2 =NCHAN
        WRITE (LPD,110) (J,J=I1,I2)
        DO 2100 I =1,LMAX
          WRITE (LPD,120) I,(W6LNT(J,I),J=I1,I2)
2100    CONTINUE
        IF(I2.GE.NCHAN) GO TO 2300
2200  CONTINUE
2300  CONTINUE
      RETURN
100   FORMAT (' ','W6LNT(JX,JZ) (VELOCITY) <WLADI1> ;AUXILIARY VELOCITY
     1FIELD OF AXIAL FLOW')
110   FORMAT (/' ',5X,10I10/)
120   FORMAT (' ',I5,10(1PD10.3))
      END
```

```
      SUBROUTINE WLADI2
      IMPLICIT REAL*8 (A-H,O-Z)
C
C              *****   WLADI2   *****
C +-------------------------------------------------------------------+
C |                                                                   |
C |   THIS SUBROUTINE COMPUTES THE PSEUDO VELOCITIES ASSUMING         |
C |                                                                   |
C |   PRESSURES AT EACH NODE POINT BE THOSE AT PREVIOUS TIME STEP.    |
C |                                                                   |
C |   : IMPLICIT IN AXIAL DIRECTION.                                  |
C |                                                                   |
C +-------------------------------------------------------------------+
C
C==== COMMON ========================================================
      COMMON /MAT/       AMT(42,42)    ,BMT(3,31)       ,Y(31)
      COMMON /GMT/       NCHAN           ,NCHANM          ,LMAX
     1 ,LMAXM            ,KMAX           ,ICB(3,42)       ,LC(42,3)
     2 ,KCHAN(42,42)  ,THETA(31)       ,IBD(42)         ,ITYPE(42)
     3 ,NHALF            ,RP             ,WT              ,GAP(60)
     4 ,PITCH(60)       ,DZ(31)         ,ZCHNL(32)       ,DS(60)
     5 ,DHW(42,31)    ,DHU(60,31)    ,A(60,31)       ,AC(60,31)
     6 ,B(42,31)      ,D(60,31)      ,VS(42,31)      ,VC(60,31)
     7 ,VW(42,31)     ,NWRAP          ,MWRAPT(18)      ,IWRAP(18)
      COMMON /CNT/       NSTEP           ,TIME            ,CRNT
     1 ,DTHLF            ,TMAX           ,NMAX            ,ITMAX
     2 ,NOUT             ,PEPS
      COMMON /BND/       INFLAW          ,MAXW            ,WXT(20)
     1 ,WDATA(20)        ,INFLAT         ,MAXT            ,TXT(20)
     2 ,TDATA(20)        ,INFLAP         ,MAXPO           ,MAXPI
     3 ,PXTO(20)         ,PXTI(20)       ,PODATA(20)      ,PIDATA(20)
     4 ,INFLAQ           ,MAXQ           ,QXT(20)         ,QDATA(20)
     5 ,PDIST(31)       ,QIN            ,SGM(42)         ,WIN
     6 ,TIN              ,PIN
      COMMON /BLK/       LBD             ,LBU             ,LBL(31)
     1 ,MESHBL           ,LBS(42,31)    ,LBCR(60,31)    ,RBLC
     2 ,CPBLC            ,CNDBLC         ,WBLK            ,TBLK
     3 ,SGMB(60)        ,DZBL
      COMMON /GRD/       DZGR            ,LGR(31)         ,MESHGR
     1 ,FLOSS(42,31)  ,JSPACE(42,31)
      COMMON /VAR/       U6LN(60,31)   ,W6LN(42,31)    ,T6LN(42,31)
     1 ,P6N(42,31)     ,Q6LN(42,31)   ,R6LN(42,31)
      COMMON /WRK/       DIVL(42,31)   ,DP6N(42,31)    ,T6LNP(42,31)
     1 ,W6LNT(42,31)  ,U6LNT(60,31)  ,UW6LN(60,31)   ,UP6LN(60,31)
      COMMON /LIQ/       CPLN(42,31)   ,VSCLXX(60,31)  ,VSCLZ(42,31)
     1 ,CNDLX(60,31)  ,CNDLZ(42,31)  ,CPIN            ,RIN
     2 ,VISCOS           ,VSCLZX(60,31)
C=====================================================================
C
      DATA               LPD             /9/
      DATA               GRVTY           /9.8/
              LST =1
              LEN =LMAX
      DO 2200 I =1,NCHAN
```

```
      DO 1000 L =1,LMAX
            BMT(1,L) =0.0
            BMT(2,L) =1.0
1000        BMT(3,L) =0.0
      DO 1700 L =1,LMAX
            LD =L-1
            LU =L+1
        IF(L.GE.LMAX) LU =L
            VWX =VW(I,L)
        IF(L.EQ.LMAX) GO TO 1300
            WU =0.5*(W6LN(I,L)+W6LN(I,LU))
            BU =0.5*(B(I,L)+B(I,LU))
        IF(WU) 1100,1100,1200
1100        DUMY =DTHLF*CONVTM(BU,VWX,WU,1.0D00)
            BMT(2,L) =BMT(2,L)-DUMY
            BMT(3,L) =DUMY
        GO TO 1300
1200        DUMY =DTHLF*CONVTM(BU,VW(I,LU),WU,1.0D00)
            BMT(1,LU) =-DUMY
            BMT(2,LU) =BMT(2,LU)+DUMY
1300    CONTINUE
            WX =DABS(W6LN(I,L))
            DHWX =DHW(I,L)
            WU =W6LN(I,LU)-W6LN(I,L)
        IF(L.GT.1) GO TO 1400
            RAV =0.5*(RIN+R6LN(I,1))
      VISCAV=0.5*(VISCOS+VSCLZ(I,1))
CC          TAUWL =FRIWLZ(RAV,WX,DHWX,I,L)
      CALL DRMA(I,L,RAV,VISCAV,FAVEX,FAVIM)
CC          BMT(2,1) =BMT(2,1)+DTHLF*TAUWL/RAV
CC          Y(1) =W6LN(I,1)-DTHLF*(P6N(I,1)-PIN)/DZ(1)/RAV-DTHLF*
CC   1        VISCTM(DZ(1),BU,VWX,VSCLZ(I,1),WU,RAV)
      BMT(2,1)=BMT(2,1)+DTHLF*FAVIM/RAV
      Y(1)=W6LN(I,1)-DTHLF*(P6N(I,1)-PIN)/DZ(1)/RAV-DTHLF*
     1    VISCTM(DZ(1),BU,VWX,VSCLZ(I,1),WU,RAV)-DTHLF*FAVEX/RAV
        GO TO 1700
1400        RAV =(1.0-THETA(L))*R6LN(I,LD)+THETA(L)*R6LN(I,L)
      VISCAV=(1.0-THETA(L))*VSCLZ(I,LD)+THETA(L)*VSCLZ(I,L)
      CALL DRMA(I,L,RAV,VISCAV,FAVEX,FAVIM)
CC          TAUWL =FRIWLZ(RAV,WX,DHWX,I,L)
            JF =MAX(JSPACE(I,LD),JSPACE(I,L))
CC        IF(JF.EQ.1) TAUWL =0.0
      IF(JF.EQ.1) FAVEX=0.0
      IF(JF.EQ.1) FAVIM=0.0
CC          BMT(2,L) =BMT(2,L)+DTHLF*(TAUWL/RAV+FLOSS(I,L)*WX/2.0)
CC          Y(L) =W6LN(I,L)-DTHLF*(P6N(I,L)-P6N(I,LD))/(0.5*(DZ(LD)+DZ
CC   1        (L)))/RAV-DTHLF*GRVTY
      BMT(2,L)=BMT(2,L)+DTHLF*(FAVIM/RAV+FLOSS(I,L)*WX/2.0)
      Y(L)=W6LN(I,L)-DTHLF*(P6N(I,L)-P6N(I,LD))/(0.5*(DZ(LD)+DZ(L)))
     1    /RAV-DTHLF*GRVTY-DTHLF*FAVEX/RAV
            BD =0.5*(B(L,LD)+B(I,L))
            WD =W6LN(I,L)-W6LN(I,LD)
            Y(L) =Y(L)-DTHLF*VISCTM(DZ(LD),BD,VWX,VSCLZ(I,LD),WD,RAV)
        IF(L.LT.LMAX) Y(L) =Y(L)+DTHLF*VISCTM(DZ(L),BU,VWX,VSCLZ(I,L),
```

```
     1       WU,RAV)
             DO 1600 M =1,3
                 J =LC(I,M)
               IF(J) 1600,1600,1500
1500             K =KCHAN(I,J)
                 ACX =0.5*(AC(K,LD)+AC(K,L))
                 DSX =(1.0-THETA(L))*DS(K)+THETA(L)*DS(K)
                 UX =(1.0-THETA(L))*U6LN(K,LD)+THETA(L)*U6LN(K,L)
                 WX =W6LN(J,L)-W6LN(I,L)
                 KSN =ISIGN(1,I-J)
                 FLK =UX*FLOAT(KSN)
               IF(FLK.GT.0.0) Y(L) =Y(L)+KSN*DTHLF*CONVTM(ACX,VWX,UX,WX)
                 Y(L) =Y(L)+DTHLF*VISCTM(DSX,ACX,VWX,VSCLXX(K,L),WX,RAV)
1600           CONTINUE
1700         CONTINUE
             DO 1800 L =2,LMAXM
                   LD =L-1
                   LU =L+1
               IF(LBS(I,LD).EQ.1) BMT(1,L) =0.0
               IF(LBS(I,LU).EQ.1) BMT(3,L) =0.0
               IF(LBS(I,L).NE.1) GO TO 1800
                 BMT(1,L) =0.0
                 BMT(2,L) =1.0
                 BMT(3,L) =0.0
                 Y(L) =0.0
               IF(L.EQ.LBD+1 .OR. L.EQ.LBU) Y(L) =WBLK
1800         CONTINUE
             IF(INFLAP.NE.2) GO TO 1900
                   BMT(2,1) =1.0
                   BMT(3,1) =-1.0
                   Y(1) =0.0
             GO TO 2000
1900         CONTINUE
                   BMT(2,1) =1.0
                   BMT(3,1) =0.0
                   Y(1) =W6LN(I,1)
2000         CONTINUE
             CALL GAUSSJ(BMT,Y,LST,LEN,2)
             DO 2100 L =1,LMAX
                   W6LNT(I,L) =Y(L)
2100         CONTINUE
2200       CONTINUE
           WRITE (LPD,100)
           DO 2400 M =1,30
                   I1 =(M-1)*10+1
                   I2 =M*10
             IF(I2.GT.NCHAN) I2 =NCHAN
             WRITE (LPD,110) (J,J=I1,I2)
             DO 2300 I =1,LMAX
               WRITE (LPD,120) I,(W6LNT(J,I),J=I1,I2)
2300         CONTINUE
             IF(I2.GE.NCHAN) GO TO 2500
2400       CONTINUE
2500       CONTINUE
```

```
      RETURN
100   FORMAT (' ','W6LNT(JX,JZ)  (VELOCITY) <WLADI2> ;AUXILIARY VELOCITY
     1FIELD OF AXIAL FLOW')
110   FORMAT (/' ',5X,10I10/)
120   FORMAT (' ',I5,10(1PD10.3))
      END
```

```
      SUBROUTINE EFFVIS
      IMPLICIT REAL*8 (A-H,O-Z)
C
C              *****   EFFVIS   *****
C +-------------------------------------------------------------------+
C |     CALCULATION OF EFFECTIVE VISCOSITY OF COOLANT                 |
C +-------------------------------------------------------------------+
C
C==== COMMON ========================================================
      COMMON /FTR/       CFR              ,CVEF
      COMMON /GMT/       NCHAN            ,NCHANM          ,LMAX
     1 ,LMAXM            ,KMAX            ,ICB(3,42)       ,LC(42,3)
     2 ,KCHAN(42,42)  ,THETA(31)       ,IBD(42)         ,ITYPE(42)
     3 ,NHALF            ,RP              ,WT              ,GAP(60)
     4 ,PITCH(60)       ,DZ(31)          ,ZCHNL(32)       ,DS(60)
     5 ,DHW(42,31)     ,DHU(60,31)     ,A(60,31)        ,AC(60,31)
     6 ,B(42,31)        ,D(60,31)        ,VS(42,31)       ,VC(60,31)
     7 ,VW(42,31)      ,NWRAP           ,MWRAPT(18)      ,IWRAP(18)
      COMMON /VAR/       U6LN(60,31)   ,W6LN(42,31)   ,T6LN(42,31)
     1 ,P6N(42,31)     ,Q6LN(42,31)   ,R6LN(42,31)
      COMMON /LIQ/       CPLN(42,31)   ,VSCLXX(60,31)  ,VSCLZ(42,31)
     1 ,CNDLX(60,31)  ,CNDLZ(42,31)  ,CPIN             ,RIN
     2 ,VISCOS          ,VSCLZX(60,31)
C=====================================================================
C
      DATA               FACTR          /10.0/
      DO 1700 I =1,NCHAN
        DO 1700 M =1,3
              J =LC(I,M)
          IF(I-J) 1300,1700,1700
1300          K =KCHAN(I,J)
          DO 1600 L =1,LMAX
              WX =DABS(0.5*(W6LN(I,L)+W6LN(J,L)))
              RAV =0.5*(R6LN(I,L)+R6LN(J,L))
      VISCOS=0.5*(VSCLZ(I,L)+VSCLZ(J,L))
              XLM =FACTR*GAP(K)
            IF(L.NE.1) GO TO 1350
              UX =0.0
              DU =0.0
              DZAV =DZ(L)
              GO TO 1375
1350          UX =DABS(0.5*(U6LN(K,L)+U6LN(K,L-1)))
              DU =DABS(U6LN(K,L)-U6LN(K,L-1))
              DZAV =0.5*(DZ(L)+DZ(L-1))
1375        IF(WX) 1400,1400,1500
1400          VSCLXX(K,L) =VISCOS
              VSCLZX(K,L) =VISCOS+RAV*(0.04*XLM)**2*DU/DZAV
            GO TO 1600
1500          RAV =0.5*(R6LN(I,L)+R6LN(J,L))
      VISCOS=0.5*(VSCLZ(I,L)+VSCLZ(J,L))
              DHWX =DHW(I,L)
              TAUWL =FRIWLZ(RAV,WX,DHWX,I,L)
              FR =TAUWL*DHW(I,L)/RAV/WX
              VSCLXX(K,L)=VISCOS+CVEF*RAV*DMAX1(UX,WX)*DHU(K,L)*FR**0.5
```

```
                VSCLZX(K,L)  =VISCOS+RAV*(0.04*XLM)**2*DU/DZAV
1600        CONTINUE
1700    CONTINUE
        RETURN
        END
```